Veröffentlichungen der DGK

Ausschuss Geodäsie der Bayerischen Akademie der Wissenschaften

Reihe C | Dissertationen | Heft Nr. 834

Omid Elmi

Dynamic water masks from optical satellite imagery

München 2019

Verlag der Bayerischen Akademie der Wissenschaften

ISSN 0065-5325 | ISBN 978-3-7696-5246-8

Veröffentlichungen der DGK

Ausschuss Geodäsie der Bayerischen Akademie der Wissenschaften

Reihe C | Dissertationen | Heft Nr. 834

Dynamic water masks from optical satellite imagery

Von der Fakultät Luft- und Raumfahrttechnik und Geodäsie
der Universität Stuttgart
zur Erlangung der Würde eines
Doktors der Ingenieurwissenschaften (Dr.-Ing.)
genehmigte Abhandlung

Vorgelegt von

Omid Elmi

aus Tehran, Iran

München 2019

Verlag der Bayerischen Akademie der Wissenschaften

ISSN 0065-5325 ISBN 978-3-7696-5246-8

Adresse der DGK:

Ausschuss Geodäsie der Bayerischen Akademie der Wissenschaften (DGK)

Alfons-Goppel-Straße 11 ● D – 80 539 München

Telefon +49 – 331 – 288 1685 ● Telefax +49 – 331 – 288 1759

E-Mail post@dgk.badw.de ● http://www.dgk.badw.de

Prüfungskommission:

Vorsitzender: Prof. Dr.-Ing. Sabine Klinkner

Referent: Prof. Dr.-Ing. Nico Sneeuw

Korreferenten: Prof. Dr.-Ing Ribana Roscher (Universität Bonn)

Tag der mündlichen Prüfung: 27.05.2019

ISSN 0065-5325 ISBN 978-3-7696-5246-8

Acknowledgment

After writing these lines I can finally close the folder "PhdThesis" on my computer after a long journey. Words can never express my gratitude towards several people who help me finally pressing "Alt+F4".

I would not have reached this stage without the advice and guidance of my supervisor Prof. Nico Sneeuw. Studying under his supervision is a privilege, not only because of his deep knowledge but also his inspiration attitude toward science. I am grateful for his patience in discussions, valuable comments and warm encouragements. For all of this I owe him more than I can describe.

I am also grateful to my co-referee Prof. Ribana Roscher for accepting to be on the committee, and reviewing my thesis. Her different perspective toward my research topic opens new outlooks for further research possibilities. The visit to her research group helped me a lot in preparing my final presentation.

I would like to express my sincere appreciation to Dr. Mohammad J. Tourian. He is one of the main instrumental in getting me to this point. The foundation of this PhD research has been laid through discussions with him. I was so lucky to be an office mate with a true friend, a supportive colleague and an excellent scientist.

I gratefully acknowledge Prof. Mohammad Ali Sharifi, my master's thesis supervisor at the University of Tehran. During his lectures I found my interest in Geodesy.

I greatly appreciate all of my colleagues at the Institute of Geodesy for creating an enjoyable environment at the institute, joining me in discussions during the lunch breaks and providing fruit and fun during the fruit breaks.

I also would like to thank the Ministry of Science, Research and the Arts of Baden-Württemberg for funding this work for three years, through the "Landesgraduiertenförderung" scholarship.

My words cannot express my gratitude that I feel for my parents. They have always backed my decisions and choices and had unwavering faith in me. I have had their unconditional support throughout my entire life. In particular, they have been a constant source of love, concern, and strength during this endeavor. I would also like to

acknowledge my uncle, Amo Reza and his family, for helping me especially during my initial days in Germany.

Last, but not least, I want to extend my deepest thanks to my lovely wife Mahsa. I could not finish this journey successfully without her help and patience. Thanks, Mahsa for cheering me up, motivating and supporting me every day.

Abstract

Investigation of the global freshwater system has a vital role in critical issues e.g. sustainable development of water resources, acceleration of the hydrological cycle, variability of global sea level. Measurement of river streamflow is vital for such investigations as it gives a reliable estimate of freshwater fluxes over the continents. Despite such importance, the number of river discharge gauging station has been decreasing. At the same time, information on the global freshwater system has been increasing because of various types of ground observations, water-use information and space-borne geodetic observations. Nevertheless, we cannot answer properly crucial questions about the amount of freshwater available on a certain river basin, or the spatial and temporal dynamics of freshwater variations and discharge, or the distribution of world's freshwater resources in the future. The lack of comprehensive measurements of surface water storage and river discharge is a major impediment for a realistic understanding of the hydrological water cycle, which is a must for answering the aforementioned questions. This thesis aims to improve the methods for monitoring the surface extent of inland water bodies using satellite images.

Satellite imaging systems capture the Earth surface in a wide variety of spectral and spatial resolution repeatedly. Therefore satellite imagery provides the opportunity to monitor the spatial change in shorelines, which can serve as a way to determine the water extent.

Each band of a multispectral image reveals a unique characteristic of the Earth surface features like surface water extent. However selecting the spectral bands which provide the relevant information is a challenging task. In this thesis, we analyse the potential of multispectral transformations like Principal Component Analysis (PCA) and Canonical Correlation Analysis (CCA) to tackle this issue by condensing the information available in all spectral bands in just a few uncorrelated variables. Moreover, we investigate how the change between multispectral images at different epochs can be highlighted by using the transformations.

This study proposes an automatic algorithm for extracting the lake water extent from MODIS images and generating dynamics lake masks. For improving the accuracy of the lake masks and computational efficiency of the algorithm, two masks are defined for limiting the search area. The restricting masks are developed according to DEM of the surrounding area together with a map of the long-term variation of pixel values. Subsequently, an unsupervised pixel-based classification algorithm is applied for defining the lake coastline. The algorithm particularly deals with the challenges of generating long time series of lake masks. We apply the algorithm on five lakes in Africa and Asia,

each of which demonstrates a challenge for lake area monitoring. However in the validation section, we demonstrate that the algorithm can generate accurate dynamic lake masks.

Rivers show diverse behaviour along their path due to the contribution of different parameters like gradient of the elevation, river slope, tributaries and river bed morphology. Therefore for generating accurate river reach mask, we need to consider additional sources of information apart from pixel intensity. The region-based classification algorithm that we propose in this study takes advantages of all types of available information including pixel intensity and spatial and temporal interactions. Markov Random Fields provide a flexible frame for interaction between different sources of data and constraint. To find the most probable configuration of the field, the Maximum A Posteriori solution for the MRF must be found. To this end, the problem is reshaped as an energy minimization. The energy function is minimized applying graph cuts as a powerful optimization technique. The uncertainty in the graph cuts solution is also measured by calculating the minimum marginal energies. The proposed method is applied to four rivers reaches with different hydrological characteristics. We validate the obtained river area time series by comparing with in situ river discharge and satellite altimetric water level time series.

Moreover, in this study, we present river discharge estimation models using the generated river reach masks. Our aim is to find an empirical relationship between the average river reach width and river discharge. The statistics in the validation periods support the idea of using river width-discharge prediction models as a complementary technique to the other spaceborne geodetic river discharge prediction approaches.

Zusammenfassung

Aufgrund der wichtigen Rolle des globalen Süßwassers für die nachhaltige Entwicklung der Wasserressourcen sowie die Beschleunigung des Wasserkreislaufs als auch die Variabilität des globalen Meeresspiegels haben sich viele Studien in den letzten Jahren auf die Untersuchung des globalen Süßwassersystems konzentriert. Flussabflussmessungen sind für solche Studien unerlässlich, da sie eine zuverlässige Schätzung der Süßwasserflüsse über die Kontinente ermöglichen. Trotz dieser bedeutenden Rolle ist die Anzahl der Flussabfluss-Pegelstationen in der Vergangenheit zurückgegangen. Im Allgemeinen wurden aber die Informationen über das globale Süßwassersystem durch die Zusammenstellung verschiedener Arten von Bodenbeobachtungen, Wassernutzungsinformationen und geodätischen Beobachtungen im Weltraum verstärkt. Wir können jedoch nicht die entscheidenden Fragen nach der Menge des in einem bestimmten Flussgebiet verfügbaren Süßwassers, der räumlichen und zeitlichen Dynamik von Süßwasservariationen und -abflüssen oder der Verteilung der zukünftigen weltweiten Süßwasserressourcen beantworten. Diese Fragen können nicht vollständig beantwortet werden, da es an umfassenden Messungen der Oberflächenwasserspeicherung und der Flussabflüsse mangelt. Diese Dissertation zielt darauf ab, die Methoden zur Oberflächenwassersüberwachung von Binnengewässern mithilfe von Satellitenbildern zu verbessern.

Satellitengestützte bildgebende Systeme erfassen die Erdoberfläche regelmäßig in einer Vielzahl von spektralen und räumlichen Auflösungen. Daher bieten Satellitenbilder die Möglichkeit, die räumliche Veränderung der Wasser-Land-Grenzen zu überwachen, die als Grundlage für die Bestimmung der Oberflächenwasserausdehnung verwendet wird.

Die Erdoberfläche wird in verschiedenen Wellenlängenbereichen in jedem Spektralband eines multispektralen Bildes erfasst. Daher offenbart jedes Band eines multispektralen Bildes eine einzigartige Eigenschaft der Erdoberflächenmerkmale wie die Oberflächenwasserfläche. Jedoch ist die Auswahl der Spektralbänder, die die relevanten Informationen liefern, eine anspruchsvolle Aufgabe. In dieser Arbeit wird das Potenzial multispektraler Transformationen wie Principal Component Analysis (PCA) und Canonical Correlation Analysis (CCA) analysiert, um dieses Problem anzugehen, indem die in allen Spektralbändern verfügbaren Informationen in nur wenigen nicht korrelierten Variablen zusammengefasst werden. Darüber hinaus wird untersucht, wie der zeitliche Unterschied zwischen zwei multispektralen Bildern durch die Verwendung der oben genannten Transformationen unterstrichen werden kann.

Diese Studie schlägt einen automatischen Algorithmus für die Extraktion des Seeoberflächenwassers aus MODIS-Bildern vor und erzeugt die dynamischen Wassermasken. Zur Verbesserung der Genauigkeit der Wassermasken und der Effizienz des Algorithmus sind zwei Masken definiert, um den Suchbereich zu begrenzen. Die Einschränkungsmasken werden basierend auf ein digitales Geländemodell (DGM) der Umgebung und die langfristigen Variatione der Pixelwerte erzeugt. Dementsprechend wird zur Definition der Wasser-Land-Grenze ein unbeaufsichtigter, pixelbasierter Klassifikationsalgorithmus verwendet. Der Algorithmus beschäftigt sich insbesondere mit den Herausforderungen bei der Erzeugung langer Zeitreihen von Wassermasken. Der Algorithmus wird auf fünf Seen in Afrika und Asien angewendet, von denen jeder eine Herausforderung für die Überwachung des Seegebiets darstellt. Im Abschnitt „Validation“ werden wir sehen, dass der Algorithmus genaue dynamische Wassermasken erzeugen kann.

Flüsse zeigen aufgrund des Beitrags verschiedener Parameter wie Höhenunterschied, Flusshang, Nebenflüsse und Flussbettmorphologie unterschiedliches Verhalten auf ihrem Weg. Um eine genaue Wassermaske von Flussabschnitten zu erzeugen, sollten wir daher neben der Pixelintensität auch eine zusätzliche Informationsquelle berücksichtigen. Der regional basierte klassifikationsalgorithmus, den wir in dieser Studie vorschlagen, nutzt alle Arten von verfügbaren Informationen, einschließlich Pixelintensität und räumlicher und zeitlicher Interaktionen. Die Markov Random Fields bieten einen flexiblen Rahmen für die Interaktion zwischen verschiedenen Datenquellen und Einschränkungen. Um die wahrscheinlichste Konfiguration des Feldes zu finden, sollte die Maximum A Posteriori Lösung für das MRF gefunden werden. Zu diesem Zweck wird das Problem in eine Energieminimierung umgesetzt. Zur Minimierung der Energiefunktion werden *graph cuts* als leistungsfähige Optimierungstechnik angewendet. Die Unsicherheit in der Lösung der *graph cuts* wird zudem durch die Berechnung der minimalen Marginalen Energien gemessen. Die vorgeschlagene Methode wird auf vier Flussabschnitten mit unterschiedlichen hydrologischen Eigenschaften angewendet. Die erhaltenen Flussgebietszeitreihen werden durch den Vergleich mit den Abflussmessungen an Pegeln und satellitengestützten altimetrischen Wasserstandszeitreihen validiert.

Darüber hinaus stellt diese Studie Abflussschätzmodelle unter Verwendung der generierten Wassermaske von Flussabschnitten vor. Ziel ist es, einen empirischen Zusammenhang zwischen der durchschnittlichen Flussreichweite und dem Abfluss zu finden. Die Statistiken in den Validierungszeiträumen unterstützen die Idee, Modelle zur Vorhersage der Flussbreite und des Abflusses als ergänzende Technik zu den anderen satellitengestützten geodätischen Vorhersageansätzen für Flusseinleitungen zu verwenden.

Contents

1 Introduction **1**
- 1.1 Development of satellite imaging: a historical overview . . . 1
- 1.2 Monitoring the inland surface water bodies by spaceborne geodetic sensors . . . 8
- 1.3 Basic principles, properties of the optical images . . . 14
- 1.4 Introduction to change detection methods for water area monitoring . . . 18
- 1.5 Objectives . . . 23
- 1.6 Case studies and data . . . 24
  - 1.6.1 Case studies . . . 24
  - 1.6.2 Data set . . . 28
- 1.7 Outline of the thesis . . . 33

2 Multispectral transformations for change detection **35**
- 2.1 Introduction . . . 35
- 2.2 Methodology . . . 36
  - 2.2.1 Principal Components Analysis . . . 36
  - 2.2.2 Tasselled Cap transformation . . . 39
  - 2.2.3 Canonical Correlation Analysis . . . 41
- 2.3 Applications of multispectral transformations in inland water body change detection . . . 46
  - 2.3.1 Principal Component Analysis . . . 46
  - 2.3.2 MAD + MAF . . . 59
- 2.4 Summary . . . 65

3 Monitoring lake surface area from satellite imagery **67**
- 3.1 Introduction . . . 67
- 3.2 Methodology . . . 68
- 3.3 Results and validation . . . 77
  - 3.3.1 Nasser Lake . . . 77
  - 3.3.2 Rukwa Lake . . . 83
  - 3.3.3 Mosul Dam Lake . . . 87
  - 3.3.4 Tharthar Lake . . . 90
- 3.4 Monitoring the desiccation of Lake Urmia in Iran . . . 92
- 3.5 Summary . . . 97

4 Monitoring river reach area from satellite imagery **99**
- 4.1 Introduction . . . 99

4.2 Methodology . . . 102
4.2.1 An overview of the mathematical concept . . . 103
4.2.2 Basics of graphs, graph cuts techniques and max-flow algorithms 106
4.2.3 Measuring uncertainty in the graph cuts solution . . . 109
4.2.4 Implementation of energy functions . . . 111
4.2.5 Review of proposed method . . . 114
4.3 Results and validation . . . 116
4.3.1 Niger River, Lokoja station . . . 116
4.3.2 Niger River, Koulikoro station . . . 123
4.3.3 Congo River, Malebo Pool . . . 125
4.3.4 Po River, Italy . . . 127
4.4 River discharge estimation using river width . . . 129
4.4.1 Simultaneous observations approach . . . 131
4.4.2 Quantile look-up table approach . . . 136
4.5 Summary . . . 139

5 Concluding Remarks and Outlook **143**

Bibliography **148**

A Performance metrics **181**

B Gauss-Helmert adjustment model **183**

Index **187**

Chapter 1

Introduction

1.1 Development of satellite imaging: a historical overview

The history of remote sensing began by Gaspard Felix Tournachon, known as Nadar, in the year 1858. He captured the first aerial photograph from a balloon over Paris, France. According to the report *History of remote sensing, aerial photography* written by Baumann (2014), the earliest surveying aerial photograph was taken by James Wallace Black and Samuel Archer King over Boston city from a balloon in 1860. Subsequently, scientists installed cameras on kites or pigeons to take aerial photos. In 1903, Alfred Maul, a German engineer, developed successfully his rocket system called Maul Camera Rocket. In the next year, his rocket took the first areal image from about 580 m altitude. The development of aerial imaging was notable during the World War I. At the beginning of the war, aerial observers did reconnaissance by making the sketch and verbally conveying conditions on the ground. But by the end of the war, both Germany and England captured the entire front at least twice a day. Until the beginning of the World War II, several significant developments occurred in the filed of remote sensing, for examples

- publishing the first book on aerial photo interpretation,
- developing the first multi-layer color film,
- increasing the use of aerial photography in non-military fields like agriculture and forestry,
- founding the American society of photogrammetry,
- recording the image of division between troposphere and stratosphere for the first time and also capturing the actual curvature of the Earth.

Aerial photoreconnaissance was recognized as a key parameter of victory in the World War II. The statement of commander of American amphibious forces in the Pacific,

> "Photographic reconnaissance has been our main source of intelligence in the Pacific. Its importance cannot be overemphasized"

demonstrates the importance of aerial photography in military applications. After the World War II in the 1950s, aerial photography continued to progress. Multispectral imaging was tested for several applications in the optical domain. Side-looking airborne radar (SLAR) and synthetic aperture radar (SAR) were developed in the radar technology domain. The need for the surveillance over the Soviet Union military hardwares, led to the development of U-2 by The United States in 1955. U-2 designed for covert reconnaissance missions over the Soviet Union at above 21 000 m altitude. U-2 flew through the world for a wide variety of non-military applications. So, launching U-2 symbolized as the beginning of using satellite to look at the Earth's surface and established the term *remote sensing* (Baumann, 2014).

The year 1957 is another historical year in the field of aerial photography and remote sensing. The Soviet Union launched Sputnik I, the first artificial satellite, which was just a polished metal sphere about the size of a beach ball. Sputnik was not equipped with any sensor but it provided valuable information about the density of the atmosphere and the ionosphere by tracking the satellite from the Earth. The US had to react properly to the advent of Sputnik by the Soviet Union, if they wanted to compete with them in the field of space technology. They increased the investment of money in scientific research and education leading to the establishment of the Advanced Research Projects Agency (ARPA) and The National Aeronautics and Space Administration (NASA). Finally in 1958, the United Stated launched Explorer I. This satellite carried a small scientific payload that eventually discovered the magnetic radiation belts around the Earth. The Explorer program continued as a successful ongoing series of lightweight, scientifically useful spacecraft (NASA, 2007). After Explorer, US continued reinforcing its reconnaissance capability by developing the Corona system which was a series of reconnaissance satellites. The Corona program was active until 1972 and mapped almost 14 million square kilometre over the Soviet Union and China in more than 100 missions (Pelton et al., 2012).

In April 1960, the first exclusive civil satellite remote sensing system was launched. The Television Infrared Observation Satellites (TIROS) demonstrated the tremendous potential of satellite images in a variety of environmental applications including weather, ice monitoring and ocean studies (Pelton et al., 2012). Launching Landsat 1 was the next progress in the field of mapping the Earth from space. Landsat 1 was the first systematic moderate resolution civil remote sensing system (Pelton et al., 2012). It carried the Multispectral Scanner (MSS) which provided images from the Earth features in four different spectral bands (green, red and two infrared IR) at 80 m resolution from 900 km altitude. The Landsat program continued in the next years and the later satellites were equipped with more advanced sensors. For example in 1984, the Landsat 5 Thematic Mapper (TM) provided images in seven spectral bands (visible, short-wave inferred (SWIR), IR) with 30 m pixel size and 16 day temporal resolution. The last member of this family was launched in 2013; Landsat 8 has been equipped with the most advanced optical cameras. As a result, it can provide 12-bit images in eleven spectral bands with various spatial resolutions.

Launching SPOT 1 (French: Satellite Pour l'Observation de la Terre, lit. "satellite for observation of the Earth") as the first commercial high-resolution optical imaging mission in 1986 was another major improvement in the history of remote sensing. This mission was initiated by the French space agency and provided images in four spectral bands with 10 m (panchromatic) and 20 m (green, red, NIR) spatial resolution and variable revisit time between one to four days depending on the latitude. SPOT 7, the last member of this family, was launched in 2014. It provides images in five spectral bands with 1.5 m (panchromatic) and 6 m (visible, NIR). The idea of using satellite images for commercial purposes caught quickly (Pelton et al., 2012) and numbers of commercial imaging satellites like GeoEye on the year 2008 and QuickBird on the year 2001 have been launched.

Development of hyperspectral sensors is one of the most significant breakthrough in the satellite imaging history. These sensors can measure the reflected radiation from the Earth surface at a series of narrow and contiguous wavelength bands. For example the light spectrum is divided in five or ten spectral bands in multispectral images. But in hyperspectral images, it is divided in very narrow spectral slots (up to 200) (Shippert, 2003). The immense variability of spectral bands facilitates the identification and quantification of the Earth surface materials' physical and chemical attributes in hyperspectral images. Hyperspectral imaging presents very difficult issues in terms of sending data back to Earth and analysing, interpreting and visualising the mountain of data (Pelton et al., 2012).

In the year 1951, Carl Wiley, an American mathematician and engineer, observed a one-to-one correspondence between the along-track coordinate of a reflecting object and the instantaneous Doppler shift of the signal reflected to the radar by that object (Mc Candless & Jackson, 2004). This finding was the basis of a major improvement in remote sensing. In 1978, Seasat, the first satellite dedicated to the use of microwave sensor for the Earth's oceans was launched by NASA (Fu & Holt, 1982). Seasat was the first Synthetic Aperture Radar (SAR) satellite specifically designed for oceanographic phenomena. Its observations were used in applications like signatures of surface wave, ocean topography, sea surface temperature etc. (Fu & Holt, 1982). Seasat is also considered as the first satellite equipped with radar altimeter to measure the distance between a satellite and the ocean surface. This development brought numerous new opportunities for scientists to study Earth related phenomena. A SAR system is independent of solar illumination, so it properly functions during day and night. Also a SAR system is unaffected by cloud coverage, therefore it can acquire images in rainy days. Ocean and ice observations were the main target for developing the primary SAR satellites. But, after a while, using SAR images has been extended to almost all Earth related applications including crop and forest management, land monitoring and management, hydrology and disaster management (Mc Candless & Jackson, 2004).

In 1991, the European Space agency (ESA) launched the European Remote Sensing (ERS-1) satellite and four years later, ERS-2 joined it in orbit. At that time, ERS satellites provided the most sophisticated Earth observations from space independent of weather condition. In 1995, the two satellites were linked together to develop the first

tandem mission which lasted for nine months. During this time, the increment of observations offered scientists a unique opportunity to observe changes over a very short period of time, as both satellites orbited Earth only 24 hours apart (ESA, 2003). The successor of ERS satellites was Environmental Satellite (ENVISAT) launched 2002. It was the largest civilian Earth observation mission and carried ten different instruments. ENVISAT provided SAR images in C-band with different spatial resolutions (30 m in image mode, 150 m in wide swath mode, 1 km in global monitoring mode). In 2014, the first Sentinel 1 satellite launched to replace ENVISAT which lost the connection with the Earth in 2012. Now, plenty of SAR satellites take images at different frequencies, C-band (Sentinel-1), L-band (ALOS-2), X-band (TerraSAR-X), with different spatial resolutions (1 m, 3 m, 5 m and 20 m) from the Earth surface.

It is about seven decades that information provided by satellites help scientists to improve their knowledge about our planet. Gail (2007) described this development interestingly:

> "Only decades ago, collecting Earth information meant journeying into the field to analyse rocks, watching stream gauges to assess flow, or peering out the window periodically to observe weather patterns. Today's remote sensing devices greatly expand the reach of our eyes, allowing us to gather information over a wide range of spatial scales, across the spectrum, and with a wide dynamic range."

At the moment, more than 1167 active satellites orbit the Earth and 33 countries have dedicated missions to observe the Earth surface from space (Berger, 2015). Figure 1.1 presents the deployment of SAR and optical imagery missions from the beginning.

Today, remote sensing data has a critical role in most Earth related studies like forestry, agriculture, hazard and disaster monitoring or water management. But in the near future, the largest motivation for more accurate and frequent observations from the Earth surface may be our growing impact on the natural world (Gail, 2007). The impact of human activities is indeed changing the Earth's climate (National Research Council, 2001) and we cannot ignore the civilization's influence in increasing the load of greenhouse gases, land cover change, aerosols. According to Carlowicz (2010), Earth surface temperature analysis conducted by scientists at NASA shows that the average global Earth temperature has increased about 0.8° C since 1880 and two-third of this increment has occurred since 1975 (Hansen et al., 2010). So, there is a general consensus that global average surface air temperature increased during the 20th century and although the magnitude of future growth is uncertain, the majority of assessments indicate that future global warming is "very likely" (IPCC, 2001; Huntington, 2006; NAST, 2001; Arctic Climate Impact Assessment (ACIA), 2004). Theoretically, it is expected that climate change will result in increasing evaporation and precipitation which may intensify the water cycle (IPCC, 2001; Del Genfo et al., 1991; Loaiciga et al., 1996; Trenberth, 1999; Held & Soden, 2000). Acceleration of the water cycle will enhance the potential of extreme events like tropical storms, severe floods and droughts, which affect human life directly and indirectly (IPCC, 2001; Manabe et al., 2004). The first step

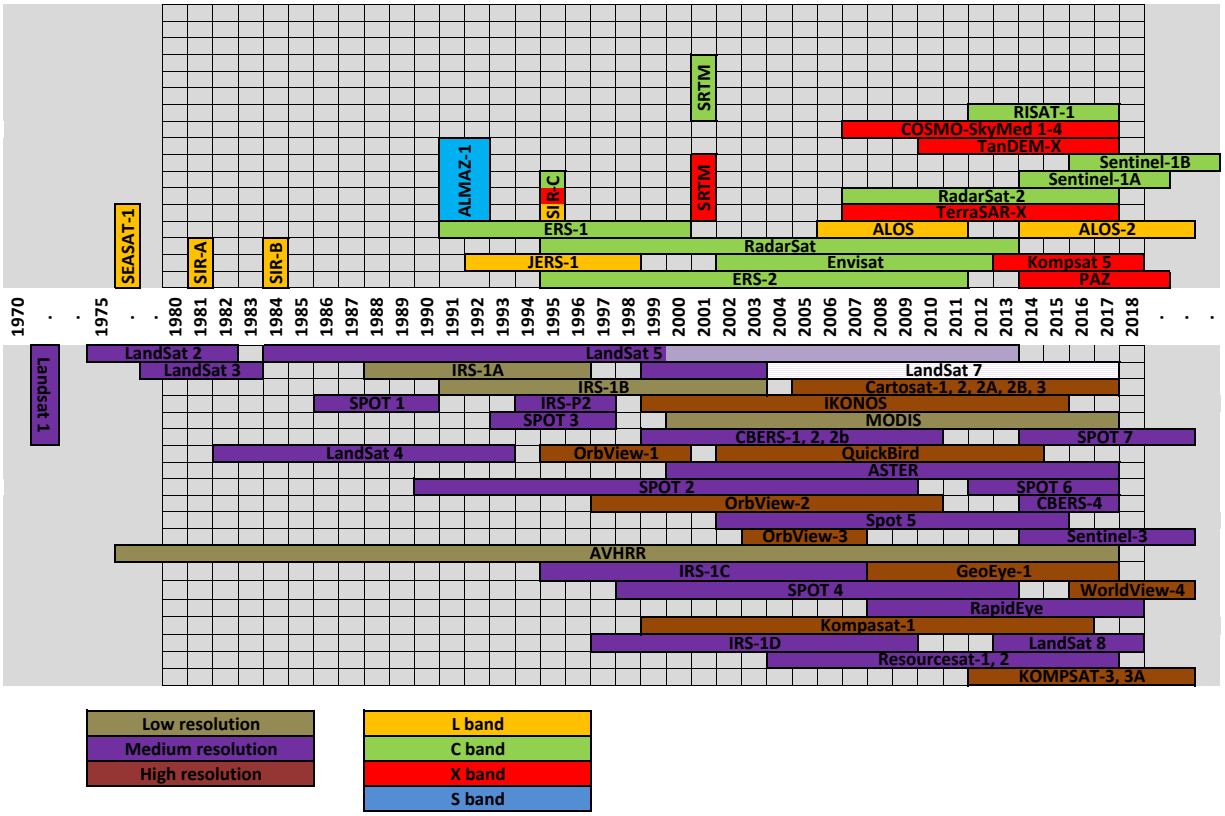

Figure 1.1: Different optical and SAR imagining missions.

to answer any scientific question about understanding the global warming and its role and affect on other relevant environmentally processes is the availability of extensive and accurate observations of hydrological water cycle variables. The aforementioned situation demands developing an advanced monitoring scheme over the hydrological cycle variables.

Hydrological cycle continues with evaporation of water from oceans and inland water bodies surface by solar energy. The atmospheric circulation carries the water vapour over the Earth. In the next step, water vapour precipitates as snow or rain. Part of raindrops intercepted by vegetation and trees which will transpire again. The rest of raindrops reach the ground and infiltrate in the soil layers. The stored water then discharges into streams and ultimately flows out into the ocean from which it will evaporate once again (Miralles et al., 2011). Figure 1.2 illustrates schematically the hydrological cycle.

Studying the hydrological cycle starts with quantifying its components. The water balance equation expresses the fact that in any river basin the difference between the amount of income and outcome water is equal to the change in the water stored in the basin

$$P - ET_a - R = \frac{dS}{dt} \tag{1.1}$$

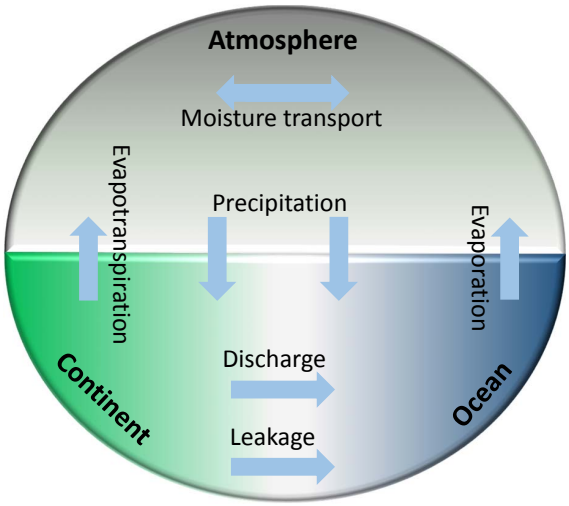

Figure 1.2: Schematic illustration of the hydrological cycle

In equation (1.1), P is precipitation which provides the incoming water to the system. ET_a is actual evapotranspiration which consists of two processes: evaporation (amount of water directly vaporizes from the surface of oceans, inland water bodies and soil) and transpiration (the process of discharging back into the atmosphere of the absorbed water by plant roots and leafs). R is the river discharge which, together with ET_a indicates the output of the system. The right hand side of the equation 1.1 describes the amount of water including surface water, soil moisture and groundwater stored in the basin.

Recently, precipitation is measured by weather satellites and radars. Therefore, global gridded precipitation data is available from different providers likes Climatic Research Unit (CRU), Global Precipitation Climatology Center (GPCC) etc. The main concern regarding the precipitation data is the quality of the data rather than the data availability (Habib et al., 2001). The quality of the gridded precipitation fields primarily depends on the number of active gauges and their spatial distribution (Lorenz & Kunstmann, 2012).

Actual evapotranspiration (ET_a) is integral to studies of the hydrological cycle, yet its quantification and determination are difficult (Rodell & Famiglietti, 1999). It is determined over land surface by soil humidity, plant specific maximum evapotranspiration, atmospheric conditions and net radiation (Maidment, 1992; Chow, 1964). In order to estimate or model the evapotranspiration, different methodologies are employed based on water balance, water vapour stream and energy balance methods.

Measuring the change of the water mass in the Earth system (atmosphere, surface, subsurface) was not directly possible before the year 2002. Therefore the water balance equation was not solvable on short time scales. Only at long time scales, the assumption that long-term averages of storage change are negligible would allow a closure of the water balance (Tourian, 2013). Since 2002, the Earth gravity field measured by

Gravity Recovery and Climate Experiment (GRACE) helps to determine continental water storage changes monthly. Although GRACE provides unique information for closing the continental water balance equation, it is not considered as a reliable hydrological sensor for most basins (Swenson et al., 2003; Velicogna et al., 2001; Han et al., 2004). Various sources of uncertainty, coarse spatial resolution (400 km), inseparability between water storage components and inconsistency between GRACE observations and hydrological models are the main challenges for monitoring the change in the water storage (Tourian, 2013).

River discharge is an important parameter in any hydrological model. It has been measured at river sections for more than a century. In situ gauge measurements are the backbone of the current understanding of global surface water dynamics. However, one-dimensional and point-based observations provided by in situ gauges are only appropriate where the water flows in a channel with a well-defined boundary. So, they provide little information about spatial dynamics of surface water extent, such as floodplain flows and the dynamics of wetlands (Alsdorf et al., 2007). In recent decades, the number of available active in situ stations has decreased dramatically because of financial and political restrictions. Figure 1.3 presents the situation of basins with publicly available in situ discharge measurements. It shows the decline of river discharge measurement stations overtime according to the Global Runoff Data Centre (GRDC) dataset which is a repository for river discharge data.

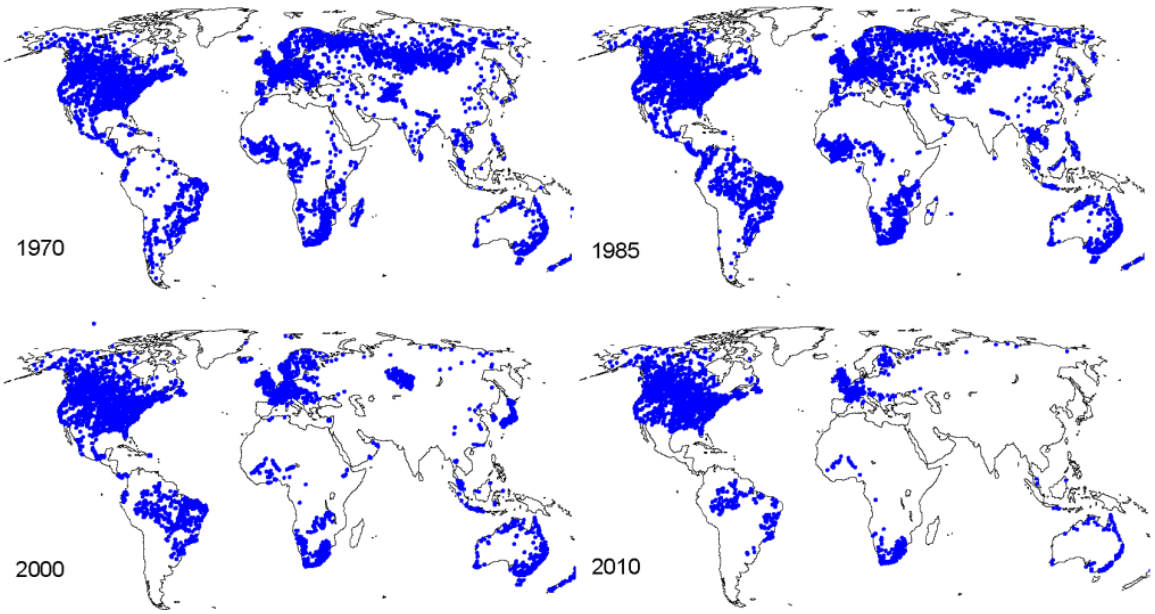

Figure 1.3: Spatial distribution of gauges with available runoff data in the data base of GRDC around the world for 1970, 1985, 2000 and 2010 (Tourian et al., 2015b).

This figure indicates that not only the number of existing stations reduced but also in situ measurements over a number of important basins in Africa and South America are not available anymore. At the moment, most of the active gauge stations are

located over developed countries whereas in the nonindustrialized nations, the density of stations is much sparser (Alsdorf et al., 2007). In the near future, due to the global warming, the extent of current water bodies will change dramatically and also new water bodies will be created. Therefore, the current active world wide gauging network could not provide suitable observations for hydrological modelling (Vörösmarty et al., 2000). Also the performance of different hydrological models are highly dependent on measurements of surface water dynamics and river discharge (Alsdorf & Lettenmaier, 2003). Without any outlook for deploying of the global gauging station network, spaceborne sensors can provide valuable information to improve the performance of hydrological models.

1.2 Monitoring the inland surface water bodies by spaceborne geodetic sensors

The term "Spaceborne geodetic sensors" refers to those satellites that measure a geodetic parameter of the Earth. In case of terrestrial surface water, satellite altimetry and imaging missions are considered as spaceborne geodetic sensor. Recently, the availability of sophisticated geodetic spaceborne observations helps scientists to develop different techniques for measuring various parameters of surface water bodies. In this section, spaceborne techniques for measuring different properties of inland surface water bodies will be mentioned.

Digital elevation models

Digital elevation models (DEM) is an important source of information for surface water monitoring and hydrological modelling. Before SAR and interferometric SAR (InSAR) technologies become widely available, producing global elevation maps with consistent scale and resolution was infeasible. The cost of deploying aircraft and inaccessibility to some areas were the main obstacles to producing global elevation maps (Farr et al., 2007). In the 1990s, the emergence of InSAR introduced the only practical way to globally generate a consistent DEM. The Shuttle Radar Topography Mission (SRTM) successfully demonstrated the potential of the new technique (Farr et al., 2007). The InSAR technique takes advantages of measured phase difference between two radar images acquired with a very small baseline relative to the shuttle height. The radar wavelength is in the range of centimeter to meter, so the satellite can receive good signal return from bare ground, ground covered with vegetation and rough water. However, the radar signal cannot penetrate into the dense vegetation significantly. So that, the generated map does not correspond to the surface in those areas.

Due to the Earth gravity, water tends to stream towards low altitude areas and to accumulate in the area with the lowest altitude. In this way, DEM map plays an important

role in any study related to the formation and stream direction of the surface water bodies.

Water level

Satellite altimetry has an honorable history of a few decades in measuring the ocean surface elevation with a few centimetre accuracy. Also, it has been successfully used to measure and monitor water height in inland water bodies like rivers, lakes and floodplains (Crétaux & Birkett, 2006; Papa et al., 2010; Frappart et al., 2006). Launching TOPEX/Poseidon and ENVISAT provided the opportunity to monitor the water level change periodically (35 days for ENVISAT and 10 days for TOPEX/Poseidon) in large rivers and lakes. Variations in the water level are easily derived from altimetric measurements since most of the altimetry missions are designed to fly in repeat orbits. An intersection between satellite orbit and the water body is needed in order to capture the variation of the water level. Therefore part of small water bodies remains unmonitored, due to few kilometers ground track spacing of satellite orbits. In the past, most of the hydrological models have been developed according to at station water level measurements. As a result, water height measurements from altimetry missions are well-suited for assimilating with in situ measurements and using in hydrological models.

Apart from satellite altimetry, the water level of inland water bodies and inundation areas can also be estimated via measuring the area covered by water in satellite images. Then water level is calculated by defining the inundated area over a DEM map (Brakenridge et al., 2005). The height accuracy of this technique is highly dependent on the availability of a high-resolution DEM (Alsdorf et al., 2007). Also, some studies directly measured the water level change in time using INSAR techniques (Kim et al., 2005; Lu et al., 2005; Alsdorf et al., 2000).

River water slope

Water level measurements collected by satellite altimetry missions can be used to determine the water slope by knowing the distance between ground tracks crossing the river. However, the time lag between height measurements could reduce the accuracy of slope calculation. Extracting the height information from a DEM map like SRTM is another approach to calculate the water slope. To decrease the noise in this method, an appropriate river reach length must be used (Alsdorf et al., 2007).

Surface water velocity

Shuchman (1979) introduced the idea of using conventional rawSAR data for surface water velocity measurements. Three decades afterward, Chapron et al. (2005) pre-

sented the Doppler centroid anomalies technique and demonstrated that the ocean surface velocity field can be measured by applying this method on the Advanced Synthetic Aperture Radar (ASAR) instrument onboard ENVISAT. Meanwhile, Goldstein & Zebker (1987) proposed the along-track interferometry (ATI) technique for current measurements. In this technique, two SAR images from the same scene with a very short time lag (some milliseconds) are used. To derive the phase shift between two images, an InSAR image is obtained. In the next step, the surface water velocity field is retrieved from the phase shift.

Romeiser et al. (2005, 2007) presented the first demonstration of current measurement by ATI from a spaceborne platform with SRTM data. The launch of TerraSAR-X in the year 2007 provided the opportunity of repeat measurements for the determination of surface water velocity. Surface current field derived from TerraSAR-X ATI data and TanDEM-X for the mouth of Elbe River was presented by Romeiser et al. (2010b); Romeiser (2015). Grünler et al. (2013) presented the possibility of using along-track InSAR technique for monitoring tidally influenced estuarine river discharge from space.

Despite an acceptable performance of derived surface water velocity fields, these techniques have some limitations. In both techniques, only the component of current field along the line-of-sight is measurable. Regarding the limitations of ATI for measuring the current fields of river (minimum river width, wind conditions, line- of-sight surface velocity, tides, seasonal discharge variation, hydrodynamic conditions), only the discharge of about 30% of estuarine rivers (based on GRDC) can be estimated by this technique (Grünler et al., 2013).

Bathymetry

The inability to penetrate into the water is a serious limitation of spaceborne sensors in hydrological applications, since depth is a necessary parameter for river discharge estimation. Turbidity, heavy surface waves, and sunglint are the most important parameters that limit the penetration (Banic & Cunningham, 1998; Davis, 2004). In practice, maximum detectable depth is no more than 2–3 times from the Secchi depth. The Secchi disk is a circular white disk with 30 or 20 cm diameter. The disk is mounted on a pole equipped with a scale. To measure the Secchi depth, the disk is lowered down in the water. The depth at which the Secchi disk is not visible any more is called Secchi depth. It indicates water turbidity (Wozencraft & Lillycrop, 2002).

Calkoen et al. (2001) demonstrated the potential of SAR images for the mapping of underwater bathymetry in coastal waters with strong tidal currents due to the fact that bathymetric features become visible in radar images because of the tidal flow modulated by the spatially varying water depth and a corresponding surface roughness modulated via wave-current interaction (Romeiser et al., 2010a). Romeiser et al. (2002)

presented a bathymetric map from airbone ATI data. They developed a surface current-water depth empirical model by availability the depth information for some reference test area.

Recently, Tourian et al. (2017) proposed a method to estimate average river depth for a river reach from both spaceborne (river surface elevation, width and slope) and in situ discharge measurements. The relied on two recognized discharge estimation models developed by Bjerklie et al. (2003) and Dingman & Sharma (1997) and considered the average riverbed as unknown. By availability of all other measurements, the average river depth was estimated for each river section. At the end, they validated the obtained river depth against surveyed cross-section information, which shows a generally good agreement in the range of 10% relative root mean squared error.

River discharge

River discharge is defined as the volume of water flowing through a river channel. This parameter is measured in $[\frac{m^3}{s}]$ or $[\frac{km^3}{day}]$. Despite its significant role in global water balance and human life, our knowledge about the dynamics of the global river systems is restricted to in situ measurements. Since none of the spaceborne technique can directly measure discharge, remote sensing of rivers is relatively immature. But fortunately, the various types of observations from spaceborne sensors provide considerable opportunities to understand the dynamics of a river system apart from traditional ground-based methods.

Finding an empirical relationship between a river hydraulic parameter measured from space and in situ discharge measurements is the most straight forward technique to estimate the river discharge. In the past, it is assumed that there is a power law relationship between river discharge and stage measured at station. By measuring numerous river discharge and stage simultaneously, model coefficients are defined. Since the river discharge-stage relationship is found, river discharge is calculated by using river stage measurements and developed model. This technique is called rating curve. Recently, due to the advancement of geodetic spaceborne techniques, altimetric water level (Koblinsky et al., 1993; Frappart et al., 2006; Birkinshaw et al., 2010) and river width from satellite images (Smith et al., 1996; Brakenridge et al., 2005; Smith & Pavelsky, 2008; Elmi et al., 2015) are used to develop rating curves. Once the model is developed, the availability of in situ measurements is not necessary. This method is highly dependent on the availability of simultaneous in situ and space observations. However, The developed models are only valid for the river section where the empirical model developed. Tourian et al. (2013) suggested an alternative technique to eliminate the need for simultaneous measurements. They introduced a statistical approach to derive discharge from altimetric water level measurements through a rating curve based on quantile functions. Unlike, the traditional rating curve method, their method constructed the rating curve based on a scatter diagram of quantile functions of river discharge and height measurements.

A number of techniques developed a relationship between the river depth and the reflectance of the water column in a multispectral optical image (Legleiter & Roberts, 2009; Legleiter et al., 2004; Marcus & Fonstad, 2008; Legleiter et al., 2009). These models provide the opportunity to estimate the river discharge directly from the space, but they are applicable only on shallow stream where the channel bottom is visible.

To define river depth and discharge, some studies developed a hydrodynamic model for the river and define its parameters via river height, width and slope measured from space using assimilation techniques (Andreadis et al., 2007; Durand et al., 2008; Biancamaria et al., 2011; Durand et al., 2010). Another group of studies developed purely empirical relationships between hydraulic variables using information of a large number of river cross sections. For example, Bjerklie (2007) used US Geological SurveyUSGS river cross sections to develop a simple regression equation to estimate bankfull mean depth. The aim of these methods is to find stable relationships between river variables which leads to estimation of river depth and discharge.

The Surface Water and Ocean Topography (SWOT) is the next satellite mission which has a high potential to overcome many obstacles of river discharge measuring from space. SWOT, a joint mission between NASA and CNES (French: Centre National D 'Etudes Spatiales, lit. "National Center for Space Studies") will launch in April 2021. The mission will use interferometric synthetic aperture radar technology to continuously map river surface elevation and extent simultaneously at high spatial resolution (Pavelsky, 2012). The main goal of SWOT mission in inland water bodies studies is to capture and monitor all lakes, reservoirs and wetlands larger than 250 m^2 and rivers with more than 100 m width approximately every 7 days.

Inland surface Water and inundation area monitoring

Surface water area is the most conventional hydrological parameter measured by satellite imagery missions. Accurate measurements of the change in the extent of inland surface water bodies are important to improve our understanding of the flow dynamics of river systems. Inland surface water bodies cover only a small fraction of the Earth surface but they have a great effect on sustaining life on Earth and they play a primary role in the global water cycle and climate change (Prigent et al., 2007). Lakes and reservoirs are highly valuable for their freshwater supply (Alsdorf et al., 2007). Lakes constitute important habitats and food resources for a diverse array of fish, aquatic life, and wildlife. Lake ecosystems can undergo rapid environmental changes, often leading to significant declines in their natural functions. Exposed to external effects from the atmosphere, their watersheds and groundwater, lakes are subject to change through time. In urban areas their condition is highly fragile because they are vulnerable to pollution.

Rivers are also classified as inland surface water. They have been essential not only to humans, but to all life on Earth, ever since life began. Plants and animals grow and congregate around rivers simply because water is so essential to all life. Cities are

typically built and developed near rivers. For humans, rivers are diverted for flood control, irrigation, power generation, municipal uses and even waste disposal.

Optical and SAR satellite imaging missions provide the opportunity to monitor the spatial change in coastlines, which can serve as a way to determine the water extent repeatedly in various time intervals over different spectral bands with variety of spatial resolution (from few centimeters to a kilometer). In recent decades, the monitoring of Earth related phenomena is more feasible than before because a lot of images from different missions are available. Recent missions provide images with better spatial and temporal resolution, so comprehensive interpretation of hydrological objects is expected. Figure 1.3 represents that before 2000 only about 10 satellite images per month were available at any given location. The number of observations has increased to more than 40 per month in 2016. This number will expand dramatically by new missions like the series of Sentinels. On the other hand, the number of active in situ stations has reduced from more than 7000 in 1980 to less than 1000 in 2017.

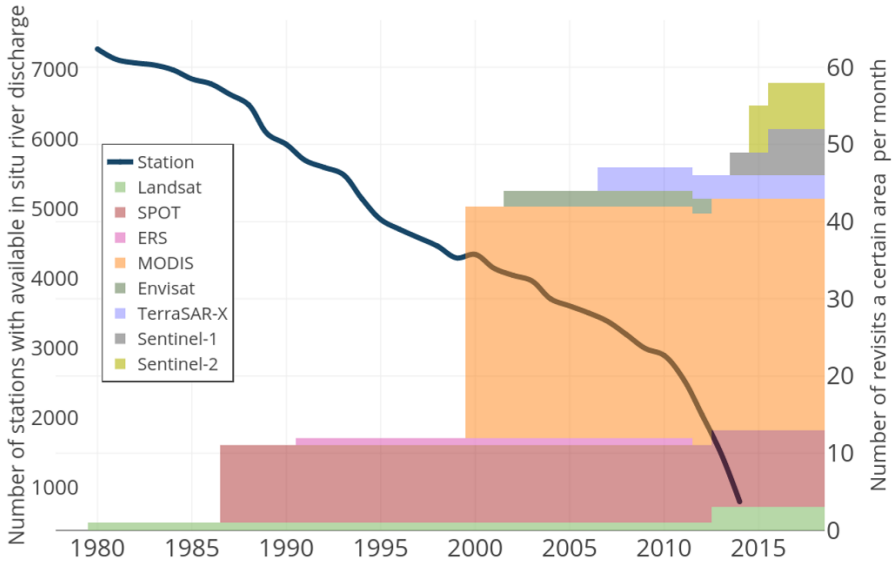

Figure 1.4: Number of available satellite images improves significantly during the last three decades. On the other hand, number of stations with available discharge measurements have decreased. In this figure, the variety of spatial resolution in the different missions is not considered.

Apart from monitoring the lake and river surface water area, satellite images are a well-suited source of information to obtain a synoptic view about large-scale flood situations and their spatio-temporal evolution especially because in situ measurements are not often possible (Solbø & Solheim, 2005; Martinis, 2010). Due to the availability and straightforward interpretability of optical satellite images, they are widely used to recognize flooded and inundated areas (Wang et al., 2002; Van Der Sande et al., 2003; Ahtonen et al., 2004; Brakenridge & Anderson, 2006; Martinis et al., 2013). However the performance of optical images in flood detection and monitoring is limited because of their inability to penetrate clouds. Since floods occur due to heavy precip-

itation, monitoring and detecting the flood and its inundation area by satellite optical imagery is impractical due to the persistent cloud cover. On the other, SAR satellite are active systems that perform independent from solar radiation and weather condition. In this way, SAR systems improve the capability of flood detection and monitoring (Richards et al., 1987; Townsend, 2001; Martinis et al., 2009). However, SAR-based estimates of surface water extent and flood monitoring are also confounded by difficulties with wind roughening of the water surface for the wavelengths used by most existing sensors in C band (Alsdorf et al., 2007).

For the purpose of monitoring water area variations, after collecting all the appropriate satellite images from the water body during the monitoring period, a contiguous procedure to quantitatively analyse spatial change in water-land boundary is needed. The basic premise in using remotely sensed data for change detection is that changes in the water body will result in changes in reflectance values that are separable from changes caused by other factors such as differences in atmospheric conditions, illumination and viewing angles, and soil moisture (Deer, 1995). In order to improve deciding about the location of water body borders at each snapshot, a variety of change detection techniques have been developed. Based on the nature of the phenomena, the most appropriate change detection method must be chosen. Indeed, as well as an applicable change detection method, a successful monitoring scheme requires careful considerations on preprocessing of multitemporal images and accuracy assessment of developed results (Townsend & Walsh, 1998). In this way, before implementing change detection analysis, the following conditions must be satisfied (Lu et al., 2004):

- precise registration of multitemporal images,
- precise radiometric and atmospheric calibration,
- normalization between multitemporal images,
- selection of the same spatial and spectral resolution images.

The main objective of this study is to develop algorithms for monitoring the area of inland water bodies using optical satellite images. So, in the next section, an overview to principles and properties of satellite optical imagery is presented.

1.3 Basic principles, properties of the optical images

Optical satellite imagery, as a passive system, consists of observing electromagnetic (EM) energy emitted from the different features of Earth surface. The Sun is the main source of EM energy. However, every object with a temperature higher than absolute zero is able to emit EM energy. The total range of wavelengths of EM radiation is called the EM spectrum. Table 1.2 presents the information about different bands of the EM spectrum.

Table 1.1: Description of different spectrum bands

Name	Wavelength range [m]	Frequency range [Hz]
Gamma Rays	$< 1.0 \times 10^{-11}$	$> 3 \times 10^{19}$
X-Rays	1.0×10^{-11} – 1.0×10^{-08}	3×10^{16} – 3×10^{19}
Ultraviolet Light	1.0×10^{-08} – 3.8×10^{-07}	8×10^{14} – 3×10^{16}
Visible Light	3.8×10^{-07} – 7.5×10^{-07}	4×10^{14} – 8×10^{14}
Infrared Light	7.5×10^{-07} – 1.0×10^{-03}	3×10^{11} – 4×10^{14}
Microwaves	1.0×10^{-03} – 1.0×10^{-01}	3×10^{09} – 3×10^{11}
Radio	1.0×10^{-01} – $1.0 \times 10^{+07}$	3×10^{01} – 3×10^{09}

The EM spectrum is generally divided into seven regions: radio waves, microwaves, infrared, visible light, ultraviolet, X-rays and gamma rays. The majority of useful information for Earth related applications is sensed in the visible and infrared range. Ultraviolet (UV) and microwaves bands also reveal information about minerals, surface roughness and moisture content of soils (Tempfli et al., 2009). In the Figure 1.5, the visible light region of the spectrum is presented. This region is called visible because human eyes are sensitive to it and able to detect it.

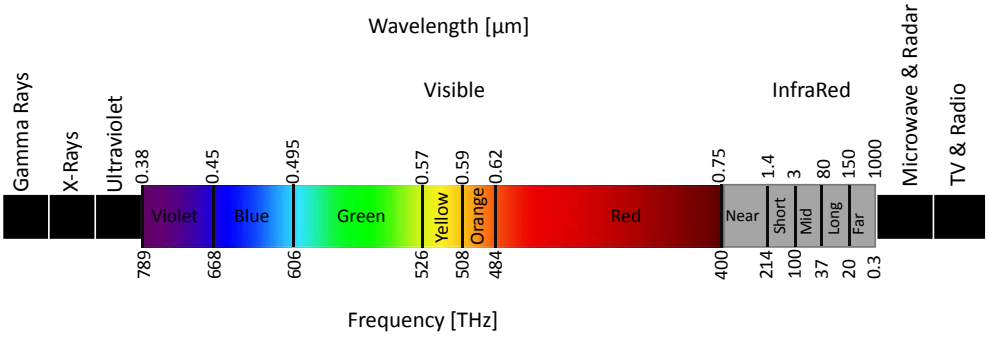

Figure 1.5: The electromagnetic spectrum

The color of different parts of the visible light spectrum is decided by its wavelength. The violet with the shortest wavelength and dark red with the maximum wavelength limit both ends of this region. Objects appear in different colors depending on the part of visible light spectrum that they absorb and reflect. Before sensing by the satellite, a number of interactions in the atmosphere happen for the Sun energy travelling from the Sun to the Earth's surface and then from Earth to the satellite. Only a small portion of the EM spectrum can travel through the atmosphere and the rest of it is absorbed by various molecules in the atmosphere like ozone, water vapour and carbon dioxide. The useful ranges are called the *atmospheric transmission windows* and include the window from 0.4 to 2 μm (visible, NIR, SWIR regions) and three windows in the Thermal InfraRed (TIR) range (Tempfli et al., 2009).

The atmospheric scattering is another interaction between the EM spectrum and atmosphere. It occurs when particles or gaseous molecules, present in the atmosphere, cause the EM radiation to be redirected from its original path (Tempfli et al., 2009). Depending on the size and type of particles, scattering can have different effects on the light spectrum. The most destructive interaction in optical satellite imaging is that we see clouds as a white body which does not allow the sunlight to pass through. A cloud consists of water droplets which scatter all wavelengths of the sunlight equally (Tempfli et al., 2009).

After passing through the atmosphere, the remaining portion of the sunlight reaches the Earth's surface. The majority of it is reflected but part of it will be absorbed or transmitted depending on the material of the target. Reflected solar energy is the most interesting part in land and water applications since it reveals useful information about the Earth surface characteristics (Tempfli et al., 2009). Different surfaces have different spectral reflectance properties regarding the material, physical and chemical attributes. For example, unlike vegetation and soil which reflect up to 50% and 30–40%, water surface reflects at most 10% of the incident energy. This reflection is in the visible and a little in the NIR range. The rate of reflectance in the visible range intensifies, by increasing the amount of silt and plants in the water.

Satellites equipped with multispectral cameras observe the reflected radiance in several intervals of the light spectrum. Sensing in several spectral bands simultaneously allows to relate properties that show up well in the specific spectral bands. But the raw measurement of the camera is the radiance at the Earth's surface attenuated by atmospheric absorption plus the radiance of scattered light and malfunctioning the sensor (Tempfli et al., 2009). As a result, many corrections are necessary for improving the quality of optical images. These corrections remove disturbances due to the radiometric imperfection caused by the noise of the sensor, change in the atmospheric conditions, variations in the Sun illumination and effect of the haze.

To obtain reliable information, the geometric representation of the image must be similar to the real world. To that end, several factors must be considered like movement of the platform or rotation of the Earth. Finally, to link the image coordinate to the map coordinate, a geometric transformation is applied to the image's pixels. This process is called *referencing*. Usually, the information needed for these corrections is accessible by the space agencies providing satellite images.

After georeferencing and applying radiometric calibration, satellite images are ready to use in land and water applications. Depending on the application, selecting the most suitable spectral bands among the available options is one of the preliminary steps for each study. Each spectral band highlights a particular property of the Earth surface. Table 1.2 briefly describes the most common spectral bands available in the satellite multispectral images. It is a modified version of the table provided by Schimmer (2009).

From this table one sees that, for mapping the water-land boundary, NIR bands are the most suitable spectral bands. Water appears very dark in these bands because

Table 1.2: Description of different spectrum bands

Name	Spectral range [μm]	Description
Blue	0.45–0.52	best data for mapping depth-detail of water-covered areas, useful for soil-vegetation discrimination, forest mapping.
Green	0.50–0.60	corresponding to the chlorophyll absorption of healthy vegetation, useful for mapping detail such as depth or sediment in water bodies.
Red	0.60–0.70	absorbing chlorophyll in healthy vegetation, useful for distinguishing plant species, soil and geologic boundaries.
NIR	0.70–0.80	sensitive to varying vegetation biomass and emphasizes soil-crop and water-land boundaries.
NIR	0.80–1.10	useful for vegetation discrimination, penetrating haze, and land-water boundaries.
SWIR	1.55–1.74	distinguishing clouds, snow, and ice, sensitive to plant water content, which is a useful measure in studies of vegetation health.
SWIR	2.08–2.35	useful for mapping geologic formations and soil boundaries, responsive to plant and soil moisture content.
Mid IR	3.55–3.93	detecting both reflected sunlight and E–emitted radiation and useful for snow-ice discrimination and forest fire detection.
Thermal	10.40–12.50	dominated completely by radiation emitted by the Earth, helping to account for the effects of atmospheric absorption, scattering, and emission, commonly used for water surface temperature measurements.

it absorbs most of the light spectrum in this domain. Moreover, visible bands also provide valuable details about the characteristic of water content.

More than original spectral bands, a number of spectral indexes are investigated for highlighting land cover features. The Normalized Difference Vegetation Index (NDVI) is the first published band ratio which is a popular tool for biomass estimation and vegetation monitoring (Rouse Jr et al., 1974).

$$\text{NDVI} = \frac{\text{NIR} - \text{Red}}{\text{NIR} + \text{Red}} \tag{1.2}$$

This product is the ratio of the difference and the sum of NIR and Red bands. The NDVI can also be applied to detect surface water since very low values are specified

for water. Later in the year 1996, Gao (1996) developed another index, Normalized Difference Water Index (NDWI), by using NIR and SWIR bands. to enhance detecting the water content in leaves.

$$\mathrm{NDWI}_{\mathrm{Gao}} = \frac{\mathrm{NIR} - \mathrm{SWIR}}{\mathrm{NIR} + \mathrm{SWIR}} \tag{1.3}$$

In the same year, McFeeters (1996) introduced another version of this index by using NIR and Green bands to enhance the determination of water bodies in the remote sensing images.

$$\mathrm{NDWI}_{\mathrm{McFeeters}} = \frac{\mathrm{Green} - \mathrm{NIR}}{\mathrm{Green} + \mathrm{NIR}} \tag{1.4}$$

To highlight water in urban areas, Xu (2006) replaced NIR with SWIR in the NDWI definition and denoted it as Modification of Normalized Difference Water Index (MNDWI)

$$\mathrm{MNDWI} = \frac{\mathrm{Green} - \mathrm{SWIR}}{\mathrm{Green} + \mathrm{SWIR}} \tag{1.5}$$

All the mentioned water indexes devote a certain range of values to the water pixels (negative and near zero values). In this way they are easily classified by applying a simple threshold. The threshold may be different from image to image.

In the selection of suitable optical satellite images for hydrological applications, a balance between spatial and temporal resolutions must be considered. For example, Landsat images with 30 m pixel size are typically available fortnightly or less often, so they cannot capture the dynamic of water bodies completely. Relatively lower spatial resolution sensors, like MODIS, scan the Earth's surface once or several times a day, but their coarse spatial resolution hampers the accurate mapping of surface water (Huang et al., 2016).

1.4 Introduction to change detection methods for water area monitoring

Change detection is the process of identifying differences in the state of an object or phenomenon by observing it at different times (Singh, 1989). Timely and accurate change detection of Earth's surface features help us to understand better the relationship and interaction between human and natural phenomena (Lu et al., 2004). Lu et al. (2004) categorized different change detection applications using remote sensing technologies in ten aspects

1. land-use and land-cover change

2. forest or vegetation change
3. forest mortality, defoliation and damage assessment
4. deforestation, regeneration and selective logging
5. wetland change
6. forest fire and fire affected area detection
7. landscape change
8. urban change
9. environmental change, drought monitoring, flood monitoring, monitoring coastal marine environments, desertification and detection of landslide areas
10. other applications such as crop monitoring, shifting cultivation monitoring, road segments and change in glacier mass balance and facies.

Considering the importance of monitoring the change in Earth surface features in these different aspects, many change detection methods have been developed and new techniques are constantly developed. Lu et al. (2004) summarized change detection methods into seven groups.

1. **Algebra**: Most of the techniques in this category determine the changed areas by selecting a threshold. Finding a suitable threshold to identify the changed areas is the difficulty of these methods. Sezgin & Sankur (2004) categorize thresholding methods into six different groups
   (i) Histogram shape-based methods, by which, the peaks, valleys and curvatures of the smoothed histogram are analysed.
   (ii) Clustering-based methods, in which the gray-level samples are clustered in two parts as background and foreground (object), or alternately are modeled as a mixture of two Gaussians images.
   (iii) Entropy-based methods result in algorithms that use the entropy of the foreground and background regions, the cross-entropy between the original and binarized image, etc.
   (iv) Object attribute-based methods search a measure of similarity between the gray-level and the binarized images, such as fuzzy shape similarity, edge coincidence, etc.
   (v) Spatial methods use higher-order probability distribution and/or correlation between pixels
   (vi) Local methods adapt the threshold value on each pixel to the local image characteristic

As well as thresholding, other change detection methods in algebra group are widely used to detect the change in the water area. For example, image differencing, image regression and taking image ratio are commonly applied to determine water bodies.

2. **Transformation**: These methods establish a numerical relationship between different bands of one image or different bands of different images to emphasize the change in the transformed components. Principal Components Analysis (PCA), the Tasseled Cap transformation, Multivariate Alteration Detection (MAD) transformations are applied in studies by, e.g., Munyati (2004); Bustos et al. (2011); Nielsen (2007, 2011). These methods also need thresholds to highlight the change area and, in some cases, interpretation of transformed images is difficult.

3. **Classification**: The methods in this group apply different image classification techniques in multitemporal images to monitor change. For example, in the post-classification comparison method all images are classified separately after which a pixel-by-pixel comparison is implemented to detect the change. Spectral-temporal combined analysis, Expectation Maximization (EM) change detection and Artificial Neural Networks (ANN) are examples in this category.

4. **GIS**: Integration of Geospatial Information Systems (GIS) and remote sensing methods to detect the change in the image is the main advantage of this category. Most of the GIS based change detection applications focus on urban areas because GIS tools are very powerful to deal with multi-source data processing.

5. **Advanced models**: In these methods, a linear or non-linear model is applied to the images and they are converted to physically based parameters or pixel fractions. For example, a spectral mixture model was applied to detect the change of land-cover in the Amazon.

6. **Visual analysis**: In this category, change in shape, size and pattern of the subject area in the multi-temporal images is detected by visual interpretation of a well experienced analyst. This method was widely used in the past, when the capability of computers to handle large amounts of data was poor.

7. **Other change detection techniques:** Apart from aforementioned techniques, some methods cannot be categorised into any group. Either they applied a combination of techniques to detect the change or their method have not yet frequently used in practice. For example, (Lambin & Strahler, 1994) used vegetation indices, land surface temperature and spatial structure from AVHRR images to detect land cover change in the west Africa.

Selecting an efficient change detection technique among the large amount of different methods is a fundamental step to reach acceptable results. This decision must be based on the knowledge about the application and available in situ and remote sensing data. In other words, the first step in a change detection application is studying carefully the application and the data and to find the best method to apply to them.

While water absorbs nearly all the sunlight in the near infrared wavelength, water bodies appear very dark at this domain in an optical image. In a SAR image, water bodies also appear dark because the smooth surface of water acts like a mirror for the incident radar pulse and most of the energy is reflected away according to the law of specular reflection. As a result, very little energy is scattered back to the radar sensor. Unlike the distinguishable difference between water and land, a precise distinction between wetlands, rivers and lakes may not be possible in some regions or seasons. Identifying and characterizing wetlands globally is further complicated by their distribution throughout tropical to boreal environments encompassing a wide variety of vegetation cover, hydrological regime, natural seasonality, and land-use impacts (Prigent et al., 2007).

Applying a threshold to the histogram of the backscatter values of the image to extract the object from the background is the most straightforward method in change detection and pattern recognition algorithms (Li & Lee, 1993). In remote sensing, thresholding an image to obtain the object is prevalent because of its efficiency and easy implementation. This technique is also widely used in inland water body monitoring to develop water masks. Apart from thresholding, other unsupervised and supervised classification algorithms are widely used to extract water bodies from satellite images. A list of different studies is presented in Table 1.3. These studies applied different classification algorithms to satellite images to detect and monitor water bodies. They are arranged based on the type of monitored water body (lake, river, or flood and inundation area), and information about the used data set, classification and type of approach is provided.

Under ideal conditions, dynamic thresholding techniques can extract water bodies precisely. However, various error sources and a complex relationship between water and land in coastal areas necessitate to define the threshold value in a supervised manner using visual inspection of the image histogram or manual trial-and-error procedures (Townsend, 2001; Brivio et al., 2002; Cao, 2013). To improve the accuracy of water body monitoring, some studies take advantage of auxiliary data sources. For example, Klein et al. (2014) introduced an approach to detecting water bodies over vast areas by automatically defining thresholds for each image. Then, to improve the accuracy of water masks, they took advantage of a static water mask and a DTM. McFeeters (2013) takes advantage of a GIS-based map to improve the accuracy of water body detection. Verpoorter et al. (2012) developed an automatic water body extraction method (GWEM) by using dynamic thresholding and PCA transformation. The results are then improved by texture analysis and shadow removal.

Apart from thresholding algorithm other unsupervised classification algorithms like k-means clustering and Iterative Self-Organizing Data Analysis Technique Algorithm (ISODATA) are widely used to extract water bodies from satellite images. Elmi (2015) presented various approaches to multispectral image transformation like Principal Component Analysis (PCA) and Canonical Correlation Analysis (CCA) in the hydrological applications. The interpretation of derived components are time consuming and need visual analysis. Changes in the water extent are emphasized in the primary components, but determining a threshold is necessary to identify the changed area.

Table 1.3: Overview of studies using satellite images to extract the water bodies.

Study	Sensor	Approach	Type
Flood and Inundation Area Monitoring			
Sandholt et al. (2003)	AVHRR	Linear spectral unmixing	Advanced model, unsupervised
	ERS2	ISODATA	
	Landsat 7	Maximum likelihood	Supervised
Bonn & Dixon (2005)	RADARSAT-1	Parallelliped classifier	Supervised
Martinis (2010)	MODIS	Dynamic thresholding	Algebra, unsupervised
	TerraSAR-X	Dynamic thresholding	Algebra, unsupervised
Garay & Diner (2007)	MERIS	Visual analysis	Supervised
Munyati (2004)	Landsat 5	PCA	Transformation, unsupervised
Wang (2004)	JERS-1	Decision tree	Supervised
Feyisa et al. (2014)	Landsat 5	Dynamic thresholding	Algebra, unsupervised
Ryu et al. (2002)	Landsat 7	Density slicing	Algebra, unsupervised
Künzer et al. (2013)	ENVISAT ASAR	Dynamic thresholding	Algebra, unsupervised
Künzer et al. (2015)	MODIS	Dynamic thresholding	Algebra, unsupervised
Lake and Reservoir Area Monitoring			
Gao et al. (2012)	MODIS	k-Means clustering	Unsupervised classification
Tourian et al. (2015a)	MODIS	ISODATA	Unsupervised
Klein et al. (2014)	MODIS, AVHHR	Dynamic thresholding	Algebra, unsupervised
Klein et al. (2017)	MODIS	Dynamic thresholding	Algebra, unsupervised
Doña et al. (2016)	Landsat 7	Parallelepiped, SVM	Supervised
		Genetic algorithm	Supervised
		maximum likelihood	Supervised
		Minimum distance, ISODATA	Supervised
		artificial neural network, k-means	Unsupervised
Carroll et al. (2016)	Landsat 5, 7	Random forest classifier	Supervised
Huang et al. (2016)	Landsat 8	Otsu Thresholding	Algebra, unsupervised
Zhang et al. (2014)	Landsat 7	Visual analysis	Supervised
McFeeters (2013)	QuickBird	thresholding, GIS-based	GIS, supervised
Verpoorter et al. (2012)	Landsat 7	GWEM	algebra, transformation unsupervised
Kallio et al. (2008)	Landsat 7	Dynamic thresholding	Algebra, unsupervised
Fisher & Danaher (2013)	SPOT 5	Dynamic thresholding	Algebra, unsupervised
River Area Monitoring			
Elmi (2015)	Landsat 7, MODIS	PCA, CCA	Transformation, unsupervised
Tourian et al. (2017)	MODIS	Graph cuts optimization	Region-based classification
Wohlfart et al. (2016)	MODIS	Random forest classifier	Supervised
Tourian et al. (2016)	Landsat 7	Tasseled cap transformation	Transformation, unsupervised
Elmi et al. (2015)	MODIS	ISODATA	Unsupervised
Pavelsky (2014)	RapidEye	Dynamic thresholding	Unsupervised
Elmi et al. (2016)	MODIS	Graph cuts optimization	Region-based classification

Wang (2004) applied supervised algorithms like maximum likelihood classification to establish a binary decision classifier on SAR and optical images. Wohlfart et al. (2016) presented an algorithm for monitoring the change in the land surface of the Yellow River basin in China over ten years, applying the Random Forest algorithm to MODIS images. Random Forest algorithms construct multiple decision trees independently. Then, the algorithm searches for a random sample of the predictors and chooses the best split among the predictors. The final classification is based on the majority vote of the ensemble (Wohlfart et al., 2016). Carroll et al. (2016) monitored the change in water bodies area in the North American high Northern latitudes for 20 years (1991–2011) by applying a decision tree classification algorithm to Landsat images. Doña et al. (2016) applied several supervised and unsupervised classification methods on Landsat 7 images to measure the water area of thirteen shallow saline lakes in Spain. Based on

their results, a generic programming method (a supervised classification algorithm) outperformed the others and provided more accurate water masks. Requiring a large amount of training sample data is a serious restriction of supervised classification. Jarihani et al. (2014) presented two advanced blending algorithms to downscale MODIS to the spatial resolution of Landsat. The accuracy of the products of algorithms were evaluated by comparing the vegetation and water indices like NDVI and the NDWI. Huang et al. (2016) applied the Enhanced Spatial and Temporal Adaptive Reflectance Fusion Model (ESTARFM) for blending the Visible Infrared Imaging Radiometer Suite onboard Suomi National Polar-orbiting Partnership (NPP-VIIRS) data with Landsat data. Their aim was to monitor the dynamics of surface water of Poyang Lake in China and generate water masks with 30 m pixel size.

Unsupervised classification algorithms are quick and fast to run and prior knowledge about the area is not required. On the other hand, they only rely on the spectral and statistical information and changes in the algorithm parameters may lead to different results. Supervised classification algorithms like maximum likelihood and random forest also have been applied on satellite images for extracting water bodies. To extract the water bodies, they need training data but in general they can provide more accurate water masks.

All of the studies mentioned in Table 1.3 applied pixel-based classification algorithms that use only the spectral information of pixels to make a decision about their label. In other words, they consider each pixel as a separate unit and ignore the spatial, temporal, and contextual relationship between pixels. Therefore, they are very susceptible to noise in the image and, in most cases, the primary results need some post-processing and cleaning steps. Moreover, when dealing with a multitude of images, post processing costs considerable time and effort. On a large scale, the performance of most of the mentioned algorithms is acceptable. However, for monitoring the water area of a small river reach, they cannot provide accurate measurements. It is also reported by Weih Jr & Riggan Jr (2010) that, when pixel-based methods are applied to high-resolution images, the accuracy of the final result may be reduced due to a so-called salt and pepper effect. Weih Jr & Riggan Jr (2010) compared the performance of pixel-based and region-based classification algorithms, and their results found that region-based algorithms are superior to the pixel-based methods.

Since more and more satellite images with high spatial and temporal resolution become available from different missions, the demand for an automatic water body extraction algorithm with reasonable computational effort is rising.

1.5 Objectives

The primary objective of this study is to monitor inland surface water bodies as one of the most important elements of the water cycle using optical satellite images. The

availability of surface water area long-term time series together with water level derived by satellite altimetry provides the opportunity to monitor the change in the water volume. Also by considering total water storage change from GRACE, our understanding of hydrological processes is improved significantly. This study is focused on investigating the performance of different change detection techniques to monitor the surface water body area.

To develop more efficient algorithms, separate methods for monitoring lakes and rivers area are developed. Lakes and reservoirs as the biggest constant inland water bodies are located at the local minimum altitude in the basin. In most cases, we deal with a stable water body and a marginal area around it which is subject to change due to annual and seasonal behaviour. On the other hand, river behaviour varies from section to section because of various parameters like the gradient of elevation, river slope, the number of small tributaries and morphology of the river bed. In tropical regions, we face rivers that completely disappear in the dry season and overflow during the wet season.

Regarding the aforementioned objectives, the following goals are defined to be addressed in this study

1. Investigation the potential of a number of multispectral transformation on multispectral satellite images in change detection application.

2. Generating automatic algorithm for monitoring the lake area using optical images

3. Developing automatic algorithm for monitoring the river area

4. Developing statistical models for river discharge estimation using satellite images.

1.6 Case studies and data

1.6.1 Case studies

To assess and analyse the performance of developed algorithms, different water bodies in Asia, Africa and Europa with different characteristics are selected. Each of them poses its own challenge in terms of measuring and monitoring the surface water area via satellite images. Figure 1.6 presents all case studies in this thesis.

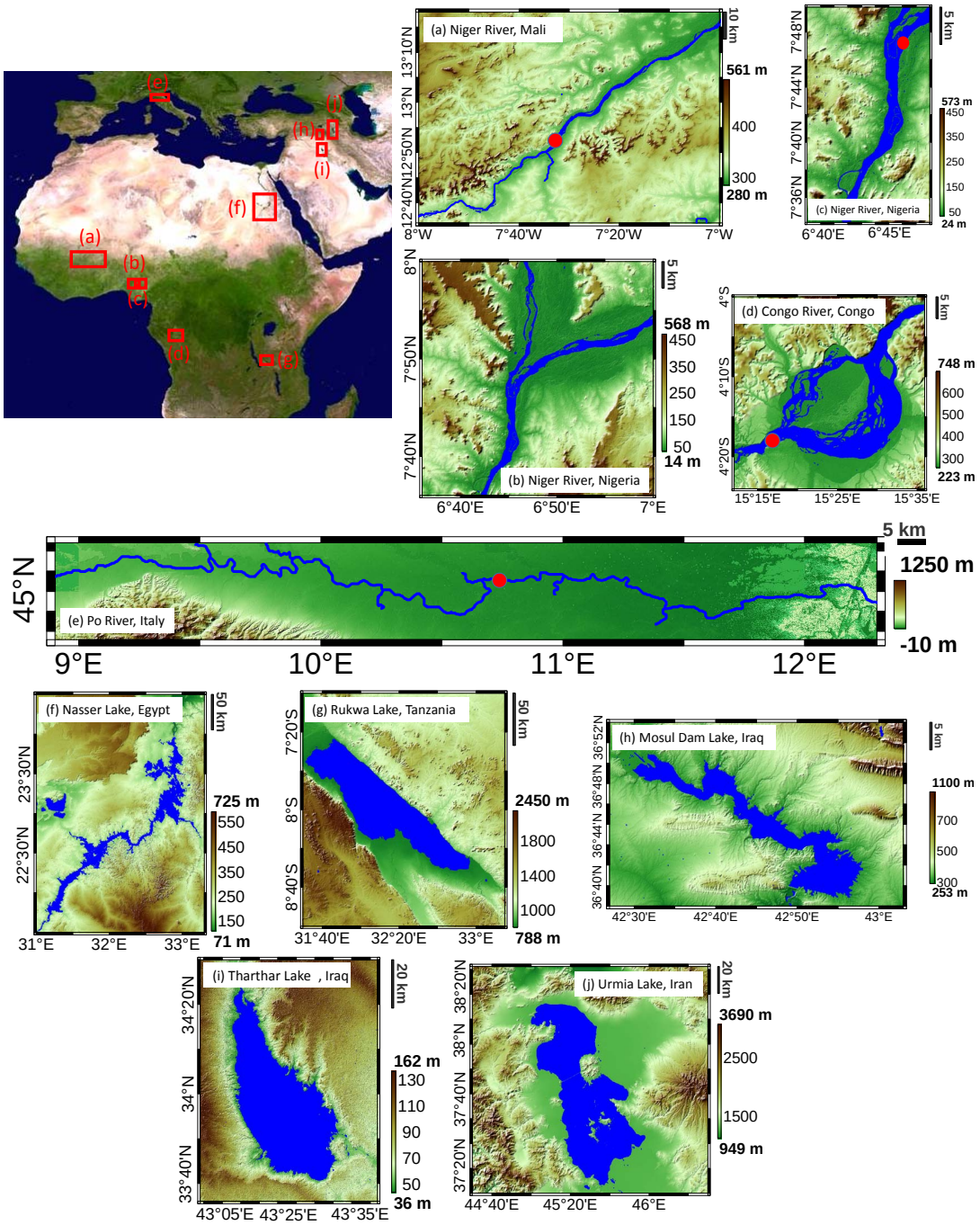

Figure 1.6: River and lakes used as case study in this thesis. Red dots in river sections present the location of in situ station

Niger River is the main case study in chapter two. On that chapter, different parts of Niger River (Figure 1.6(b)) are used to present multispectral transformations. The inland delta of the Niger River is one of the most fragile ecosystems of Sub-Saharan Africa. Patterns of land cover and land use vary extremely due to pre-flood and post-flood hydrological conditions of Niger River and its tributaries. The Niger River is the

third largest river (4200 km) in Africa, and the fourteenth longest river in the world. The river flows through Guinea, Mali, Niger, Benin, Nigeria and it discharges on the Gulf of Guinea. The Niger basin is composed of very diverse ecoregions ranging from the arid Sahel to the extremely wet coastal Niger delta (McGinley, 2013). The confluence of two rivers , Niger and Bani, is located in this delta and they provide approximately 1490 $\frac{km^3}{day}$ water for the delta. The amount of precipitation in the basin is highly variable between dry and wet season. Therefore, river area changes with very complex patterns depending on the topography of the river channels or the presence of vegetation, and on the total amount of water filling the river. During flood periods, the land is also subject to noticeable vegetation growth, mixed with water and dry soil. So, reliable frequent observation of the water extent, spatial distribution and temporal variation of the river's floodplain is vital. Two parts of Niger River are selected for monitoring the river section area in order to access the performance of the algorithm introduced in chapter 4. The proposed algorithm encounters with different challenges to monitor the variation of these river sections. Niger River section in Figure 1.6(a) will use as the main case study in chapter 4. The algorithm will demonstrate its capabilities by facing a river section with intense annual discharge variations (from about 0.3 $\frac{km^3}{day}$ in dry season to 1.6 $\frac{km^3}{day}$ in the wet season) and two islands along the river section. Niger River section in Figure 1.6(c) has also a significant annual discharge variation from 0.05 $\frac{km^3}{day}$ to 0.5 $\frac{km^3}{day}$. However, the length of this river section (114 km) is the main challenge for the algorithm in this case.

Congo River is the third river section used as case study in this thesis. The selected river section is called Malebo Pool (Figure 1.6(d)) located near Kinshasa. The Congo River— the second largest river in terms of catchment area in the world— has an average discharge of 41 800 $\frac{km^3}{day}$ (O'Loughlin et al., 2013). The river is located in the equatorial zone, where heavy rainfall occurs throughout the year. As a result, the river area changes rapidly. Therefore monitoring the variable extent of the River and its tributaries is a challenging task.

Po River is the last case monitored in this thesis (Figure 1.6(e)). The Po River, located in the Po valley in Italy, flows eastward through many important Italian cities. Since the river is subject to heavy floods, over half of its length is controlled with dikes. In this study, a reach about 400 km is selected. This river section with its narrow width varying between 150–650 m and its complex path could highlight the strength of river mask extraction algorithm.

Apart from river sections, five lakes in Asia and Africa are selected.

Nasser Lake as the largest man-made lake, is located along the Nile River between Egypt and Sudan in Africa (Figure 1.6(f)). This lake is formed after construction of the Aswan High Dam over the Nile in Egypt. As the main freshwater reservoir, Nasser Lake has a vital importance for both countries (Mostafa & Soussa, 2006). A minor

change in the lake water level causes an enormous change in the lake's shoreline. According to Moser & Serpico (2006), only one meter increase in the lake water level can expand the shoreline for six kilometers. The shoreline is composed of about 85 major khors (side extensions of the main part of reservoir) expanded into the dessert for a long distances (Mostafa & Soussa, 2006). The complex nature of Nasser Lake's shoreline makes it a challenging case for extracting the lake area from the satellite images. This lake is selected as the main case study in the third chapter.

Rukwa Lake presents in Figure 1.6(g). This case study is located in Africa. The lake is in the Rukwa Valley which is in the soutwest of Tanzania. Although the variation in the lake water area and level is not significant, Rukwa Lake is an interesting water body due to negative and positive trends in its water level and area over time. The northeast shoreline of the lake is occupied by rock cliffs and rolling hills (Lake Rukwa Basin Water Board, 2014). As a result the lake cannot enlarge from its longest shoreline.

Mosul Dam Lake in the north of Iraq is another case study in this thesis (Figure 1.6(h)). The building of Mosul Dam in the year 1986 in the Tigris River caused this artificial lake. The main role of the Mosul Dam is to control the water flow in the Tigris. The lake can hold 11.1 km^3 water volume at its full capacity (Annunziato et al., 2016). Due to inadequate maintenance, concerns about the safety of the dam recently have increased. Therefore, in the year 2003, the Iraqi government decided to reduce the maximum lake water level from 330 to 319 m (Annunziato et al., 2016). As a result, monitoring the area of the lake is important and also challenging.

Tharthar Lake is the biggest lake in Iraq. It is located in the center of the country and about 120 km northwest of Baghdad (Figure 1.6(i)). In 1956, the Therthar Depression was changed to an artificial reservoir to collect the flood waters of Tigris River during the flood seasons. Respectively, the Lake feeds Tigris and Euphrates Rivers during the dry season (Sissakian, 2011).

Urmia Lake is located in the northwest of Iran (Figure 1.6(j)). It is the largest inland permanent hypersaline lake in the world. In the twentieth century, it had an area varying from 5200 to 6000 km^2 (Zarghami, 2011; Hassanzadeh et al., 2012). But in the first decade of the new century, the Urmia basin have suffered from an environmental disaster. It is reported by Tourian et al. (2015a) that, from the year 2000 until 2014, on average the lake water level decreased at a rate of $34 \pm 1 \frac{cm}{year}$ and water area at $220 \pm 6 \frac{km^2}{year}$. If the Lake completely dries up, about 8 gigatonne of salt is released. This amount of salt could lead to an ecological, agricultural and social catastrophe in Iran and neighbouring countries (Pengra, 2012).

Hassanzadeh et al. (2012) declared that 65% of the lake desiccation is due to the reduction of inflow water because of climate change and overuse of surface water resources.

The construction of four dams on rivers located in the upstream rivers of the lake is responsible for 25% of the desiccation and a reduction in the annual precipitation is responsible for the remaining 10%. The vulnerable situation of the lake indicates the need for coherent measurements of the lake area as a prerequisite for making critical decisions to rescue the lake. The case studies and their locations are listed in Table 1.4.

Table 1.4: Information about case studies of this thesis

Case	Name	Country	Location	
			Lat (°)	Lon (°)
a	Niger River	Mali	13.27° N	7.00° W
b	Niger River	Nigeria	7.80° N	6.80° E
c	Niger River	Nigeria	7.68° N	6.75° E
d	Congo River	Congo	4.25° S	15.50° E
e	Po River	Italy	44.92° N	10.50° E
f	Nasser Lake	Egypt	23.00° N	32.80° E
g	Rukwa Lake	Tanzania	8.00° S	32.10° E
h	Mosul Dam Lake	Iraq	36.73° N	42.75° E
i	Therthar Lake	Iraq	34.00° N	43.30° E
j	Urmia Lake	Iran	37.70° N	45.50° E

1.6.2 Data set

In this thesis, optical images from MODIS, Landsat 7 and 8 are used for surface water area monitoring. In the following section, these products are introduced briefly.

Landsat 7, 8

The Landsat missions is the oldest space civil Earth observation program. The first Landsat satellite acquired images from the Earth surface in 1972. Since then, the Landsat program continuously provides worldwide images in several spectral bands. These remote sensing images are a valuable source of information for agriculture, geology, forestry, mapping and global change researches. Landsat satellites follow a sun-synchronous orbit

Landsat 7 was launched in April 1999. It flew at 705 km altitude. The satellite revisits a certain area every 16 days in an ideal situation. Landsat 7 carries the enhanced thematic mapper plus (ETM+), providing 8 bit images in 8 spectral bands: 6 bands in visible and IR domains with 30 m spatial resolution, a thermal band with 60 m and a 15 m panchromatic band. Since 2003, due to the failure of the scan line corrector (SLC),

Landsat 7 images have had strip shape gaps which ruin about 22% of each image. Regardless the failure of SLC, this mission still takes images from the Earth's surface in 2017. Table 1.5 provides information about Landsat 7 spectral bands.

Table 1.5: List of available bands in Landsat 7

Band	Spectral range [μm]	Description	Spatial resolution [m]
1	0.45–0.52	Blue	30
2	0.52–0.61	Green	30
3	0.63–0.69	Red	30
4	0.76–0.90	NIR	30
5	1.55–1.75	SWIR	30
6	10.4–12.5	Thermal	60
7	2.08–2.35	SWIR	30
8	0.52–0.90	Panchromatic	15

Landsat 8 was launched in the year 2013 and until now it is the most advanced optical imagery system available. Its orbit and revisit time are like Landsat 7. Landsat 8 carries two push broom sensors: the Operational Land Imager (OLI) and the Thermal InfraRed Sensor (TIRS), both of which provide improved signal to noise ratio and 12 bit images. The OLI provides data in 9 different spectral bands with 30 m spatial resolution and a panchromatic band with 15 m pixel size. TIRS captures data in two long wave thermal bands with 100 m resolution. Table 1.6 presents the details about the different spectral bands of Landsat 8.

Table 1.6: List of available bands in Landsat 8

Bands	Spectral range [μm]	Description	Spatial resolution [m]
1	0.43–0.45	Coastal-aerosol	30
2	0.45–0.51	Blue	30
3	0.53–0.59	Green	30
4	0.64–0.67	Red	30
5	0.85–0.88	NIR	30
6	1.57–1.65	SWIR 1	30
7	2.11–2.29	SWIR 2	30
8	0.50–0.68	Panchromatic	15
9	1.36–1.38	Cirrus	30
10	10.6–11.2	Thermal 1	100
11	11.5–12.5	Thermal 2	100

One of the most interesting features of Landsat 8 is the narrow band 9 (1.36–1.38 μm). This part of the spectrum is absorbed by the atmosphere, so anything visible in this band must be above most of the atmosphere. As a result, band 9 is dedicated for the cloud detection, especially for cirrus clouds.

MODIS

MODIS is a scientific instrument launched by NASA. MODIS is one of the five sensors which are mounted on Terra satellite. Terra was launched in 1999. It flies in a circular sun-synchronous polar orbit with 705 km altitude. In the year 2002, Aqua satellite joined Terra in the same orbit. It is equipped with six operating instruments including MODIS. Both of them have been active till now and provide images from Earth surface globally every 1-2 days. They provide images with high radiometric sensitive (12 bit) in 36 spectral bands from 0.405 μm to 14.338 μm. MODIS acquires data at three different spatial resolutions (2 bands at 250 m, 5 bands at 500 m and 29 bands at 1 km). This wide variety of spectral and spatial options and also daily data acquisitions makes MODIS an important source for land surface boundaries and properties, atmospheric water vapour and temperature, surface temperature, ocean color. There are many standard MODIS data products derived from original data for different purposes. For example, level one data (MOD01) is useful for calibration, MOD07, MOD04 and MOD06 are widely applied in atmosphere studies and MOD16, MOD11 and MOD09 are used in land monitoring applications.

In this thesis, apart from Landsat 7 and 8 images, the MODIS surface reflectance product, MOD09A1, is used in chapter two for multispectral transformation methods. This product is an estimate of the surface spectral reflectance for each band as it would have been measured at ground level if there were no atmospheric scattering or absorption. Seven different spectral bands with 500 m spatial resolution are available in this product. Malfunctioning of one of the detectors on Terra causes sharp and repetitive noise in the band 5 image, so this band is omitted and here we have just six different spectral bands. The following table presents information about the spectral bands of this product.

Bands	spectral range [μm]	Description
1	0.620–0.670	Red
2	0.841–0.876	NIR
3	0.459–0.479	Blue
4	0.545–0.565	Green
5	1.230–1.250	SWIR 1
6	1.628–1.652	SWIR 2
7	2.105–2.155	SWIR 3

Table 1.7: List of available bands in MODIS MOD09A1

In chapters 3 and 4, MODIS MOD09Q1 images are used for monitoring the spatial change in lakes and river area. This product has two spectral bands (red and NIR) in 250 m pixel size and 8 days temporal resolution in the Sinusoidal projection. Each MOD09Q1 pixel contains the best possible observation during a 8 days period as selected on the basis of high-observation coverage, low-view angle, the absence of clouds

or cloud shadow, and aerosol loading. Science Data Sets provided for this product include reflectance values for Bands 1 and 2, and Quality information (Vermote et al., 2011). Table 1.8 provides information about satellite images.

Table 1.8: Satellite images used in this thesis

Case	Name	Source of images	Period	Spatial Resolution [m]	Temporal Resolution [day]	Number of images
a	Niger River	MOD09Q1	2000–20016	250	8	724
b	Niger River	MOD09A1	-	500	16	3
b	Niger River	Landsat 7	-	30	16	1
b	Niger River	Landsat 8	-	30	16	2
c	Niger River	MOD09Q1	2000–20015	250	8	680
d	Congo River	MOD09Q1	2000–20016	250	8	724
e	Po River	MOD09Q1	2000–20017	250	8	720
f	Nasser Lake	MOD09Q1	2000–20014	250	8	620
g	Rukwa Lake	MOD09Q1	2002–20017	250	8	620
h	Mosul Dam Lake	MOD09Q1	2002–20017	250	8	620
i	Tharthar Lake	MOD09Q1	2002–20017	250	8	620
j	Urmia Lake	MOD09Q1	2000–20017	250	8	800

Additional data set

Directly validating the correctness of the derived water masks is impossible, since in situ measurements of water bodies area are impractical. It is obvious that a monotonic relationship between geometric variables of water bodies is established. It means that there must be a great positive agreement between the behaviour of water body variables like water level and area.

For the propose of validating the derived lake water masks, the behaviour of lake area time series are compared in chapter 3 with in situ and altimteric water level time series. Table 1.9 presents information about data set used for validation of derived lake water masks.

Table 1.9: Datasets used for validation of Lake water masks

Case	Name	Average area (km^2)	In Situ water level	Altimetry				
				Lat (°N)	Lon (°E)	Period	Mission	Source
f	Nasser	5250	2000–20015	23.25°	32.86°	2002–2012	ENVISAT	HydroSat
f	Nasser	5250	2000–20015	22.53°	31.88°	2002–2012	ENVISAT	HydroSat
g	Rukwa	5800	–	23.25°	32.86°	2002–2012	Jason-1,2	HydroSat
h	Mosul Dam	250	–	36.71°	42.82°	2002–2011	ENVISAT, Jason-1,2, Topex	DAHITI
i	Therthar	2710	–	33.98°	43.25°	2002–2017	ENVISAT, Jason-1,2, Topex	DAHITI
j	Urmia	5200	2000–2017	37.64°	45.35°	2002–2011	ENVISAT, Jason-1,2, Topex	HydroSat

Only for Nasser and Urmia Lakes daily in situ water level measurements are available. Since the accuracy of in situ measurements is higher than any spaceborne observation, they provide a great opportunity to validate derived lakes area time series and analyse the long term behaviour of surface area.

All lakes are selected in a way that different satellite altimetry sensors pass over them, so long and dense water level time series for all the case studies are available. In this study, lake level time series from two online data bases are used.

- HydroSat [1], as an online repository for monitoring global water cycle, provides different hydrological parameters of water bodies all over the world. HydroSat is developed in the Institute of Geodesy, University of Stuttgart in 2016.
- DAHITI[2] , the Database for Hydrological Time Series of Inland Waters, is developed by the DGFI-TUM (German: Deutsches Geod ätisches Forschungsinstitut der Technischen Universit ät München, lit. German Geodetic Research Institute of the Technical University of Munich) in 2013. This online source provides water level time series from multimission altimetry for inland water bodies like rivers, lakes and reservoirs (Schwatke et al., 2015).

In chapter four, river masks generated by the proposed method are validated indirectly by comparing the behaviour of river area time series with in situ discharge and altimetric water level measurements. In a natural river channel, river reach area must have a monotonic relationship with discharge and water level on that section (Leopold & Maddock Jr, 1953). Therefore, the corresponding time series should show significant correlation. This fact provides the opportunity to validate our water area estimations indirectly against river discharge and water level time series. Information about in situ and altimetric measurements is presented in Table 1.10.

Table 1.10: Information about datasets used for validation of river water masks

Case	Name	Reach Lenght (km)	In Situ Discharge					Altimetry			
			Station	Lat (°)	Lon (°)	Period	Source	Lat (°)	Lon (°)	Period	Mission
c	Niger	22	lokoja	7.80° N	6.77° E	2000–2006	GRDC	6.65° N	6.65° E	2003–2012	ENVISAT
a	Niger	115	Koulikoro	12.87° N	7.55° W	2000–2006	GRDC	12.74° N	7.73° W	2002–2015	ENVISAT, Saral
d	Congo	50	Kinshasa	4.30° S	15.30° E	2000–2010	GRDC	4.28° S	15.30° E	2002–2014	ENVISAT, Saral
e	Po	400	Borgoforte	45.05° S	10.75° E	2000–2012	AIPO	-	-	2000–2014	ENVISAT, Jason-2 Topex, CryoSat-2

For the first three case studies, in situ discharge measurements are used from GRDC dataset. For the Po River section in situ measurements are provided by AIPO (Italian: Agenzia Interregionale Fiume Po, lit. "The Interregional Agency for the Po River"). For the altimetric water level measurements, the location of virtual stations are provided. The altimertic time series for the Po River section is generated based on the method introduced by Tourian et al. (2016). This time series is generated by defining multiple virtual stations over the River reach. Finally, in situ discharge measurements are also used for developing empirical models between river width and discharge.

[1] http://hydrosat.gis.uni-stuttgart.de/
[2] http://dahiti.dgfi.tum.de/en/

1.7 Outline of the thesis

Each objective will be investigated in the following chapters. This thesis continues with introducing the applications of multispectral transformations in change detection analysis in the second chapter. First, the mathematical aspects of multispectral transformations are discussed. Then their potentials to be used as a tool for retrieving important information about water content from the original image bands and highlighting the change between two multitemporal images will be investigated.

In the third chapter, an algorithm for monitoring lake area will be presented. Each step of the algorithm will be introduced there in detail. Then its performance will be evaluated by applying it to different lakes with various behaviours. Finally, the desiccation of Urmia Lake during the last seventeen years will be investigated.

Chapter four deals with introducing a region-based change detection algorithm specifically developed for river area monitoring. The chapter starts with presenting mathematical concepts and algorithm steps. Then, for assessing the performance and validating the results of the proposed algorithm, it will be applied to a number of river reaches. At the end, empirical models for predicting river discharge will be developed and validated by comparing with in situ measurements.

Chapter 2

Multispectral transformations for change detection

2.1 Introduction

Multispectral transformations generate a new set of image components by combining original multispectral image bands. The new components represent an alternative description of the original data since they are related to the old brightness values via a linear operator. The transformed image bands may reveal features and properties of the Earth's surface which are not recognizable in the original spectral bands (Richards & Jia, 1999). In change detection applications, a fundamental issue is to find a way to define a change mask free of unimportant or nuisance forms of change like sensor noise, atmospheric absorption etc. (Radke et al., 2005). Nielsen (2007) mentions that nontrivial change includes:

- An additive shift in the mean level (offset) or a multiplicative shift in the calibration of a measuring device (gain);
- Data normalization or calibration schemes that are linear (affine) in the gray values of the original variables;
- The changes which cannot be detected by multispectral transformations, such as Principal Component Analysis (PC) or Maximum Autocorrelation Factor (MAF).

Moreover, multispectral transformations can be applied as a tool to enhance the signal to noise ratio level by isolating the noise of image bands in certain components. A transformed data set may also represent a certain physical characteristic of the sensed environment like different types of vegetation.

Multispectral transformations are widely applied in remote sensing applications. Gong (1993) applied PCA to the difference of two multitemporal images to emphasize the change in primary principal components. Nielsen et al. (2002) applied Empirical Orthogonal Function (EOF) decomposition to analyse the change in the sea surface temperature. Multivariate Alteration Detection (MAD) and MAF analysis and their combined transformation (MAD/MAF) were introduced in Nielsen et al. (1998). As

presented in their study, these transformations are insensitive to the variation in gain and offset between different images. Therefore, there is no need to apply radiometric and atmospheric corrections prior to the transformations. Canty & Nielsen (2008) applied iteratively re-weighted MAD transformation for radiometric normalization of multitemporal images. More sophisticated methods in this domain are listed in Nielsen (2011).

In this chapter, a number of multispectral transformations will be presented. Our focus is on presenting different characteristic of multispectral images and highlighting the change between different measurements epochs visually. Our main objectives are:

- Enhancing the quality of an image by reducing the noise level and then using the enhanced image bands to define the change more easily and precisely. PCA is an appropriate tool for this goal. The main concern is to select the right PCs to reconstruct the image bands.
- Highlighting the spatial change between two multitemporal images. MAD transformation has a great ability to highlight the change between two data sets and MAF transformation can emphasise where there is a high correlation with neighbouring pixels.

2.2 Methodology

2.2.1 Principal Components Analysis

PCA is a mathematical technique to establish a linear relationship between a set of observations of (possibly) correlated variables. The new set of variables are orthogonal to each other. In the new dataset, the major part of the information concentrates in the primitive components.

In remote sensing applications, PCA has been applied to three groups of applications:

- image compression, by considering only a number of primary principal components;
- image enhancement, by ignoring the later components, as they are usually dominated by noise;
- change detection, by highlighting the area where the significant change occurs in the primary components.

Suppose that a multispectral image with k spectral bands, each of which has m rows and n columns, is available. First of all, the image in each band is reshaped as a single column vector of length ($m \times n = N$):

$$\mathbf{X}_{N\times k} = [x_1, x_2, ..., x_k], \tag{2.1}$$

so the matrix $\mathbf{X}$ is the reshaped form of a multispectral image in two dimensions. The mean pixel value in each spectral band is defined according to

$$\widehat{x}_i = \frac{1}{N}\sum_{n=1}^{N} \mathbf{X}_{ni}, \tag{2.2}$$

where $\widehat{\mathbf{X}} = [\widehat{x}_1, \widehat{x}_2, ...\widehat{x}_k]$ is the set of mean values of all spectral bands. To describe the spread of pixels from the mean, the covariance matrix is defined as

$$\Sigma_{\mathrm{X}_{ij}} = \frac{1}{N-1}\sum_{n=1}^{N} (\mathbf{X}_{ni} - \widehat{\mathbf{X}}_i)(\mathbf{X}_{nj} - \widehat{\mathbf{X}}_j)^{\mathrm{T}}. \tag{2.3}$$

If there is any correlation between different pairs of spectral bands, the corresponding off-diagonal element in the covariance matrix would be large. On the other hand, the off-diagonal elements are near zero if there is no correlation among different spectral bands. The aim of the principal components transformation is to set a new coordinate system in the multispectral space so that the covariance matrix in the new coordinate system is diagonal. In other words, image bands in the transformed product are orthogonal to each other and there is no correlation between them. Here, it is assumed that $\mathbf{X}$ is transformed by an orthonormal transformation matrix, $\mathbf{C}$, such that the covariance matrix of the resulting matrix $\mathbf{W}$ is diagonal

$$\mathbf{W}_{N\times k} = \mathbf{X}_{N\times k}\, \mathbf{C}_{k\times k}\ , \tag{2.4}$$

with

$$\widehat{\mathbf{W}} = \mathrm{E}(\mathbf{W}) = \mathrm{E}(\mathbf{X}\mathbf{C}) = \widehat{\mathbf{X}}\mathbf{C}, \tag{2.5}$$

we can write the covariance matrix of $\mathbf{W}$ as

$$\begin{aligned}
\Sigma_{\mathrm{W}} &= \mathrm{E}((\mathbf{W} - \widehat{\mathbf{W}})(\mathbf{W} - \widehat{\mathbf{W}})^T) \\
&= \mathrm{E}((\mathbf{X}\mathbf{C} - \widehat{\mathbf{X}}\mathbf{C})(\mathbf{X}\mathbf{C} - \widehat{\mathbf{X}}\mathbf{C})^T) \\
&= \mathbf{C}\ \mathrm{E}((\mathbf{X} - \widehat{\mathbf{X}})(\mathbf{X} - \widehat{\mathbf{X}})^T)\ \mathbf{C}^T \\
&= \mathbf{C}\ \Sigma_{\mathrm{X}}\ \mathbf{C}^T.
\end{aligned} \tag{2.6}$$

Since Σ_{W} is assumed to be diagonal, $\mathbf{C}$ can be recognised as the transposed matrix of eigenvectors of Σ_{X}. As a result, Σ_{W} can be identified as the diagonal matrix of eigenvalues of Σ_{X}:

$$\Sigma_{\mathrm{W}} = \begin{bmatrix} \lambda_1 & 0 & & & \\ 0 & \lambda_2 & & & \\ & & \cdot & & \\ & & & \cdot & \\ & & & & \cdot \\ & & & 0 & \lambda_k \end{bmatrix}$$

The diagonal elements of the covariance matrix are the variances of respective transformed data. The eigenvalues are conventionally arranged in a descending order, $\lambda_1 \geq \lambda_2 \geq ... \geq \lambda_k$, so that the largest variance is in W_1, the next is in W_2 and so on. To find the eigenvalues and eigenvectors of Σ_W, the following equation must be solved:

$$\det(\Sigma_W - \lambda I) = 0 \,. \tag{2.7}$$

By knowing the eigenvalues and eigenvectors, principal components can be determined.

Eklundh & Singh (1993) stated that in remote sensing applications, PCs derived from a covariance matrix do not represent characteristics of the original data well because each band observes the sunlight in a different spectral range, so their origin and scale are varied. To solve this problem, the correlation matrix is used for deriving PCs instead of the covariance matrix. In this thesis, we follow their recommendation and replace the covariance matrix with the correlation matrix to derive PCs.

Singular Value Decomposition

Singular Value Decomposition (SVD) has certain characteristics making it a suitable technique for defining principal components:

- Generating a set of uncorrelated variables from correlated ones,
- Ordering the dataset in a way that exhibits the dominant variations in the primary components,
- Reducing the dimension of the dataset by accumulating the noise and trivial variations in the latest components (Baker, 2005).

SVD is based on a theorem from linear algebra that any matrix can be broken down into the product of three matrices. Suppose that $\mathbf{A}$ is a matrix with n rows and m columns ($\mathbf{A}$ is not necessary a full rank matrix). This matrix can be decomposed into a diagonal and two orthogonal matrices like the following equation

$$\mathbf{A}_{m\times n} = \mathbf{U}_{m\times p}\, \Sigma_{p\times p}\, \mathbf{V}^T_{p\times n} \tag{2.8}$$

where $\mathbf{U}_{m\times p}$ and $\mathbf{V}_{p\times n}$ are two column orthogonal matrices and $\Sigma_{p\times p}$ is a diagonal matrix. The singular values (σ_i) are diagonal elements of the matrix Σ which are non-negative and ordered so that $\sigma_1 \geq \sigma_2 \geq ... \geq \sigma_p \geq 0$, where $p = \min(n, m)$. Since $\mathbf{U}$ and $\mathbf{V}$ are orthogonal matrices, their columns form a basis for their vector spaces. SVD of matrix $\mathbf{A}$ has a strong relationship with eigenvalue decomposition of matrices $\mathbf{A}\ \mathbf{A}^T$ and $\mathbf{A}^T\ \mathbf{A}$. To derive the eigenvalues and eigenvectors of $\mathbf{A}\ \mathbf{A}^T$, we start with the transpose of Equation (2.8)

$$\mathbf{A}^T = (\mathbf{U}\,\Sigma\,\mathbf{V}^T)^T = (\mathbf{V}^T)^T\,\Sigma^T\,\mathbf{U}^T = \mathbf{V}\,\Sigma\,\mathbf{U}^T \,. \tag{2.9}$$

Since the matrix Σ is diagonal, $\Sigma^T = \Sigma$. Now we multiply matrix $\mathbf{A}$ by both sides of Equation (2.9)

$$\begin{aligned} \mathbf{A}^T\,\mathbf{A} &= (\mathbf{V}\,\Sigma\,\mathbf{U}^T)\,\mathbf{A} && (2.10)\\ &= \mathbf{V}\,\Sigma\,\mathbf{U}^T\,\mathbf{U}\,\Sigma\,\mathbf{V}^T && (2.11)\\ &= \mathbf{V}\,\Sigma^2\,\mathbf{V}^T\,. && (2.12) \end{aligned}$$

Respectively we can write

$$\mathbf{A}\,\mathbf{A}^T = \mathbf{U}\,\Sigma^2\,\mathbf{U}^T\,. \tag{2.13}$$

From these equations, we can conclude that the diagonal elements of Σ^2 are the eigenvalues and the matrices $\mathbf{V}$ and $\mathbf{U}$ are the matrices of eigenvectors of $\mathbf{A}^T\,\mathbf{A}$ and $\mathbf{A}\,\mathbf{A}^T$.

2.2.2 Tasselled Cap transformation

The idea of defining a new coordinate system for the multispectral remote sensing images has been applied to develop another group of methods. In each band of the transformed product, specific information is highlighted by setting new axes. To extract physical characteristics from the spectral features, it is necessary to understand the spectral signature of Earth surface features on different image bands. This group of transformations is able to compress various spectral bands into a reasonable number of bands (Crist & Cicone, 1984).

The *Tasselled Cap* transformation introduced by Kauth & Thomas (1976) is a means for highlighting the most important phenomena of crop development. This transformation converts the original spectral bands into a new set of bands which defines useful interpretations for mapping the vegetation properties. The first Tasselled Cap band corresponds to the overall brightness of the image. The second one corresponds to the greenness and is typically used as an index of photosynthetic activity. The third Tasselled Cap band is often interpreted as a wetness index of soil or surface moisture. For hydrological applications, the third band is useful as it emphasizes on the water contents in the image. Although this transformation produces the same number of bands as input bands, not all of the Tasselled Cap output bands will be useful. In most cases, the first three Tasselled Cap bands contain the most useful information and subsequent bands are considered as noise and not used. This transformation is known as Tasselled Cap because of its shape. Figure 2.1 presents the basic shape of the KT transformation. The plant starts growing approximately orthogonal to the plane of soils. After a curving trajectory toward the region of green stuff, the reflectances fold over the region of yellow and finally back to the soil plane.

The transformation was first introduced for Landsat MultiSpectral Scanner (MSS) by Kauth & Thomas (1976). They define that KT is a fixed orthogonal transformation,

$$\mathbf{W}_{N\times 4} = \mathbf{X}_{N\times 4}\,\mathbf{C}_{4\times 4} + r_{N\times 4}\,, \tag{2.14}$$

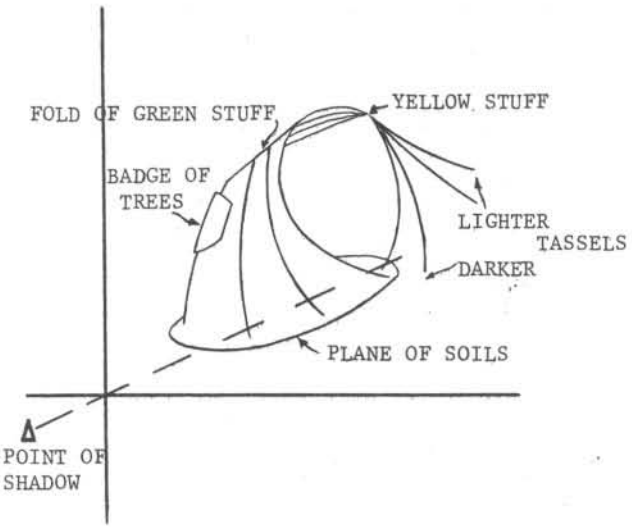

Figure 2.1: A schematic sketch of the Tasselled Cap transformation (Kauth & Thomas, 1976)

where **X** is the Landsat MSS image bands (four bands in different spectral range) which are reshaped as a 2 dimensions matrix. **W** is the transformed product, **C** is the transformation matrix containing the coefficients, and finally r is an offset vector introduced to avoid negative values in the final product. The **C** matrix contains four unit vectors which are orthogonal to each other. Based on Kauth & Thomas (1976), the first row of this matrix (c_1) is defined to point along the major axis of soil. This vector is called the soil brightness unit vector. c_2 is chosen in a way that is orthogonal to c_1 pointing the green stuff. c_2 is generated using the Gram-Schmidt orthogonalization procedure. c_3 is defined orthogonal to both c_1 and c_2 in the direction of the yellow stuff using Gram-Schmidt also. The last vector of **C** is defined like the previous ones and does not contain any specific information.

Therefore KT transformation is also a linear orthogonal transformation of the original bands. But, unlike PCA, the transformation matrix (**C**) is *user-defined*. However the transformed product of PCA can be different from KT transformation since any linear combination of eigenvectors creates an orthogonal transformation matrix (like **C**).

Following this strategy, Crist & Cicone (1984) developed a physically-based transformation for Landsat TM. The brightness, greenness and wetness are the main three components of their TM Tasselled Cap transformation. Now this transformation is available for other popular multispectral optical satellite systems such as MODIS, IKONOS, Landsat TM, ETM+ and QuickBird. They provide the opportunity to analytically compare land cover features directly using satellite imagery.

KT transformation is widely used in land cover applications because it provides a way to detect and compare changes in vegetation, soil, water content and man-made features over time. Also it is helpful to compress an image with several multispectral bands to an image with three primary components.

2.2.3 Canonical Correlation Analysis

CCA is a way of measuring the linear relationship between two sets of multidimensional variables. CCA can find two sets of basis vectors such that the correlation between projections of these basis vectors are mutually maximized. The first linear combination with the largest correlation is called the first canonical variate. The second two linear combinations have the biggest correlation such that they are orthogonal to the first pair. This condition must be satisfied by the further pairs as well. An important property of canonical correlation is that they are invariant to affine transformations between variables. This is the most important difference between CCA and ordinary correlation analysis which highly depends on the basis of variables (Borga, 1998).

CCA was developed by Hotelling (1936) and is now widely applied not only in statistical analysis but also in economics or medical sciences. Nielsen (1995) and Nielsen et al. (1998) first applied this technique in a change detection applications. The following procedure by Nielsen (1995), is suggested to find the nontrivial change between two multitemporal images.

One selects two multitemporal images with k spectral bands each of which has m rows and n columns. As before each image band is reshaped as a single column vector of length $N = m \times n$.

$$\mathbf{X}_{k\times N} = [x_1, x_2, ..., x_k]^T \quad , \quad \mathbf{Y}_{k\times N} = [y_1, y_2, ..., y_k]^T. \tag{2.15}$$

Now, $\mathbf{X}$ and $\mathbf{Y}$ are rewritten as a single matrix split into two groups like $\mathbf{Z}_{2k\times N} = [\mathbf{X}\ \ \mathbf{Y}]^T$. We assume that $\mathbf{Z}$ follow a Gaussian distribution with the following parameters:

$$\mu_{2k\times 1} = \begin{bmatrix} \mu_x \\ \mu_y \end{bmatrix} \ , \ \Sigma_{2k\times 2k} = \begin{bmatrix} \Sigma_{xx} & \Sigma_{xy} \\ \Sigma_{xy} & \Sigma_{yy} \end{bmatrix} \tag{2.16}$$

Here Σ_{xx} and Σ_{yy} are the variances of $\mathbf{X}$ and $\mathbf{Y}$, Σ_{xy} (Σ_{yx}) is the covariance between them. It is assumed that all portions of Σ are non-singular and $E(\mathbf{X}) = E(\mathbf{Y}) = 0$. Here, a linear transformation between $\mathbf{X}$ and $\mathbf{Y}$ is desirable like

$$\mathbf{U}_{k\times N} = \mathbf{a}_{k\times k}^T \, \mathbf{X}_{k\times N} \ , \ \mathbf{V}_{k\times N} = \mathbf{b}_{k\times k}^T \, \mathbf{Y}_{k\times N} \tag{2.17}$$

where

$$\mathbf{a}_{k\times k} = [a_1, a_2, ..., a_k]^T \quad , \quad \mathbf{b}_{k\times k} = [b_1, b_2, ..., b_k]^T. \tag{2.18}$$

are the coefficients matrices. By knowing $\text{var}(\mathbf{U}) = \mathbf{a}^T\Sigma_{xx}\mathbf{a}$, $\text{var}(\mathbf{V}) = \mathbf{b}^T\Sigma_{yy}\mathbf{b}$ and $\text{cov}(\mathbf{V}, \mathbf{U}) = \mathbf{a}^T\Sigma_{xy}\mathbf{b}$, the correlation between $\mathbf{U}$ and $\mathbf{V}$ is equal to

$$\rho^2 = \text{corr}(\mathbf{U}, \mathbf{V}) = \frac{\text{cov}(\mathbf{U}, \mathbf{V})}{\sqrt{\text{var}(\mathbf{U})\text{var}(\mathbf{V})}} = \frac{\mathbf{a}^T \, \Sigma_{xy} \, \mathbf{b}}{\sqrt{\mathbf{a}^T \, \Sigma_{xx} \, \mathbf{a} \, \mathbf{b}^T \, \Sigma_{yy}\mathbf{b}}} \tag{2.19}$$

To find the coefficients which maximize the correlation, the following equation must be maximized by introducing Lagrange multipliers $\lambda/2$ and $\nu/2$.

$$F = \mathbf{a}^T \Sigma_{xy}\, \mathbf{b} - \frac{\lambda}{2}(\mathbf{a}^T\, \Sigma_{xx}\, \mathbf{a} - 1) - \frac{\nu}{2}(\mathbf{b}^T\, \Sigma_{yy}\, \mathbf{b} - 1) \tag{2.20}$$

By setting $\partial F/\partial b = 0$ and $\partial F/\partial a = 0$, the cost function can be solved. Now by inserting the results, ρ^2 can be expressed as

$$\rho^2 = \frac{\mathbf{a}^T\, \Sigma_{xy}\, \Sigma_{yy}^{-1}\, \Sigma_{xy}\, \mathbf{a}}{\mathbf{a}^T\, \Sigma_{xx}\, \mathbf{a}} \quad = \quad \frac{\mathbf{b}^T\, \Sigma_{yx}\, \Sigma_{xx}^{-1}\, \Sigma_{xy}\, \mathbf{b}}{\mathbf{b}^T\, \Sigma_{yy}\, \mathbf{b}} \tag{2.21}$$

or

$$\Sigma_{xy}\, \Sigma_{yy}^{-1}\, \Sigma_{yx}\, \mathbf{a} \;=\; \rho^2 \Sigma_{xx} \mathbf{a} \tag{2.22}$$

$$\Sigma_{yx}\, \Sigma_{yy}^{-1}\, \Sigma_{xy}\, \mathbf{b} \;=\; \rho^2 \Sigma_{yy} \mathbf{b}\,. \tag{2.23}$$

This derivation shows that the desired projections for $\mathbf{U} = \mathbf{a}^T\mathbf{X}$ are given by the eigenvectors a_1, a_2, ..., a_k, corresponding to the eigenvalues $\rho_1^2 \geq \rho_2^2 \geq ... \geq \rho_k^2$ of $\Sigma_{xy}\Sigma_{yy}^{-1}\Sigma_{yx}$ with respect to Σ_{xx}. Similarly, the desired projections of $\mathbf{V} = \mathbf{b}^T\mathbf{Y}$ by considering the conjugate eigenvectors b_1, b_2, ..., b_k of $\Sigma_{xy}\, \Sigma_{xx}^{-1}\, \Sigma_{yy}$ with respect to Σ_{yy} corresponding to the same eigenvalues ρ_i^2. Now we are able to determine the respective canonical variates for each of the eigenvalues.

Multivariate Alteration Detection transformation

To highlight the area where the maximum change occurs between two images, Multivariate Alteration Detection (MAD) is applied. The name, MAD is chosen due its application in change detection in remote sensing (Nielsen, 1995). MAD transforms two sets of multivariate data (multispectral satellite images with k bands) into the k number of linear combinations of their difference. The output of the MAD transformation is ordered in a way that the maximum change is highlighted in the first MAD component.

Analysing the difference between pixel values is a common way to detect changes. Pixel differences with zero or low absolute value represent stable area and pixels with high absolute value represent the change. Two multitemporal images are reshaped like equation (2.18), and a simple subtraction operator is applied to them

$$\mathbf{X} - \mathbf{Y} = [x_1 - y_1, x_2 - y_2, ..., x_k - y_k]^T \tag{2.24}$$

If the images have more than three spectral bands, it is not possible to visualize the change in all bands. Moreover selecting just three bands among six or seven is not a wise choice. To overcome this problem and to highlight the changes in different spectral bands, a linear transformation that will maximize a measure of change (like

variance) can be used. If we replace the variance matrix with the correlation matrix, it leads us to find principal components of the simple image difference. This technique is highly vulnerable to the variations in the gain and offset between spectral bands.

Another approach to highlight the change is described by Fung & Ledrew (1987). They defined a certain basis for all spectral bands like

$$\mathbf{a}^T\mathbf{X} = a_1x_1 + a_2x_2 + ... + a_kx_k \tag{2.25}$$
$$\mathbf{b}^T\mathbf{Y} = b_1y_1 + b_2y_2 + ... + b_ky_k \tag{2.26}$$

and then apply PCA on their difference to find $\mathbf{a}$ and $\mathbf{b}$ coefficients. The other approach is to define the coefficients simultaneously by maximizing $\text{var}(\mathbf{a}^T\mathbf{X} - \mathbf{b}^T\mathbf{Y})$ subject to the constraints that $\text{var}(\mathbf{a}^T\mathbf{X}) = \text{var}(\mathbf{b}^T\mathbf{Y}) = 1$. If we write

$$\text{var}(\mathbf{a}^T\mathbf{X} - \mathbf{b}^T\mathbf{Y}) \quad = \quad \text{var}(\mathbf{a}^T\mathbf{X}) + \text{var}(\mathbf{b}^T\mathbf{Y}) - 2\text{cov}(\mathbf{a}^T\mathbf{X}, \mathbf{b}^T\mathbf{Y}) \ , \tag{2.27}$$

and consider the equation (2.19), the variance can be rewritten like

$$\text{var}(\mathbf{a}^T\mathbf{X} - \mathbf{b}^T\mathbf{Y}) \quad = \quad 2(1 - \text{corr}(\mathbf{a}^T\mathbf{X}, \mathbf{b}^T\mathbf{Y})) \tag{2.28}$$

It is clear that there must be a positive correlation between $\mathbf{a}^T$ and $\mathbf{b}^T$. To highlight the change between two images, the coefficients providing minimum positive correlation between $\mathbf{a}^T\mathbf{X}$ and $\mathbf{b}^T\mathbf{Y}$ should be found. To define the coefficients, CCA is applied as mentioned in the previous section. Finally MAD modes are introduced as:

$$\text{MAD}_i = a_i^T\mathbf{X} - b_i^T\mathbf{Y} \quad i = 1, 2, ..., k \tag{2.29}$$

The MAD components are ordered decreasingly in terms of highlighting the pixels with the minimum change in two epochs. Therefore the first MAD shows the maximum similarity and the minimum change. The second MAD has the maximum correlation between pairs subject to the condition that they are uncorrelated with the first MAD component. This condition is valid for other pairs as well. Since monitoring and detecting the change is the main goal of this study, the order of MAD variables is reversed. It means that the first MAD highlights pixels with the least similarity and the last MAD represents the constant area.

Consider $\mathbf{U} = \mathbf{a}^T\mathbf{X}$ and $\mathbf{V} = \mathbf{b}^T\mathbf{Y}$, defined from CCA. Now the covariance of the MAD components is given by

$$\text{cov}(\mathbf{U}_i - \mathbf{V}_i, \mathbf{U}_j - \mathbf{V}_j) = 2\delta_{ij}(1 - \rho_j) \tag{2.30}$$

where δ_{ij} is Kronecker's delta

$$\delta_{ij} = \begin{cases} 1 & \text{for } \ i = j \\ 0 & \text{for } \ i \neq j \end{cases} . \tag{2.31}$$

Thus the components are orthogonal to each other and

$$\text{var}(\mathbf{U}_i - \mathbf{V}_i) = \sigma^2_{\text{MAD}_i} = 2(1-\rho_i) \quad \rho_1^2 \geq \rho_2^2 \geq ... \geq \rho_k^2 \,. \tag{2.32}$$

MAD variates have approximately a Gaussian distribution because of the central limit theorem (Rice, 2006). MAD values of a pixel would be near zero if no change occurs between two images. Finally, MAD variates are independent from each other. So, it is expected that the sum of the squared MAD values for each pixel after normalization follows a χ^2-distribution with k degrees of freedom

$$T_j = \sum_{i=1}^{k} \left(\frac{\text{MAD}_{ij}}{\sigma_{\text{MAD}_i}} \right)^2 \sim \chi^2(k) \tag{2.33}$$

This distribution can be used to generate a *change / no-change* map. For example highlighting the change areas with 99% confidence interval is the goal. The pixel is tagged as *changed* if the T-value for this pixel is larger than 18.5 (the degree of freedom is 7). An automatic radiometric normalization for satellite images is introduced by Canty et al. (2004) and Canty & Nielsen (2008) based on this idea. As the MAD transformation is invariant to linear transformations, pixels with a small T-value can be considered as reference points for the radiometric normalization process. For example, if the degree of freedom is 7 then the critical value for the stable pixels with 99 % confidence would be 1.24.

Maximum Autocorrelation Factor transformation

To find areas with maximum change, applying the MAF postprocessing transformation to the outputs of MAD and PCA transformation is suggested. MAF, which was developed by Switzer & Green (1984), takes advantages of the fact that there is usually a strong spatial correlation between the pixel values of Earth surface features. Accordingly, noise shows weak spatial correlation. In change detection applications, if we assume trivial changes between two multitemporal images as noise components, then they present a small spatial correlation. Therefore, MAF transformation can highlight the major changes between two epochs.

Despite PCA transformation maximizing the data variance. The MAF transformation is equivalent to a transformation of the coordinate system in which the covariance matrix of the spatially shifted image data is the identity matrix (Nielsen, 1995).

Here, we consider each spectral band as a two-dimensional random variable $\mathbf{Z}_k(\mathbf{x})$, where $\mathbf{x} = [i, j]$ is the coordinate of the pixel $\mathbf{Z}_k(\mathbf{x})$. If each spectral band has p rows and q columns, then $1 \leqslant i \leqslant p$ and $1 \leqslant j \leqslant q$. Therefore, the multispectral images with K spectral bands can be stated as follows

$$\mathbf{Z} = [\mathbf{Z}_1(\mathbf{x}), \mathbf{Z}_2(\mathbf{x})..., \mathbf{Z}_K(\mathbf{x})] \tag{2.34}$$
$$\mathrm{E}(\mathbf{Z}(\mathbf{x})) = 0 \tag{2.35}$$
$$\mathrm{var}(\mathbf{Z}(\mathbf{x})) = \Sigma\,. \tag{2.36}$$

We define a spatial shift $\Delta = (\Delta_1, \Delta_2)$ and introduce the spatial covariance function

$$\Gamma(\Delta) = \mathrm{cov}(\mathbf{Z}(\mathbf{x}), \mathbf{Z}(\mathbf{x}+\Delta))\,. \tag{2.37}$$

This function has certain properties

$$\Gamma(0) = \Sigma \tag{2.38}$$
$$\Gamma(\Delta)^T = \Gamma(-\Delta) \tag{2.39}$$

Now the aim is to find a vector basis (e.g. $\mathbf{a}$) for $\mathbf{Z}(\mathbf{x})$ in a way that minimizes the correlation between $\mathbf{Z}(\mathbf{x})$ and $\mathbf{Z}(\mathbf{x}+\Delta)$. So the following equation must be minimized.

$$\mathrm{corr}(\mathbf{a}^T\mathbf{Z}(\mathbf{x}), \mathbf{a}^T\mathbf{Z}(\mathbf{x}+\Delta)) = \frac{\mathrm{cov}(\mathbf{a}^T\mathbf{Z}(\mathbf{x}), \mathbf{a}^T\mathbf{Z}(\mathbf{x}+\Delta))}{\sqrt{\mathrm{var}(\mathbf{a}^T\mathbf{Z}(\mathbf{x}))\ \mathrm{var}(\mathbf{a}^T\mathbf{Z}(\mathbf{x}+\Delta))}} \tag{2.40}$$

It is clear that $\mathrm{var}(\mathbf{a}^T\mathbf{Z}(\mathbf{x})) = \mathrm{var}(\mathbf{a}^T\mathbf{Z}(\mathbf{x}+\Delta)) = \mathbf{a}^T\ \Sigma\ \mathbf{a}$. Considering the mathematical details provided in Nielsen (1995) yields

$$\mathrm{cov}(\mathbf{a}^T\mathbf{Z}(\mathbf{x}), \mathbf{a}^T\mathbf{Z}(\mathbf{x}+\Delta)) = \mathbf{a}^T(\Sigma - \frac{1}{2}\Sigma_\Delta)\mathbf{a}, \tag{2.41}$$

where

$$\Sigma_\Delta = \mathrm{var}(\mathbf{Z}(\mathbf{x}) - \mathbf{Z}(\mathbf{x}+\Delta))\,. \tag{2.42}$$

Now we rewrite the equation (2.40)

$$\mathrm{corr}(\mathbf{a}^T\mathbf{Z}(\mathbf{x}), \mathbf{a}^T\mathbf{Z}(\mathbf{x}+\Delta)) = \frac{\mathbf{a}^T(\Sigma - \frac{1}{2}\Sigma_\Delta)\mathbf{a}}{\mathbf{a}^T\ \Sigma\ \mathbf{a}} = 1 - \frac{1}{2}\frac{\mathbf{a}^T\ \Sigma_\Delta\ \mathbf{a}}{\mathbf{a}^T\ \Sigma\ \mathbf{a}}\,. \tag{2.43}$$

Our aim is to minimize the correlation, therefore we need to maximize the Rayleigh quotient

$$R(\Sigma_\Delta, \mathbf{a}) = \frac{\mathbf{a}^T\ \Sigma_\Delta\ \mathbf{a}}{\mathbf{a}^T\ \Sigma\ \mathbf{a}}\,, \tag{2.44}$$

in the equation (2.43). The smallest value for the Reyleigh quotient is equal to λ_k (the last eigenvalue of Σ_Δ) if $\mathbf{a}_k$ is the corresponding eigenvector of Σ_Δ in respect to Σ. The largest value for equation (2.44) is equal to λ_1 if $\mathbf{a}_1$ is equal to the first eigenvector.

By reversing the order of MAF modes, pixels with a strong spatial correlation would be highlighted in the primary MAFs and the major part of the noise component gathers in

the latest MAFs, if the MAF transformation is applied to MAD variables. The change information with high spatial correlation between multitemporal images is concentrated in the first three or four bands of MAD/MAF. In this thesis, the Matlab code provided at A. Nielsen's website [1] is used to perform the MAF transformation.

2.3 Applications of multispectral transformations in inland water body change detection

2.3.1 Principal Component Analysis

In this section, PCA transformation is presented as a tool for reducing the noise level and highlighting the desired physical characteristic of multispectral images. Figure 1.6(b) shows the study area of this section.

To monitor the change in the river extent during wet and dry seasons, three MODIS MOD09A1 images on different dates were collected. The images are available in six spectral bands from visible to near infrared. In Table 1.7, information about this product is provided. In Figure 2.2, three RGB images of the river reach on different epochs are presented.

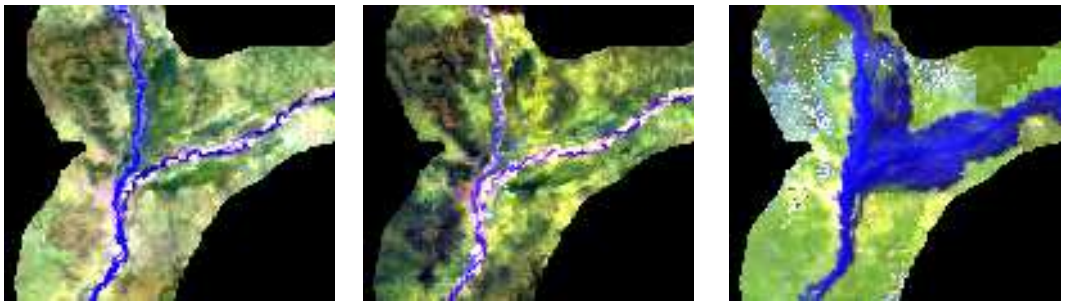

(a) 2012.01.0.1 **(b)** 2012.04.01 **(c)** 2012.09.19

Figure 2.2: RGB images of the Niger River derived from MODIS MOD09A1 at three different epochs

To enhance the quality of the images, PCA transformation is applied to each of them separately. Figure 2.3 roughly describes the procedure which is applied to each of the image bands.

Based on the algorithm in Figure 2.3, each image with m columns and n rows in a certain spectral band is reshaped as a vector. So, a multispectral image with k bands is reshaped to a two-dimensional matrix with k columns and $n \times m$ rows. PCA transformation is then applied to the reshaped image bands according to the previous section.

[1] http://www.imm.dtu.dk/~alan/software.html

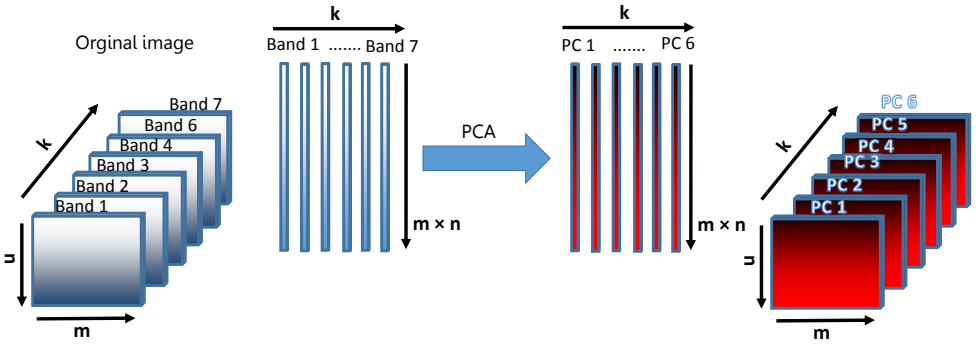

Figure 2.3: The procedure of PCA transformation on a single multispectral image

To evaluate the result of PCA transformation, each PC reshapes to a matrix with m columns and n rows. Unlike the original image bands which are ordered based on their wavelength, PCs are sorted by importance. Therefore the first PC contains the largest portion of total variance and the last PC contains hardly any useful information. The routine is applied to image bands acquired on January 1, 2012 and in Table 2.1, eigenvalues derived from covariance and correlation matrix are presented.

Table 2.1: The eigenvalues and their percentage derived from both covariance and correlation matrices.

	Covariance		Correlation	
Mode	Eigenvalue	Percentage	Eigenvalue	Percentage
1	1.7138	99.95%	3.8098	63.5%
2	0.0006	0.07%	1.7322	28.9%
3	0.0001	0.01%	0.3783	6.3%
4	0	0%	0.0372	0.6%
5	0	0%	0.0262	0.4%
6	0	0%	0.0160	0.2%

In the second and third columns of Table 2.1, we can see more than 99% of the variance concentrates in the first PC. So, the rest of the PCs are hardly containing any information because less than 1% of variance is divided between them. On the other hand, when the correlation matrix is used to derive PCs, the correlation is shared more evenly between all PCs descendingly. Therefore it is recommended that the correlation is used to generate PCs.

The images in the first row of Figure 2.4 present different spectral bands of the study area. For example in the NIR image (band 2) which is the most sensitive one to the water, the river is clearly visible. On the other hand, each image in the second and third rows is a linear combination of all spectral bands. Since they are sorted by their contribution in the variance and correlation, the latter modes are saturated by the noise

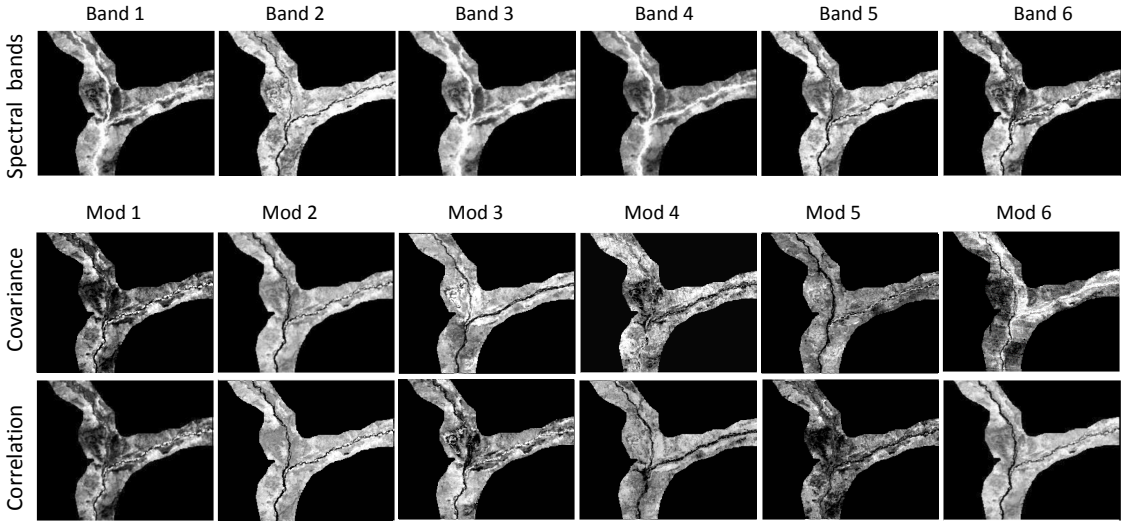

Figure 2.4: Different image bands and PCs derived from covariance and correlation matrices

(the noise level in the last modes in Figure 2.4 is clear in the images with a bigger size). Applying classification techniques on PCs directly is not possible because they are defined based on a mathematical process. Therefore it is not possible to assign physical characteristics to them. In general PCs are used in change detection applications in two different ways:

1. Enhancing the signal to noise ratio of the image bands by reconstructing the image bands from a reduced number of PCs.

2. Placing PCs in the color channels and generating an RGB image with PCs instead of spectral bands.

To reduce the noise level in the image bands, it is assumed that there is no valuable information in an PC if it contains less than 1% of the correlation. In Table 2.2, eigenvalues and their percentage from the correlation are presented.

Table 2.2: The eigenvalues and their percentage from the total correlation for all three measurement epochs.

	2012.01.01		2012.04.01		2012.09.19	
Mode	Eigenvalue	Percentage	Eigenvalue	Percentage	Eigenvalue	Percentage
1	3.809	63.5%	3.214	53.9%	3.347	55.8%
2	1.732	28.9%	2.109	43.1%	2.109	35.2%
3	0.378	6.3%	0.128	2.1%	0.454	7.6%
4	0.037	0.6%	0.057	0.9%	0.063	1.1%
5	0.026	0.4%	0.006	0.1%	0.018	0.3%
6	0.016	0.2%	0.003	0.1%	0.005	0.1%

Table 2.2 shows that the first three PCs are enough for reconstructing the images acquired on 2012.01.01 and 2012.04.01. But in the last image, the fourth PC also contains valuable information. Therefore the first four PCs are applied to reconstruct the image on 2012.09.19.

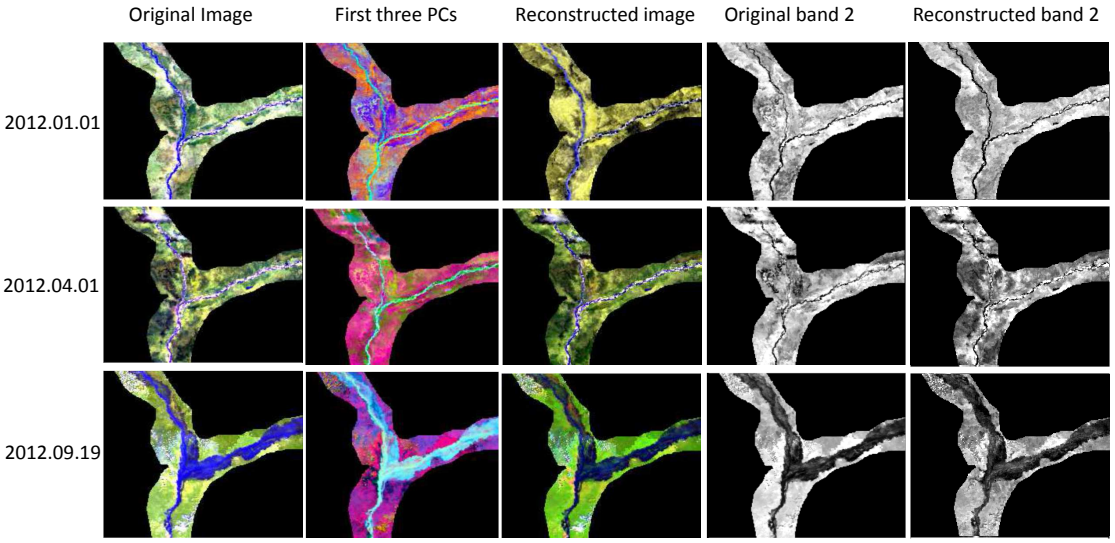

Figure 2.5: Improving the signal to noise ratio by reconstructing the images considering few primary PCs. Original RGB images are in the first column. The reconstructed images by removing the later PCs are in the second columns. The original and reconstructed band 2 of the three epochs are presented in the third and fourth columns.

The first column of Figure 2.5 presents the RGB images of all three epochs and the reconstructed RGB images are shown in the second column. By comparison between the two columns we can easily find that images in the second columns are less noisy. For example, in the first row, the vegetation around the river changed from green to yellow and the river border is more visible. In the second row, some parts of the river are highlighted which makes water detection easier in the reconstructed image. In the last row, some parts of the original image are slightly affected by clouds. The PCA transformation could partially overcome this problem in the reconstructed image. In the third and fourth columns of Figure 2.5 only the band 2 of three epochs are compared. It is interesting that in the third row the main river border is recognizable from the flooded area after the transformation.

Placing PCs directly into the color channels can help to map different characteristics of the Earth surface. For visualizing multispectral images we are limited to select only three spectral bands. Therefore different spectral band combinations are developed to highlight specific features of the Earth surface. However, any band combination leads to ignoring the rest of the bands. Presenting PCs directly in the color channels is an alternative for representing the multispectral images. Each PC contains information from all the spectral bands, therefore by presenting them as color channels, we can explore more details about the area. In the following figure, the first three PCs are

presented in the different color channels for the image acquired on 2012.01.01. Since these PCs contains almost all the valuable information in the spectral bands, we expect that the new image presents more details than the ordinary RGB image.

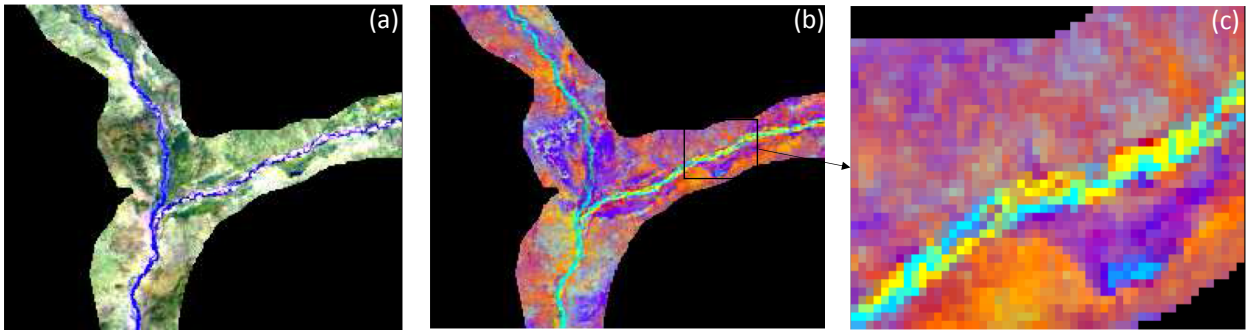

Figure 2.6: (a) ordinary RGB image. (b) combination of first three PCs as image bands. (c) is the selected area for more investigation. Date of the image: 2012.01.01

The color combination of the new RGB image (Figure 2.6(b)) created by the first three PCs looks strange at first glance. But after comparing with the original RGB image, we can find out the relationship between colors and the Earth surface features. The river shows up in light blue but those parts of the river bed which are dry in this image appear in yellow. In Figure 2.6(c) we can see how pixels with different coverages are presented in different colors. The dry areas are presented in different colors based on their vegetation coverage. Areas with a dense vegetation appear in purple and the color orange presents the area with a sparse vegetation. It must be mentioned that this interpenetration is not valid before comparing the product with the original image. In the next figure we compare the maps of primary PCs for all three epochs.

Since the transformation is applied to the images separately, each image has its own color map. For example, pixels covered with dense vegetation in the first image may be presented in purple but in the second image they may be shown in pink. In the second row, the river is presented in green but in the last image, the main part of the river and the flooded area appear in blue.

This approach to use only the primary PCs is just based on mathematical assumptions and does not have any physical constraints. Ignoring the last PCs is not the best strategy when dealing with Earth related phenomena as they have special signature on different spectral image bands. Therefore the decision about selecting PCs is based on the dispersion of pixel values from the mean value of all pixels. Moreover there is a big difference between the value of water and land in the image bands.

Another strategy to select PCs comes about when studying the role of different spectral bands in each PC. By looking at eigenvectors, the appropriate PCs are determined by investigating the information highlighted in each PC. The following table contains eigenvectors derived by PCA transformation for the image acquired on 2012.01.01.

To select the appropriate PCs for presenting into the color channels, an extensive overview about image bands and objective of the study is necessary. The spectral

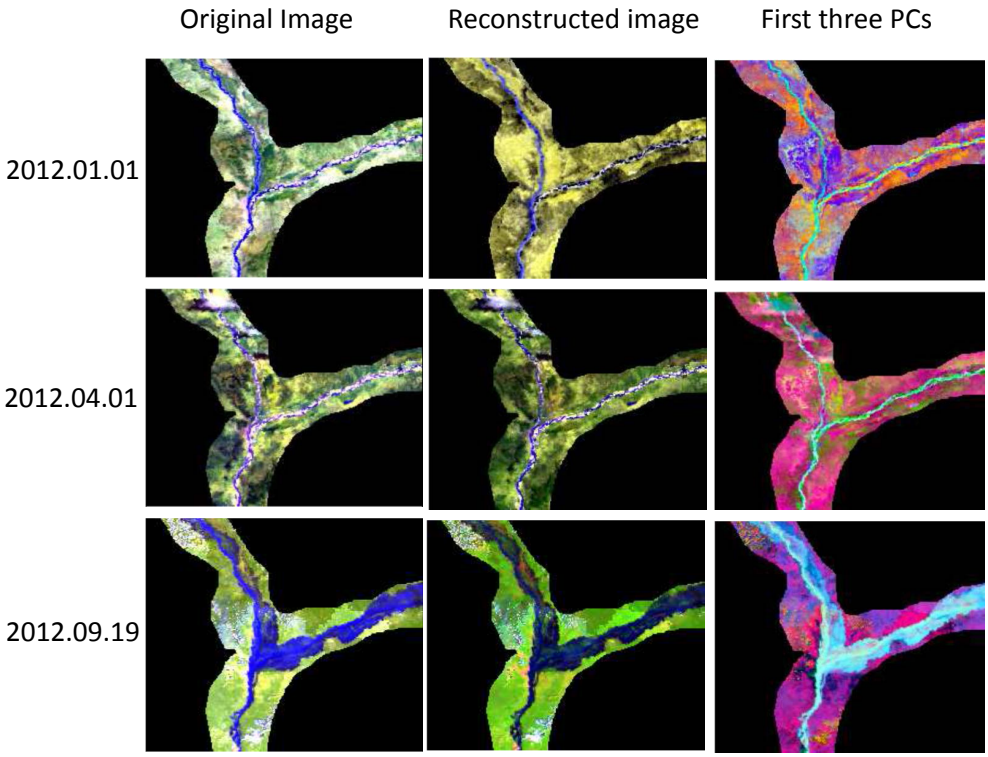

Figure 2.7: Ordinary RGB images are presented in the first column. The second column shows the reconstructed images and the maps of first three PCs are presented in the last column.

Table 2.3: Eigenvectors of all image bands (date: 2012.01.01)

Eigenvector	1	2	3	4	5	6
Band 1	0.462	0.235	0.463	0.427	0.377	0.435
Band 2	0.311	−0.579	0.300	0.387	−0.490	−0.292
Band 3	0.044	0.735	0.038	0.292	−0.257	−0.551
Band 4	0.192	0.095	−0.667	0.344	−0.409	0.471
Band 6	−0.504	0.170	0.486	−0.055	−0.531	0.441
Band 7	−0.628	−0.169	−0.101	0.678	0.317	−0.072

bands of the MODIS MOD09A1 product range from visible till near infrared (Table 1.7).

The aim is to highlight different characteristics of the river. In this way, first based on Table 1.2, it is clear that the ability and sensitivity of different bands against water content are different. So, the most reasonable PCs to reconstruct the image must be selected.

With respect to Table 1.7, bands 2, 3 and 4 contain the most important information to explore the information about the water extent and water area. Band 2 is the best for detecting the water-land boundary which is the main concern. Also, the tiny part of

sunlight which can slightly penetrate the water column is observed in band 3 and 4. So, PCs in which these bands have bigger coefficients are selected and we assume that these linear combinations retrieve more information about the river. We select PCs 2, 3 and 6 because the mentioned spectral bands are highlighted in them considering Table 2.3.

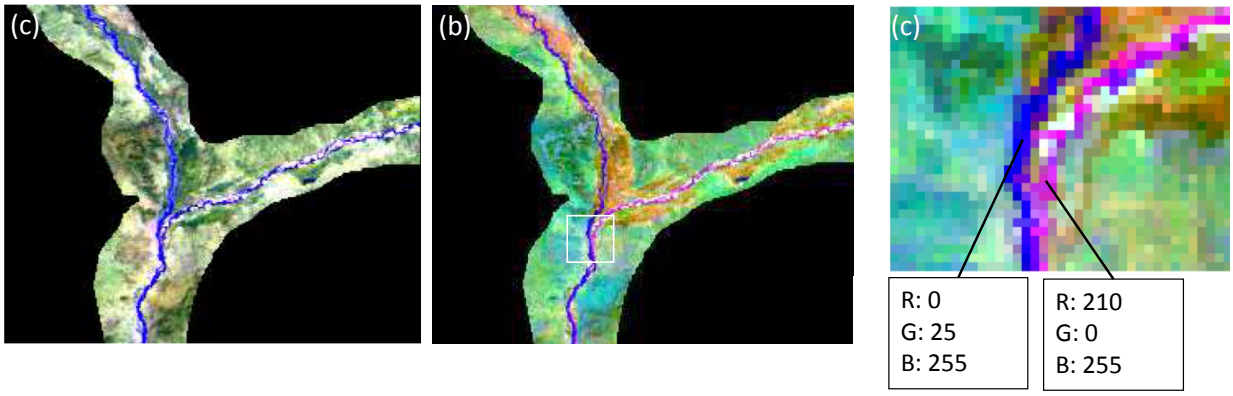

Figure 2.8: Comparison between RGB image and map of the selected PCs. Image date 2012.01.01

Since we concentrate on highlighting the water bodies, it is hard to provide any further interpretation about the vegetation coverage in Figure 2.8(b). In this figure, it is interesting that two river branches show up in different colors. The east part appears in pink and when it joined to the other branch, its color changed to blue. For more investigation about this difference, we select two pixels located in the river with different colors in Figure 2.8(c).

By looking at the coefficients in the color channels we find out that the major difference is between the pixel values in the red band. In this band we placed PC3 and in Table 2.3 we see that in this PC band 4 is the most highlighted one. It is mentioned in Table 1.2 that band 4 is useful for mapping detail such as depth or sediment in water bodies.

Without any external source of information, it is not possible to define the reason for this pattern. It is most likely that two river branches contain different types or amount of sediments. Therefore they appear in different colors. In the next figure we follow the same strategy to select PCs for images acquired on different dates.

In the image acquired on 2012.04.01 the right branch of the river is also pink. The north part of the river is not visible in both RGB and PCs map because of the cloud coverage. The last example in this figure is the most interesting one. In this case the main river body is blue but the flooded area is separated with different color (pink). The areas which are covered by clouds are presented in red.

Up to here, PCA transformation is mainly used as a tool for reducing the noise level and highlighting a certain characteristic in the different spectral image bands. Now PCA transformation will be presented as a tool to highlight the change between two multitemporal images from the same area. For this purpose, images in Figure 2.2(a) and (c) are selected, because a significant change in the river extent and flooded area

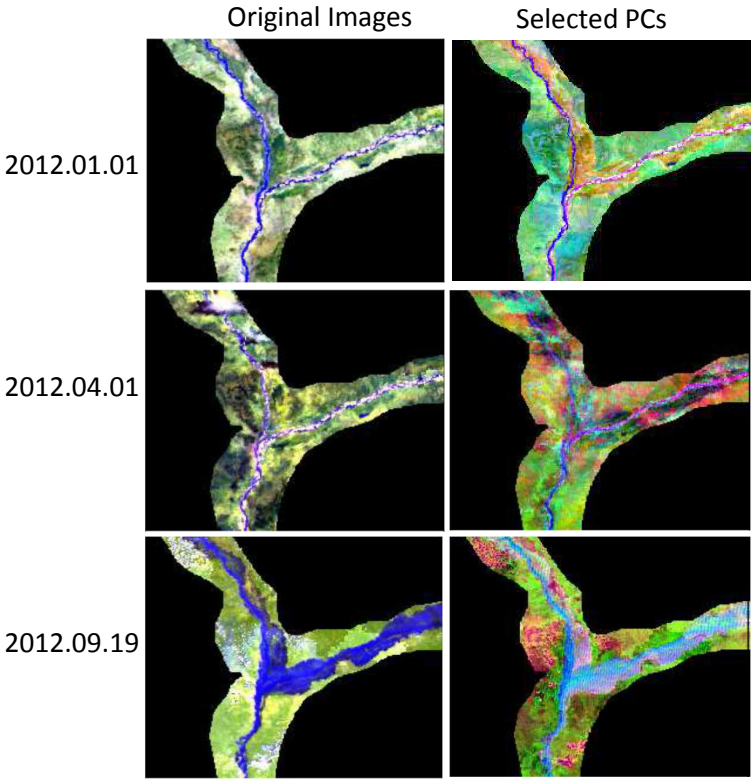

Figure 2.9: Comparison of original RGB images and maps generated by three selected PC. In the second row, each PCs map includes respectively PCs number: (2, 3, 6), (6, 2, 5), (5, 3, 2).

have occurred between two epochs. In the following figure the procedure to map the change between two images is described.

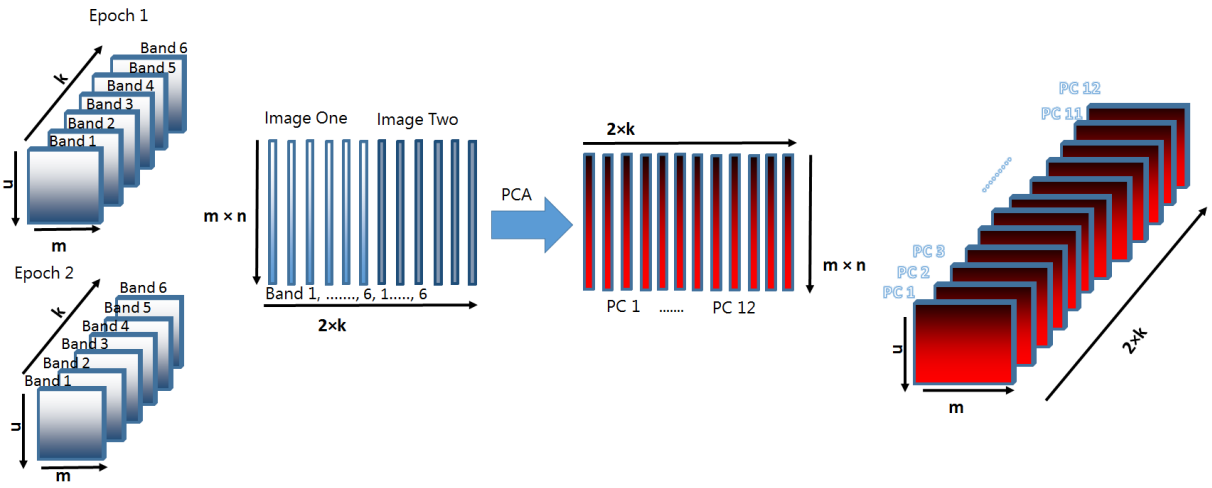

Figure 2.10: Procedure of applying PCA on multitemporal images

Based on Figure 2.10, all spectral bands from both multitemporal images are reshaped as a column vector and then all the vectors are concatenated together. So the final

matrix includes pixel values from different spectral bands of the first image in the first k columns. Pixel values of the second image are located in the second k columns. After applying PCA, each PC must be reshaped to the original dimensions. As a result the final product of this procedure is a 3 dimensional matrix with m columns and n rows and $2 \times k$ bands. Now the main concern is selecting appropriate PCs to describe the river state in each image and also the occurred change. In other words, PCA is applied here to highlight the change between multitemporal images visually.

Choosing the primary PCs is not an appropriate selection mechanism because here the definition of correlation matrix is completely different from previous examples. Here, correlation matrix represents the difference from the mean pixel values among each image bands and also between two multitemporal images. So, picking the primary PCs for interpretation is not the solution because they are ordered based on their variance portion. Therefore, PCs must be chosen carefully by investigating the eigenvectors. To do this, first the quantity of interest must be defined, for example river extent or flooded area. Then, based on Table 1.2, the most important PCs from both images are selected for presenting as color channels. Selected PCs must assign noticeable coefficients for the spectral bands providing information about water content in both images.

The previous experiment found that most of the important information for the goal of this study concentrates in bands 2, 3 and 4. So, among all PCs, those in which their coefficients for desirable bands are dominant should be selected.

In Table 2.4, the first PC highlights the flooded area in the second image. Also in PCs number 11 and 4, the critical spectral bands in both images are eminent. These three PCs are selected to present the characteristics of both images and also the change between them.

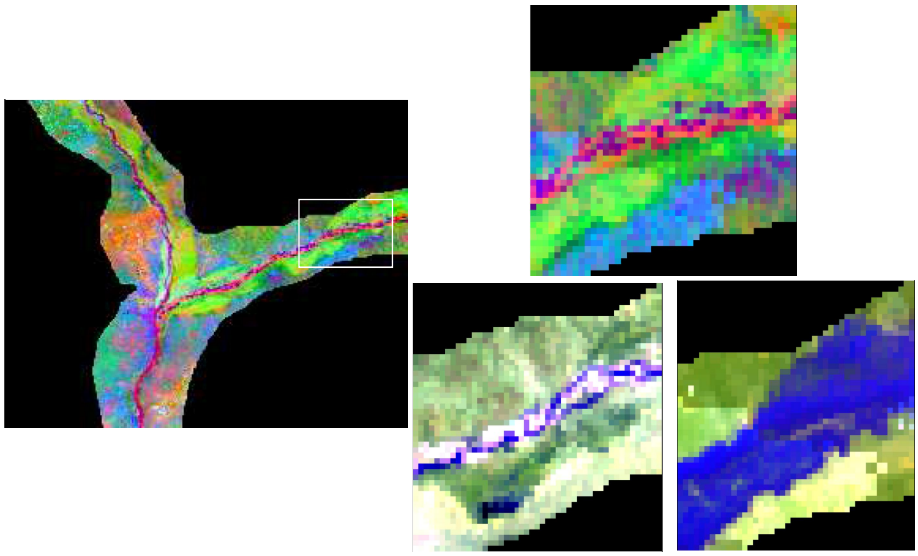

Figure 2.11: (left) an image composed of PCs 1, 4, 11. (right) comparison of a small part of the product with the original images. Image dates 2012.01.01 and 2012.09.19

Table 2.4: Eigenvectors of combination of two multispectral image bands PC1 to PC6

Eigenvector	1	2	3	4	5	6
Band 1	−0.438	−0.252	−0.441	−0.389	−0.401	−0.451
Band 2	−0.103	0.050	−0.100	−0.157	0.055	0.032
Band 3	0.195	−0.164	0.184	0.276	−0.205	−0.113
Band 4	−0.264	0.625	−0.262	−0.239	0.387	0.192
Band 6	0.091	0.668	0.097	0.260	-0.286	−0.587
Band 7	0.064	−0.030	0.039	−0.061	0.045	0.050
Band 1	−0.057	0.002	−0.197	0.075	−0.120	0.195
Band 2	−0.408	−0.127	0.645	−0.200	0.402	−0.362
Band 3	−0.425	0.195	0.430	−0.066	−0.589	0.475
Band 4	−0.545	−0.112	−0.196	0.726	0.170	0.006
Band 6	0.145	0.001	0.031	−0.174	0.009	−0.032
Band 7	0.085	0.023	0.033	−0.094	−0.078	0.034

Eigenvector	7	8	9	10	11	12
Band 1	0.010	−0.067	0.054	0.022	−0.101	−0.119
Band 2	0.239	0.421	0.385	0.340	0.452	0.493
Band 3	0.503	−0.293	0.382	0.439	−0.267	−0.136
Band 4	0.163	−0.252	0.157	0.150	−0.238	−0.176
Band 6	−0.022	0.153	−0.099	−0.012	0.075	0.022
Band 7	−0.059	0.671	0.115	0.175	−0.071	−0.693
Band 1	0.483	0.122	−0.758	0.270	0.045	−0.003
Band 2	0.122	−0.014	−0.198	0.112	0.013	−0.007
Band 3	−0.032	0.032	0.085	−0.072	−0.054	0.013
Band 4	−0.180	0.135	0.063	0.077	−0.159	0.084
Band 6	−0.017	0.357	−0.050	−0.005	−0.784	0.447
Band 7	−0.612	−0.175	−0.159	0.734	0.007	0.056

In Figure 2.11, the most important details about the status of the river at both epochs are presented. In the right part of the figure, the flooded area appears green, the area covered by water in both dates appears pink. The area which is dry on the first date, and covered by water on the second appears orange. This kind of product is useful to understand the behaviour of the object and also for comparison of its state on different dates. However for interpretation, the original images are still needed and this is one of the drawback of this method.

The other way to detect the change in two multitemporal images is to study the difference between pixel values of their spectral bands. The difference in value of the same pixel in two images represents the change in the physical characteristic if both images have the same radiometric basis. To detect the significant changes and also to reduce the trivial variations, PCA is applied to the difference image. Figure 2.12 presents the flowchart of this procedure.

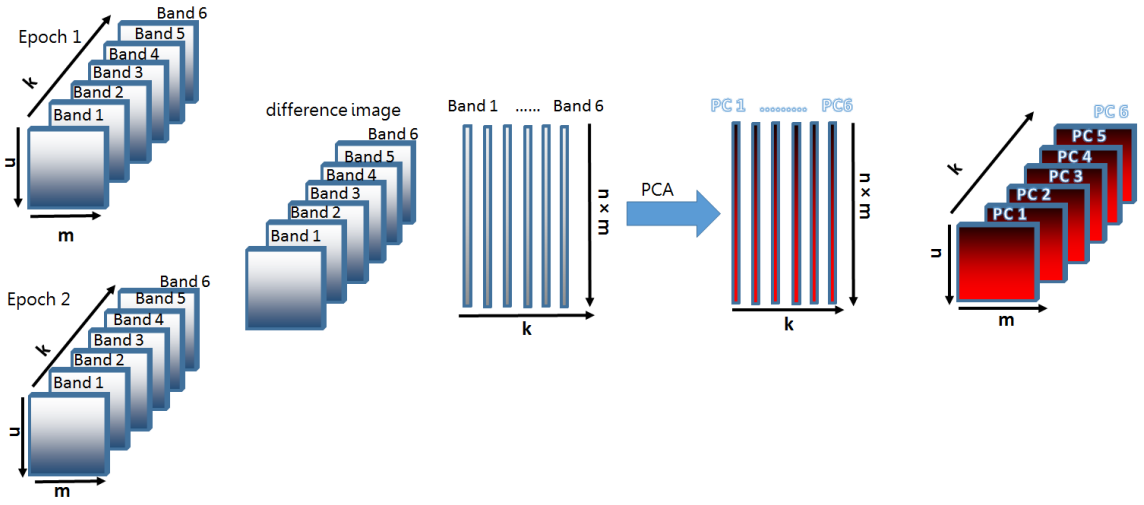

Figure 2.12: Applying PCA on an image difference of two multitemporal images.

First of all, image difference bands must be reshaped as a two dimensional matrix, then PCA is applied to the matrix and finally the transformed matrix is reshaped to its original form. This technique is applied on images presented in Figure 2.23(a) and (c). To reduce the amount of the noise in the image difference product, the image will be reconstructed using just those PCs containing a significant portion of the correlation.

We decide to keep the first three PCs for reconstructing the image because they contain about 98.5% of valuable information of the image difference (PC1: 70.1%, PC2: 23.5%, PC3: 4.9%). Since the rest of them contain less than 1% of the signal, we assume that they contain noise and trivial changes. In the following figure the original image difference and the reconstructed one are presented.

Since monitoring the change in the river extent is our main goal, we place the difference between spectral bands number 2, 3, 4 as color channels in Figure 2.13(c). First of all due to the cloud coverage in the second image, part of this map appears white. Also it is hard to detect the change between river extent in some parts of the map (north and south parts) in Figure 2.13(c). For plotting Figure 2.13(d), the first three PCs are placed as color channels. By comparing this map with the original images we find out that the flooded areas in the second epoch are shown in light blue and white. Finally we reconstructed the image difference again by using the first three PCs. Comparison between Figure 2.13(c) and (e) shows that it is significantly easier to define the change between the state of the river after reducing the noise components. However applying PCA transformation leads to a change in color range in 2.13(e).

Tasselled Cap transformation

The idea of highlighting specific physical characteristics in satellite images leads to the Tasselled Cap transformation described in the section 2.2.2. For hydrological purposes,

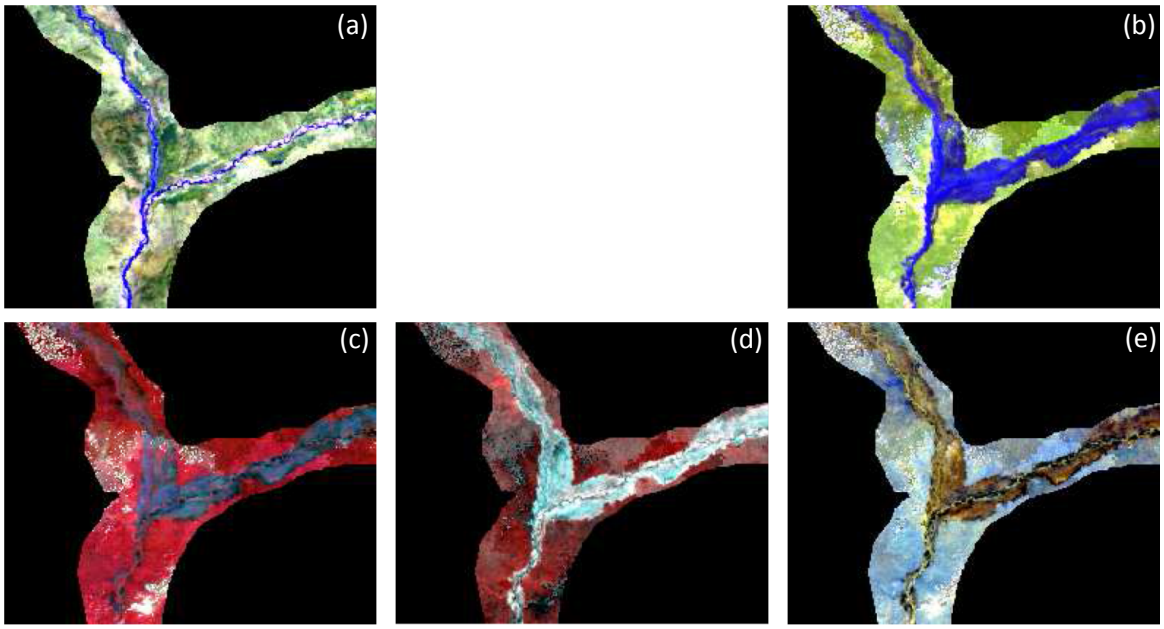

Figure 2.13: (a) and (b) are the original RGB images. Map in (c) is the ordinary spectral bands difference. (d) is the map of the first three PCs as color channels and (e) is the reconstructed map using the first three PCs.

the wetness component could be useful for extracting the water bodies easily. To evaluate its performance we apply this transformation to the Landsat 7 images of Po River (Figure 1.6(e)). To map 500 km of Po River from the Adriatic Sea to near the city of Turin in Italy, we need to create an image mosaic from 3 Landsat 7 images acquired in May 2000, in Figure 2.14(a). Now, by using the coefficients provided in Table 2.5 the components of the KT transformation are generated.

Table 2.5: Coefficients of Kauth-Thomas Tasseled Cap Transformation for LandSat 7 image

Index	Band 1	Band 2	Band 3	Band 4	Band 5	Band 6
Brightness	0.3561	0.3972	0.3904	0.6966	0.2286	0.1596
Greenness	−0.3344	−0.3544	−0.4556	0.6966	−0.0242	−0.2630
Wetness	0.2626	0.2141	0.0926	0.0656	−0.7629	−0.5388
Fourth	0.0805	−0.0498	0.1950	−0.1327	0.5752	−0.7775
Fifth	−0.7252	−0.0202	0.6683	0.0631	−0.1494	−0.0274
Sixth	0.4000	−0.8172	0.3832	0.0602	−0.1095	0.0985

Figure 2.14(b) presents the final product of the KT transformation. To generate this map we place the first 3 components in the color channels. In this product clouds are shown in red mainly because they have a high value in the brightness band and low values in greenness and wetness bands.

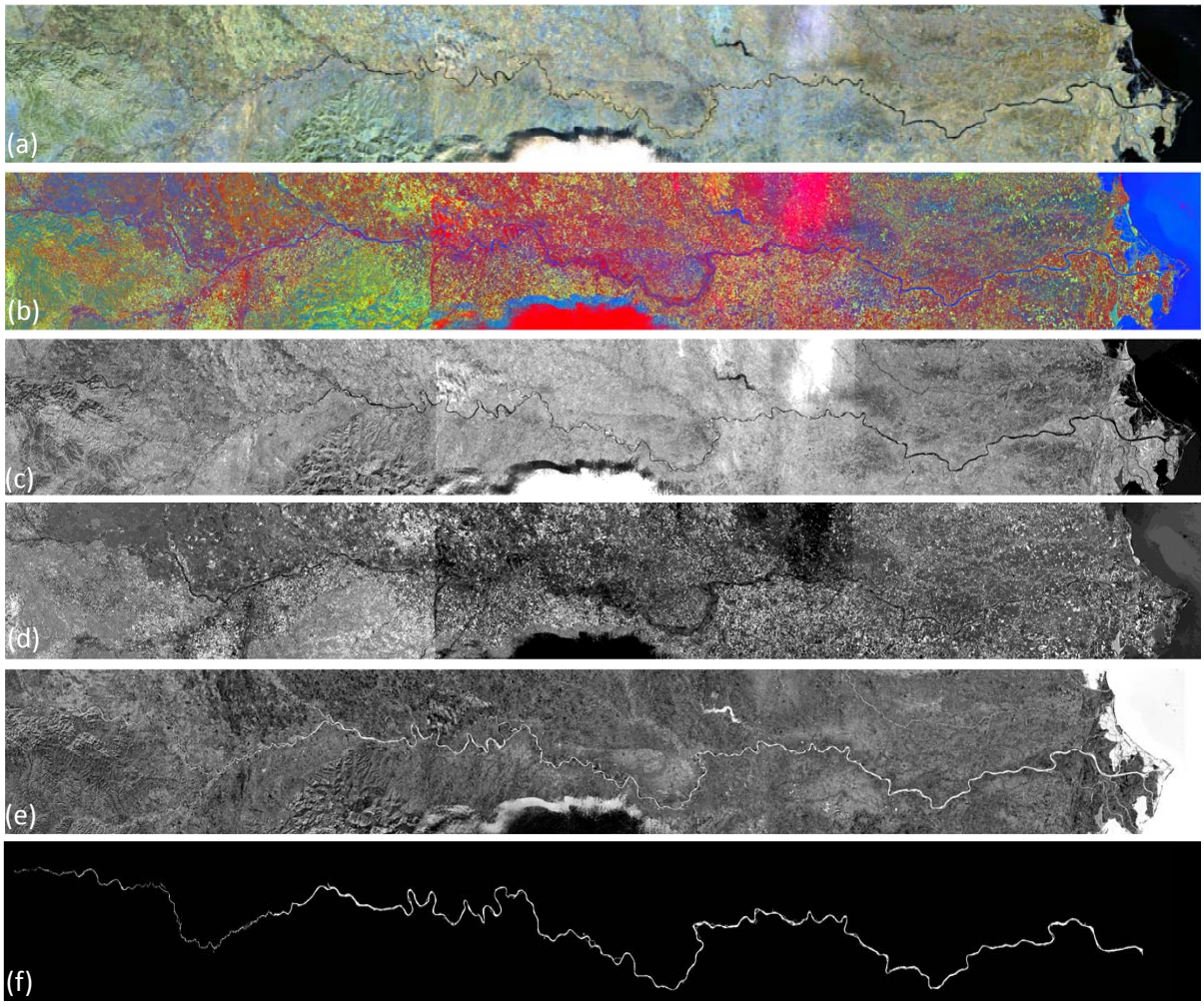

Figure 2.14: Result of Tasseled Cap transformation on a Landsat 7 images mosaic of Po River. (a) is the image mosaic consisting of 3 Landsat images. In (b) brightness, greenness and wetness components are placed in the color channels. The next three maps are brightness (c), greenness (d) and wetness (e) components of the transformed image. The map of the river extracted from wetness component is presented in (f).

The wetness component (Figure 2.14(e)) is the most appropriate one for mapping the water bodies. The river and its border are clearly detectable in the wetness component even in the case where we deal with a long and narrow river with a complex geometry. It is a prominent sign for water extent monitoring as there is a high contrast between water and land in this component. Clouds, as one of the main sources of error, appear dark in the wetness component. So, unlike infrared bands, the separation between water and cloud is possible in this component. In an ideal example, the range of pixel values in this band should be between zero and one. The lower the pixel value, the higher the water in the vegetations. Therefore, zero represent the pixels completely covered by water. On the other hand, large values and one represent the urban areas. Finally in Figure 2.14(f) the river is extracted by applying a zero threshold to the wetness component of the river. Since the pixels covered by water have negative values

in the wetness component, we can easily detect and extract the river by applying a zero threshold on this component (Figure 2.14). This figure shows the potential of this transformation to map the Po River with such a meandering behaviour.

2.3.2 MAD + MAF

Analysing the change in multitemporal images is not possible unless some preprocessing steps are applied. Among them, geometrical rectification, image registration, radiometric, atmospheric and topographic corrections (specially in mountainous regions) are necessary. Advanced optical systems like MODIS and Landsat provide relatively precise geolocation information with their products, so as long as they are compared with themselves, there is no need for applying geometric and image registration. Maintaining radiometric consistency between multitemporal images is not possible due to different atmospheric conditions, variations in the solar illumination angles and sensor calibration trends (Du et al., 2002). Most of the solutions that are suggested are based on the assumption that the relationship between the radiance recorded at two different times from the same region can be approximated by a linear function. In addition to refining images before analysing the change, applying change detection techniques which are invariant to affine transformations (including linear scaling) is a possible solution. Both MAD and MAF transformations have this property, meaning they are not sensitive to offset and gain between multitemporal images (Nielsen et al., 2002). So by taking advantage of these methods, the real change due to different environmental patterns can be extracted without any preprocessing.

In this section, two Landsat 8 images with 30 m spatial resolution of the Niger River from different dates are used. MAD and MAF transformations are used to the original image bands without any correction. Unlike level 2, 3 MODIS products, Landsat images need a careful consideration before being compared together. So, applying MAD and MAF transformations for detecting the change could be an alternative to the cumbersome process of radiometric calibration and normalization.

As shown in Figure 2.15, a significant change in the river extent and wetland occurred during a month. Also the pattern of vegetation changed especially in the north west of the image. As expected, clouds covered parts of both images which may affect the change detection process. It is assumed that change in the river extent will become visible in the first MADs as long as they are the most dominant change over time. On the other hand, the change in cloud cover will play a destructive role. Figure 2.16 illustrates the procedure of this transformation. In this figure, n is the number of rows and m is the number of columns in each spectral band and k is also the number of different spectral bands.

To detect the change between two images, a map based on equation (2.33) is generated. As discussed before, a χ^2 distribution for the MAD components is assumed with seven degrees of freedom. Figure 2.17 represents the probability of the change in the state of each pixel. Based on this distribution, the possibility of change in pixels with a

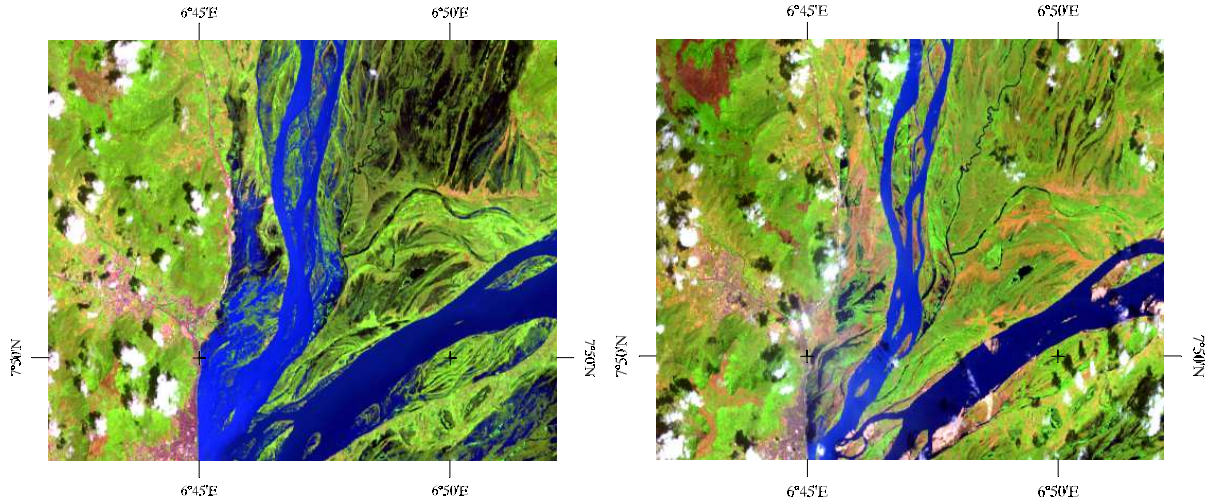

(a) Date : 2013-10-17 **(b)** Date : 2013-11-18

Figure 2.15: Part of Niger River from Landsat 8 images.

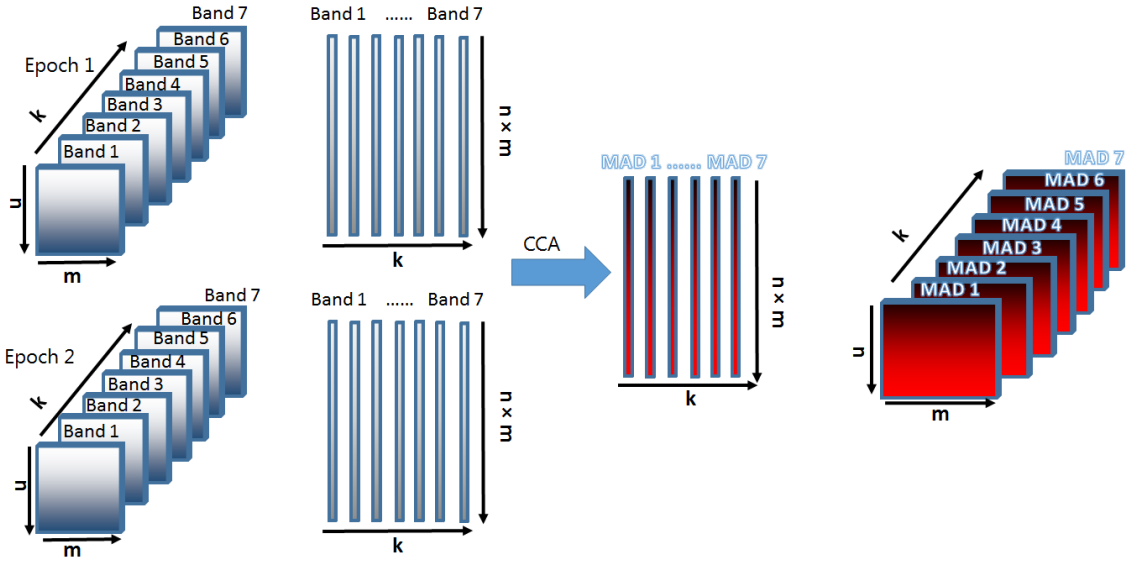

Figure 2.16: Procedure of applying MAD transformation on multitemporal images

value less than 1.96 is approximately about 2.5% and they are illustrated in dark blue. Accordingly the possibility of change in pixels with the value bigger than 25 is about 99.9%. The change in the river boundary in the middle of the image is highlighted in red. Unfortunately, the different cloud patterns in two images spoils the result because they are also dominant in all spectral bands. Figure 2.17(c) and (d) present two *change/no-change* binary maps. These maps are generated by applying two mentioned critical values as a threshold to the pixel values of map in Figure 2.17(a).

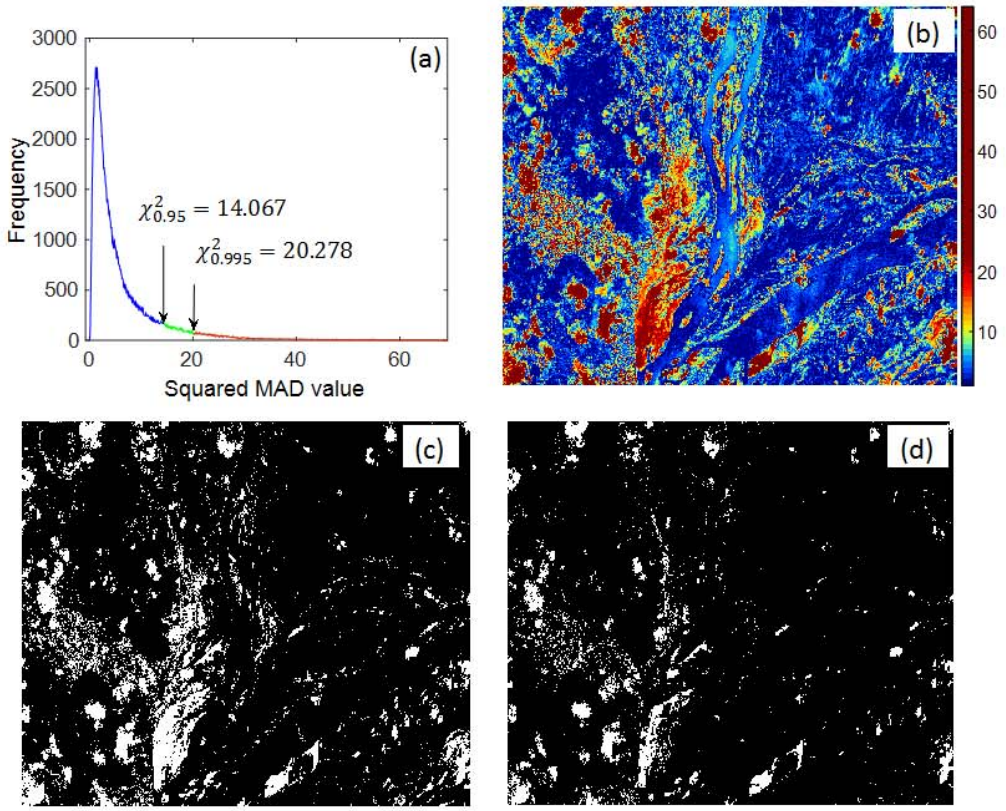

Figure 2.17: (a) is the histogram of sum of squared and normalized MADs. (b) is the map of sum of squared and normalized MADs. (c) and (d) are the binary *change/no-change* maps considering two critical values: 14.067 and 20.278

Analysing the MAD variables separately to detect the change is another way to define changes between two epochs. The first MAD highlights the area where a significant change occurred because the maximum spread in the pixel intensities occurred in that area. The second MAD also carries important information about the change because it has the maximum variance subject to the condition that it is uncorrelated with the first one. Other MADs are also arranged so they are uncorrelated with each other and the variance between two linear combinations is descending from first to last MAD (Figure 2.18).

Given the variances of Figure 2.18, it is expected that the map of the first two or three MADs projects the majority of change in multitemporal images. In Figure 2.19, all MADs are presented. In MAD1, the main part of the river appears black because it remained stable during the time. Flooded area appears white as it includes the most drastic change from wet to dry land. Different gray levels indicate the change in the type and density of vegetations. Interestingly, boundaries between the stable part of river and the flooded area are clearly distinguishable. By looking at all MADs, it is concluded that there is little valuable information about the change in the last four MADs. They are assumed to contain the noise component and the trivial changes.

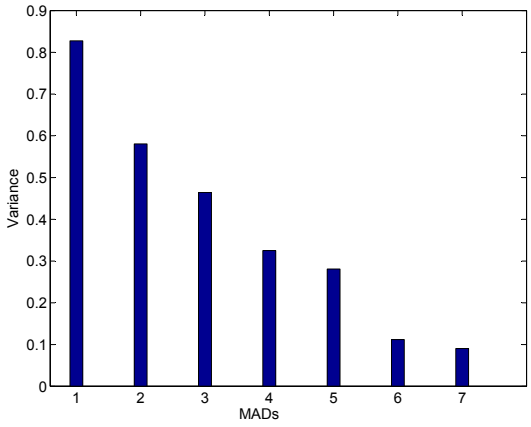

Figure 2.18: Variance of the MAD components

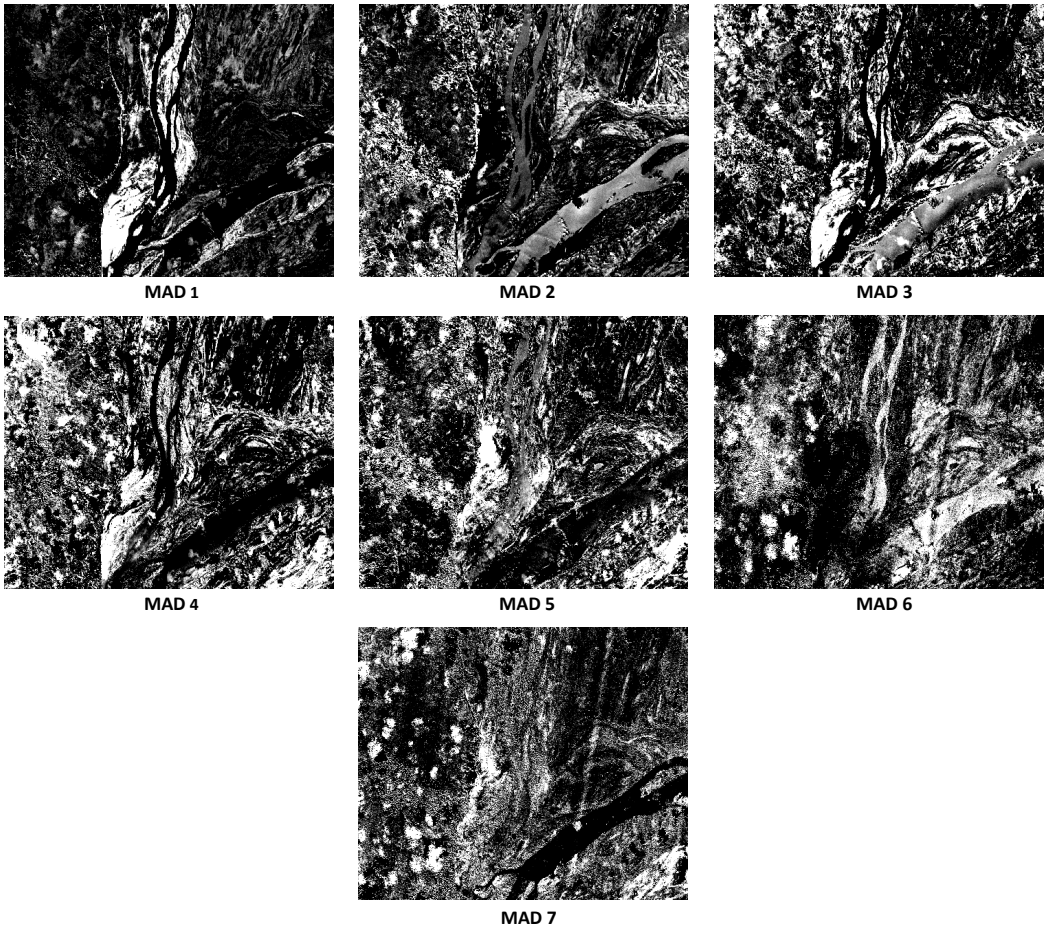

Figure 2.19: MAD components of the two multitemporal images

Based on the assumption that there is no valuable information in the last four MADs, the first three MADs are presented as an RGB composite. This map might be helpful to better understand and interpret the physical characteristics of the river and the surrounding area at both epochs and also the change over time. Inspection of Figure 2.20

and comparison with Figure 2.15 gives a novel basis for interpretation of the river status on both dates.

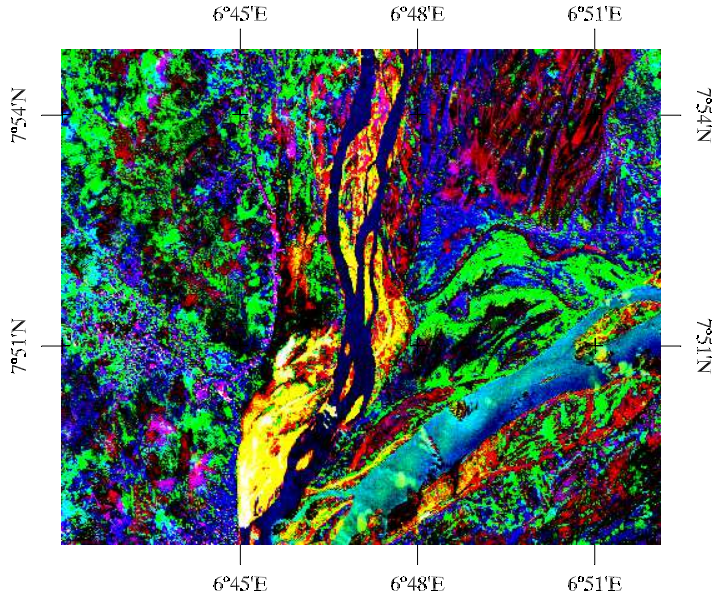

Figure 2.20: Color composite of the last three MADs (red: MAD2, blue: MAD1, green: MAD3)

In Figure 2.20, the part of the river that is consistent in both acquisition dates is shown in dark blue. Yellow indicates the area covered by water in the first and dry in the second images. Areas with little change are presented in light blue and green. Finally, the change in vegetation type and intensity are presented in black and red. Unfortunately, the change in cloud coverage reduces the quality of the result as in the right branch of the river.

The first MAD variables provide valuable information about the change, however, they are partially saturated by noises. Specifically, the parts where there is minor change in vegetation. In Figure 2.20, the left side of the river appears noisy because the level of change is negligible in respect to the other parts. Physical objects observed in the images occupy several pixels, so any change occurring to them must follow a physical pattern. In this way, applying MAF transformation to highlight areas with a high spatial correlation will effectively improve the final results. If the MAF transformation is applied to the MAD components, the real change in the physical condition with high spatial correlation can be determined.

In Figure 2.22, as expected, in the first and second MAFs, changed area with high correlation is clearly recognized. Like MADs, here also after the third MAF, there is no valuable information about change. Accordingly the last two MAFs mostly contain noise. As before, the first three MAFs containing the most valuable information are presented in different color channels of an RGB image.

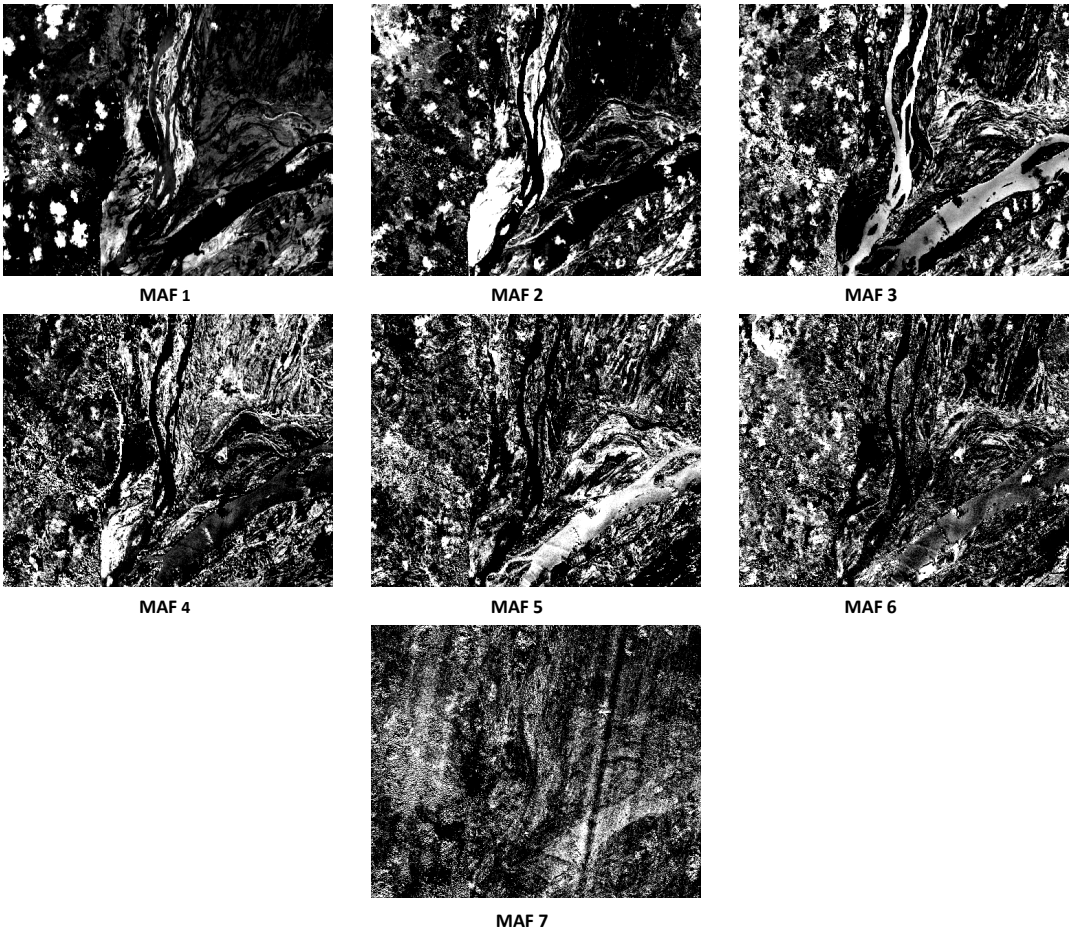

Figure 2.21: The result of MAF transformation on of the MAD components

Figure 2.22 is clearly improved visually compared to Figure 2.20. In this figure, dark and light blue indicate the stable area. The area covered with water in the first image and dry in the second one is shown by yellow and green. The change in vegetation patterns presents in black especially in the upper part of the image. However noise reduction is the most significant improvement in this figure, therefore it is easier to deal with MAF components because the noise is reduced spatially in the primary components. Even clouds are detectable in this product as they appear in pink. In the following figure ordinary image difference is compared with results of MAD and MAF transformations.

In the ordinary image difference map, Figure 2.23(a), finding the changed area is not trivial because two images do not have the same origin and scale. Also selecting three spectral bands out of seven is a hard decision since each band represents a certain spectral range. Here we placed bands 6, 5, 4 in the color channels based on visual interpretation. Figure 2.23(b) provides more valuable information about the change because most of the valuable information is highlighted in the first three MADs. In Figure 2.23(c), the spatial correlation between neighbouring pixels are maximized. So, the comparison between Figure 2.23(a) and (c) shows the ability of MAD transformation

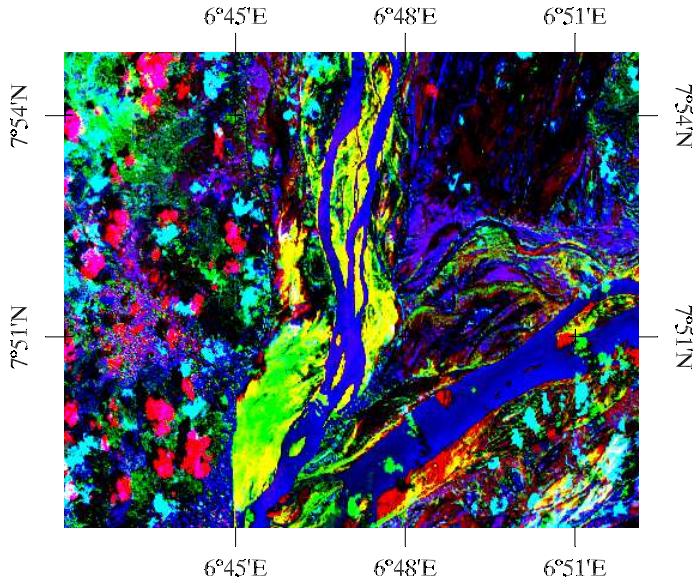

Figure 2.22: The map of the first three MAFs (red: MAF2, blue: MAF1, green: MAF3)

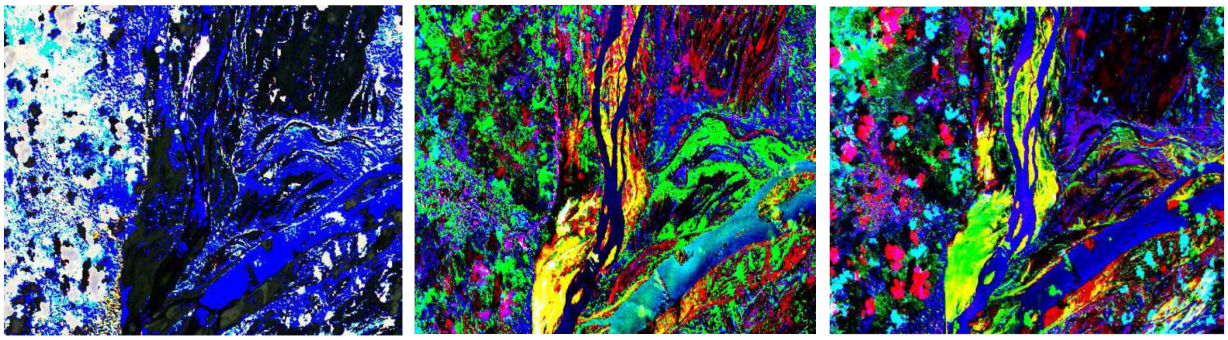

Figure 2.23: (a) ordinary difference of bands 6, 5 and 4 (b) color composite of MADs, (c) color composite of MAFs

to capture the real change and also reorder the image bands based on their importance. Also, MAF transformation keeps the coherency of the changed area and in the first MAFs, the area with high spatial correlation are highlighted.

2.4 Summary

This chapter has described how transformations like PCA and CCA reduce noise levels in multispectral imagery and also improve interpretation of the change in two multitemporal images.

To isolate the noise level in a multispectral image, PCA is applied to the image bands. To select the appropriate PCs, two approaches are followed: First, PCs containing the

majority of the total correlation are selected to reconstruct the image. The result (Figure 2.5) showed that if only a number of primary PCs are used to reconstruct image bands, the final product is a clear image which helps to detect the river extent. In the next experiment, to select appropriate PCs for presentation in color channels, physical interpretation of different spectral bands is considered. For example, the aim of this chapter is to highlight the information about the water content. So, first it is defined which spectral bands provide the most valuable information about water content and then appropriate PCs were selected. Figures 2.8 and 2.9 indicated that if PCs are carefully selected, the products can exhibit more information than the original spectral bands.

Another way to take advantage of the PCA transformation for change detection is applying this transformation to the spectral bands of two multitemporal images simultaneously. The result is a number of PCs which is equal to the sum of the two image bands. By selecting the PCs carefully, the final product illustrates the state of the river in both dates and also the change that occurred in between. Interpreting the result regarding the input images is the biggest obstacle in these techniques. PCA is also used as a tool to reduce noise and highlight the change in the image difference of two multitemporal images. Figure 2.13 presents how PCA highlights the change between two images.

In the final section, CCA was applied to two different Landsat 8 images to derive MAD variations. MAD has special characteristics which make it a valuable tool in change detection. For example, since it is invariant to gain and offset between image bands, applying radiometric normalization between two images is unnecessary. Figure 2.20 presents the first three MADs as a RGB image. In this product, different types of change in river boundaries, vegetations and cloud coverage pattern are highlighted and presented with different colors. In the next step, by applying the MAF transformation to the MAD variables, areas with high spatial correlation are highlighted in the primary MAF variables. Comparison of Figure 2.23 and 2.15 shows that the combination of these two transformation can capture the major changes between two images.

Chapter 3

Monitoring lake surface area from satellite imagery

3.1 Introduction

Lakes and reservoirs are essential elements of the hydrological and biogeochemical water cycles because of their critical abilities to store, retain, clean and provide water (Lehner & Döll, 2004). They have also an essential role in making life feasible on the Earth by modifying many biochemical and hydrological processes. According to the inventory developed by Verpoorter et al. (2014), more than 117 million lakes larger than 2000 m^2 with a total surface area of 5 000 000 km^2 is available. Despite the importance, our knowledge about the spatial distribution and extent of the surface water bodies is based on the global datasets and inventories. These databases provide only static information about the location and extent of water bodies. Therefore, annual and seasonal variations in inland water bodies extent, due to the change in the environmental conditions and human activities, are not considered by static datasets. Due to recent spaceborne technique breakthroughs, the number of available open access (and commercial) satellite images with high temporal and spatial resolution has been increased significantly. This situation provides a great opportunity not only to monitor the long term annual and interannual behaviour of water bodies area but also detect the extreme events like floods.

The Increased demand for long time series of lake area necessitates the development of algorithms to extract lake extent from satellite images. In this chapter the main aim is to develop an automatic algorithm for monitoring lake area. The algorithm consists of the following steps

- defining a proper search area around the water-land border line,
- applying a classification algorithm,
- generating water area time series and lake extent shapefiles.

To generate the lake area time series, NIR band of MODIS MOD09Q1 images are used. After gathering all images in the monitoring period, an image stack in three dimensions is generated in which the third dimension is sampling time. For better understanding, Nasser Lake images (Figure 1.6(f)) are used to describe the further steps.

3.2 Methodology

The algorithm, which has three main steps, starts with narrowing down the search area in a way that the classification algorithm can focus on pixels located around the water-land boundary. Defining an appropriate search area is a critical step for deriving accurate water masks. The search area must be restricted based on physical specifications of the water body. Lakes and reservoirs, as the biggest constant inland water bodies, are located in the lowest possible altitude of the area. Therefore, except in the tropical regions, their seasonal behaviour is small. So, the lake consists of a big stable interior part surrounded by a marginal part. The interior part is always covered by water and the marginal part is subjected to change due to the natural and artificial changes.

Crétaux et al. (2016) suggested that the search area could be restricted based on lake boundaries when the lake is in the maximum and minimum area during the monitoring period. Applying this suggestion is time consuming and inaccurate. To define the lake area extrema, all images in the image stack must be classified once. In this situation, images acquired on rainy days or during a flood would demolish the search area.

Due to the Earth gravity water tends to gather in the area with the lowest possible altitude and slope. Therefore, pixels located at the high altitude or steep slope can be removed from the search area. Klein et al. (2014) suggested using a DEM to restrict the search area. They generated an SRTM-based slope map and then ignored pixels with a slope steeper than 1%. This approach is pretty suitable to shrink the search area, however handling an external source of data is its drawback. In this study before starting to extract the lake extent, a DEM-based mask based on the Advanced Spaceborne Thermal Emission and Reflection Radiometer (ASTER) data with 30 m spatial resolution and a slope map derived from ASTER DEM is generated. To modify the search area, two criteria are defined.

1. Pixels in the search area should not have a slope steeper than 1%.
2. The maximum elevation in the search area should not be higher than 100 m above the minimum elevation.

Figure 3.1 presents the procedure of defining the DEM-based mask. Figure 3.1(a) is the MODIS image of Nasser Lake on 25 May, 2000. Figure 3.1(b) is the DEM map of the Lake and surrounding area from the ASTER mission. A considerable height difference (about 800 m) is obvious between the main part of the Lake and the neighbouring area.

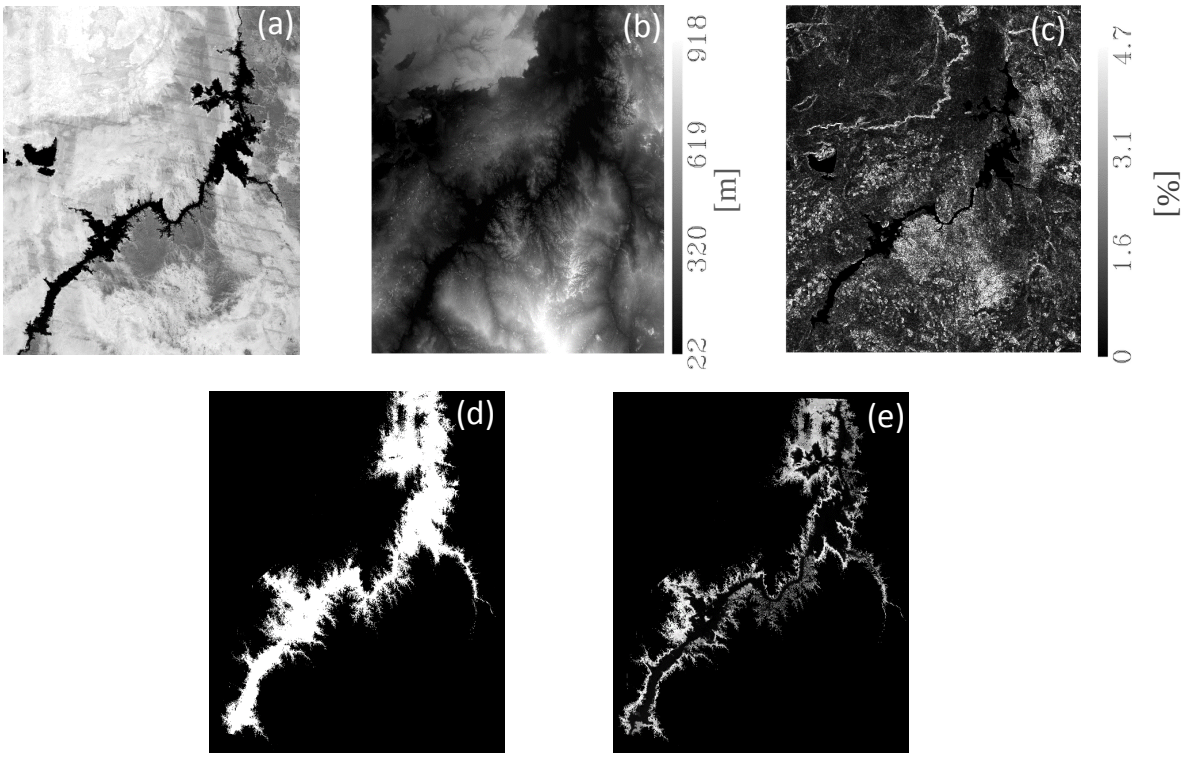

Figure 3.1: (a) NIR band of MODIS MOD09Q1 image of Lake Nasser (date: 2000.05.25), (b) ASTER DEM map of the Lake, (c) slope map derived from the DEM map, (d) DEM-based mask developed regarding the DEM and slope maps, (e) the result of applying the defined mask on the image (a). By applying this mask, the search area is reduced from about 58 000 km^2 to 6 082 km^2 (about just 10% of the initial image).

Figure 3.1(c) is the slope map of the area which varies from 0 to 5%. Figure 3.1(d) is the generated DEM-based map considering the aforesaid conditions. This mask excludes pixels with higher altitude or steep slope from the search area. Figure 3.1(e) presents the result of applying the mask on the Lake image. Except for a small margin around the main part of the Lake, the rest of the area is removed by the mask. By applying this mask, the label of pixels inside the mask can be assigned as land before starting the classification procedure. Applying the DEM-based mask not only reduces the computational effort but also improves the accuracy of the lake boundary extraction. Mainly because, the possibility of assigning isolated pixels far from the lake boundary is reduced by restricting the search area by the DEM-based mask.

To improve the accuracy of the final product, the search area is still further modified. The lake surface can be separated into two parts. The middle part is always stable and covered by water during the monitoring period. The marginal part has a time-variable area due to the annual and interannualannual behaviour of the lake. The main aim of the algorithm is to capture the chance in the marginal part, since the middle part has a constant status and its label as water can be assigned confidently.

Removing the middle part of the lake from the search area also ignores a number of deficiencies which may occur in optical imagery. If the lake surface water is calm and smooth, a perfect reflection of the sunlight might happen along the track of the satellite. Therefore, this part of the water surface appears bright in the image. This phenomenon is called *sunglint*. Moreover, cloud coverage always threatens optical imagery. The area covered by cloud also appears bright in the NIR band. Both of the mentioned destructive effects would be avoidable by restricting the search area.

For defining an appropriate constant-water mask, first, the long term variations of pixel values located at different parts of the lake must be analysed.

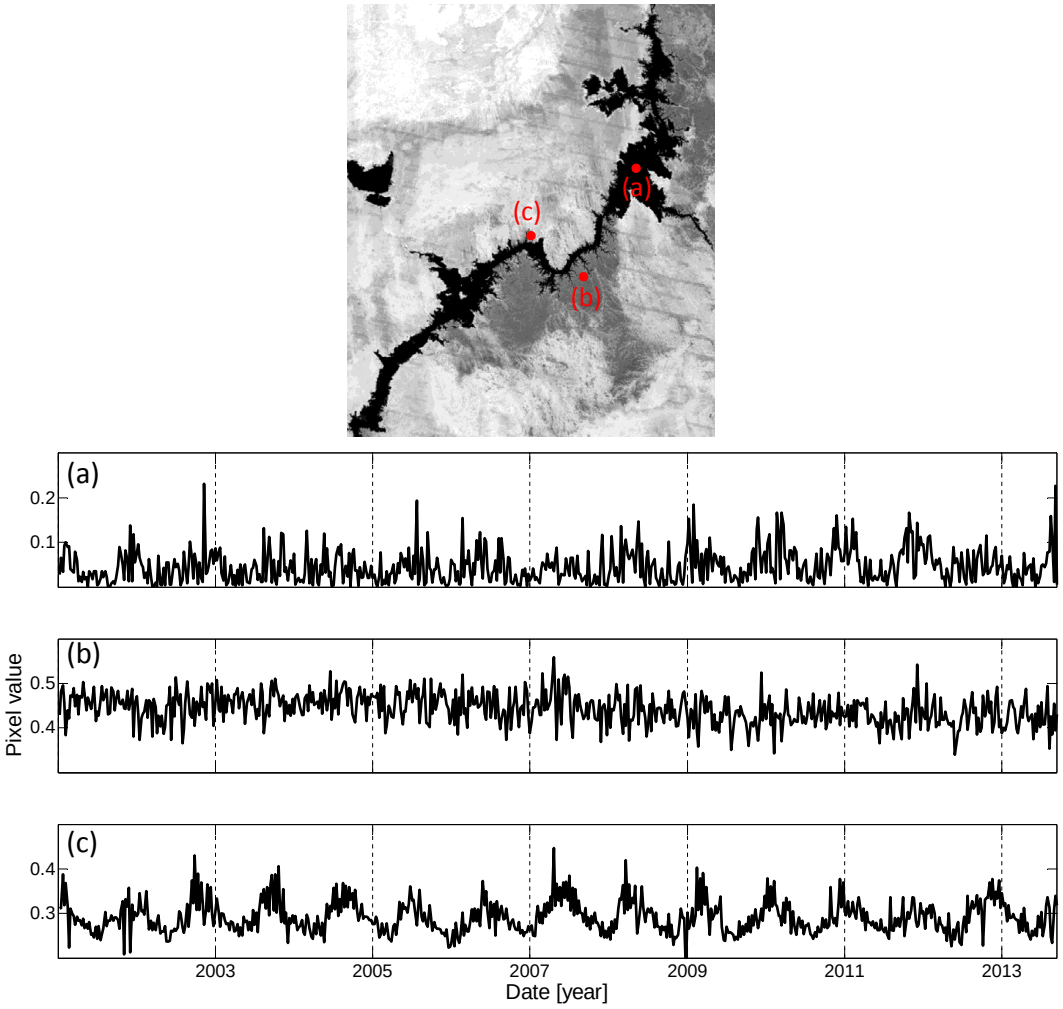

Figure 3.2: Time series of three different types of pixel value behaviour during the time. Pixel (a) is always covered by water. Pixel (b) is located outside the lake territory. Pixel (c) is located in the borderline between the water and land.

Figure 3.2 presents three different types of pixels available in the search area. The time series in Figure 3.2(a) represents the behaviour of a pixel which is always covered by water during the monitoring period. It has almost a constant low value (near zero) because water absorbs most of the sunlight energy in NIR domain. In some epochs, the

pixel has a larger intensity value due to the atmospheric effect, sensor error, sunglint or cloud coverage. The time series in Figure 3.2(b) is a representative of pixels located outside the lake boundary. It is always dry and the variation in the value just indicates the change in vegetation type and intensity during the year. As a result, only a tiny annual behaviour is detectable. In some epochs, due to the sensor error and cloud coverage, a number of blunders are visible. The last time series (Figure 3.2(c)) is an example for pixels located in the coastal area of the lake. There is a huge change in their pixel value in different seasons. They have a low value whenever covered by water and a high value when they are dry.

Pixels categorized in the third group (Figure3.2(c)) are the main interest in lake area monitoring, because unlike the first and second group, the third group is responsible for the change in the lake area over time. Part of pixels in the second group are already removed in the previous step by applying the DEM-based mask.

For removing the area in the first group, a mask regarding the behaviour of the pixel value must be developed. Since, a pixel is located in the middle of the lake, it will always be covered by water. Therefore its value should be relatively low and constant. In this area, only small variations in the pixel values are expected due to changes in the water column and atmosphere properties. So, assessing the mean and variance of the pixel values is a way to distinguish pixels in the first group. In Figure 3.3, the process of generating water mask is described.

Figure 3.3(a) is the map of mean values. As it is expected, the mean value of pixels in the middle of the lake is almost zero. Closer to the lake boundary, the mean value also increases due to the considerable difference in pixel value in wet and dry seasons. Figure 3.3(b) is the variance map of the search area which shows a similar behaviour as the mean map. Near-zero values appear in the middle of the lake and higher values are toward the borders. Both maps show that pixels located in the middle of the lake (with red color) have a constant label (as water) over time because they have low and almost stable values.

Accordingly, a constant-water mask is defined by applying a near zero threshold on the mean and variance maps (Figure 3.3(a,b)). The masked pixels are labelled as water before starting the classification procedure. Therefore, this part of the lake can be omitted from the search area. Figure 3.3(c) shows the constant-water mask generated based on the mean and variance maps. At the end, the final search area is restricted just to pixels which are subject to change between water and land during the time.

To extract the lake boundary, a classification algorithm must be applied to the image stack after modifying the search area. Selecting an appropriate classification technique is the most important part of a monitoring process because it is affected by spatial, spectral, thematic and temporal constraints. Even after restricting the search area, the classification algorithm deals with a relatively large number of pixels. Therefore, the selected classification algorithm must establish a balance between the accuracy of the result and the computational effort.

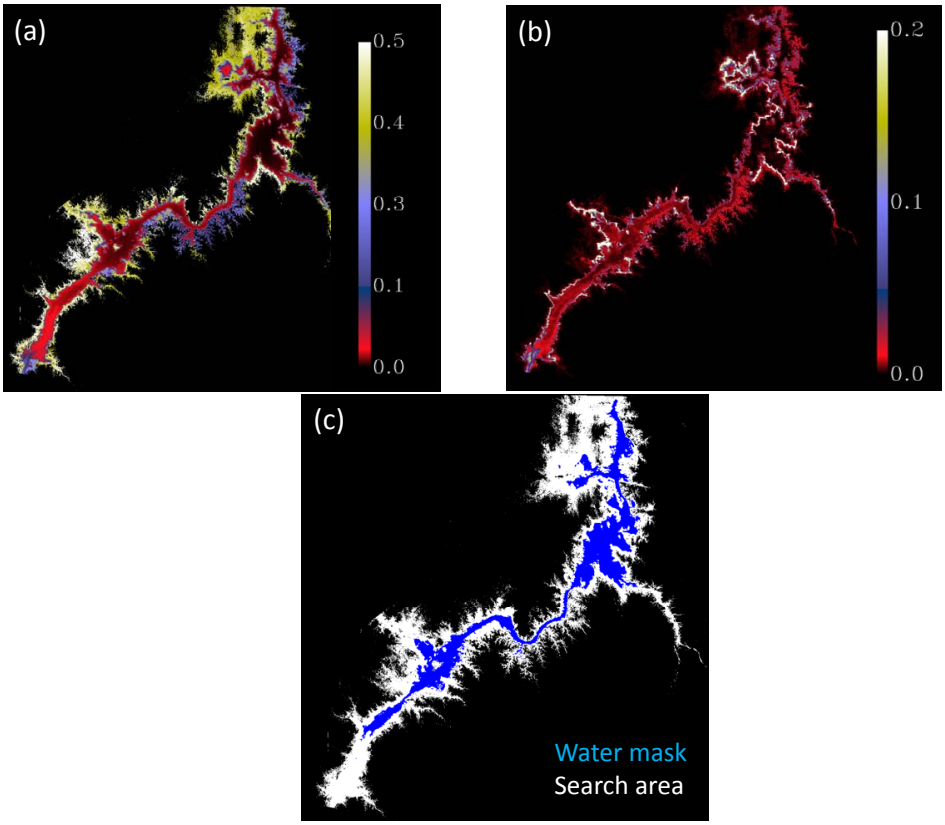

Figure 3.3: (a) and (b) are the maps of mean and variance of the pixel values during the monitoring period. (c) presents the water mask generated regarding the mean and variance maps.

The performance of region-based classification algorithms to detect the lake extent are significantly better than pixel-based algorithms because they consider spatial correlation in addition to the pixel values. On the other hand, their high computational effort restricts their application especially when dealing with a large dataset. Supervised classification algorithms might be another option, since they have proven their capability in many applications. On the other hands, they are dependent on the training data. The accuracy and distribution of training dataset have a critical role for the final result quality. However, in this application specifying the training dataset is almost impractical. Defining a unique training data sets at each epoch needs evaluate each image separately which requires too much effort and time. On the other hand, considering the same training sample for the whole image stack reduces the accuracy of classification significantly.

Based on this situation, applying an unsupervised classification algorithm to extract the lake boundary is the most appropriate solution. This group of algorithms does not need training data and can be performed automatically. They are fast and easy to implement. Under certain conditions they provide accurate results. Most of the unsupervised classification algorithms decide about the label of a pixel based on the distribution of pixel intensities. So, before we select an appropriate unsupervised clas-

sification algorithm, first histogram of pixel values for a few random epochs are analysed in Figure 3.4.

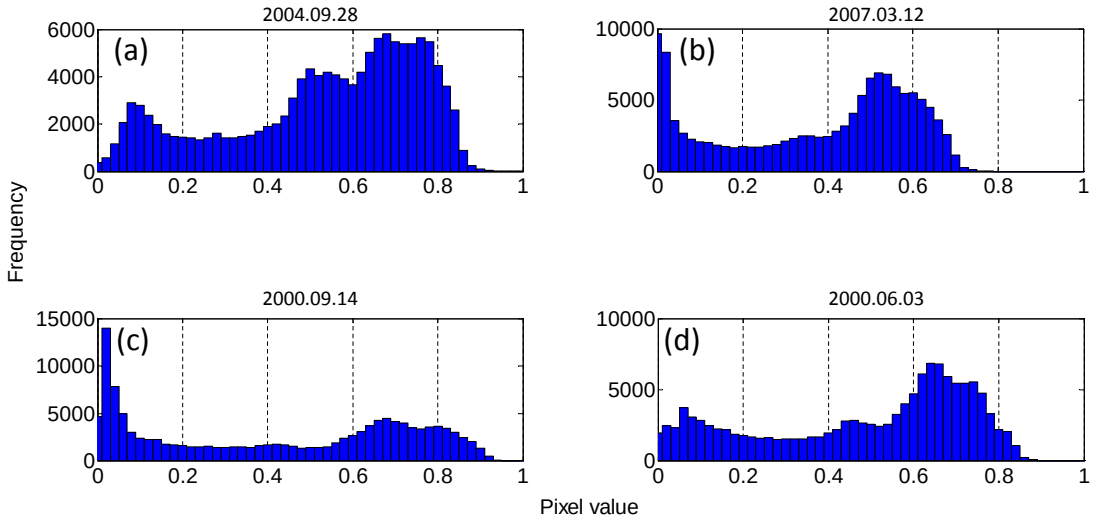

Figure 3.4: Four examples of pixel value histogram of modified search area of Nasser Lake.

First of all, Figure 3.4 indicates the importance of restricting the search area. If the water mask was not applied, then the accumulation of pixels with low values in the primary part of the histogram would have reduced the performance of any classification algorithm. This figure presents four histograms for different epochs. In general, it is obvious that the pixel value distribution varies from image to image. In all examples, a big portion of pixels, representing the wet area, has low value and gathers in primary columns. But the remaining pixels are distributed with different patterns. The pixel value in the NIR band is sensitive to water depth, amount of chlorophyll and suspended particles in the water content, vegetation type and density. Any change in the aforementioned parameters has an impact on the image histogram shape.

Considering the Figure 3.4, it is not appropriate to apply a static threshold to all images for extracting lake boundary. Defining and applying a dynamic threshold for each image separately is the next solution. Klein et al. (2015) introduced a method for defining a threshold for each MODIS image by using the MODIS static water mask (MOD44W). They collected all pixels flagged as water in MOD44W water mask from the NIR band of each image as a training set and then consider the mean value plus twice standard deviation as the threshold value for the whole image. After a number of preprocessing and filtering steps, their method provides acceptable dynamic water masks on a global scale. But at the small scale, this solution is not applicable. Since the majority of selected pixels locate in the middle of the lake, they have a very low pixel value and reduce the threshold value. One can think about applying other dynamic thresholding algorithms. The main assumption of most of these algorithms is to consider the image histogram as a combination of two normal distributions. However, this assumption is not always valid. For example, it is not possible to assign two normal distributions for histograms like Figure 3.4(a, d). Therefore, some thresholding algorithms can not con-

verge and provide an answer. As a result, applying a dynamic thresholding algorithm is not the solution for extracting the lake boundary accurately.

In this situation, the Iterative Self-Organizing Data Analysis Technique (ISODATA), as an unsupervised classification, is the best solution. It does not need initial values or training samples. Unlike k-means clustering, ISODATA does not require the exact number of clusters as prior knowledge.

The ISODATA procedure is introduced by Ball & Hall (1965). It finds the appropriate cluster for each pixel in an iterative manner. Moreover, ISODATA has the ability to merge or split clusters, with respect to the defined criteria (Memarsadeghi et al., 2007). To perform ISODATA, the following parameters must be defined (this overview of the algorithm is summarized from Memarsadeghi et al. (2007)):

- initial number of clusters (INTCLUS), minimum (MINCLUS) and maximum number (MAXCLUS) of clusters,
- maximum number of iterations (MAXITR),
- minimum number of pixels that can create a cluster (MINPIX),
- maximum standard deviation among pixels value in the cluster (MAXSTD),
- minimum distance between two cluster centers (MINDIST),
- maximum number of clusters that is possible to merge in one iteration (MAXMERG).

After adjusting initial parameters, the algorithm performs the following steps to classify pixels into different clusters.

1. defining center of initial clusters randomly after determining the INTCLUS
2. assigning each pixel to the closest cluster center and generating clusters
3. removing clusters which have fewer members than MINPIX. If any cluster is eliminated in this step, the number of clusters is adjusted
4. relocating the centers of remaining clusters to the mean value of all pixels associated with that cluster
5. calculating the average distance of all points in the cluster with their cluster center and, computing the overall average distance
6. jumping to step 9 if the algorithm reaches the MAXITR or if number of clusters is larger than MAXCLUS and lower than MINCLUS
7. computing the standard deviation for all pixels within their cluster
8. splitting each cluster with a maximum standard deviation larger than MAXSTD into two clusters. The center and amount of pixels in each cluster are defined based on the variance of the primitive cluster. If any cluster is split in this step, the algorithm jumps back to step 3

9. calculating the distance between all pairs of cluster center and merging each pair which has a distance less than MINDIST. Number of clusters supposed to merge must be less than MAXMERG

10. terminating the algorithm if it reaches the MAXITR, otherwise return to step 3.

Setting the initial parameters is one of the critical steps in the segmentation procedure. In this study, initial parameters are tuned by visual comparison between the number of extracted lake masks and the original images. For this purpose, a number of images from different seasons and years are selected.

All images in the image stack are segmented into different clusters by applying ISODATA algorithm. The number of clusters can be varied between images. Figure 3.5 is one example of a lake mask derived by applying ISODATA.

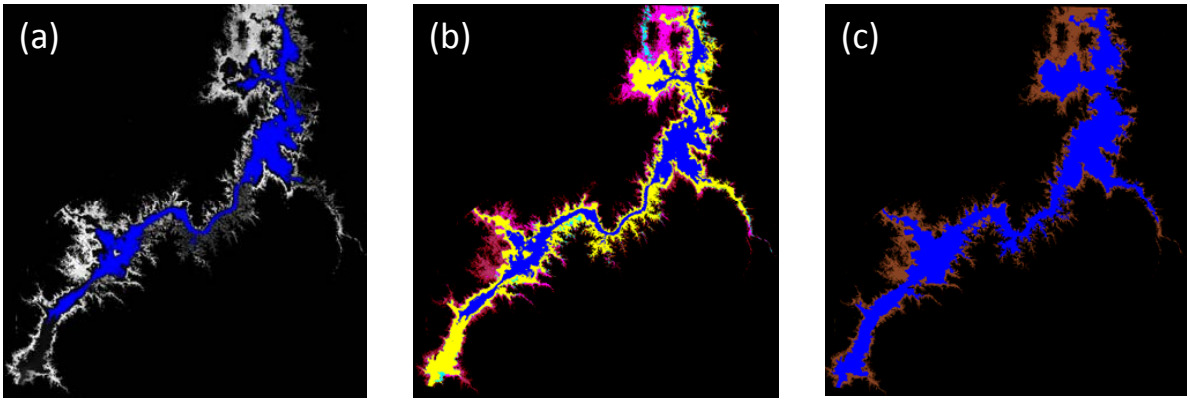

Figure 3.5: (a) is the image of the modified search area which is the input for the ISODATA algorithm. The blue part is the constant-water mask with an area of 2 602.5 km^2. After applying this water mask, the final search area is reduced to 3 479.7 km^2. (b) is the result of the ISODATA classification, the search area divided into 4 clusters. In (c), the first cluster (yellow) is labelled as water and joined to the water mask. The other clusters are labelled as land.

Figure 3.5(a) presents the modified search area after applying two defined mask. By applying them, the search area is reduced from 58 408 km^2 to about 3 479.7 km^2. It means that the input to the ISODATA algorithm is only about 6% of the lake and surrounding area. Figure 3.5(b) presents the result of ISODATA algorithm. The search area is divided into four clusters by ISODATA. The lake extent is defined by combining the water mask (blue) and the first cluster (yellow). In the third lake mask (Figure 3.5(c)), many isolated pixels, that do not belong to the lake are visible. These pixels are wrongly labelled as water and they are the major source of error in lake area measurements. The coarse spatial resolution of MODIS images and misclassification by the algorithm are the main reasons for this error. To eliminate them, the biggest continuous water body is considered as lake area. Figure 3.6 presents two examples of the final result of the algorithm.

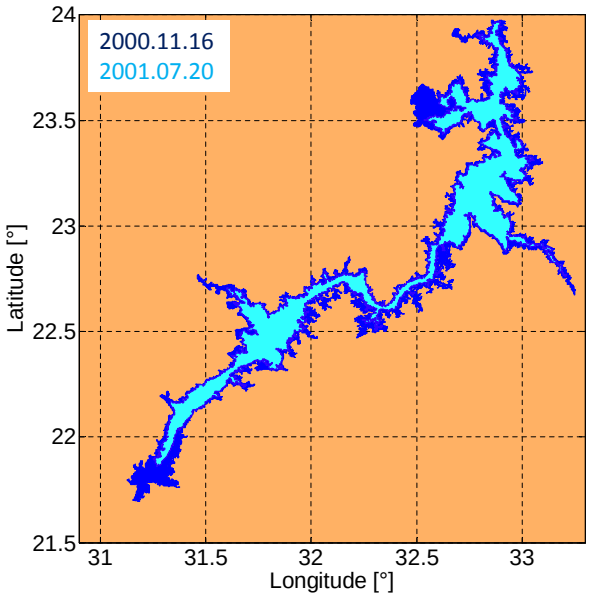

Figure 3.6: Two examples of lake extent shapefiles. The Lake area is 6 017.5 km^2 on Nov 16, 2000 and 3 671.7 km^2 on July 20, 2001.

Figure 3.6 presents the lake boundary at two different epochs. Considering the difference between the two shapefiles, the lake area variation mostly takes place in the southwest and northeast parts. Also by increasing the water volume, a number of small branches (khors) appear all around the lake. Generating lake area time series from the lake shapefiles is the final step of the proposed algorithm.

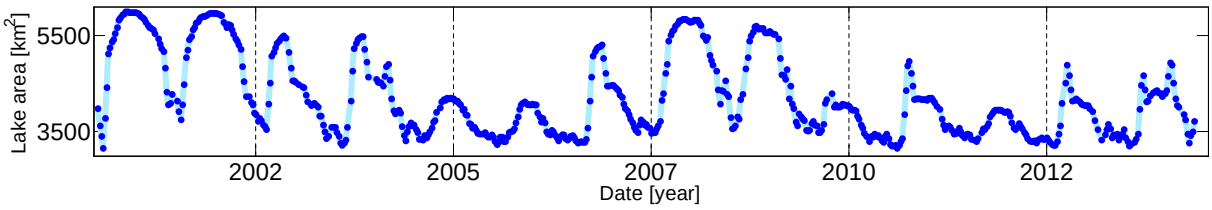

Figure 3.7: Time series of Nasser Lake surface water area. Monitoring period 2002–2015

Figure 3.7 presents the time series of Nasser Lake area between the years 2000–2015. The blue dots in the time series represent the satellite observations. The lake has a clear annual behaviour and its area varies between 6 100–3 150 km^2. The mean area of the lake is 4 227 km^2 and the standard deviation is 835 km^2. Since Nasser Lake is an artificial lake, its water volume during the years has been regulated by the Aswan Dam. Therefore, the lake presents various different behaviour over the years. For example, the patterns of annual behaviour have changed in different years. For a better understanding of the lake area variations during the monitoring period, water coverage frequency map of Nasser Lake will be presented. The value for each pixel in water coverage frequency map is defined by using the following equation

$$P(i,j) = \frac{1}{N} \sum_{n=1}^{N} L_n(i,j) \tag{3.1}$$

In this equation, $L_n(i,j)$ is the label (zero for land and one for water) of the pixel located in row i and column j for each image n and N is the number of images. In other words, water coverage frequency for each pixel presents the ratio of number of epochs in which the pixel has been labelled as water to the total number of epochs. For simplicity, this value is presented as percentage. For example, if a pixel has a value equal to 50% (green color), it means that this pixel is covered by water in the half of the images.

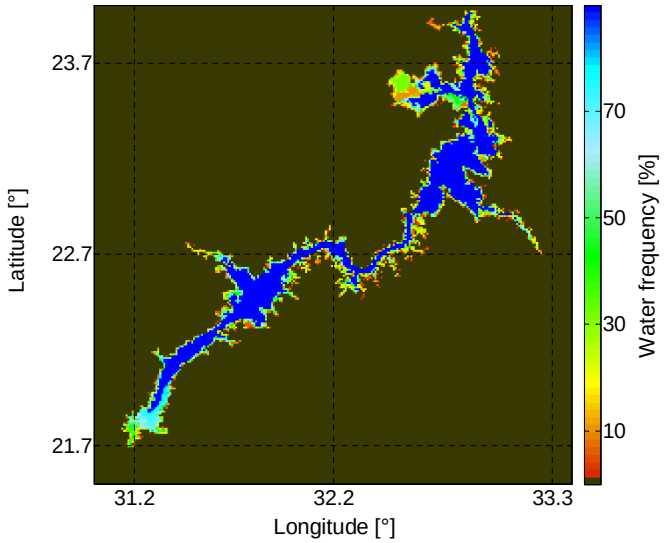

Figure 3.8: Water coverage frequency map of Nasser Lake for the period 2000–2015

Considering Figure 3.8, the main part of the lake is always covered by water. By increasing the lake water level, first the southwestern part of the lake covers by water and then small khors all around the main body fill with water. In the next section, the time series of Nasser Lake water area together with four other examples are presented and validated indirectly by comparing with in situ and altimetric water level measurements, since a strong positive correlation must exist between the different geometrical parameters of water bodies.

3.3 Results and validation

3.3.1 Nasser Lake

To validate the derived product, time series of lake area and level are plotted together. Figure 3.9(a) presents the comparison between the behaviour of lake area and in situ

water level. Figures 3.9(b, c) present the time series of water area and water level time series derived from satellite altimetry measurements at two different virtual stations.

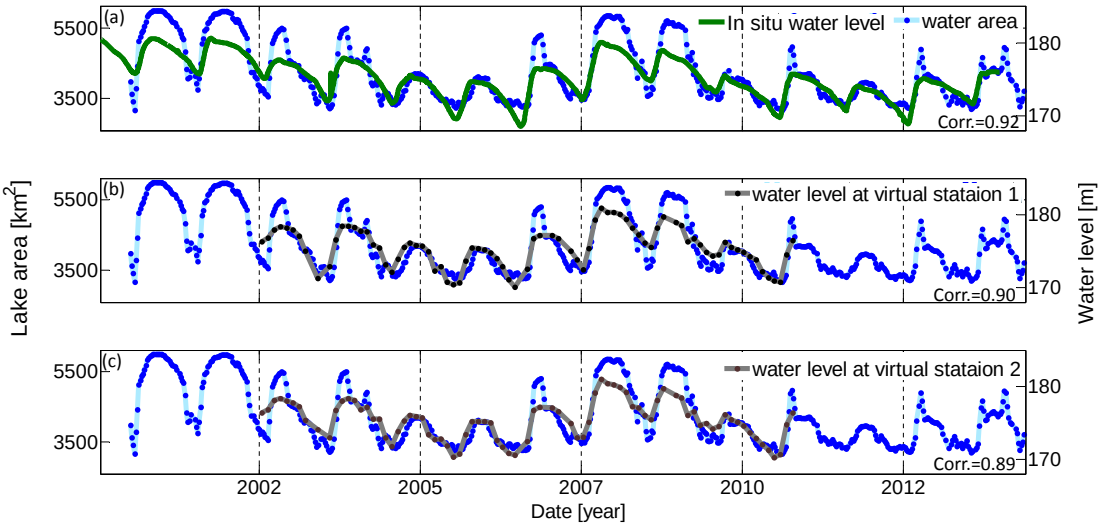

Figure 3.9: Comparison between Nasser Lake water area time series with in situ water level measurements (a) and altimetric water level measurements at two virtual stations (b, c). Monitoring period: 2000–2015

The high correlation between the lake area and in situ water level (Figure 3.9(a)) represents the significant performance of the algorithm to extract the lake extent. Almost all considerable variations in the lake water level are reflected in the lake area time series. However, small variations in the lake area especially in the dry season reduce the correlation between two time series. Time series of lake area and altimetric water level at virtual station 1, which is located in the north part of the lake, is plotted in Figure 3.9(b). Again, high correlation (0.9) between two time series indicates a good agreement between the behaviour of water area and level. Low temporal resolution of ENVISAT makes it hard to capture short-term variations in water level which are visible in the lake area. A comparison between lake area and level at the second virtual station, located in the south west of the lake, is presented in Figure 3.9(c). Like the first virtual station, the high correlation between two time series represents the agreement between them. Although the lake has a very complex shoreline, the agreement between variations of lake water area and level admit that the algorithm can extract the lake extent accurately. Figure 3.10 shows the scatter plot of all three pairs of time series in Figure 3.9.

The scatter plot shows a non-linear relationship between the lake water area and level. The shape of the point cloud depicts the different lake bathymetry. For example, the lake bed has a steep slope when the lake level is below 172 m. When the water level is between 172 m and 176 m, the slope of the lake bed gets milder and the mildest slope appears when the water level is above 176 m. The point cloud gets wider when the lake area is between 4000–5000 km^2, mostly because the algorithm could not define the correct lake extent.

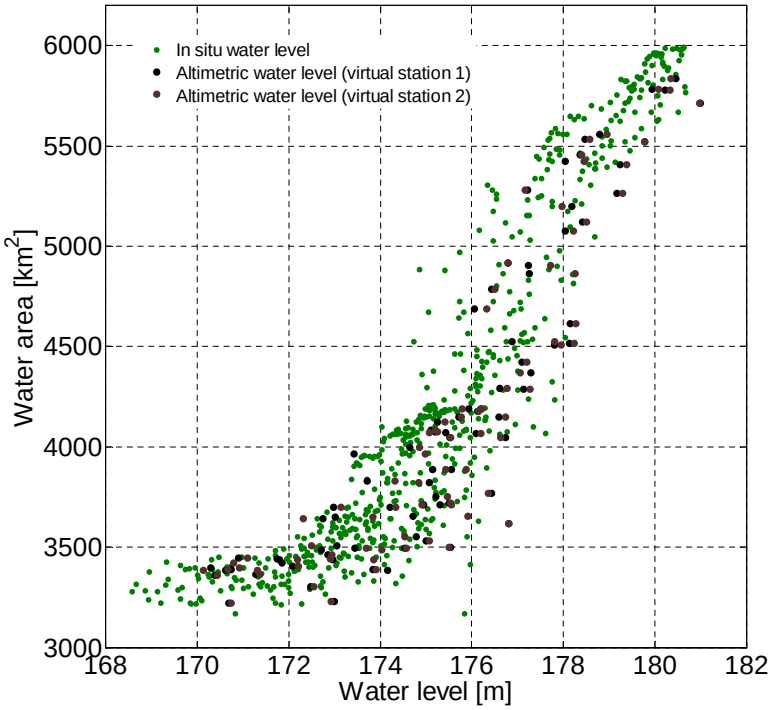

Figure 3.10: Scatter plot of water area vs. level time series of Nasser Lake.

Black and brown dots in Figure 3.10 reflect the relationship between lake area and altimetric water level in both virtual stations. Like in situ water level, altimetric water level measurements also indicate the non-linear behaviour between lake area and level. Due to less simultaneous observations, it is hard to interpret the lake geometry via altimetric water level measurements.

To evaluate the performance of the algorithm, a quantile matching model between lake area and in situ water level measurements is developed. As it is presented in the previous figures, a monotonic dependency exists between lake area and level. So, any empirical function establishing a connection between lake water area and level is a nondecreasing function. On the other hand, the quantile function is also a non-decreasing function. Also a nondecreasing function (here relationship between water area and level) of a nondecreasing function (quantile function) must itself be a non-decreasing function. Therefore, a look-up table between lake water area and level by means of their quantile functions (instead of the simultaneous measurements) can be established. This technique is applied by Tourian et al. (2013) for river discharge estimation using water level from satellite altimetry. Quantile look-up table is preferred to conventional empirical rating curve, due to the following reasons:

- Synchronous measurements in both datasets are not necessary for developing a quantile look-up table.

- Quantile function inherently reduces the effect of uncertainty in the dataset.

- If measurements spread over the whole data distribution, a look-up table can estimate the unknown variable accurately.
- The mismodeling error is eliminated by avoiding fitting a line to the scatter plot.

The quantile function, $Q(.)$, provides a way of describing the statistical distribution of dataset (Gilchrist, 2000). The following equations describe the quantile functions of lake area and level

$$Q_{\mathrm{A}}(p) = \inf\{X_{\mathrm{A}} \in \mathbb{R} : p \leq F(X_{\mathrm{A}})\} \tag{3.2}$$

$$Q_{\mathrm{L}}(p) = \inf\{X_{\mathrm{L}} \in \mathbb{R} : p \leq F(X_{\mathrm{L}})\}, \tag{3.3}$$

where X_{A} and X_{L} refer to the lake water area and level. $F(.)$ represents the Cumulative Distribution Function (CDF). For a given probability $0 \leq p \leq 1$, the quantile function determines the maximum value that the dataset (X_{A} or X_{L}) can achieve. Lake area and water level can be linked by the monotonic function $T(.)$

$$X_{\mathrm{A}} = T(X_{\mathrm{L}}). \tag{3.4}$$

Instead of mapping the data directly, we map the quantile functions.

$$Q_{\mathrm{A}} = T(Q_{\mathrm{L}}). \tag{3.5}$$

Figure 3.11 shows how the quantile look-up table is determined. In this Figure, quantile functions of lake water area and level are presented. Also the developed quantile look-up table together with simultaneous observations point cloud are plotted.

Figure 3.11(a, b) present the quantile functions of lake water area and level measurements. To derive the quantile functions, first both lake water area and level are sorted ascending, then the rank of each dataset normalized through

$$p_i = \frac{k_i}{N+1}. \tag{3.6}$$

In this equation, p_i is the occurrence probability of a certain value, k_i is the rank of the sorted value and N is the number of observations. Finally for each corresponding probability, the sorted value is plotted. The quantile functions declare the probability that a certain lake area or level occur during the monitoring period. Therefore, a direct relationship between the two quantile functions at the corresponding probabilities (Figure 3.11(c)) represents a look-up table between lake water level and area. In Figure 3.11(d), the estimated quantile look-up table is plotted on the scatter plot of simultaneous observations. The line passes exactly through the point cloud. To evaluate the performance of lake area measurements and the quantile look-up table, the lake area time series is reconstructed by using the in situ water level measurements and the derived quantile look-up table, Figure 3.12.

The comparison between two time series in Figure 3.12(a) presents the overall good agreement between the measured and estimated lake area in general. In Figure 3.12(b),

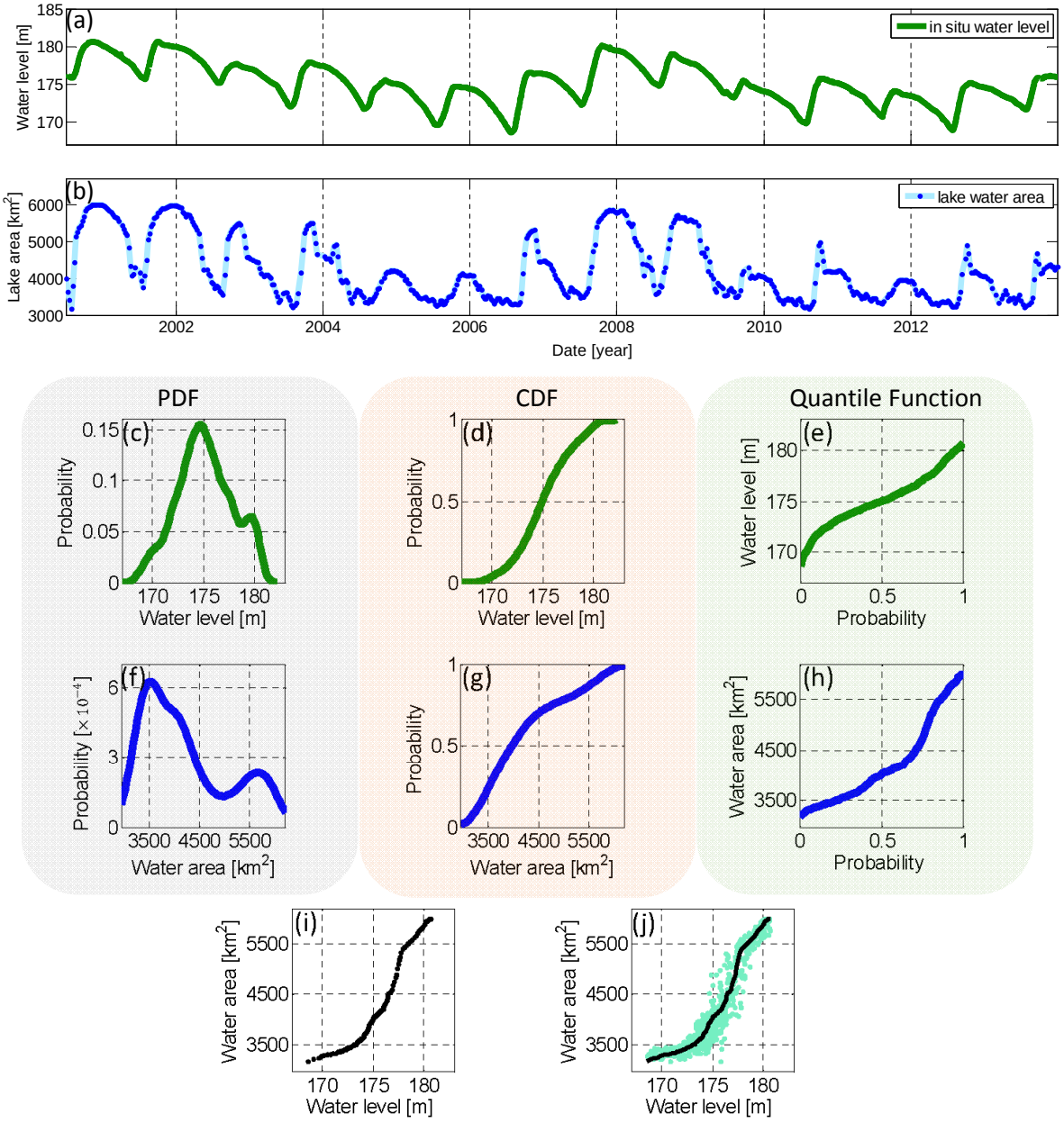

Figure 3.11: (a) and (b) are the time series of in situ water level and lake water area of Nasser Lake. (c) and (f) are probability density functions of water level and area measurements. (d) and (g) are cumulative distribution functions of the two dataset. (e) and (h) are quantile functions of in situ water level and lake area measurements. (i) is the quantile look-up table derived from both quantile functions. In (j) obtained quantile function is plotted together with simultaneous lake height and area measurements.

the difference between two time series is plotted together with the lake water area measurements. The average difference between two time series is about $-3.3\,\mathrm{km}^2$ with a standard deviation equals to $261\,\mathrm{km}^2$. In the scatter plots in Figure 3.12(c, d), the measured lake area vs. the difference between measured and estimated are plotted.

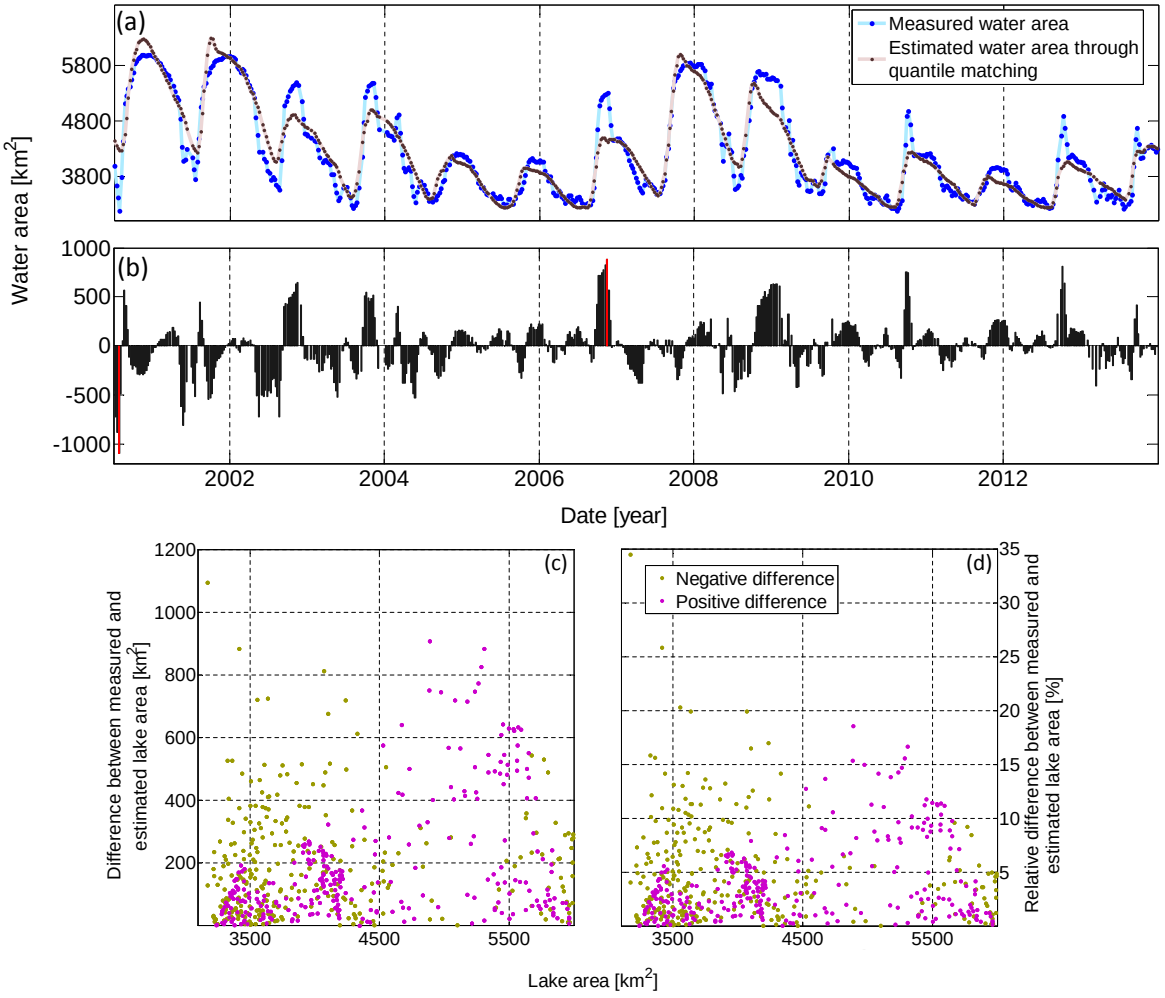

Figure 3.12: (a) Lake water area measurements and estimation via quantile look-up table. The time series in (b) is the difference between estimated and measured lake area. In this time series, two epochs with the largest positive and negative residuals are highlighted for more investigation. (c,d) The scatter plot of the measured lake area and its difference with estimated ones.

In the scatter plots, over- and underestimated values by the model are separated by different colors.

Misclassification and mismodeling of the one-to-one relationship between lake area and level are the main sources of differences between the two time series in Figure 3.12(a). Therefore, the residual between two time series (Figure 3.12(b)) can be considered as the uncertainty of lake masks. Considering the scatter plot in Figure 3.12(d), the behaviour of the lake area and uncertainty is uncorrelated. It means that the lake is always big enough to extract from MODIS images with a relatively coarse spatial resolution. About 89% of lake area measurements have the uncertainty less than 10% of the lake area and just five measurements have the uncertainty higher than 20%. The mean relative uncertainty is approximately 4.5% with a standard deviation equal to 4.1%.

To address the question about the performance of the algorithm, MODIS images and derived lake masks are compared for epochs with the largest under- and overestimation are presented in the Figure 3.13.

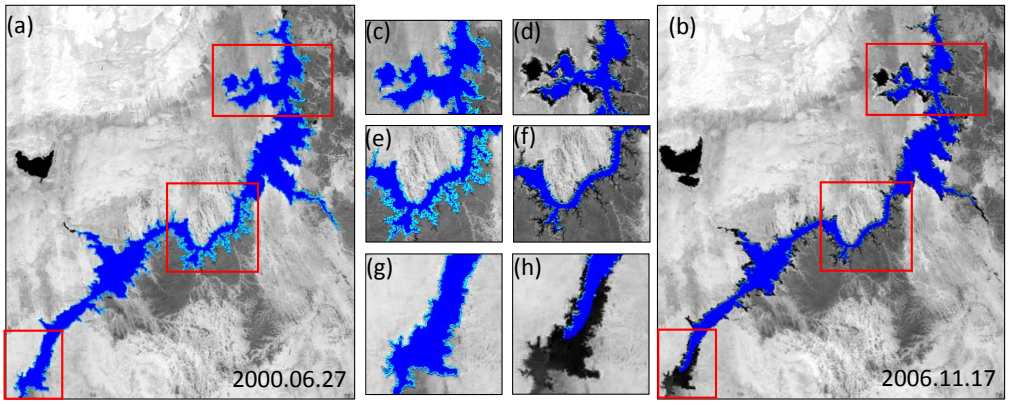

Figure 3.13: Comparison between Nasser Lake derived shapefile and MODIS image on 27 June, 2000 (a) and 17 November, 2006 (b). The shapefiles are compared in three different parts in (c–h).

Figure 3.13(a) is the MODIS image and derived mask on 2000.06.27. In this epoch, the algorithm measured the lake area 800 km^2 larger than the estimation by the model. The comparison shows that the algorithm detects all small branches along the lake. Since these branches are very small, misclassification of pixels around them is the main suspect for increasing the uncertainty in the lake area estimation.

Figure 3.13(b) is the satellite image and the derived lake mask on 2006.11.17 which has the largest uncertainty. In this epoch, there is more than 1000 km^2 difference between the measured and the estimated lake area. The reason for this large amount of error is obvious after comparing the image and the mask. The algorithm can not detect a number of small khors along the lake especially in the middle part, due to their small size. In the north of the lake, the algorithm ignored three small branches connected to the lake. The algorithm omitted them during the cleaning step because it detected them as separate water bodies since the connection between these branches and main lake body is smaller than one pixel.

3.3.2 Rukwa Lake

Rukwa Lake (Figure 1.6(g)) in Africa is the next lake monitored in this study. Monitoring is a challenging task because of its short time variations in lake level and area, despite the fact that shorelines are stable.

To extract the lake area, the procedure described in the previous section is applied to each MODIS image. Figure 3.14 provides two epochs of derived lake shapefiles, when it has its maximum and minimum water area.

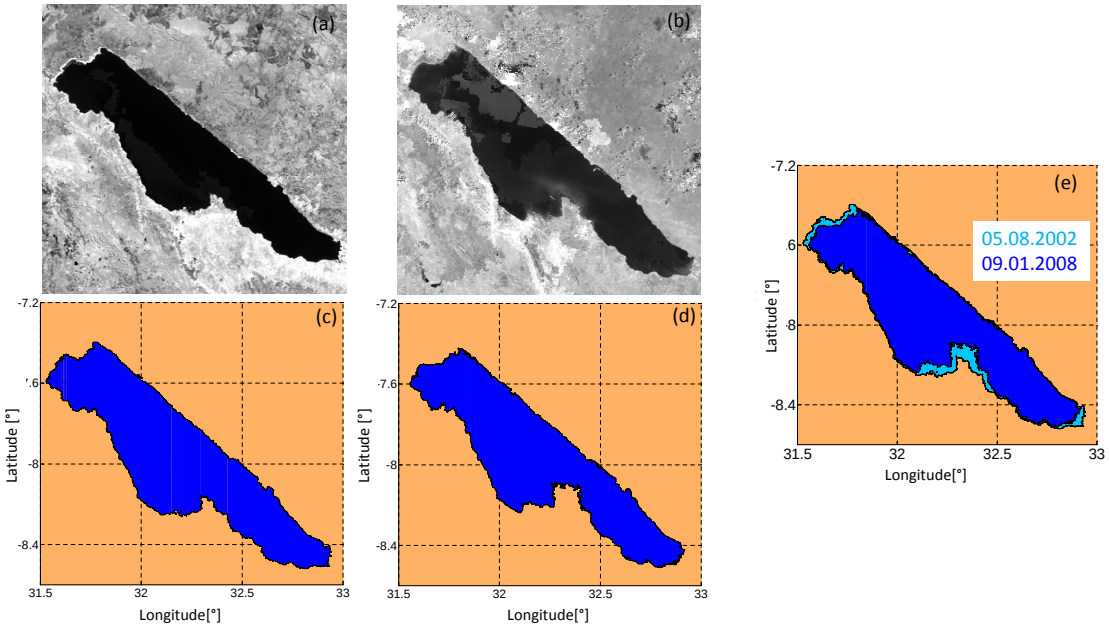

Figure 3.14: (a) is the MODIS image of the Rukwa Lake on April 15, 2002. (b) is the MODIS images of the lake on October 21, 2007. (c,d) are the Lake shapefiles extracted by the algorithm. (e) is the comparison between extracted Rukwa lake shapefiles on two different dates

The algorithm is able to detect the lake shoreline accurately in both dry and wet seasons. The lake in the Figure 3.14(b) is partially covered by clouds, nevertheless, the algorithm can capture the water-land boundaries.

Figure 3.14(e) shows the difference between the two epochs, which is about 821 km^2. The north and south coasts are subject to change between two epochs. Rukwa Lake is restricted to extend from the east side due to the higher elevation of this side of the shoreline and basin. Figure 3.15 presents the lake area time series .

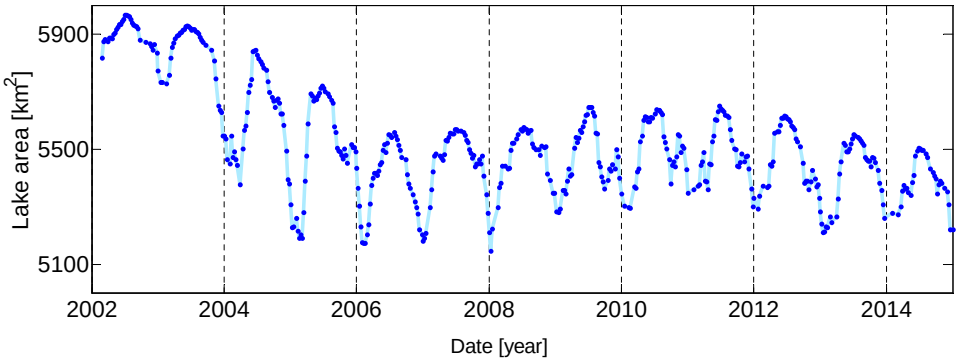

Figure 3.15: Rukwa Lake area time series. The monitoring period is 2002–2015

Figure 3.15 is the time series of lake area during the years 2002–2015. In the first year, lake was larger than 5 900 km^2, but its behaviour started to change from the year 2004.

The lake lost its area with a negative trend until 2006 and experienced stronger annual variations during this time frame. Therefore, the difference in lake area between wet and dry seasons increased. After 2006, the negative trend was stopped and the lake started to gain area slightly in the following years. So, a small positive trend is obvious between years 2007–2010. But in the last five years (2000–2015), a small negative trend is visible again. Water coverage frequency map for Rukwa Lake is presented in the Figure 3.16.

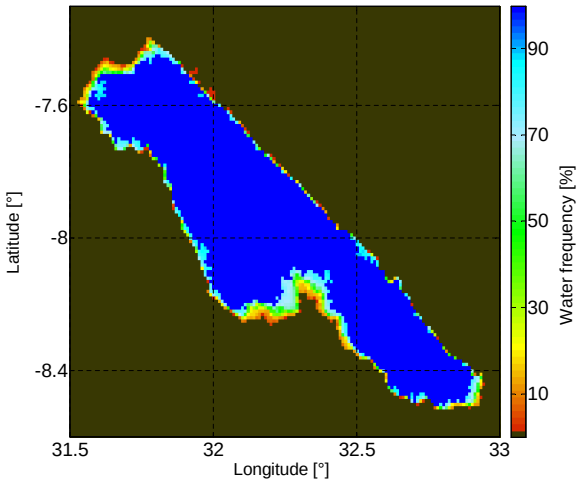

Figure 3.16: Water coverage frequency map of Rukwa Lake for the period 2002–2015

Figure 3.16 indicates that lake area has not changed considerably during the monitoring time frame and the majority of lake boundaries have always remained stable. Due to the topography of the region, the northeast and east side of shoreline has been constant. Therefore, the annual variations of the lake caused change in the south and northwest part of the shoreline. To assess the performance of the proposed algorithm, in the next figure, the lake area is compared with altimetric water level time series obtained from HydroSat data repository.

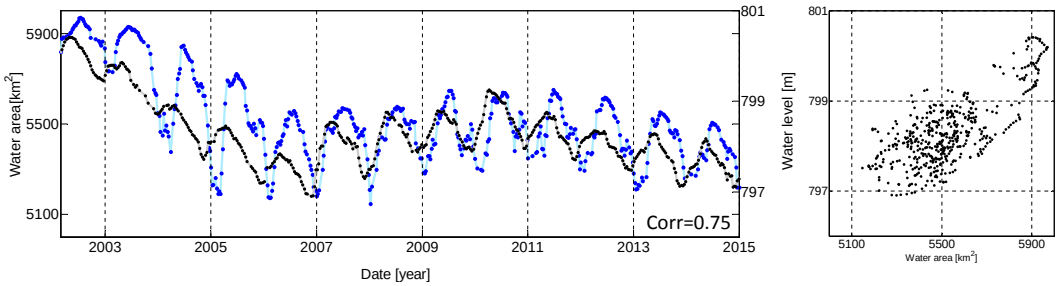

Figure 3.17: Comparison between Rukwa Lake water area (blue) time series with altimetric water level(black).

The comparison between Rukwa lake water level and area in Figure 3.17 shows a consistent agreement between their behaviour. The correlation between the two time series is 0.75 which is acceptable considering the dynamic behaviour of the lake. Like

the lake area, the negative trend in water level between the years 2002–2006 is obvious. The lake water level decreased about 4 m during this period. Subsequently, the water level increased until the end of year 2010 and again by starting the year 2011, a tiny negative trend is visible. Therefore, water level variations also followed the lake area in terms of trends. A phase shift between the two time series is obvious in Figure 3.17, especially in the dry season. As a result, the point cloud got wider in the scatter plot. To find the reason for the phase shift, lake water area and level time series are compared with monthly precipitation of Rukwa basin from the GPCP dataset. It is assumed that the amount of precipitation in the basin is the main reason for lake water area and level variations. As a result, both time series must follow the behaviour of the precipitation variations.

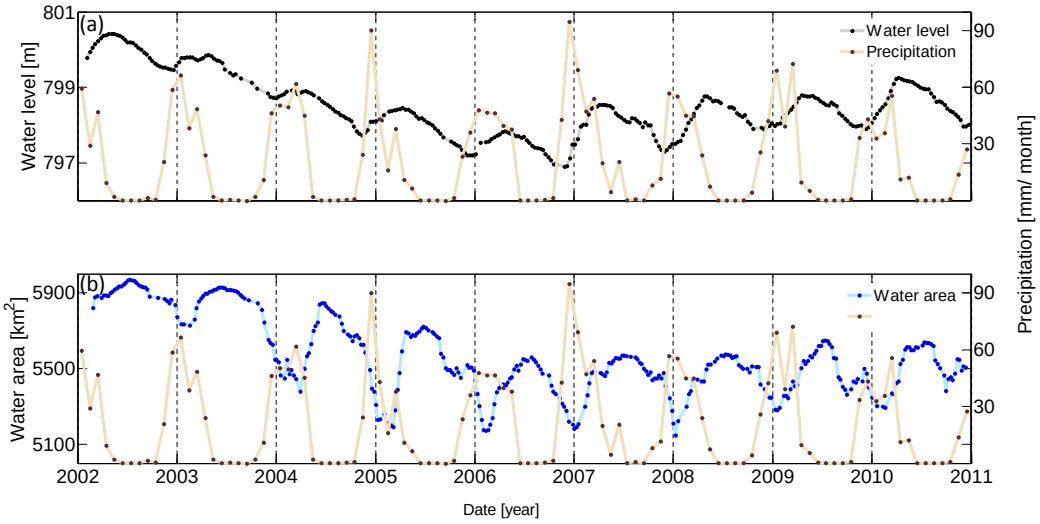

Figure 3.18: Rukwa basin monthly precipitation is plotted together with altimetric water level in (a) and lake surface area (b)

In Figure 3.18(a), the agreement between precipitation and water level variations is clear. As long as there is no precipitation over the basin, lake level decreases. Then, in the rainy months, the water level starts rising. But by comparing lake water area and precipitation time series, it is clear that lake area measurements are not so accurate especially in the rainy months. Regarding this Figure, by increasing the precipitation, lake area decreases in some epochs. This pattern is against the lake natural behaviour. Cloud coverage in the MODIS images is the first suspect for this destructive pattern. For a deeper investigation of this problem, images acquired at the end of the year 2007 and starting the year 2008 are shown in Figure 3.19

To understand the reason why water level starts rising but lake area still decreases at the end of each year, MODIS images related to end of the year 2007 and beginning of 2008 are investigated. Rukwa is a closed basin, therefore the amount of precipitation during the wet season should accumulate in the lake. Accordingly, lake area must increase from Figure 3.19(a) to Figure 3.19(b), but the algorithm estimated a smaller

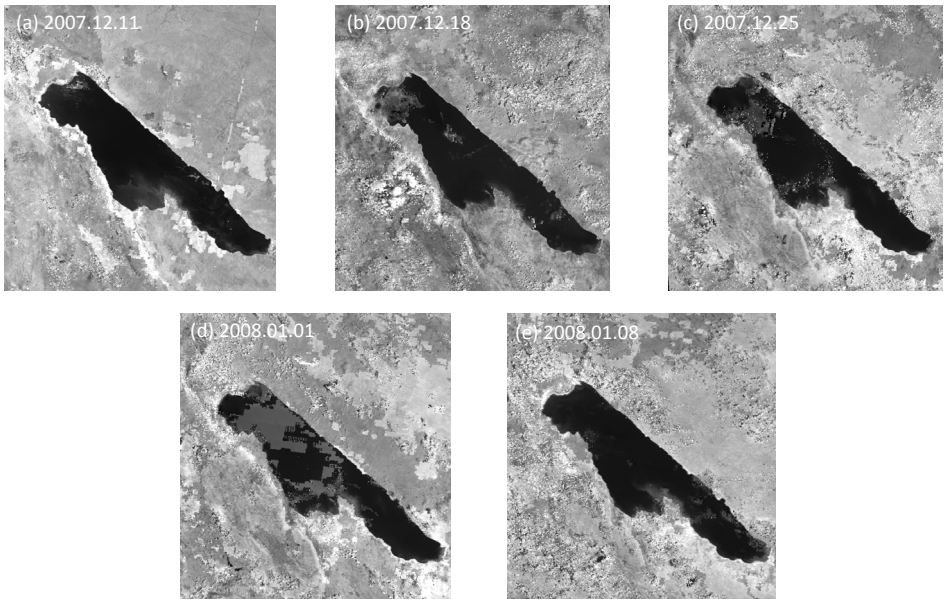

Figure 3.19: Five MODIS images of Rukwa Lake from different epochs

value for the lake area in the second epoch. By looking at the lake image in the Figure 3.19(b), the reason is obvious. Due to the cloud coverage in the upper part of the lake shoreline, the algorithm can not define the proper shoreline and underestimates the lake area. In the next epoch, Figure 3.19(c), the cloud covered a bigger portion of the lake boundary, therefore, the algorithm made a bigger mistake in area estimation from the previous epoch. For Figure 3.19(d) the situation is similar and part of the shoreline is covered by cloud. Finally in the last image, the algorithm can extract the lake shoreline accurately. Since the variation of the lake area is negligible, the effect of cloud coverage is obvious. As a result, it could be concluded that cloud coverage is responsible for the occurred phase shift between water area and level.

3.3.3 Mosul Dam Lake

Mosul Dam Lake (Figure 1.6(h)) is the next case study. This artificial lake was generated by building the Mosul Dam across the Tigris River in the year 1986. Because of the poor maintenance of the dam, the government decided to reduce water level from 330 to 319 m (Annunziato et al., 2016). The following figure presents the two MODIS image and derived shapefiles of the lake at its maximum and minimum state.

The proposed algorithm can extract complex shoreline of the lake in both cases. This lake has variable shorelines, so by increasing the lake water volume, lake extent increases from all directions. By reducing the water level in the year 2006, the north western part of the lake had disappeared. Apart from the north western part, the lake area decreased right behind the dam in the south east part. The comparison between two shapefiles in Figure 3.20(e) presents the evolution of the lake over the time.

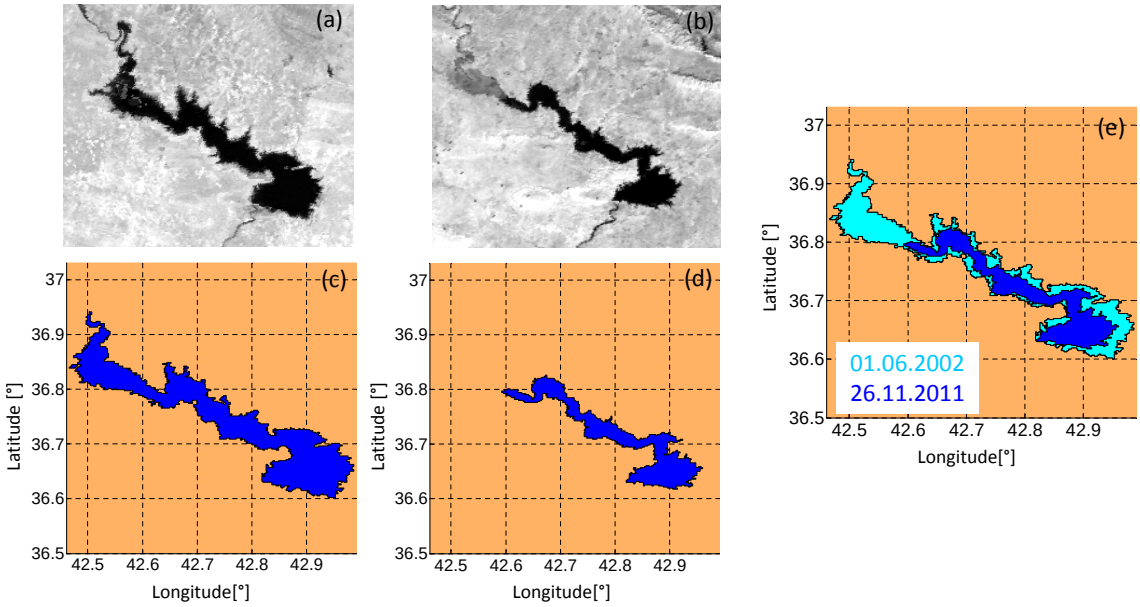

Figure 3.20: (a) is the MODIS image of the Mosul Dam Lake on June 1, 2002. (b) is the MODIS images of the lake on November 26, 2011. (c,d) are the lake shapefiles extracted by the algorithm. (e) is the comparison between Mosul Lake shapefiles on two different dates

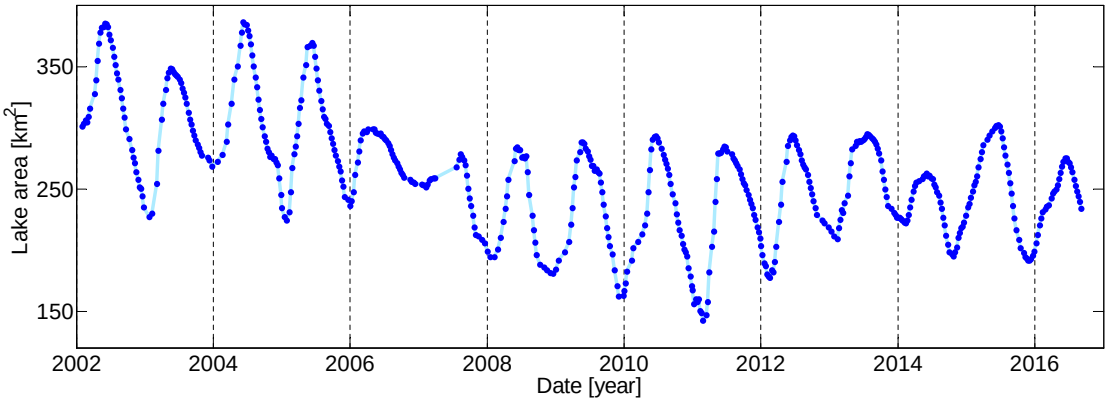

Figure 3.21: Mosul Dam Lake area time series. The monitoring period is 2002–2017

Figure 3.21 shows a significant annual behaviour. The difference between lake area in dry and wet season is more than 100 km^2, which is about 40% of the average lake area. But, after the year 2012, the annual amplitude of the lake decreased. The average lake area is 262 km^2 with a variation equal to 49 km^2.

Figure 3.22 presents the frequency map of water coverage. Regarding the water area time series, the red area represents the lake boundary before reducing the water level and the green area indicates the annual behaviour of the lake. The southeastern and middle part of the lake are always covered by water so they are presented in blue. The northwestern part with light blue color indicates that this part was dry in some epochs.

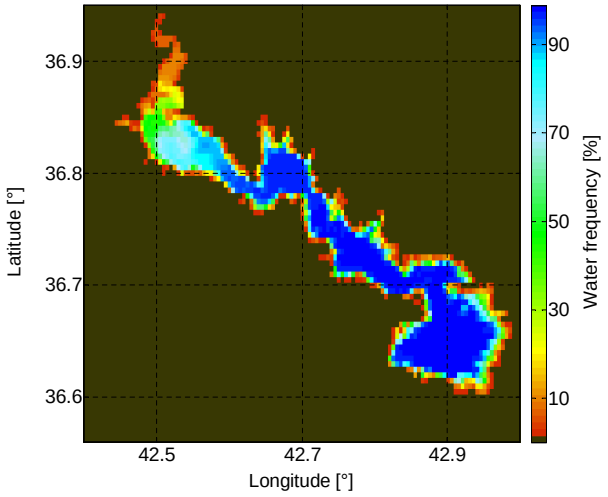

Figure 3.22: Water coverage frequency map of Mosul Dam Lake for the period 2002–2017

Regarding the lake area time series, these epochs belong to the dry seasons of the years between 2010–2012.

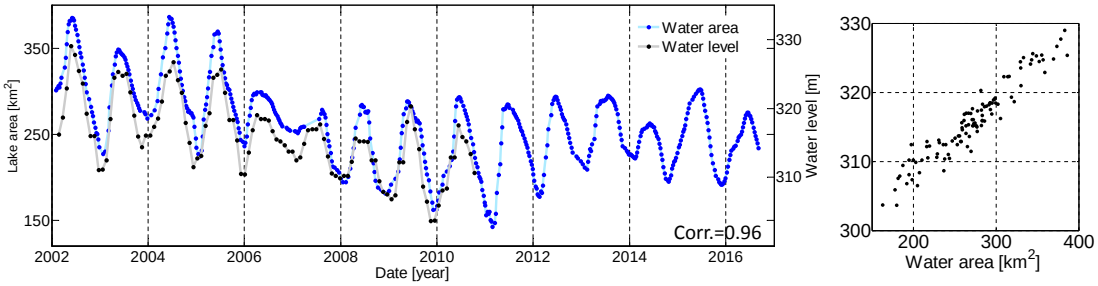

Figure 3.23: Comparison between Mosul Dam Lake water area time series with altimetric water level together with its scatter plot

Figure 3.23 presents the comparison between derived lake area and altimetric water level time series. The altimetric time series is available from the year 2002 until 2011 from DAHITI dataset. The high correlation (0.96) between two time series admits that their behaviours have a good agreement together. Annunziato et al. (2016) mentioned that the Iraqi government decided to reduce the lake water level from 330 to 319 m in the year 2003. But both water area and level time series show reduction after the year 2006. By comparing the lake area after and before 2006, it is understood that the Mosul Lake shrank about 100 km^2 due to 10 m reduction in water level. The scatter plot in Figure 3.23 shows the linear relationship between lake water level and area. The accumulation of simultaneous observations is in the middle part of the scatter plot since the water level varied between 310 and 320 m. Since this range belongs to the water level in the dry season in 2002–2006 and wet season in 2007–2017.

3.3.4 Tharthar Lake

Tharthar Lake (Figure 1.6(i)) is another lake located in the Middle East. The main function of this artificial reservoir is to collect the overflow of the Tigris River during the flood season. On the other hand, Tharthar Lake feeds Tigris and Euphrates Rivers respectively in the dry season. In the next figure, two examples of MODIS images and their extracted lake extent shapefiles are presented.

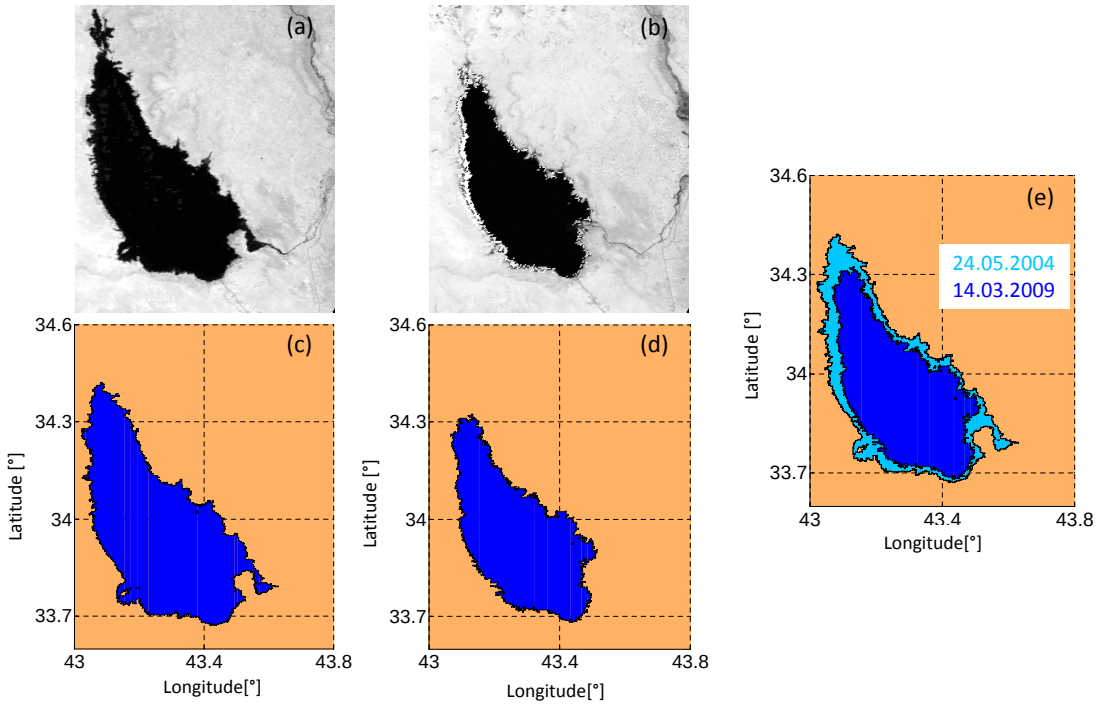

Figure 3.24: (a) and (b) are images of Tharthar Lake on May 24, 2004 and March 14, 2009 and (c) and (d) are their extracted shapefiles. (e) is the comparison between Tharthar Lake on two different dates

It must be mentioned that the small water body in the north part of Figure 3.24(a) is not considered as being within the search area, because it is separated from the main body of the lake. The lake image in the Figure 3.24(a) and its corresponding shapefile present the state of the lake at its maximum area (2 030 km^2) and Figure 3.24(d) presents the lake extent when the Lake has its minimum area (1 483 km^2).

The comparison between lake images and shapefiles shows that the algorithm can extract the lake extent accurately. By looking carefully at Figure 3.24(a) and (c), it is clear that the algorithm could not detect the small variations in the lake extent especially in the west coast. The lake has a more complex boundary in Figure 3.24(b), however the algorithm detected this complex pattern. Finally, the comparison between the two shapefiles are presented in Figure 3.24(e)

Like previous cases, dark and light blue colors represent the maximum and minimum lake area between the years 2002–2017. This comparison shows that the lake shrinks

almost from all directions during the dry season. Figure 3.25 presents the Tharthar Lake water area time series.

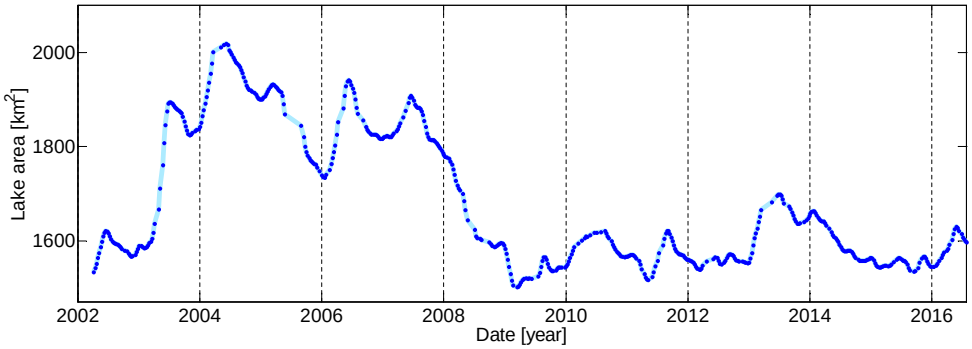

Figure 3.25: Tharthar Lake water area time series between the years 2002–2017.

Starting 2002, the lake area increased significantly. Then, in the year 2008, it was shrinking to its previous area. Starting 2009, the lake area was almost equal to the measurement on the first epoch in the year 2002. Unlike the previous examples, this lake has not a clear annual variation.

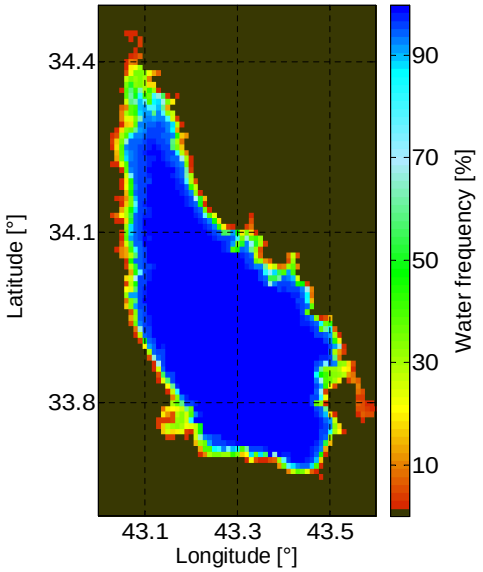

Figure 3.26: Water coverage frequency map for Tharthar Lake for the period 2002–2017

The water coverage frequency map of Tharthar Lake is presented in Figure 3.26. The major part of the lake is blue which means that this area is always covered by water. The lake gained and lost area from the north side during the positive and negative shift, therefore this area is presented in light blue, green and yellow. The green and yellow pixels are subjected to the annual behaviour.

Figure 3.27 compares water area and lake level. In general, the two time series have high correlation of 0.9. Like the lake area, the positive and negative shifts in the water

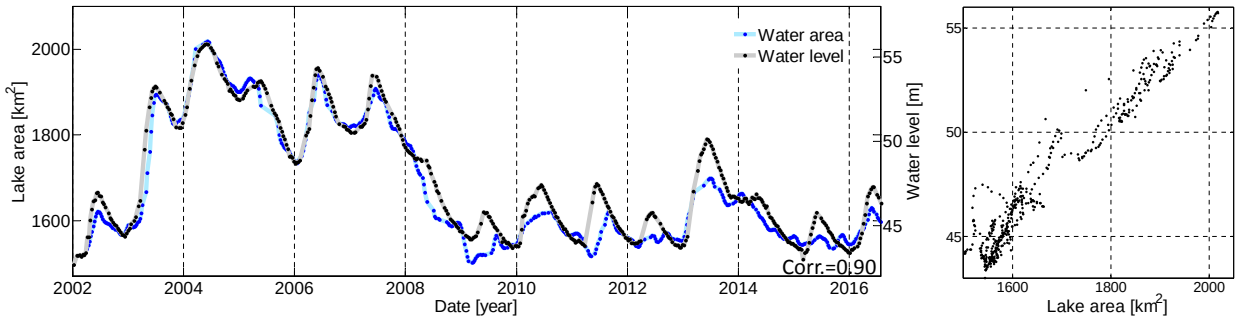

Figure 3.27: Comparison between Tharthar water area and altimetric water level

level are also visible in the years 2003 and 2008. However, the annual behaviour is more obvious in water level variation. In the period 2002–2009, the behaviour of the two time series is very similar, but after 2010 there is a slight disagreement between them, due to a complex of the lake boundary when the water level is below 45 m. In this period, variations of lake area are too small and it is hard for the algorithm to extract the proper lake boundary from MODIS images with 250 m spatial resolution.

3.4 Monitoring the desiccation of Lake Urmia in Iran

Urmia Lake is the last example in this chapter. To monitor the Urmia Lake water area, MODIS MOD09Q1 images with 8 days temporal resolution and 250 m spatial resolution are gathered and make them ready to apply the proposed algorithm to extract the lake boundary. Figure 3.28 presents five images from different years, each in February.

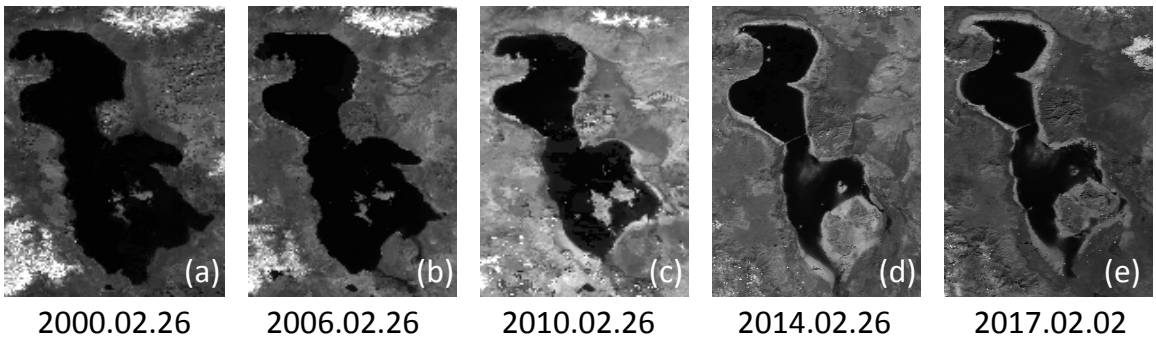

Figure 3.28: Examples of MODIS MOD09Q1 images of Urmia Lake from different years (February)

Comparison between them shows the catastrophic desiccation of the lake. The reduction in area is visible from the year 2006 until 2010 and after 2010, Urmia Lake started to dry almost from all directions. Figure 3.28 demonstrates that the situation of the lake is an environmental disaster. To analyse more carefully the situation of the lake during

2000–2017, the proposed algorithm is applied on lake images. Like previous examples, the search area is restricted by DEM-based mask. But due to the drastic change in the lake boundary during the monitoring period, the constant-water mask does not apply in this case. In the Figure 3.29, the derived lake mask on February 2000 is compared with lake masks of the same month in the following even years.

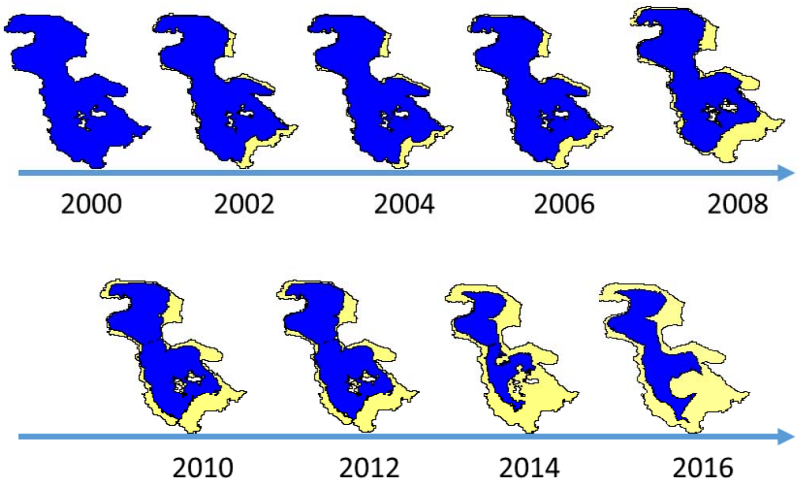

Figure 3.29: Shapes of the Urmia Lake over the years 2000–2016.

The lake mask on February 26, 2000 is considered as the reference mask for the comparison with the following years. In the snapshot acquired in 2002, the lake started to shrink from the north east, east and especially south east. From 2002 to 2006, the lake area decreased at a steady pace from the same directions. After 2006, a clear desiccation is visible especially in the south part. In 2010, the south western part of the lake started to become dry. After 2010, the situation of the lake became irreversible, and every year, the Urmia Lake lost a huge portion of its area. In the year 2014, it endured the worst situation during the monitoring period. In this year, the Lake has lost the majority part of its area especially in the southern part. To rescue the lake from complete disappearing, Iran government restricted farmers to use groundwater for farming and pays them to stop farming in the basin. As a result, lake surface water increased in the year 2016. Time series of lake area measurements together with their nonlinear trend is presented in the Figure 3.30 for the years 2000–2017.

In the early years of monitoring, the lake had a slight annual behaviour with a small negative trend. After the year 2007, the negative trend and also the annual behaviour are more obvious. The lake reached its smallest area in the summer of 2014 and 2015. However, fortunately, the desiccation stopped in the following year and the lake returned to its state of January 2012.

Due to complex behaviour of the time series, assigning a linear trend to the lake area variations is not practical. So singular spectrum analysis (SSA), a nonparametric es-

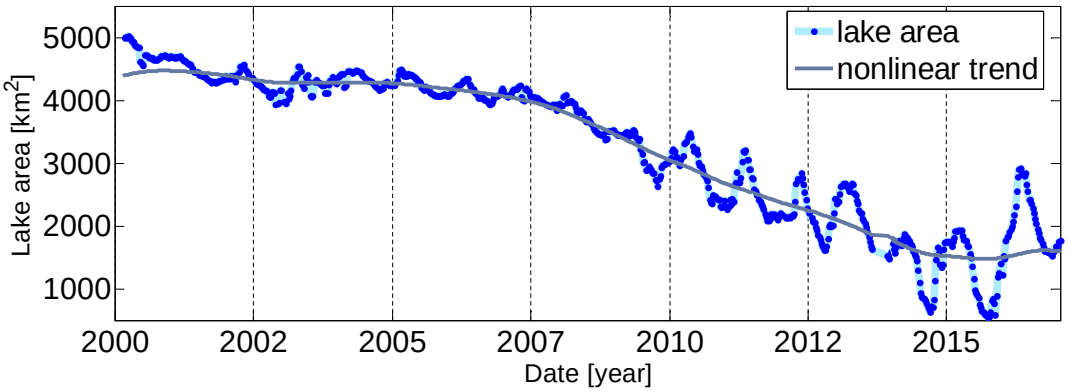

Figure 3.30: time series of Urmia Lake surface water area together with its nonlinear trend.

timation method, is applied to the time series of lake area to separate the nonlinear trend and time-variable seasonal signals. In this way, the annual signals do not affect the trend estimation procedure (Blewitt & Lavallée, 2002). This technique is a data-driven approach to extract information from short and noisy time series without prior knowledge of dynamics affecting the time series (Broomhead & King, 1986). The obtained trends by SSA are not necessarily linear, so oscillations can be modulated in both amplitude and phase (Ghil et al., 2002). In this study, the window size for SSA was three years and the Matlab code developed by Chen et al. (2013) was used.

At the beginning of monitoring period, the Urmia Lake had an area about 5 000 km^2. In addition to annual behaviour, the lake had a small negative trend due to the overuse of the water resources in the basin. Regarding the nonlinear trend, Urmia Lake lost about 74 km^2 every year from 2000–2006. From the year 2006, the rate of desiccation became faster. This fact is clear in both time series and trend. The lake approximately lost about 283 km^2 per year between the years 2006–2010. After 2010 the rate of decline increased dramatically. In July 2014, the lake had an area about 890 km^2 which is less than one-fifth of its area at the beginning of the monitoring.

Due to the change in the different geometry of lake seabed, the annual variations are more obvious after 2008. In the period of 2010–2015, Urmia Lake lost almost 330 km^2 per year which is the highest negative rate. The reduction rate nearly stopped after 2015, the lake experienced positive trend for the first time. In this way, between the years 2015–2017, Urmia Lake has gained nearly 300 km^2.

Figure 3.31(a) presents a map of water coverage frequency for the whole monitoring period (2000–2017); Figures 3.31(b, c, d) are maps for three sub-period. The middle part of the north part of Urmia Lake is always covered by water. The rest of the middle part is covered by water in between 60–90% of epochs. A big portion of the lake area covers by green representing pixels covered by water in 30–60% of the images. Finally, marginal pixels, that belonged to the lake in the early years (2000–2006), are presented in yellow and red colors. Figure 3.31(b) shows that the lake was shrinking from the south part in the first six years and the rest of the shoreline was just subjected to the

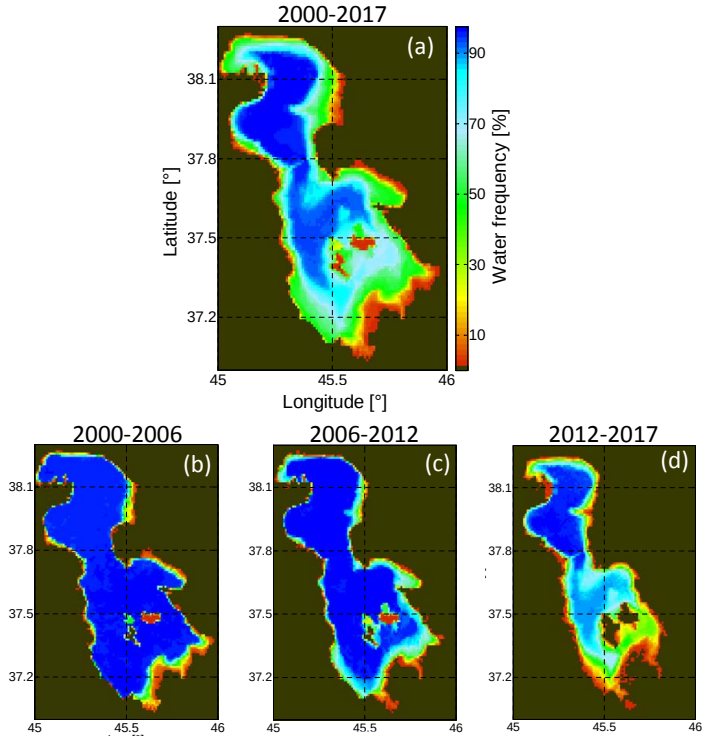

Figure 3.31: Water coverage frequency maps for Urmia Lake. (a) is for the period 2000–2017, (b) is for the first six years 2000–2006, (c) for the period 2006–2012 and (d) for the last 5 years 2012–2017.

annual variation. After the year 2006, the desiccation of the lake was accelerated at the southern side. Also in this period, the north part of the lake started to decline. In 2012–2017, only a small portion of the lake on the north side always covered by water. The lake experiences a considerable annual change in this period. A large number of pixels with light blue and green colors indicate that the major part of the lake is subject to the annual cycle in this period.

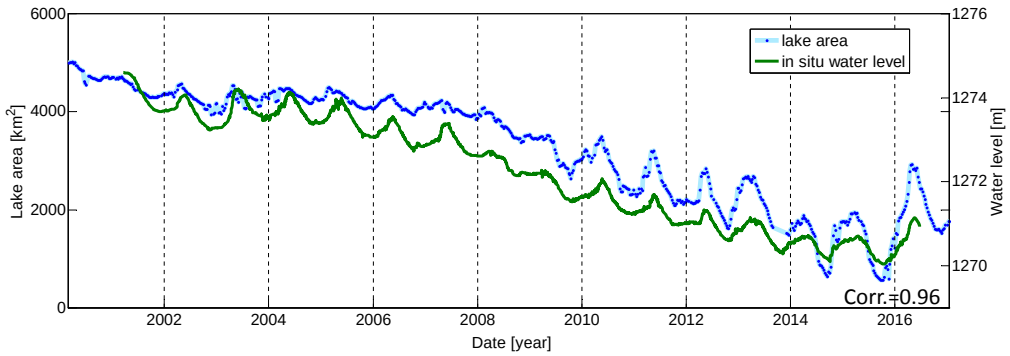

Figure 3.32: Comparison between Urmia Lake surface water area and in situ water level time series.

In order to validate lake area estimations, Figure 3.32, water area time series compared with in situ water level measurements. The high correlation between two time series (0.96) reflects a high consistency. Like surface area, water level measurements also shows a negative trend in the first fifteen years of monitoring. After 2015 a tiny positive trend in water level is visible. This validation shows that the proposed algorithm is able to extract the lake extent accurately from the satellite images. However, it was applied to MODIS images with relatively rough spatial resolution.

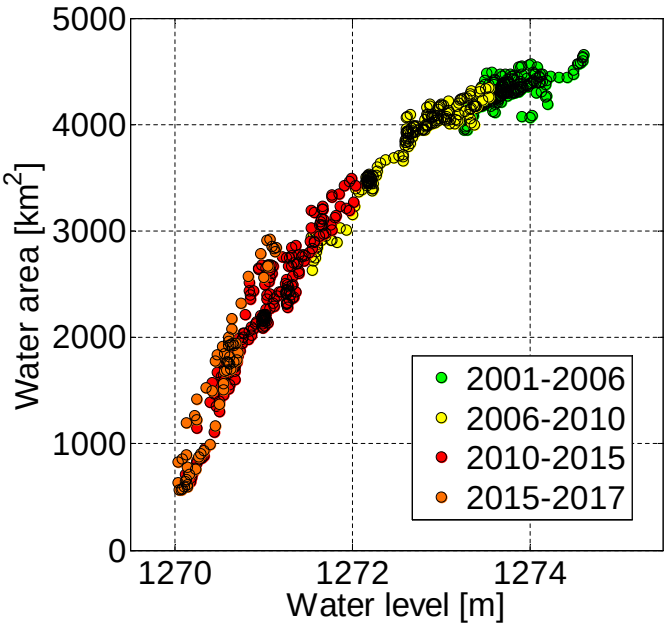

Figure 3.33: Scatter plot of surface water area versus in situ water level of Urmia Lake. The scatter plot is divided into four different time periods regarding the state of the Lake: 2001–2006, 2006–2010, 2010–2015, 2015–2017.

Figure 3.33 presents the scatter plot of simultaneous surface water area and in situ water level measurements. The high correlation between the two time series in Figure 3.32 assures a clear one-on-one relationship in the scatter plot. The point cloud depicts four different phase of the lake status regarding the trend. The first three colors (green, yellow, red) reflect three different patterns between lake water area and level. These patterns represent the different lake bed characteristic over different parts of the lake. If the lake bed has an intense slope by occurring a small change in water level, leads to a relatively big change in the lake area. In this way, yellow dots represent the deepest slope in the lake bed and green dots indicate the mildest slope. The change in the lake desiccation trend is also obvious in the scatter plot. Green, yellow and red dots represent a negative trend in the lake surface water area and level. The simultaneous measurements (orange dots) after the year 2015 indicate the positive trend in this period.

The successful monitoring of the complex evolution of Urmia Lake proves the ability of the proposed algorithm to extract the lake masks from the satellite images and generate long time series of the lake area.

3.5 Summary

In this chapter, an algorithm for lake area monitoring using spaceborne optical images is introduced and applied to five lakes with different situations and behaviours. The algorithm has three main steps to generate accurate and reliable surface lake masks:

1. defining a proper search area,
2. applying classification algorithm,
3. cleaning derived water masks and generating lake area time series.

Regarding the behaviour of the lake over time, the lake surface and surrounding area can be divided into three different regions

1. The area inside the lake which is always covered by water,
2. The area which is always dry because it is located at higher altitude than the surrounding area,
3. The area located near the shoreline on both sides which could be covered by water and subject to the annual variations.

Among these three regions, pixel labels in the first two groups are known. Therefore, the classification algorithm must define the label for pixels in the third group.

To define and ignore pixels which are always dry during the monitoring period, a mask regarding the DEM and slope maps is developed. For generating the DEM-based map, two criteria are considered:

- Pixels in this mask must have an elevation higher than the minimum elevation in the map plus 100 m,
- Pixels in the mask must have a slope higher than 1%.

The aim of the second mask is to remove the middle part of the lake from the search area. To define this mask, long term variations of each pixel value is analyzed separately. Any pixel which is always covered by water has almost constant and low value in the NIR image band. So the water mask is described by assigning a threshold on mean and variance of all pixels. By applying this mask, the middle of the lake is labelled as water. As a result, the final search area just includes pixels which are subject to change during the time.

To extract the lake boundary the unsupervised classification algorithm, ISODATA, is applied to the search area. At the end, the pixels allocated into the first cluster by ISODATA are added to the water mask. Isolated pixels are removed from lake masks to improve the quality of the final results and the time series of the lake area is generated.

The proposed algorithm has been employed over five lakes in Africa and Asia. Each of the selected case studies demonstrated a challenging situation for lake area monitoring:

- Nasser Lake: complex shoreline and small branches.
- Rukwa Lake: partially constant shoreline and small area variation.
- Mosul Dam Lake: artificial water volume reduction.
- Tharthar Lake: the negative and positive trends in the area.
- Urmia Lake: the drastic desiccation.

Since ground-based measurements of lake areas are not available, derived lake masks are indirectly validated by comparing lake water area and level during the monitoring period. For Nasser and Urmia Lakes, daily in situ water level measurements are available. In both cases, a high correlation between water area and level (0.92 for Nasser Lake and 0.96 for Urmia Lake) demonstrates that the algorithm can extract water area accurately. In other cases, water area time series is validated by comparing with satellite altimetric water level measurements. Except for Rukwa Lake, the correlation coefficients are about 0.9. Although the proposed algorithm has acceptable performance in general, it has a number of limitations. The cloud coverage in optical images is always a threat to the performance of the proposed method. For example in Rukwa Lake, the lake basin has a seasonal precipitation, so the cloud coverage imposes a systematic error in the lake area monitoring. As a result, the correlation coefficient is reduced to 0.75. Due to the coarse pixel size of the MODIS images, the algorithm cannot extract the small details of shoreline variations and tiny branches which was clear in the case of Nasser Lake.

Chapter 4

Monitoring river reach area from satellite imagery

4.1 Introduction

Measuring and monitoring river reach area is important for river discharge estimation, hydrological model calibration, water management, or hazard monitoring. But our knowledge about the spatio-temporal variations of river hydraulic parameters (water level, river width and slope) is surprisingly poor. In situ gauge stations are limited in spatial and temporal coverage, and the number of available stations has been decreasing during the past decades. On the other hand, remote sensing techniques have proven their ability to measure different geometrical aspects of rivers. Satellite imagery, for instance, can provide river reach area variations with a fine spatial and temporal resolution.

Unlike lakes and reservoirs, rivers show various behaviour along their path due to the contribution of different parameters like the gradient of elevation, river slope, tributaries and morphology of the river bed. In the sub-tropical regions, some rivers completely disappear in the dry session and overflow during the wet season. The pixel value of the water surface in a satellite image depends on the quality of water, the roughness of its surface, its chemical properties, load and type of sediments and the depth of the water column. Also, in river borders, we usually deal with shallow water covered by vegetation and complicated combinations of wet and dry areas within a pixel. Therefore, selecting an appropriate change detection algorithm which can confront these complexities, needs careful investigation.

Evaluation of different classification algorithms for river reach area monitoring

To begin, we will evaluate the performance of four common dynamic thresholding algorithms for extracting a reach of the Niger River near Lokoja station (Figure 1.6(c))

from MODIS images (Table 1.8). In the following, the thresholding algorithms are briefly introduced:

- **Convex hull thresholding** is based on the shape of the image histogram. After calculating the convex hull of the image histogram, the biggest difference between the pixel value frequencies and the convex hull is defined as the threshold (Rosenfeld & De La Torre, 1983).
- **Otsu thresholding** is a clustering-based method that the image histogram is a bimodal (object and background pixels). Then the optimum threshold is defined so that the variance within the classes is minimized (Otsu, 1979).
- **Maximum entropy thresholding** considers the image as two different sources of data (object and background). When the sum of the two class entropies reaches its maximum, the image is optimally segmented into two classes (Glasbey, 1993).
- **Moment preserving thresholding** considers the input images as a blurred version of an ideal binary image. The threshold value is defined by matching the first three moments of the input image and the binary map (Tsai, 1985).

Apart from these, the classification algorithm proposed in the previous chapter is also applied to derive river mask time series.

Figure 4.1 presents the water area time series generated by applying the aforementioned methods. Additionally two post-classification steps, a blunder removal step regarding the variance of the measurements and a moving average with a window size of three, are applied to time series to improve the final results.

The correlation coefficients indicate that none of the algorithms can generate reliable river masks. Among them, ISODATA and convex hull can partially capture the annual variations of the river area. Unlike convex hull, ISODATA cannot extract the river area correctly during the wet season.

In general, the maximum entropy and Otsu algorithms perform well when the pixel values of the object and background in an image create a combination of two normal distributions in the histogram. This situation is not valid in our case study because the river occupies only a small portion of the whole image. Moreover, different parameters like water depth, soil and vegetation moisture have a contribution in defining the pixel value of water.

The moment preserving thresholding algorithm cannot provide accurate water masks because it is incapable of segmenting an image properly if there is a huge difference between histogram peaks and valleys.

As a result, we can conclude that these techniques have their limitations to estimate the water mask properly as they are not able to find a correct threshold because of

1. a huge difference between the number of pixels in each class,
2. the complex relationship between wet and dry areas in the river border.

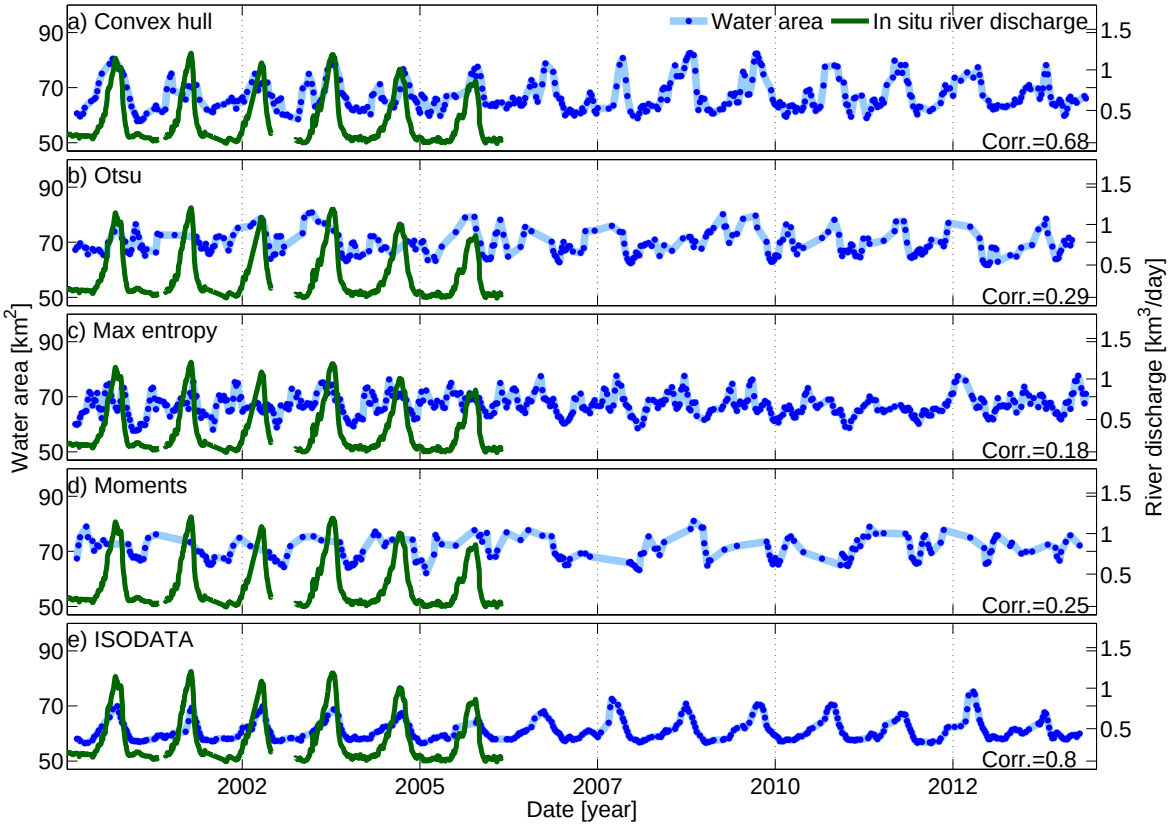

Figure 4.1: Comparison between different river mask time series of Niger River reach derived by mentioned thresholding algorithms. Monitoring period: 02.2000–09.2014.

All of the implemented methods try to segment the image based on the pixel intensities. But beyond pixel intensity, spatial correlation between neighboring pixels is another source of information that can be used to segment an image. Like all natural phenomena, water bodies have a high spatial correlation in satellite images. Therefore, including contextual information as an additional constraint in the procedure of the river area monitoring should significantly improve the quality of final river masks. Moreover, the coverage of each pixel has a particular temporal behavior, mainly driven by annual and seasonal climatology, so in addition to spatial correlation, a strong temporal correlation is typically available.

Region-based classification approach

Markov Random Fields (MRF) has the potential to model the interaction between different constraints and auxiliary sources of information in an image. Developing an efficient MRF model and finding the maximum a posteriori (MAP) solution in the model is a common region-based classification approach in image processing and remote sensing.

MRF provides a convenient frame for modeling spatial and temporal interactions between pixels (Veksler, 1999). The method was first introduced into image analysis applications by Geman & Geman (1984), and subsequently in several studies (Ishikawa & Geiger, 1998; Couprie et al., 2011; Boykov et al., 1998, 2001). In the remote sensing community MRF is quite popular because of its ability to integrate information related to pixel intensity and spatial correlation. MRF, as an advanced technique, is applied to extract the change in satellite images (Bruzzone & Prieto, 2002). Also integration of temporal (Mota et al., 2007) and spatio-temporal (Solberg et al., 1996) information to the Markov model are proposed. A hybrid multi-contextual MRF for flood detection in SAR images is presented by Martinis & Twele (2010). Generally, the object is recognized from the background of the image finding the MAP solution in an MRF. The problem of finding the MAP estimate is usually solved by describing an energy function specified towards the problem. Then, the aim is to search for a pixel label structure minimizing the energy function.

A number of search methods are commonly applied to solve energy minimization problems. Simulated annealing (SA), as an efficient global optimization technique, is widely used for this purpose (Geman & Geman, 1984). SA is able to find the optimal solution by defining a random and flexible sampling step, but in practice, SA is time-consuming and does not guarantee that the final result is the global minimum (Veksler, 1999). Graduated non-convexity is used as an alternative to SA. This is a deterministic annealing technique with much less cost than the ordinary SA. Iterated conditional modes (ICM) (Besag, 1986) is a local energy minimization, approach to find the best labels for the segments (Martinis & Twele, 2010). However both of them are very sensitive to initial values due to the local minima (Szeliski et al., 2006).

Greig et al. (1989) presented for the first time how to find the global minimum of a certain energy function by applying the so-called graph cuts technique for a two-dimensional energy function. They proved that finding the minimum cost cut is equivalent to the maximum flow in a two-terminal graph. The Greig approach is the backbone of a number of efficient maximum flow algorithms recently developed like those presented by Boykov et al. (2001); Boykov & Kolmogorov (2004); Goldberg et al. (2011). In the literature, graph-based minimization problems are widespread in different vision applications like image segmentation (Ishikawa & Geiger, 1998; Veksler, 2000), camera stereo correspondence (Boykov et al., 1998; Kolmogorov & Zabin, 2004), shape reconstruction and object recognition.

4.2 Methodology

In this section, it will be justified that maximizing the posteriori probability in an MRF and minimizing the defined energy function are equivalent. Then, to minimize the energy function, the graph cuts technique will be introduced. Additionally, some basic notations and definitions of graph theory are provided. Subsequently, the most common search algorithms to solve the maximum flow (minimum cut) in the graph are

described. At the end, the Kohli and Torr method will be described which introduces a measure for the uncertainty in labels (Kohli & Torr, 2006). Definitions and notations presented in this chapter follow the contributions by Veksler (1999); Boykov & Jolly (2001) and their followings papers.

4.2.1 An overview of the mathematical concept

An MRF has been defined in several ways in different disciplines. In the image processing community, MRF properties are usually defined as follows:

$\mathcal{P} = \{1, 2, ..., m\}$: a set of sites p (pixels).

$\mathcal{N} = \{\mathcal{N}_p \mid p \in \mathcal{P}\}$: a neighbourhood system where $\mathcal{N}_p$ is a subset of the pixels in $\mathcal{P}$ located adjacent to the pixel p (Figure 4.2 is an example of a four-neighbour structure for pixel p). For a smoother result, one can think about a bigger system with 8 or 24 pixels.

$\mathcal{L} = \{l_1, l_2, ..., l_k\}$: the set of possible labels that can be assigned to a pixel. In this case, they are either water or land.

$F = \{F_p \mid p \in \mathcal{P}\}$: a field of the random variable which takes a value f_p depending on the possible label l.

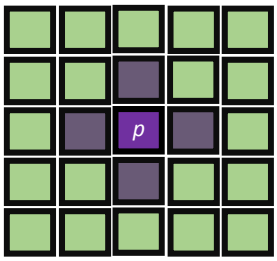

Figure 4.2: A four-neighbourhood system structure for the pixel p

A particular realization of the field is given by $f = \{f_p \mid p \in \mathcal{P}\}$. It is called a configuration of the field F. In order to be an MRF, all $f \in F$ must satisfy

$$\mathrm{P}(f) > 0 \tag{4.1}$$

$$\mathrm{P}(f_p \mid f_{\mathcal{P}-\{p\}}) = \mathrm{P}(f_p \mid f_{\mathcal{N}_p}), \tag{4.2}$$

where $\mathcal{P} - \{p\}$ denotes the set difference, $f_{\mathcal{N}_p}$ denotes all labels of subset $\mathcal{N}_p$. This condition indicates that a pixel label is only directly dependent on its neighbours. An MRF is usually specified by a joint distribution. The Hammersley-Clifford theorem

provides a convenient way to define an MRF (Besag, 1974) by proving that MRF and Gibbs random fields are equivalent. This theorem also states that the probability of a particular configuration is defined as:

$$\mathrm{P}(f) = \mathrm{Z}^{-1}\exp\left(-\sum_{c\in\mathrm{C}} V_c(f)\right), \tag{4.3}$$

where Z is the normalizing constant and C is the set of all cliques. A set of sites (pixels) is called a clique if every two separate pixels are adjacent. Here we just consider cliques of size two in a neighbouring system. $V_c(f)$ is called the clique potential function

$$V_c(f) = V_{\{p,q\}}(f_p, f_q), \tag{4.4}$$

where $V_{\{p,q\}}(f_p, f_q)$, the neighbour interaction function, measures the similarity of two neighbour pixels p and q in terms of their values. Now we are rewriting equation (4.3) which is an MRF with the joint distribution

$$\mathrm{P}(f) = \mathrm{Z}^{-1}\exp\left(-\sum_{\{p,q\}\in\mathcal{N}} V_{\{p,q\}}(f_p, f_q)\right). \tag{4.5}$$

The field F is not directly observable, but we can find a relationship between any realized configuration of the field f and an observation, for example d, via the likelihood function $\mathrm{P}(d \mid f)$. In most studies, this problem is solved using Bayes 's theorem. The posterior probability can be written as

$$\mathrm{P}(f \mid d) = \frac{\mathrm{P}(d \mid f)\mathrm{P}(f)}{\mathrm{P}(d)}. \tag{4.6}$$

The MAP solution estimates f^* (one of the possible realizations of the field) which maximizes the likelihood function

$$f^* = \arg\max_{f\in F} \mathrm{P}(d \mid f)\mathrm{P}(f). \tag{4.7}$$

To find the solution we need a model for $\mathrm{P}(d \mid f)$. If d_p is the pixel value for the pixel p then we assume that

$$\mathrm{P}(d_p \mid f) = \prod_{p\in\mathcal{P}} \mathrm{P}(d_p \mid f_p)\,. \tag{4.8}$$

When the noise is independent at each pixel then

$$\mathrm{P}(d_p \mid l) = C_p \exp(-D_p(l)) \;\;, l \in \mathcal{L}. \tag{4.9}$$

In this equation C_p is a normalizing constant and $D_p(l)$ is a non-negative function which reveals how much the assigned label l agrees with the pixel value p. So the likelihood function is equal to

$$\mathrm{P}(d \mid f) \propto \exp\left(-\sum_{p\in\mathcal{P}} D_p(f_p)\right) \tag{4.10}$$

now, by deriving $\mathrm{P}(d)$ and $\mathrm{P}(d \mid f)$ with the above assumption, we can rewrite the equation (4.7)

$$f^* = \arg\max_{f\in F} \exp\left(-\left(\sum_{p\in\mathcal{P}} D_p(f_p)) + \sum_{\{p,q\}\in\mathcal{N}} V_{\{p,q\}}(f_p, f_q)\right)\right). \tag{4.11}$$

To find f^*, we must maximize the equation (4.11) which is equivalent to minimizing the following equation

$$E(f) = \sum_{p\in\mathcal{P}} D_p(f_p) + \sum_{\{p,q\}\in\mathcal{N}} V_{\{p,q\}}(f_p, f_q) = E_{\text{data}}(f) \; + \; E_{\text{smooth}}(f). \tag{4.12}$$

This equation is the general energy function in the energy based optimization method in image processing. The first term of the equation, $D_p(f_p)$, is a function that just deals with the pixel value and its possible label. The second term, $V_{\{p,q\}}(f_p, f_q)$, is a function that measures the agreement between two adjacent pixels in terms of their value. For convenience we introduce a balancing term into equation (4.12)

$$E(f) = (1-\lambda)E_{\text{data}}(f) + \lambda E_{\text{smooth}}(f) \tag{4.13}$$

where

$$E_{\text{data}}(f) = \sum_{p\in\mathcal{P}} D_p(f_p)\ ,\ E_{\text{smooth}}(f) = \sum_{\{p,q\}\in\mathcal{N}} V_{\{p,q\}}(f_p, f_q)$$

The balancing term $\lambda \in [0,1]$ allows us to control the contribution of each term in the total energy function. If λ is small, the role of the neighbour interaction between pixels is not considered, so the final result just relies on the pixel intensities. On the other hand, if λ tends to 1, we ignore the contribution of pixel values in the process of segmentation and just rely on the structure of the pixels.

Now the aim is to find a labeling structure for the image which leads to minimizing the energy function $E(f)$. The method of graph cuts as a powerful optimization algorithm has been commonly used to solve this problem. The graph cuts technique is able to include piecewise smoothness since it considers sharp discontinuities in the image (Boykov & Veksler, 2006). In the next part, some concepts of a graph and then an overview of the graph cuts technique are briefly introduced.

4.2.2 Basics of graphs, graph cuts techniques and max-flow algorithms

Let $\mathcal{G} = \langle \mathcal{V}, \mathcal{E} \rangle$ be an undirected weighted graph where $\mathcal{V}$ is the set of vertices. In image processing applications, all pixels are vertices. Also we define two additional vertices called terminals: *source* and *sink*. The line that connects two adjacent vertices is called an edge ($\mathcal{E}$). Edges that connect a vertex to one of the terminals are called terminal link (t-link) and edges that connect two adjacent vertices are named neighbour link (n-link) (Figure 4.3).

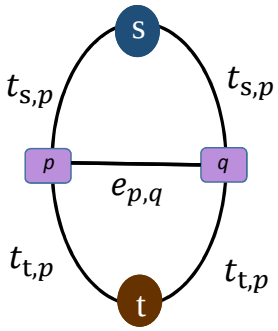

Figure 4.3: A graph with two pixels in one dimension. Here we have four vertices (two pixels; p and q, two terminals; s and t) and five edges (four t-links $t_{s,p}$, $t_{s,q}$, $t_{t,p}$, $t_{t,q}$ and one n-link $e_{p,q}$)

We introduced the functions D and V in the previous section to assign weights for the edges. For example, the t-link $t_{s,p}$ connects the pixel p and the terminal s, so its value must indicate how much the pixel value agrees with this label. The function $D_p(s)$ exactly measures this agreement. On the other hand the n-link $e_{p,q}$ must describe the likeness of p and q pixel values, expressed by the function $V_{p,q}(l_p, l_q)$.

Now to find the optimal configuration of the graph which minimizes the total energy function, the concept of *cut* is introduced. The properties of a *cut* are discussed by Boykov et al. (2001). A cut, $\mathcal{C}$, is a set of edges in the graph, which separates the graph into two discrete graphs so that every vertex connects to just one terminal in the new configuration of the graph. The cost of each cut is equal to the sum of the weights of all edges that are part of the cut. The goal of the min-cut solution is to find the cut with the lowest cost. For example in Figure 4.4, to define the label of pixels, the total cost of all possible cuts is assessed. Then the cut with the minimum cost will be selected and the labels for the pixels will be defined.

Most techniques to find the min-cut solution take advantage of the dual property in combinatorial optimization that the min-cut problem can be solved by finding the maximum flow from source to sink (Boykov & Kolmogorov, 2004). In this technique, edges in the graph are considered as water pipes with a capacity equal to the edge weights. By letting the maximum amount of water flow that can be sent from one terminal to the other, a set of edges are saturated. As a result, the primary graph will be divided

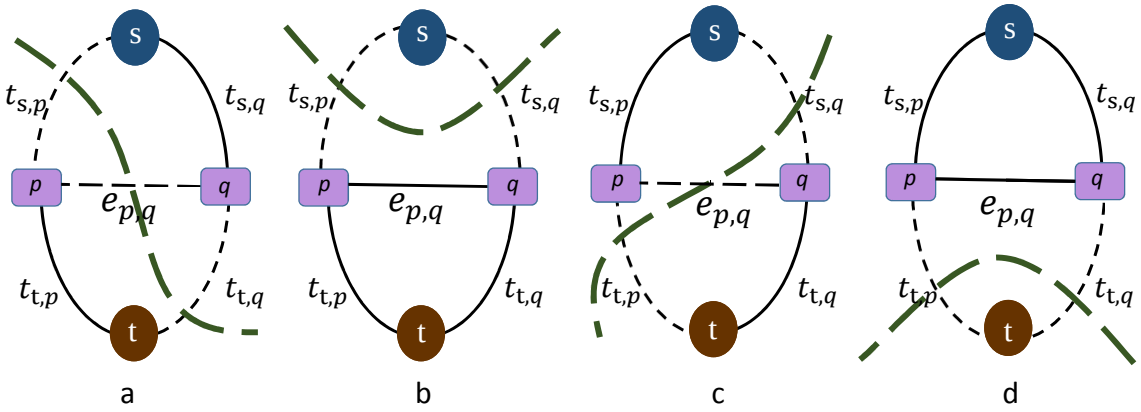

Figure 4.4: Four different cuts can be applied to a graph with 2 pixels. The cost of each cut is equal to the sum of the weight of the respective dashed lines. The scenario with the smallest weight will be selected and, regarding remaining edges in the graph, new labels for the pixels will be assigned.

into two separate graphs if the saturated edges are eliminated. In fact, the maximum flow value is equal to the cost of the minimum cut (Boykov & Kolmogorov, 2004).

Most of the algorithms for solving the min-cut or max-flow problem with two terminals are based on two general methods: Ford-Fulkerson style *augmenting paths* (Ford & Fulkerson, 1962) or Goldberg-Tarjan style *push-relabel* (Goldberg & Tarjan, 1988). Augmenting paths algorithms repeat the following steps until at least one of the edges in all possible paths between source and sink is saturated. First, in the initial phase, a residual graph identical to the original graph is defined. Also, before starting the iteration, the flow from source to sink is equal to zero. The iteration runs as follows:

- Find a valid route between source and sink.
- Push a water flow equal to the capacity of the path into the defined s-t path. This flow saturates at least one edge in the graph.
- Decrease the capacity of the path edges in the residual graph and increase the maximum flow regarding the previous step.

The iteration will be terminated if the algorithm cannot find an unsaturated path any more from source to sink in the residual graph. At this stage the flow is equal to the maximum capacity of the graph. Figure 4.5 is an example of a graph with nine vertices in the last iteration. After saturating the last s-t path, the final labels for the vertices are defined.

Push-relabel algorithms find the maximum flow using a completely different approach. Instead of pushing a feasible flow through the graph, the algorithm pushes the maximum possible flow from source to sink, called *preflow*. On its way, the preflow satisfies the capacity of passing edges and saturates them. This means that every

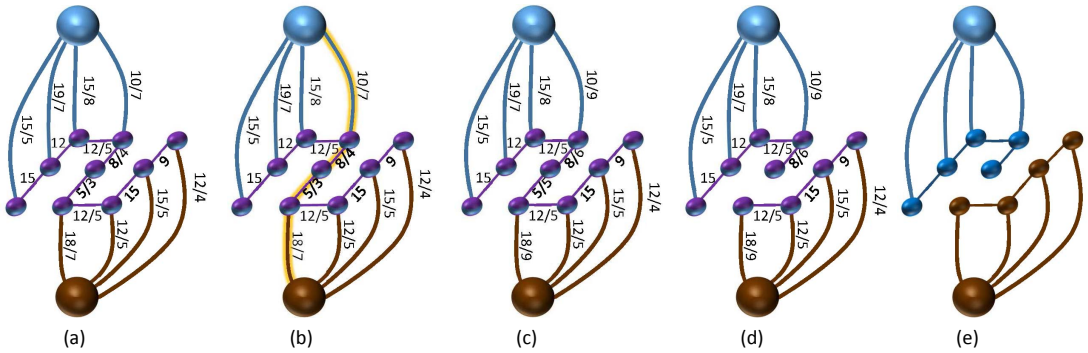

Figure 4.5: A simple scheme of an augmenting path procedure. (a) is a residual graph after a number of iterations. Here for each edge the capacity and the current flow is presented (capacity/current flow) and all the saturated edges are removed. In (b) another path from source to sink is found, in (c) a flow equal to the maximum capacity is pushed through the path and the residual graph is updated by eliminating the saturated edge. (d) is the final configuration of the residual graph because there is no connection between source and sink anymore. So, now based on the residual graph, the final labels structure for the pixels is defined

vertex has more incoming flow than outgoing flow. At the end the excess flow in all vertices is zero. At this point, the preflow turns to feasible flow.

In this study we apply Dinic's algorithm to find the maximum flow solution in the graphs. The Dinic algorithm is a powerful technique for computing the maximum flow in a network (graph) introduced by Dinits (1970). This algorithm is considered as an augmenting path technique. So the flow in the graph has been iteratively increasing until all the s-t paths are saturated. In this algorithm, the graph is organized into different layers in a way that the first layer contains all vertices which connect to one of the terminals. The remaining vertices are divided into subsequent layers according to their vicinity to the vertices which are located in the prior layers. Then all the paths with the shortest length are saturated by applying the breadth-first search (BFS). Given the vertex p in the graph $\mathcal{G}$, BFS partitions the vertices in the graph into different layers based on their distance from the pixel p. Therefore, only its direct neighbour pixels are located in the first layer and then all vertices at distance 2 are available in the second layer. The Dinic algorithm repeats the following steps until saturating all available s-t paths:

1. Find all paths from source to sink with length k in the residual graph applying BFS.
2. Augment the detected paths, update the residual graph, increasing the total flow.
3. Replace k with $k+1$

At the first step the total flow is equal to zero, and the assumed length of s-t shortest path (k) is also zero. Every iteration starts with a new BFS with increased length regarding the previous step. After augmenting all the possible paths between terminals, we define the label for each pixel by applying a depth-first search (DFS) in the final

residual graph. Finally, based on the assigned labels for the pixels, the modified water masks will be generated. DFS, which is a searching algorithm, helps us to define the path between a pixel and a terminal.

To generate a reliable water mask time series, apart from finding the most likely configuration of labels, providing additional information like marginal probability for each pixel assigning a certain label is essential. Measuring the uncertainty of the assigned labels plays a critical role in generating an accurate water mask, since the exact river area is not available in most cases.

4.2.3 Measuring uncertainty in the graph cuts solution

Unlike some inference algorithms like Loopy Belief Propagation, Generalized Belief Propagation, and Tree Re-weighted message passing, graph cuts technique suffers from a disadvantage. It does not provide any uncertainty measure associated with the determined labels for the pixels (Kohli & Torr, 2008). However, graph cuts is preferred over other algorithms and it has been extensively used for various computer vision problems that deal with computing the MAP solution (Kohli & Torr, 2006). The main reason is its ability to find a global solution in polynomial time. Even in problems where the availability of a global optimum solution is not guaranteed, graph cuts can find the most appropriate local minimum in the graph (Kohli & Torr, 2006; Boykov et al., 1998).

To overcome this deficiency, Kohli & Torr (2008) introduced a method to measure uncertainty in the graph cuts solution. Here we just provide a brief review of their method. Details and mathematical concepts are described in the contributions by Kohli & Torr (2008) and Tarlow & Adams (2012). The min-marginal energy function is defined as

$$\psi_p(l) = \min_{f \in \mathcal{F},\, l_p = l} E(f \mid l) \tag{4.14}$$

which is the result of a constrained minimization problem. To solve this problem, the pixel p is labelled as l and then the energy function E is minimized by tuning all other variable labels. In other words, a realization of the field, f, must be found in a way that minimizes the total energy function, E, considering the constraint that the pixel p has the label l. So $\psi_p(l)$ is the min-marginal energy of pixel p when its label is l.

To estimate the confidence measure for the MAP solution of the MRF, the max-marginal probability for each variable of the field must be calculated. For this purpose, the max-marginal probability function, $\mu_{p;l}$, is introduced as:

$$\mu_{p;\,l} = \max_{f \in \mathcal{F};\, l_p = l} \mathrm{P}(f \mid \mathcal{P}). \tag{4.15}$$

The max-marginal probability $\mu_{p;\,l}$ measures the maximum probability over all possible realizations of the field in which the label of the pixel p is considered as a constraint, $l_p = l$. Now we use the max-marginal probabilities to obtain a confidence measure for any labelled variable (pixel) (Kohli & Torr, 2008):

$$\sigma_{p;\,l} = \frac{\max_{f \in \mathcal{F};\, l_p = l} \mathrm{P}(f \mid \mathcal{P})}{\sum_{k \in \mathcal{L}} \max_{f \in \mathcal{F},\, l_p = k} \mathrm{P}(f \mid \mathcal{P})} = \frac{\mu_{p;\,l}}{\sum_{k \in \mathcal{L}} \mu_{p;\,k}}. \tag{4.16}$$

Since we are dealing with a binary segmentation problem, just two different labels are available i.e. water (W) and land (L). Therefore the confidence measures for these two labels are defined as:

$$\sigma_{p;\,W} = \frac{\mu_{p;\,W}}{\mu_{p;\,W} + \mu_{p;\,L}}\,,\ \sigma_{p;\,L} = \frac{\mu_{p;\,L}}{\mu_{p;\,W} + \mu_{p;\,L}}. \tag{4.17}$$

The relationship between max-marginal probability and min-marginal energy for any pixel p is described in Kohli & Torr (2006)

$$\mu_{p;\,l} = \frac{1}{Z} \exp(-\psi_p(l)), \tag{4.18}$$

in which Z is the partition function. Thus we are able to reshape equation (4.17) using min-marginal energies

$$\sigma_{p;\,W} = \frac{\exp(-\psi_p(W))}{\exp(-\psi_p(W)) + \exp(-\psi_p(L))} \tag{4.19}$$

$$\sigma_{p;\,L} = \frac{\exp(-\psi_p(L))}{\exp(-\psi_p(W)) + \exp(-\psi_p(L))} \tag{4.20}$$

Since the partition function (Z) is cancelled in the mentioned equations, the confidence measures can be obtained by calculating only the min-marginal energies.

In the max-flow problem, min-marginal energy for any pixel is equal to the sum of the maximum flow and the pixel flow potential in the final residual graph ($\mathcal{G}(f^*)$) (Kohli & Torr, 2008).

The maximum flow is the sum of the total flow passed from source to sink leading to saturating some edges, and disconnecting all available paths between two terminals. The flow potential is defined separately for each node in the final residual graph. Let us assume that label W (water) is assigned to the pixel p by the graph cuts solution. This means that in the residual graph, p connects to the terminal *water* directly with an t-link or via its adjacent pixels through an n-link. On the other hand, there is no connection between the pixel p and the other terminal *land*.

Since f^* represents the MAP solution for the graph, the flow potential for the pixel p related to the land terminal is zero ($C_{L,p} = 0$). Now, to define the flow potential for

p related to its defined label (W), we add an t-link between p and land terminal with infinite weight ($t_{L,\mathrm{p}} = \infty$). By adding this imaginary edge, the connection between source and sink is established again. After augmenting all possible s-t paths because of the new t-link, the flow-potential for the pixel p is equal to the sum of the flow capacity of all new paths. This procedure is described visually in Figure 4.6.

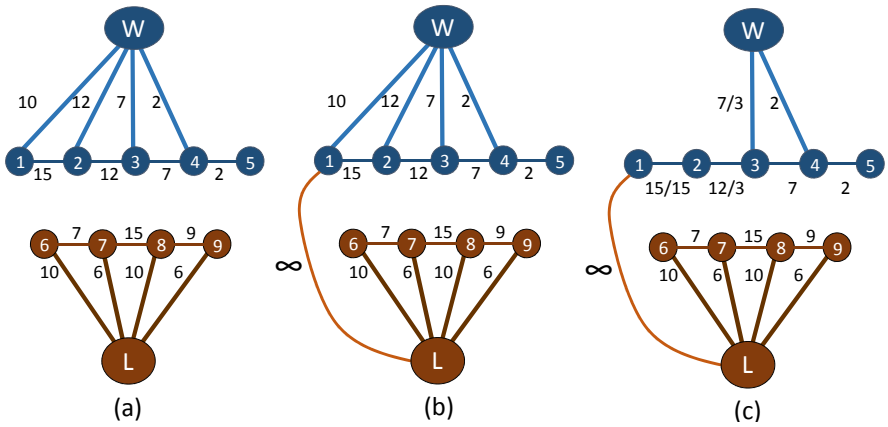

Figure 4.6: (a) representation of the final residual graph of Figure 4.5. (b) to measure the flow potential for the pixel 1, we assume that an t-link with an infinite capacity is available between pixel 1 and the land terminal. Now the connection between two terminals is established and the process of finding and augmenting new s-t paths starts again. (c) after augmenting all the new paths, the flow potential for the pixel 1 assigned the label water ($C_{W,1}$) is equal to the sum of the capacity of new paths ($C_{W,1}$=25). On the other hand, $C_{L,1}$=0 because pixel 1 does not connect to the other terminal in the residual graph.

By measuring the min-marginal energy and max-marginal probability for all pixels — apart from a binary water-land mask— a probabilistic water mask can be generated as a grayscale image to illustrate the confidence measure for the assigned label.

4.2.4 Implementation of energy functions

Carefully defining the components of equation (4.13) as well as selecting an appropriate optimization algorithm for finding the max-flow solution is critical. This equation includes two weight functions (pixel value and neighboring interaction) and one constant λ. If the weight functions are specified properly, all s-t paths will be found and saturated in a few iterations, because only a small amount of pixels located around the river shoreline are involved in the process.

In general, there is no restriction for defining the D_p function (Veksler, 1999). But Kolmogorov & Zabin (2004) state that in a binary labelling problem, satisfying the following condition

$$V_{p,q}(0,0) + V_{p,q}(1,1) \geq V_{p,q}(1,0) + V_{p,q}(0,1) \tag{4.21}$$

is necessary and sufficient for defining the function $V_{p,q}(f_p, f_q)$. This property is called *regularity* and plays a critical role in defining the graph. This condition states that in

a graph, the cost of cutting an n-link between two vertices must be larger when two vertices have the same label compared with the situation when they have different labels.

In the max-flow problem, we consider edges as a network of pipes. The assigned weight for an edge is equivalent to the capacity of the pipe. As described before, $D_p(f_p)$ measures the agreement between the value of pixel p and label f. The function $D(.)$ must assign a large weight to the corresponding t-link if the pixel value indicates the characteristics of the label. For example in our study if a pixel (like a) has a very small value in the infrared band, then the weight of $t_{W,a}$ (the t-link that connects a to the label water) must be significantly larger than $t_{L,a}$ (the t-link connects a to the label land). Since we deal with a long time series of images, every pixel has a long-term behaviour in terms of pixel value variation. Therefore considering the temporal statistic of each pixel by generating a water coverage frequency map can improve the accuracy of the final river masks significantly. At the beginning of the procedure, the water coverage frequency map is generated using initial river masks generated by applying a k-means clustering to the images. Now we define the $D_p(f_p)$ for a standard binary labelling problem:

$$D_p(f_p) = \begin{cases} D_p(L) \propto \mathrm{P}\left(L \middle| I_p\right) \times \mathrm{P}(L) \\ D_p(W) \propto \mathrm{P}\left(W \middle| I_p\right) \times \mathrm{P}(W) \end{cases} \tag{4.22}$$

The t-link is calculated by multiplying the probability of assigning a label within the pixel value (I_p) to the probability of assigning the label considering the long-term behaviour of the pixel. First we introduce two models for the conditional probabilities in equation (4.22).

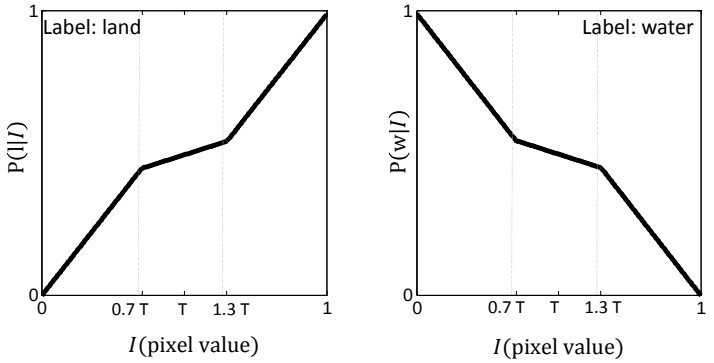

Figure 4.7: Models for defining the conditional probabilities in equation 4.22. T is the threshold value for separating water and land in the initial water mask.

Within these models we measure the possibility of assigning a label to a pixel depending on its pixel value. The middle parts of both models have a milder slope than at each end. Therefore pixels located in the critical regions near the river border can participate in the augmenting path process more efficiently.

$P(L)$ and $P(W)$ measure the probability of assigning the labels depending on their temporal behaviour. To do this, we define separate models for each label.

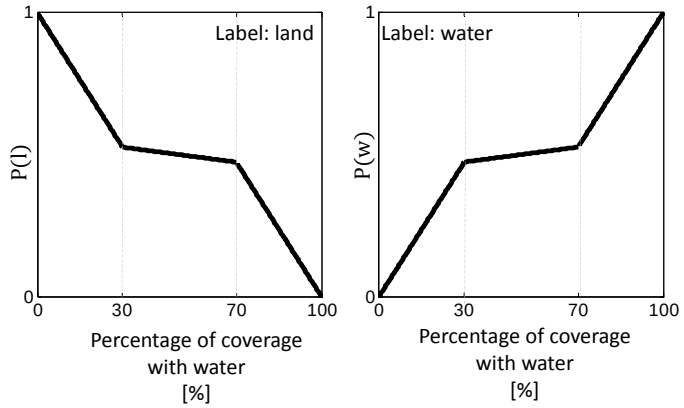

Figure 4.8: Two functions introduced for assessing the temporal behaviour of the pixels

According to the model developed for the water label in Figure 4.8, if a pixel is covered by water in most epochs, then the probability of covering by water for that pixel is high. Here the models also have a milder slope in the middle part.

The second part of equation (4.13) measures the interaction between neighboring pixels. Here we introduce $V_{p,q}(f_p, f_q)$, which measures the cost of assigning the same label to two adjacent pixels. In general, $V_{p,q}(f_p, f_q)$ devotes a small weight to an edge connecting two pixels with a big difference in their pixel values. On the other hand, the weight assigned to the connecting edge between two pixels with a similar value is large. For defining this function first we need to investigate about the spatial patterns available in the image. Apart from small pixel value variations in the middle of the river reach and also in the dry part of the image, a clear discontinuity in the pixel values is available in the water-land boundary (Figure 4.9). The goal of the algorithm is to detect the border between water and land, so it is assumed that the pixel values follow the piecewise smooth prior model. Figure 4.9 is an example of this type of pattern.

0.70	0.60	0.70	0.55
0.60	0.55	0.60	0.60
0.40	0.40	0.70	0.55
0.25	0.25	0.35	0.30
0.30	0.35	0.30	0.25
0.20	0.30	0.35	0.20

Figure 4.9: Example of pixel values near the water-land boundary. This pattern is considered as a piecewise smooth prior

Since the problem categorizes as a piecewise smooth prior, n-links must be defined so they can handle the discontinuities in the image by setting appropriate weights for the

boundaries. To this end, w_{pq} is introduced as a function of pixel values connecting via an n-link

$$w_{pq} = \frac{(I_p - I_q)^2}{2\sigma^2}, \tag{4.23}$$

in which I_p and I_q are the pixel values and σ^2 is the variance of pixel values over the whole image. Next, we define the cost of the neighboring interaction between two adjacent pixels:

$$V_{p,q}(f_p, f_q) \propto \exp(-w_{pq}) \times \mathrm{P(Q)} \tag{4.24}$$

For modifying the function we consider the temporal behaviour of a pair of pixels connected via an n-link. Therefore we introduce an event like Q, in which two pixels have the same label. To measure the probability of this event, P(Q), we use the models introduced in Figure 4.8.

We notice that the $V_{p,q}(f_p, f_q)$ function assigns a large weight for an n-link connected two pixels with almost the same pixel value and temporal behavior. However, it assigns a small weight to adjacent pixels with a significant difference in their pixel intensities. The function also defines in a way that the weight never vanishes even if the difference between two pixel values is huge.

4.2.5 Review of proposed method

The procedure of generating water area time series is presented in Figure 4.10. The algorithm starts with expelling images which are covered with clouds. They not only impose wrong river reach area estimations but also spoil the area estimation in other epochs since the temporal behaviour contributes to the weight functions. Apart from visual interpretation, an automatic algorithm to detect clouds precisely in optical images–especially in a single spectral band–is difficult to achieve. We apply two filters for detecting cloud-free images. First, we assume that consecutive images nearly look alike because the time interval between them is relatively short (8 days). So the cloud cover is the likeliest reason for significantly reduced correlation between two consecutive images. For the second filter, we take advantage of the fact that the observed value for clouds in the near infrared band is almost constant. So the variance of the pixel values in an image would be small if clouds cover the majority part of it. The sensitivity of these two filters is adjustable based on the situation. For example, by reducing the sensitivity, images with a partial cloud coverage could be accepted.

To construct the graph, we should assign weights to the graph edges using the introduced weight functions. The primary input for calculating the n-links is pixel values of the cloud-free images. But for calculating t-links, we also need initial water masks.

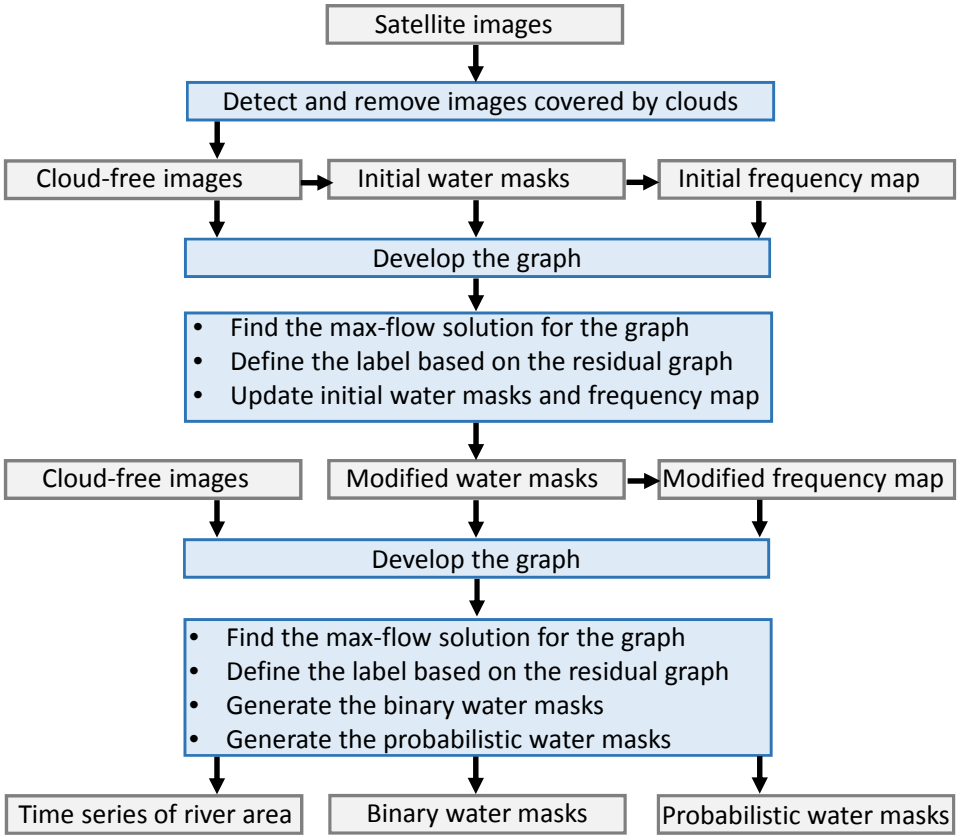

Figure 4.10: Flowchart of the proposed method

The third requirement for developing the graph edges is the initial water coverage frequency map. At the beginning this map is generated using the initial water masks, but it will be updated after every iteration.

After calculating all edges in the graph, now we search for the optimal pixel label structure by finding the max-flow solution in the graph. To generate more accurate water masks, we repeat the river reach area extraction process. In the second round, however, the initial water masks are replaced with the river masks generated in the first iteration. The frequency map is also updated with the modified water masks.

The final product in every measurement epoch is a binary water-land map, so any further information about the uncertainty in the assigned labels is not provided. Therefore, apart from visual comparison with the original images, an evaluation of the water masks quality is not possible. For further assessment, we generate the confidence measure map for each water mask by calculating the max-marginal probabilities applying the Kohli method to the residual graphs. To do this, the maximum flow for each graph is measured during the max-flow procedure. Then, the min-marginal energy is calculated for each pixel based on the final residual graph. By knowing these two variables, we are now able to measure the labels'uncertainty. The final products of the proposed method include the binary and probabilistic water masks and river area time series.

4.3 Results and validation

In this section, we describe the procedure for the first case study (Niger River, Lokoja station) in detail in order to provide insight into the proposed method.

4.3.1 Niger River, Lokoja station

Figure 4.11 shows five images of the Niger River at different months in the year 2000. The epochs are indicated on the time series of in situ river discharge (Figure 4.11 top).

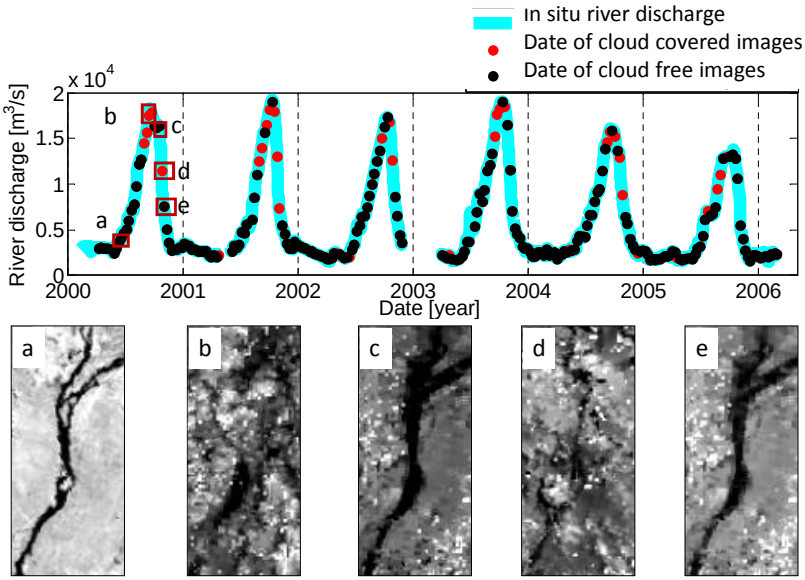

Figure 4.11: (a-e) the cloud detection filters accept images (a, c, e), and remove images (b, d). Images

This figure shows that cloud coverage occurs more often in the wet season. Hence, eliminating cloud-covered images may lead to undersampling of the wet seasons.

Graph edges are defined according to the weight functions defined in section 4.2.4, for which we need an initial water mask. In order to define an initial water mask, we apply k-means clustering. We consider the long-term behaviour of the water bodies in weight functions by defining two probabilities ($P(W)$, $P(L)$) according to the water coverage frequency map. The temporal behaviour for each pixel is estimated by dividing the sum of all binary water masks by the total number of samples.

In Figure 4.12 dark brown pixels represent the area which is always dry, and blue ones indicate the area always covered by water. The critical region can be defined between 30% and 70%, which is predominantly located along the river shorelines. By looking at the time series of initial water masks over these regions, we recognize an annual behaviour switching between the water and land label. This means that the k-means

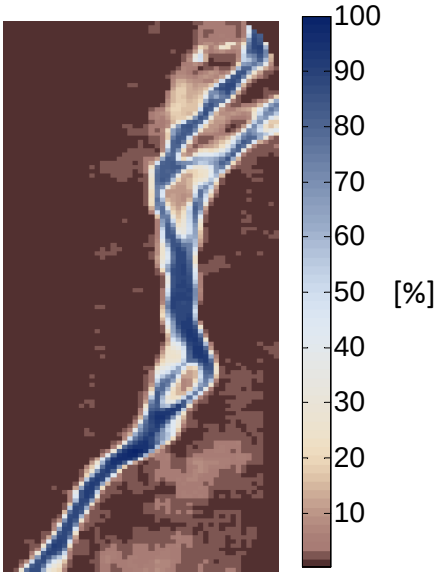

Figure 4.12: Water coverage frequency map for the Niger River reach near Lokoja station.

clustering classifies them as part of the river during the wet season, and as land for the dry season.

After assigning weights to the graph edges, the max-flow solution in the graph can be sought. This step starts with repeatedly augmenting the shortest s-t paths until two terminals become completely disconnected from each other. Then regarding the residual graph, the modified water mask is defined. To discuss the performance of the method, we compare four final water masks with the initial ones for the selected river reach (Figure 4.13).

Figure 4.13(a1) relates to the dry season, in which no cloud appears in the image, and the surrounding area is dry. As a result, the river borders are clearly distinctive. By comparing the graph cuts solution (Figure 4.13(c1)) with the initial water mask (Figure 4.13(b1)) and the original image, we find that our proposed method can accurately determine the river extent, although the improvement is small. In Figure 4.13(a2), the river area increases due to the increment of the water stream, and we see that adjacent areas are also wet. As a consequence, the initial water mask (Figure 4.13(b2)) is not accurate, as some land pixels are labelled as water. However, the graph cuts method is able to overcome this situation to a large extent and improve the final water mask (Figure 4.13(c2)). Our algorithm is even able to remove most of the isolated pixels which are wrongly labelled as water in the initial water mask.

In Figure 4.13(a3), the land around the river border in the bottom of the river is wet and the upper part of the river is also covered by cloud. The graph cuts method extracts the river extent from the surrounding wet area, and it can recover the cloudy part of the river (Figure 4.13(c3)). The last example reveals the ability of the method to ignore clouds and determine the water mask as accurately as possible (Figure 4.13(c4)).

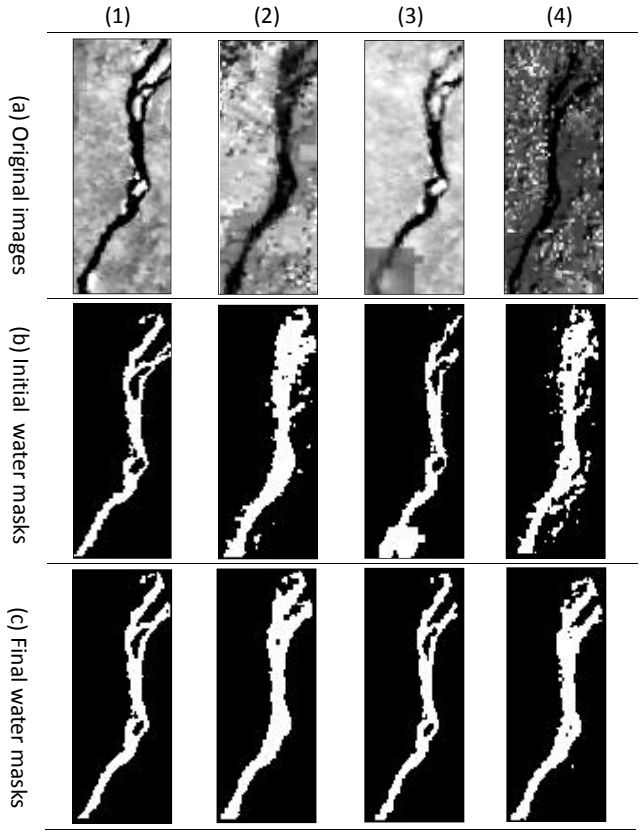

Figure 4.13: Four examples of generated water masks in different situations. (a) original images; (b) initial water masks; (c) final water masks; (1, 2) relate to the dry and wet seasons. (3, 4) images suffer from cloud contamination.

These results indicate that the weight functions for defining graph edges are properly defined.

Next, we measure the marginal probability for each pixel in the water mask applying the Kohli method to the residual graph. To do this, after measuring the maximum flow passed through the graph, min-marginal energies are calculated for each pixel. By knowing these two variables now we are able to measure the label's uncertainty.

Figure 4.14 presents an example of probabilistic water and land masks, in which marginal probabilities of land and water are provided. In the probabilistic water masks (Figure 4.14(c, e)), pixels which are located in the middle part of the river reach have a water label with high accuracy since their probabilities are higher than 80%. The level of confidence decreases gradually when the pixels are located closer to the river shoreline. For example in most of the pixels around shorelines, the label correctness probabilities are less than 20%. The probabilistic land masks (Figure 4.14(d, f)) represent the same pattern. It can be seen that pixels located far from the river have land labels with a high probability. However, this confidence measure decreases closer to the river border.

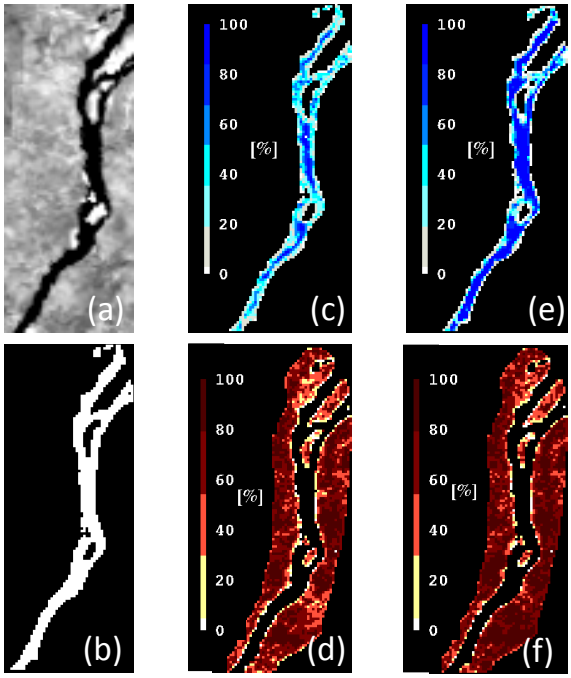

Figure 4.14: (a) original image (date: 21.09.2000), (b) modified water mask from proposed method; (c, d) are water and land marginal probability maps in the first iteration; (e, f) after the second iteration.

Comparing the probabilistic water and land masks of the first and second iterations, we observe that the number of pixels with a high marginal probability value have improved. Replacing the water coverage frequency map with a more accurate one in the second iteration is the main reason for this improvement. Figure 4.15 presents the histogram of the image and also the probabilistic water and land masks.

Figure 4.15 presents statistics of the maps in Figure 4.14. The histogram of pixel values is presented in Figure 4.15(a). The columns are coded by blue and brown colors. The separation of labels is defined by k-means clustering in the initial water mask. The shape of the histogram describes why pixel-based classification algorithms cannot perform efficiently in the river extent extraction problem:

- a large difference between the amount of pixels in each class,
- no clear distinction between each class distribution.

Figure 4.15(b) shows the confidence measure for water and land masks derived in the first iteration. Columns in blue on the left side present the confidence level of the pixels in the water mask, those in brown on the right side are part of the land mask. Although the water coverage frequency map is not so accurate in the first iteration, a significant amount of pixels in both masks accumulate at both ends. In the second iteration (Figure 4.15(c)) most of the pixels gather in the last columns because they have high marginal probabilities.

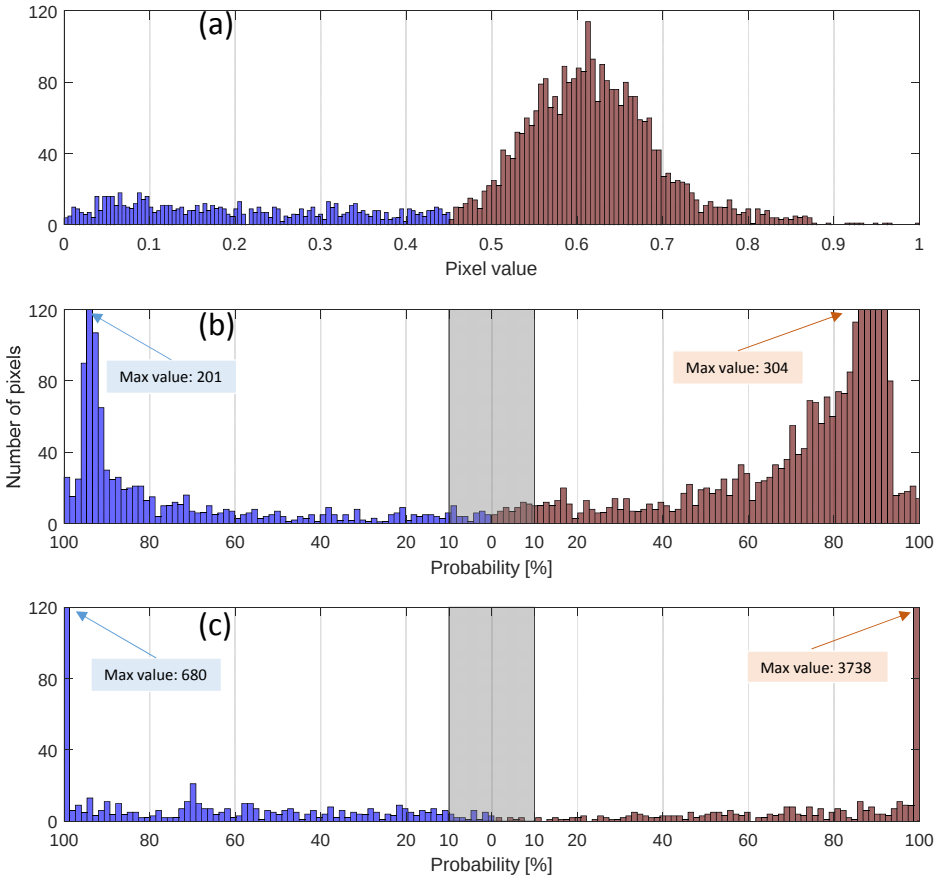

Figure 4.15: Pixel value histogram of the image in Figure 4.14 is presented in (a), water and land separated by different color. Histogram of the water and land probabilistic masks in the first iteration (b) and the second iteration (c).

Figure 4.16 shows the time series of label probabilities for the water masks of both iterations, in which the improvement after the second iteration is clearly visible. In fact, by replacing the initial water masks with the modified ones in the second iteration, only a small number of pixels have a low marginal probability in the final product.

In order to generate a reliable water area time series, we estimate river reach area together with its uncertainty. We accept the assigned labels for pixels with marginal probabilities higher than 10% in both water and land masks. This leaves a third region which contains pixels with marginal probabilities less than 10% in both masks. This is the uncertain region (the gray area in both Figure 4.16(b, c)), for which we cannot define a proper label based on the available information. It is clear that the area of this region correlates with the image pixel size. In other words if we used Landsat image with a pixel size of 30 m $\times$ 30 m, the area of this region would be much smaller.

Figure 4.17 represents the time series of the three different regions. Pixels labelled as water with a higher than 10% confidence level are presented in blue. Pixels in the land

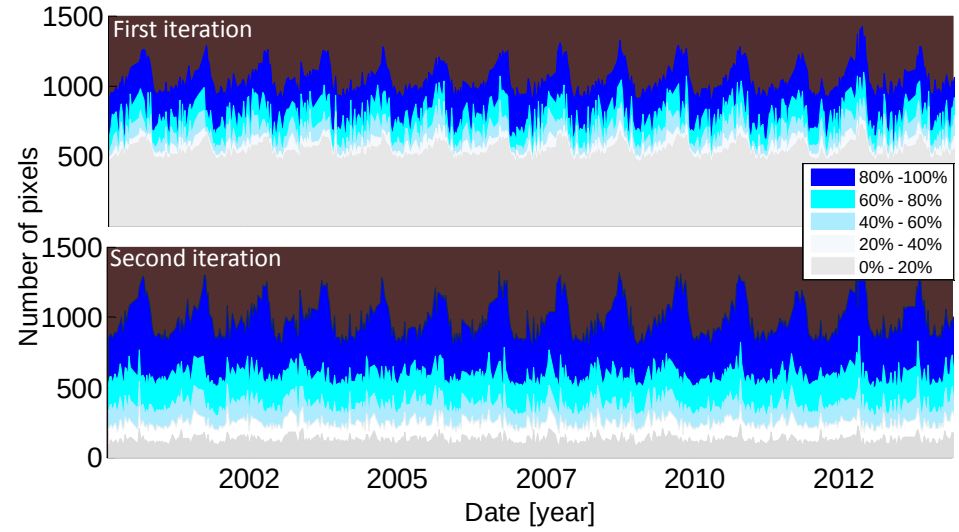

Figure 4.16: Time series of water masks marginal probabilities for the first and second iterations. Monitoring period: 02.2000–09.2014

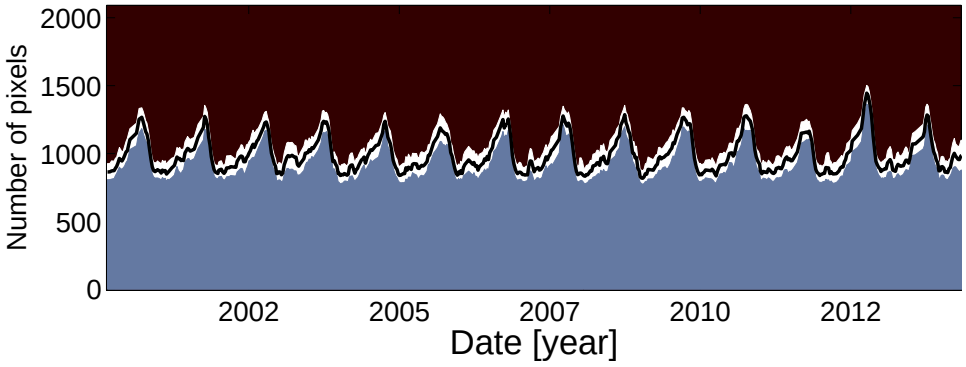

Figure 4.17: Water and land pixels present in blue and dark brown, respectively. The number of pixels with less than 10% marginal probability are shown in white. The black line represents the MAP solution in the graph. Monitoring period: 02.2000–09.2014

masks with a confidence measure higher than 10% appear in brown. Pixels with less than 10% marginal probability in either mask are in white.

We calculate the area of the river reach by multiplying the number of pixels in the water mask by the area of a pixel (625 m^2). We consider the area of the uncertain region as the uncertainty of the water area measurement. Figure 4.18(a) shows the result of our method for Niger River reach near Lokoja station. The river reach has an obvious annual behaviour, associated with annual variability of precipitation. The blue dots in the time series represent the satellite observations. During the wet season, a number of images were removed due to cloud contamination. Therefore, the sampling is denser during the dry season.

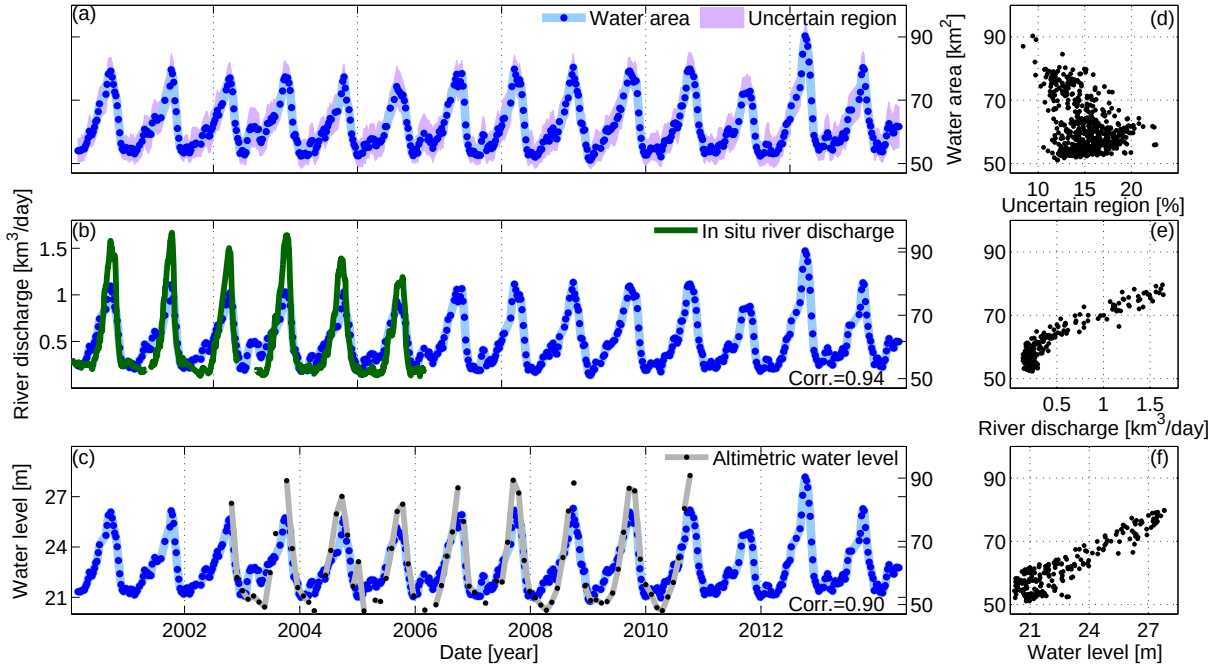

Figure 4.18: (a) Water area with its uncertainty. (d) Scatter plot of water area vs. percentage of uncertainty. (b, c) Water area is plotted with in situ discharge and altimetric water level. (e, f) Scatter plots of simultaneous water area measurements against discharge and water level. Period of monitoring: 02.2000–09.2014

We analyse the uncertainty of river reach area estimations to understand the error behaviour. Figure 4.18(d) is a scatter plot of water area measurements vs. uncertainties. It shows that the uncertainty varies between 9% and 22%, with an average uncertainty being around 15% of the area. Figure 4.18(d) shows that our algorithm estimates the water area more accurately during the wet season (when the river reach area is larger) than during the dry season. In the dry season, when the river becomes narrower, the middle part of the river just includes a few pixels. So the remaining pixels in the river mask are adjacent to the dry area and have a small marginal probability. However, sometimes even during the dry season, we obtain relatively low uncertainty due to the shape of the river reach.

The Kohli technique provides just an internal criterion for validating the pixel labels. In order to assess the correctness of our river area estimation, results are compared with in situ river discharge and with altimetric water level measurements.

The high correlation (0.94) between the two time series in Figure 4.18(b) indicates a high consistency between the behaviour of river reach area and river discharge. The discharge-area scatter plot (Figure 4.18(c)) shows a non-linear relationship, although partially in the low-discharge regime. As expected, the area estimates during the wet season are more accurate than the dry season. In the bottom-left side of the plot, we

see an irregular behaviour, due to the weak performance of the algorithm or poor discharge measurements during the dry season.

Further, we validate river reach area measurements against altimetric water level, since there is a 9 year (2002–2011) overlap in river reach water level and area measurements (Figure 4.18(c)). Similar to the validation against discharge, water level and water area measurements are highly correlated (0.90). The scatter plot represents such a high correlation between river reach water area and height (Figure 4.18(f)). Like previous plots, in the wet season, the scatter of points is narrow, which indicates that both water level and area are measured accurately.

4.3.2 Niger River, Koulikoro station

We have employed our algorithm over another part of the Niger River with a different morphological character near Koulikoro station. In this case, we selected a long river reach of about 115 km, which has a calmer stream flow than the first example. Figure 4.19 shows two examples of river masks. In the dry season (Figure 4.19(1)), the average river width is less than 0.5 km, which is a challenge for our method because of the 250 m MODIS pixel size. Despite this limitation, the algorithm successfully retrieves the river extent, as it takes advantage of all possible sources of information. Figure 4.19(2) is taken during the wet season, when the river width is wide enough to be precisely determined by the algorithm. Here, also due to a clear distinction between river borders and the surrounding area, the river reach mask is extracted more accurately.

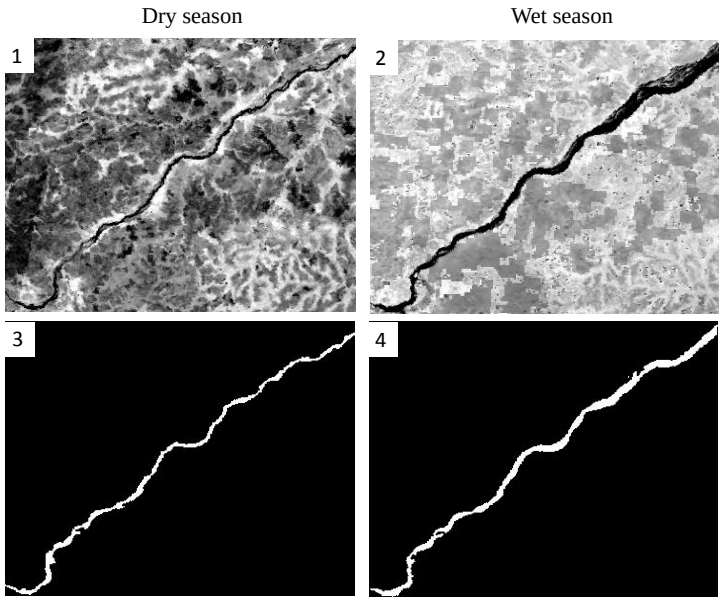

Figure 4.19: Subfigures (1, 2) are two examples of the river reach (Niger River, Koulikoro Station) in dry and wet seasons. Subfigures (3, 4) are the river reach masks derived by the proposed algorithm

In the time series of river reach area, we see a clear annual behaviour during the monitoring period (Figure 4.20(a)). The magnitude of the uncertain region in the dry season is much larger than in the wet season. The scatter plot of water area and percentage of uncertainty (Figure 4.20(d)) shows a clear non-linear relation between them. In the wet season the relative uncertainty is less than 10%. With decreasing water area the number of pixels with a high marginal probability also decreases. As a result, the uncertainty ratio increases up to 25% in the dry season

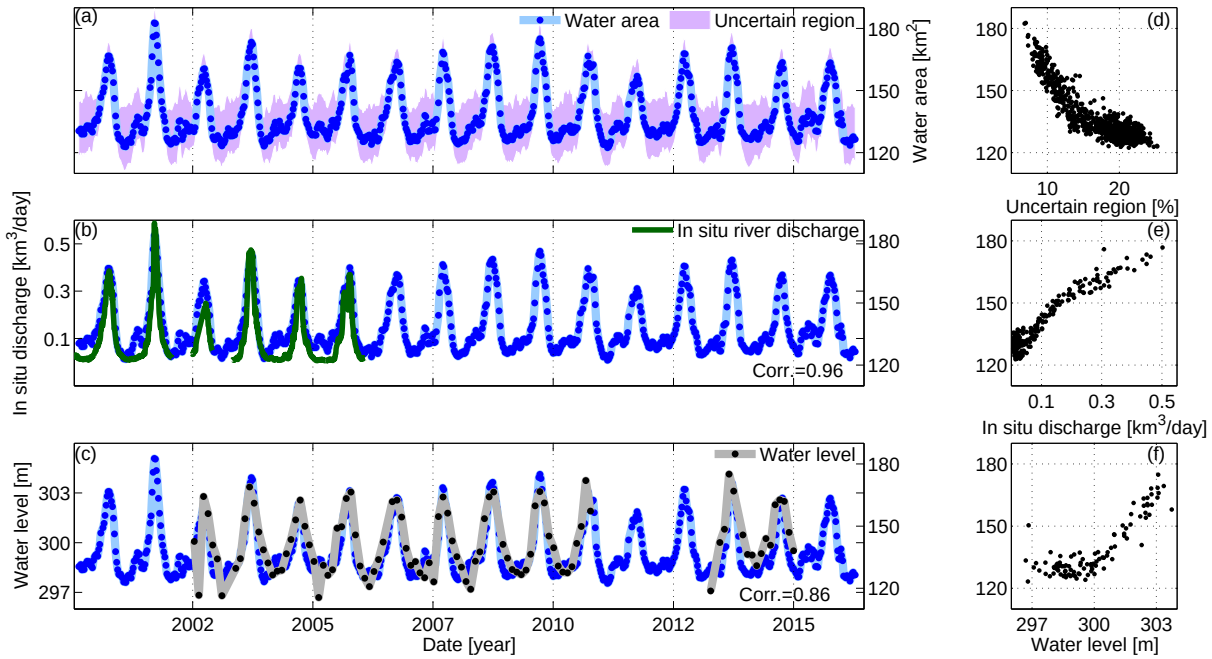

Figure 4.20: (a) Water area vs. uncertainty. (d) Scatter plot of water area vs. percentage of uncertainty. (b, c) Water area vs in situ discharge and altimetric water level. (e, f) Scatter plots of simultaneous water area measurements against discharge and water level. Period of monitoring: 02.2000–02.2016

Like the previous example, we compare daily in situ discharge with river reach area measurements during the years 2000–2006, which are correlated with a correlation coefficient of 0.95 (Figure 4.20(b)). As we expect, water area estimation is less accurate in the dry season because in spite of a constant river discharge, river reach area measurements show small variations. On the other hand, in the wet season, the algorithm can extract the river extent more accurately due to larger water area. Figure 4.20(e) shows the scatter plot of simultaneous discharge and river reach area measurements. The non-linear relationship between them is evident in this plot. The wide scatter where the river discharge is less than 0.1 $\frac{km^3}{day}$ indicates the limitation of the method to estimate the correct water area in the dry season. The coarse pixel size of the MODIS images is the main reason for this problem.

Finally, we compare the river area with the altimetric water level time series (Figure 4.20(c)). We see that due to the orbit configurations of both ENVISAT and Saral/AltiKa missions, they are not able to measure water level as frequently as water area measured

by MODIS. On average, for water area time series we have 48 values in a year, but at best only 11 water level observations are available. This highlights an advantage of imagery for monitoring the dynamic of river reaches.

In the end, a scatter plot of simultaneous altimetric water level and area measurements is presented in Figure 4.20(e). The correlation of 0.86 is not as high as the previous case because satellite altimetry fails to properly estimate the water level during the dry season. The vast cloud of points in the water area-level scatter plot demonstrates the fact that both time series do not accurately represent river reach water level and area, when the river flows in a narrow channel (Figure 4.20(f)).

4.3.3 Congo River, Malebo Pool

A part of the Congo River near Kinshasa is selected as the third case study. This case has an entirely different hydrologic character and morphology from the previous examples. Upon leaving the Maloukou, the Congo River divides into two branches that forms a vast lacustrine area about 24 by 27 km, geographically known as Malebo Pool. After flowing about 24 km they join and pass through Brazzaville city. The amount of water flowing in this river reach is several times higher than the previous examples. The middle part of the river contains a complex braided system including a number of islands and narrow branches. Due to the complexity of the river system, the area monitoring is a challenging task. Figure 4.21 shows two examples from wet and dry seasons.

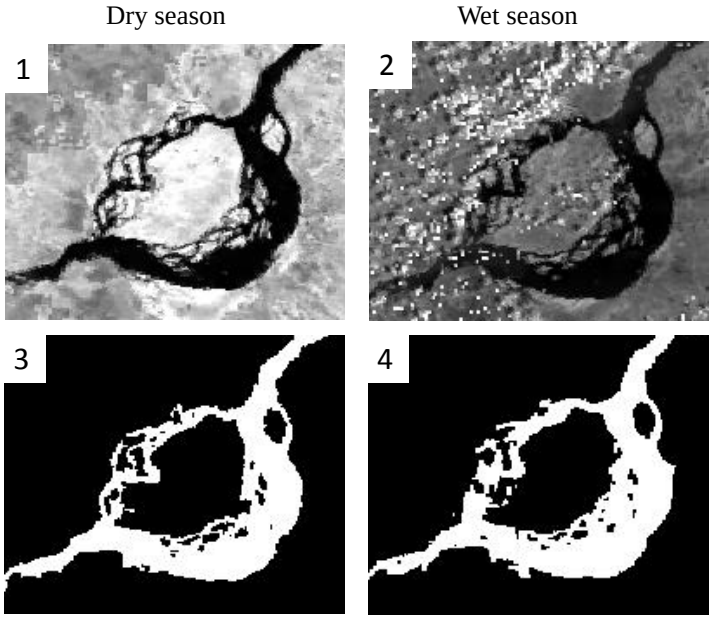

Figure 4.21: (1, 2) are two examples of the river section (Congo River, Malebo Pool) in dry and wet seasons. (3, 4) are the water masks determined by the proposed method.

The river section is clearly visible in most epochs during the dry season (Figure 4.21(1)). But in the wet season, the majority of images are partially covered by clouds e.g. (Figure 4.21(2)). However, the algorithm overcomes this obstacle to a large extent by considering the temporal behaviour of pixels. Therefore the cloud covered pixels in the upper part of Figure 4.21(2) have not been labelled as water in the river mask (Figure 4.21(4)). Figure 4.21(3) is the water mask generated out of image in Figure 4.21(1). The middle part of the Malebo Pool indeed provides a challenge for the graph cuts procedure to find the true labels for the pixels. By comparing the original image and the water mask, we find that some of the tributaries in the braided system are not well classified by the algorithm. The reasons are: (1) complexity of the braided system and (2) the spatial resolution of MODIS images. During the wet season the surface water area of side arms of Malebo Pool does not increase significantly (Figure 4.21(4)) and only the middle braided streams of the river become wider.

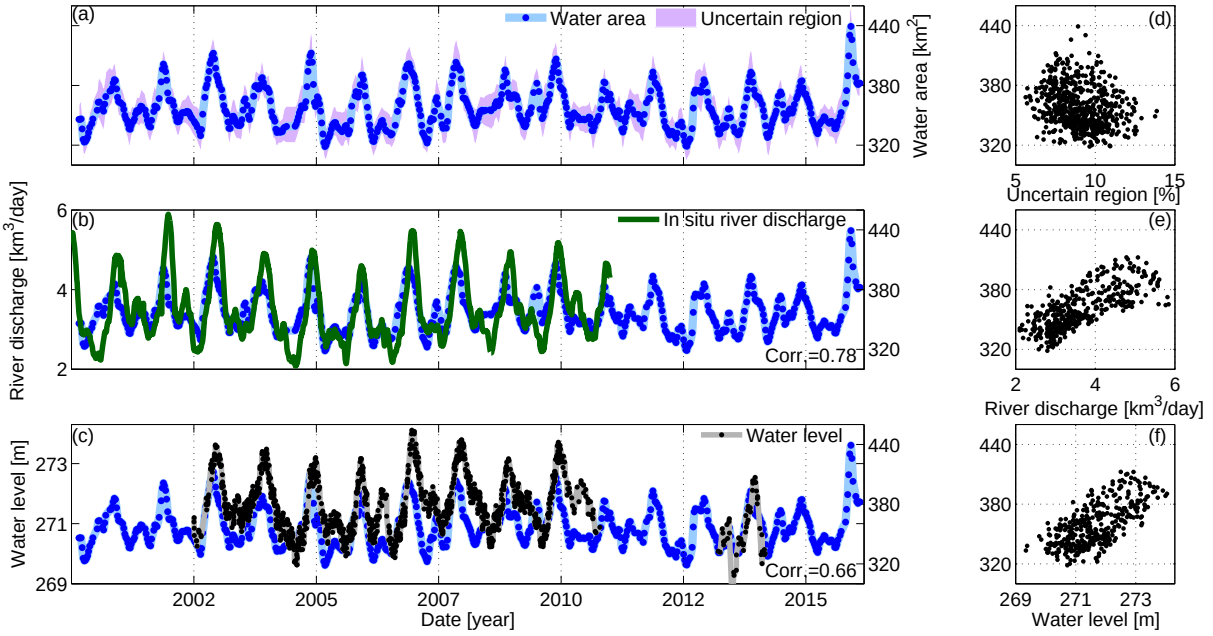

Figure 4.22: (a) Water area monitoring together with the uncertainty. (d) Scatter plot of water area vs. percentage of uncertainty. (b, c) Water area is plotted with in situ discharge and altimetric water level. (e, f) Scatter plots of simultaneous water area measurements against discharge and water level. Period of monitoring: 02.2000–02.2016

Unlike the previous cases, the river area does not change drastically here (Figure 4.22(a)). The variations of the river reach area and the uncertainty percentage is presented in the scatter plot (Figure 4.22(d)). The behaviour of these two parameters is uncorrelated, since the river reach area of the braided river system is much larger than the MODIS pixel size.

Water area and in situ discharge are compared in Figure 4.22(b). In this case, daily river discharge is available for ten years (2000–2010). This part of the river passes through urban areas and the river shoreline is restricted in Brazzaville city. Therefore

the river does not behave naturally in this reach. As a result the correlation (0.78) is not as high as previous cases. The scatter plot of simultaneous river discharge and each area measurements is plotted in Figure 4.22(e). However, it is hard to recognize such a linear relationship because the scatter plot is too noisy. In the wet season the scatter is wider because of a phase shift in the area and discharge measurements.

Finally, we validate the water area measurements against densified altimetric water level time series (Figure 4.22(c)). The densification algorithm for satellite altimetry measurements is developed by Tourian et al. (2016). The correlation of the two time series (0.66) is low in comparison to the previous examples, mainly because of a phase shift between the two time series. The phase shift occurs due to the less dynamic behaviour of Malebo Pool, and having the altimetric virtual station downstream. Such a behaviour can be explained by the vast area of Malebo lacustrine. This large and flat area leads to small water level variations due to the upstream inflow. The phase shift also results in a wide scatter, which highlights another aspect of the complexity of the river system (Figure 4.22(f)).

4.3.4 Po River, Italy

The last river reach monitored in this chapter is the Po River in Italy. The Po River flows for 652 km eastward in the Po valley and passes through many important cities in Italy like Turin, Piacenza and Ferrara. The complex dynamic behaviour of the river and its relatively narrow width (150–650 m) make it a challenging case for the proposed algorithm to extract the river masks. Figure 4.23 presents an example of the Po River and the extracted river mask.

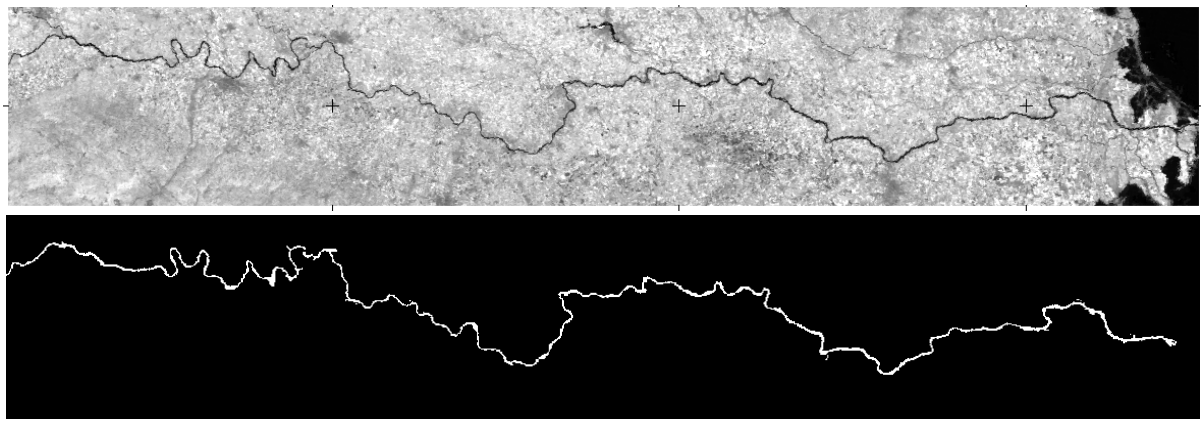

Figure 4.23: An example of the Po River image acquired in 2000.07.28 is in the top panel and in the bottom panel is the extracted river mask by applying the proposed method.

The comparison between the MODIS image and the obtained river mask shows that the algorithm is able to capture the continuity of the narrow and meandering river path. The algorithm is successful at capturing this narrow river mainly because of considering spatial and temporal correlations.

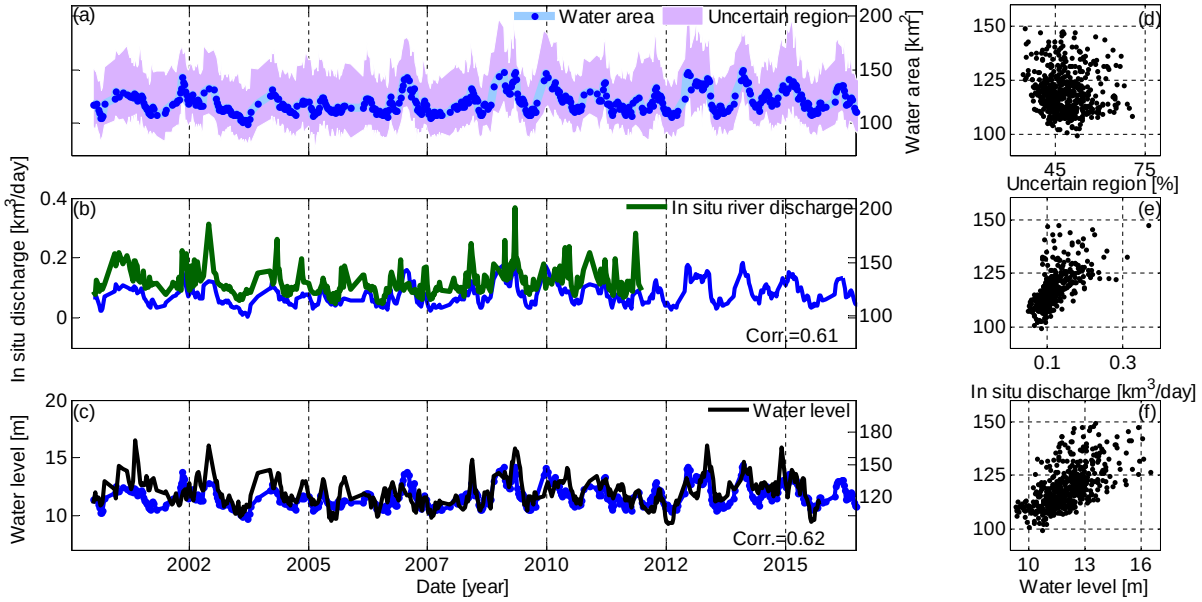

Figure 4.24: (a) Time series of river reach area measurements together with their uncertainties. (d) Scatter plot of river reach area vs. percentage of uncertainty. (b, c) River area is plotted with in situ discharge and altimetric water level. (e, f) Scatter plots of simultaneous water area against river discharge and water level measurements. Period of monitoring: 02.2000–07.2016

Figure 4.24(a) presents the time series of water area of the Po River during the monitoring period. Since the river is very narrow compared to the MODIS pixel size, the magnitude of uncertainty in the measurements is relatively large (40%–70%). In the scatter plot of river reach area measurements and uncertainties (Figure 4.24(d)), we see that the behaviour of their variations is uncorrelated because: (1) the river is narrow even in the wet season, (2) the river reach area variations are too small during the wet and dry seasons. The Po River flows through urban areas and it is also subjected to heavy floods. Therefore, more than half of its length is controlled with dikes and dams. This management leads to a decline in the natural behaviour of the river. As a result, it is very hard to detect any annual behaviour in the river reach area variations.

Figure 4.24(b) presents the comparison between river reach area and in situ river discharge measurements. In this case, daily discharge measurements are available from the year 2000 until about the end of the year 2011. For better visualization, only simultaneous measurements in both datasets are collected. The in situ discharge time series shows the complex behaviour of the river. Due to the construction of dikes and dams, the natural behaviour of the river is reduced. A number of high peaks are visible which could be a sign of extreme events like heavy rains and floods. The correlation between the two time series (0.61) is not as significant as previous examples mainly because of the constructions over the river. The scatter plot in Figure 4.24(e) also shows a relatively linear behaviour between the two variables. Due to the aforementioned issues it is also noisy, especially in the wet seasons. Figure 4.24(c) is the comparison

between river area and mean altimetric water over the whole river using the densified water level time series (Tourian et al., 2016). The correlation between the two time series (0.62) is not significantly high because the river reach is too narrow for both spaceborne techniques to measure river water height and area accurately. The linear relationship in their scatter plot (Figure 4.24(f)) is partially obvious but it is very noisy, as expected.

4.4 River discharge estimation using river width

The importance of river discharge monitoring is obvious in various critical applications like water supply management, hazard monitoring and urban development. For more than a century, river discharge has been measured directly near river sections. Despite various attempts, some major rivers are still unmonitored. Also, decreases in the number of worldwide gauging stations since the 1970s (Figure 1.3, 1.4) makes river discharge monitoring even harder (Fekete & Vörösmarty, 2007). Even in the case of the existence of a good monitoring network along the river, hydrologic variables between stations must be interpolated or modelled (Adams et al., 1995).

This situation increases the interest in applying remote sensing for estimating and monitoring river discharge. The conventional way to estimate river discharge using remotely sensed measurements is to develop an empirical function between simultaneous spaceborne measurements and in situ discharge observations. Such a function allows estimating river discharge without any ground-based observation.

In the previous section, we showed that a highly monotonic dependency is available between river reach geometrical parameters like river discharge, river water level and area in natural channels. Therefore, river discharge can be defined as a product of any other variable. Leopold & Maddock Jr (1953) explained that in a natural river channel, a power law relationship between different river hydraulic parameters and discharge can be described. For example we can state that

$$Q = aW^b, \tag{4.25}$$

where Q is river discharge, W is the river section width, a and b are the model parameters. Dynamic river masks, obtained in the previous section, can be converted to *effective river width* (W_e). Effective river width (W_e) is firstly introduced by Smith et al. (1996) and measured by dividing the river reach water area by the length of the reach. This value is considered as the average river width for the whole river reach. Therefore the estimated discharge is only valid for the river reach which the effective river width is obtained from. For simplicity, from now on, we use the term river width instead of effective river width.

In this study our aim is to develop river width-discharge empirical models (W-Q models) for estimating river discharge in the river reaches mentioned in Figure 4.25.

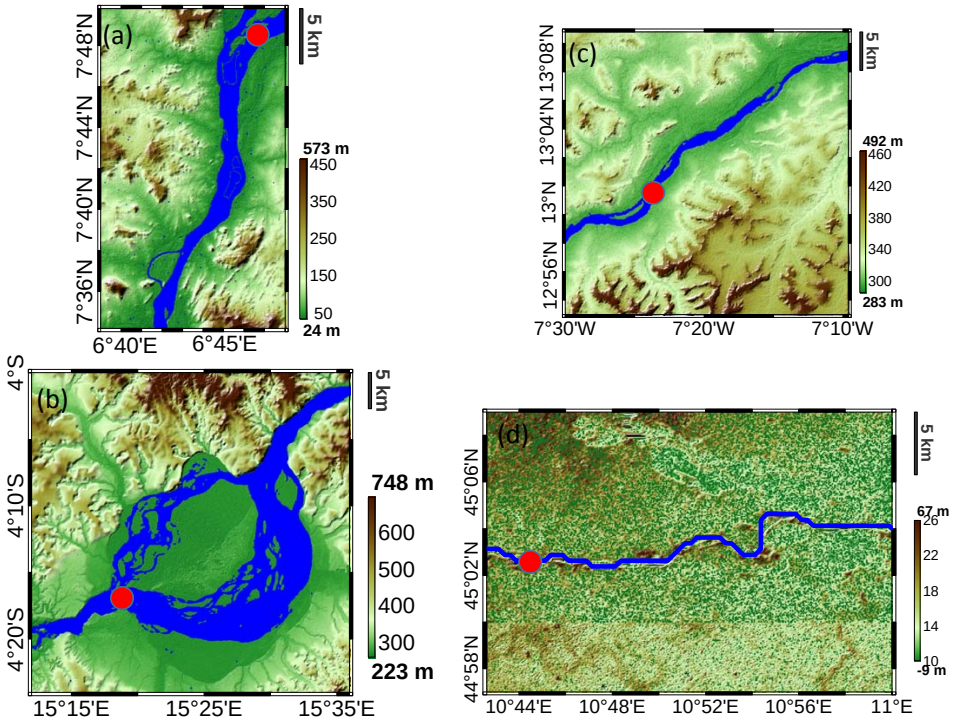

Figure 4.25: River reaches selected for developing river width-discharge models. (a) Niger River near Lokoja station. (b) Congo River near Brazzaville station. (c) Niger River near Koulikoro station. (d) Po River near Borgoforte station. The red dots are the in situ stations. Additional information about the in situ stations is provided in Table 1.10

We derive river width measurements for the first and second case studies using dynamic river masks obtained in the previous section. For the last two case studies, we only consider a few kilometres around the in situ stations for calculating effective river widths, therefore we need to generate new dynamic river masks. In the following table, complementary information about selected river reaches and datasets are used for models developing is provided.

Table 4.1: Information about training and validation datasets used for developing river width-discharge models

Case	River	Station	Lenght (km)	Training period	Validation period
a	Niger	Lokoja	20	2000–2004	2004–2006
b	Congo	Kinshasa	50	2000–2008	2008–2011
c	Niger	Koulikoro	40	2000–2004	2004–2006
d	Po	Borgoforte	30	2000–2009	2009–2012

Because we want to validate our estimated models against discharge measurements which are not used in the development of the models, we separate the last few years of our dataset as the validation period.

4.4.1 Simultaneous observations approach

In this part we will develop discharge estimation models using simultaneous measurements for all four case studies. Then we will introduce the quantile matching technique for estimating the river discharge. We will present the result derived by this method for Congo and Po River reaches.

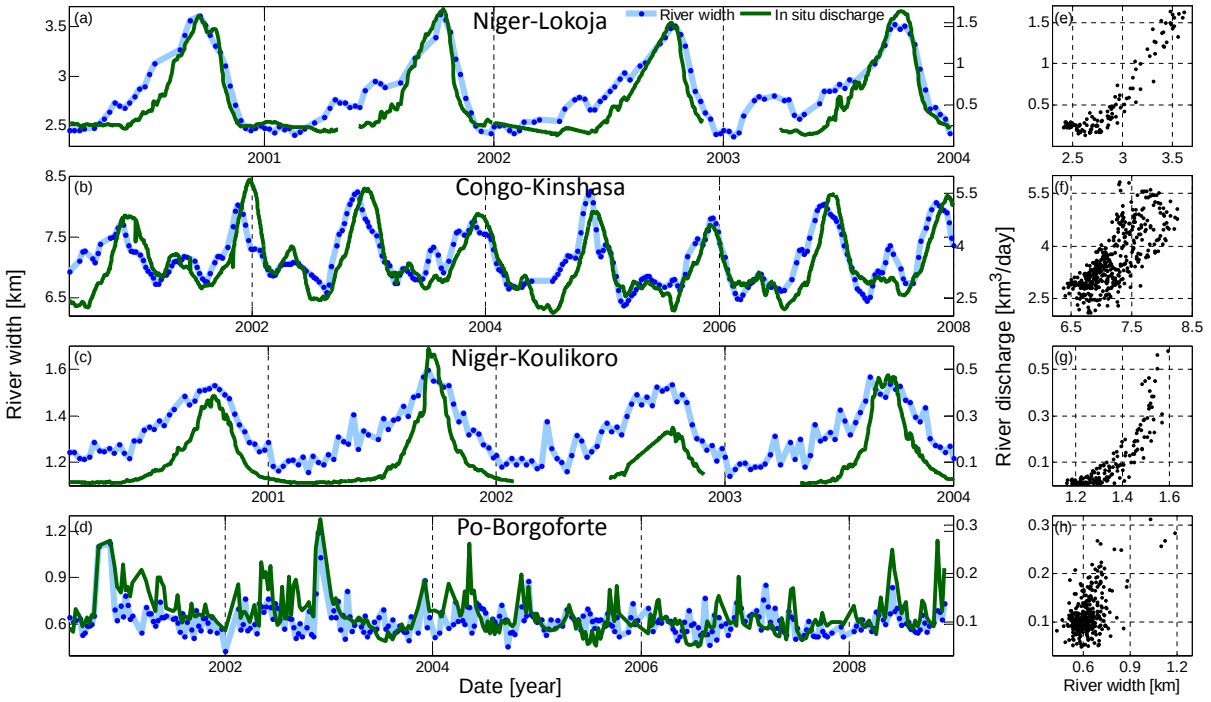

Figure 4.26: River discharge and width measurements used to develop *W*-*Q* models for all four case studies. Time series in (a-d) are time series of river width and discharge measurements and the scatter plots of simultaneous measurements are in (e-h).

Figure 4.26(a, c) are the training observations for the two river reaches selected over the Niger River. Both their time series and scatter plots (Figure 4.26(e, g)) present a great correlation between the river width and discharge measurements. In both cases, the monotonic behaviour is obvious. As a result, it is expected that the developed *W*-*Q* models can estimate the discharge accurately. In the Congo River example, the variations of the river width cannot project the behaviour of the river discharge properly. The wide scatter plot of Congo River reach measurements indicates that it is hard to develop an efficient *W*-*Q* model. The time series and scatter plot of the Po River reach measurements (Figure 4.26(d, h)) reveal that due to the following reasons width measurements do not project properly the numerous fluctuations in the river discharge: (1) limited number of observations especially in the wet seasons, (2) narrow river sections along the river reach.

Our proposed algorithm for extracting river masks is able to estimate the river reach area together with its uncertainty, therefore we can estimate the average river width

with its uncertainty. In contrast the uncertainty for the discharge measurements is not available. In hydrological applications, it is usually assumed that in situ discharge measurements have a multiplicative uncertainty around 10% of the measurements. Since both sides of the equation (4.25) are corrupted by error, we can then rewrite the equation as

$$Q = a(W - e_W)^b + e_Q \,, \tag{4.26}$$

where a and b are the model parameters and e_Q and e_W are unknown inconsistencies. Since our aim is to estimate the model parameters and the inconsistencies at the same time, we reformulate equation (4.27) as a non-linear Gauss-Helmert model with unknowns like

$$f(a, b, e_Q, e_W) = Q - e_Q - a(W - e_W)^b = 0 \,, \tag{4.27}$$

and, after linearization, apply the least squares estimation to derive unknown model coefficients, together with the variance covariance matrix of unknown parameters. The Gauss-Helmert model (mixed model) is a combination of Gauss-Markov model in which every observation is a linear or non-linear function of all unknown quantities and the adjustment with condition equations model in which a linear or non-linear equation between observations is available (Niemeier, 2008). The mathematical concept and implementation of the Gauss-Helmert model is provided in Appendix A. In Figure 4.27, we present the scatter plots of training periods and also developed models for all four cases.

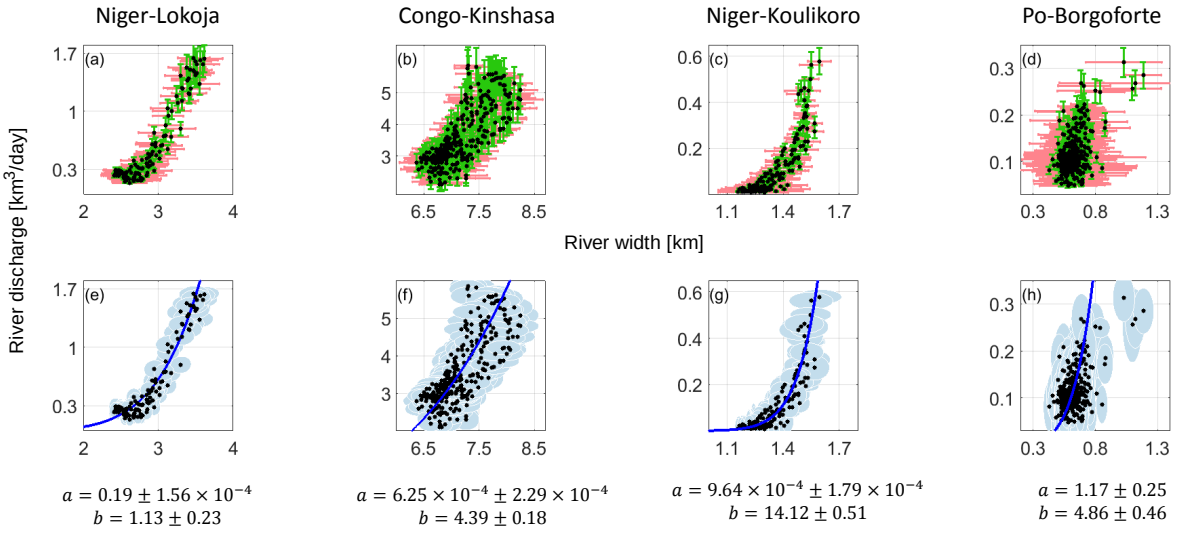

Figure 4.27: Scatter plots in (a-d) are the simultaneous observations used for developing models. Red and green bars are the measurement uncertainties. The W-Q rating curve models are presented in (e-h).

We plot the estimated rating curve for the Niger River reach near Lokoja station in Figure 4.27(e). The model passes through the observations properly, although we see there is a mismatch between the model and the points in the lower part of the scatter plot. This part of the scatter plot is related to the dry season when the river width is

between 2.5–3 km and discharge is less than 0.2 $\frac{km^3}{day}$. We also plot the error ellipse for each observation in the training period by using the variance and covariance matrix of adjusted observations. In this example, the error ellipses for the observations in the dry season are smaller because of the availability of more observations in this part of the scatter plot. The developed model for the other case study along the Niger River (Figure 4.27(g)) looks like a fit to the measurements. However in the lower part of the scatter plot we can detect some measurements far from the model. In general, these plots show that two developed models along the Niger River can model the river width-discharge relationship.

The training observations and developed model for the Congo River are presented in Figure 4.27(b, f). The point cloud in this case is wide and most of the measurements have a relatively large uncertainty in both directions. The point cloud gets wider with increasing river width in the wet season. Therefore, the magnitude of the uncertainty is quite large because of the wide point cloud. However the rating curve successfully passes through the observations.

In Figure 4.27(d) we see that, on average, the river width of the Po River reach is narrower than 0.8 km and that it has a lot of fluctuations during the training period. Unlike discharge measurements, the uncertainty in river width measurements is significant at almost all epochs. The accumulation of measurements in the middle part of the scatter plot reduces the accuracy of the rating curve. The W-Q model (Figure 4.27(h)) can not perform well especially in the wet season since there is a significant distance between the measurements and the rating curve model in the upper part of the scatter plot. Because of the limited number of observations, we cannot conclude that the isolated measurements are blunders in the upper part of the scatter plot.

By comparing the uncertainties in the observations (Figure 4.27(a–d)) and error ellipses of adjusted observations Figure 4.27(e–h), we can conclude that

- The covariance between adjusted measurements in each epoch is negligible according to the orientation of the error ellipses.
- In most epochs $\widehat{\sigma}_{\widehat{W}}$ is smaller than σ_W. It means that we can reduce the area of the uncertain region by considering a lower threshold for the marginal probability of pixels.

In the next step, we will predict the river discharge by using the developed W-Q models for the validation periods and then we compare the estimated and measured river discharge for validating the models and assessing their correctness. Since the variance-covariance matrices of model coefficients are provided by the Gauss-Helmert model, we are able to calculate the uncertainty in the predicted discharge by using error propagation (4.28):

$$\sigma_Q^2 = W^{2b}\sigma_a^2 + a\ln(W)\ W^{2b}\sigma_{ab} + (a\ln(W))^2\ W^{2b}\sigma_b^2 + (abW^{b-1})^2\sigma_W^2, \tag{4.28}$$

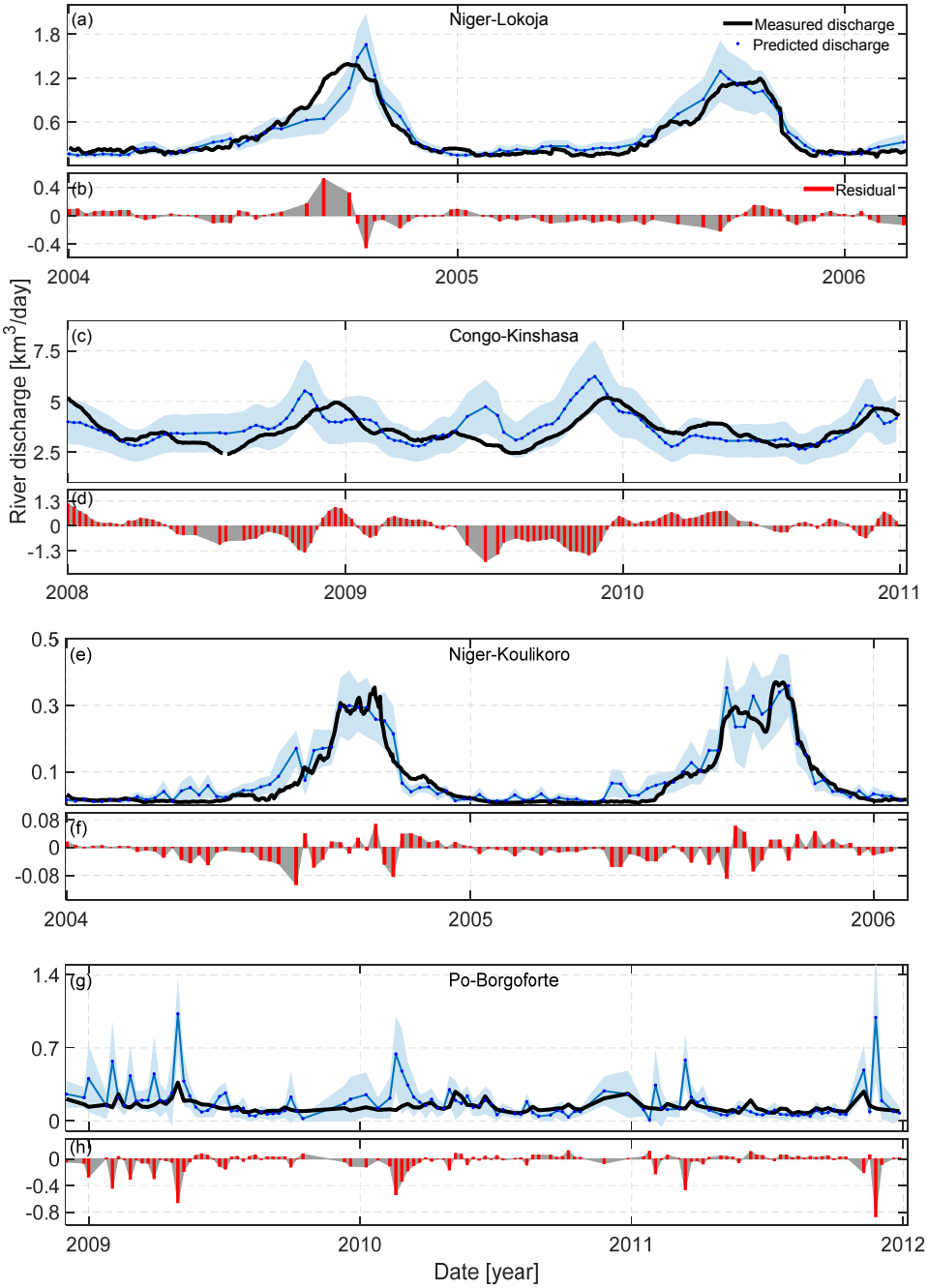

Figure 4.28: Comparison between measured and predicted river discharge via developed *W-Q* models. The red bars are the difference between measured and predicted values. (a) Niger (Lokoja station), (b) Congo River (Kinshasa station), (c) Niger River (Koulikoro station), (d) Po River (Borgoforte station).

Measured and predicted river discharge for the Niger River reach near Lokoja station are compared in Figure 4.28(a). Due to the high correlation between river width and discharge measurements, the derived model is able to predict discharge accurately. The residual values (Figure 4.28(b)) in most epochs are less than $\pm 0.1 \frac{\text{km}^3}{\text{day}}$. As we expect the

model cannot estimate discharge accurately in the wet season. So we see in Figure 4.28(b) that the residuals are in the range of $\pm 0.4 \frac{km^3}{day}$.

Figure 4.28(c) is the comparison between predicted and measured discharge of the Congo River reach. Relatively large uncertainty in the model coefficients leads to large uncertainties in the estimated discharges. Therefore, the error envelope for the estimated values is large in all epochs. Due to the phase shift between river width and discharge measurements in the training period, the model predicts discharge with a phase shift in the wet seasons too. This leads to a large difference between estimated and measured river discharge in wet seasons (Figure 4.28(d)). Nevertheless, in the dry season, the residuals are smaller than $1 \frac{km^3}{day}$.

The Niger River at Koulikoro station (Figure 4.28(e)) shows a drastic annual behaviour. The river discharge is very small (less than $0.02 \frac{km^3}{day}$) in the dry season. Then due to heavy precipitation in the wet season, river discharge increases up to $0.4 \frac{km^3}{day}$. However, the developed model can predict the river discharge in both seasons accurately. The model can predict not only small water flow variations in the dry seasons but also the extreme events in the wet seasons. The average residual between measured and predicted values is less than $0.03 \frac{km^3}{day}$, however the residual is relatively large in a few epochs.

The Po River reach is the most challenging in terms of developing a *W*-*Q* model. At first glance, the performance of the derived *W*-*Q* model (Figure 4.28(g)) is acceptable considering the narrow river reach. However, the model predicts the river discharge with a large residual in the wet season. The main reasons for the poor performance of the model in wet season are the lack of observations in the upper part and aggregation of observations in the lower part of scatter plot (Figure 4.27(h)). The model overestimates the discharge when the river is wider than 0.2 km. Therefore in some epochs, the model estimates discharge with an error larger than $0.5 \frac{km^3}{day}$ which is two times larger than the actual value.

For assessing quantitatively the performance of derived models, statistics are presented in the Table 4.2.

Table 4.2: Statistics for evaluating the performance of the derived *W*-*Q* models.

Case	**River**	**Station**	**Period**	**Corr.**	**RMSE**	**NSE**	**PBIAS**
			Training Validation	[ ]	[%]	[ ]	[%]
1	Niger	Lokoja		0.97 0.95	7.6 9.28	0.92 0.89	−6.0 0.29
2	Congo	Kinshasa		0.76 0.64	16.73 22.98	0.41 0.17	−2.38 −2.37
3	Niger	Koulikoro		0.91 0.96	5.51 8.82	0.79 0.90	−6.65 −14.22
4	Po	Borgoforte		0.51 0.46	59.20 52.14	−23.43 −8.90	−29.49 −32.44

As we expect statistical indicators also show that the *W-Q* models for the Niger River reaches near Lokoja and Koulikoro stations estimate river discharge accurately. In both cases, a high correlation coefficient between estimated and measured discharge shows a significant agreement between variations of both time series in terms of direction and magnitude. The normalized RMSE in both cases is less than 10% which is acceptable in hydrological studies. Both models have NSE values near one, which means that they are capable of predicting the river discharge accurately. The first model does not show any tendency to overestimate or underestimate the discharge (PBIAS $= 0.29\%$). But the *W-Q* model for the Koulikoro river reach predicts discharge higher than the real value on average, since its PBIAS is negative. Inability of the model to estimate the correct discharge value in the dry season is the main reason for this negative PBIAS.

The *W-Q* model for Congo River is unable to predict river discharge accurately based on its statistics. The correlation coefficient is just 0.64 and the normalized RMSE is relatively large (26.1%). The main reason for this weak performance is the phase shift between two time series. Considering the very low NSE value (0.17), there is no significant difference if we replace the estimated discharge with the mean measured discharge of the training period. The negative PBIAS shows that the model has a tendency to overestimate the discharge.

The last case study, Po River reach near Borgoforte station, is the most challenging one in terms of discharge modelling because of its narrow width and unusual fluctuations. The statistics in Table 4.2 show the poor performance of the model. The correlation coefficient is 0.44 because the model cannot predict tiny fluctuations in the river discharge due to the large uncertainty in width measurements. The normalized RMSE is too large (52.14%) because in a number of epochs, the model predicts the discharge much larger than the real value. The NSE is sensitive to blunders in the discharge prediction. Since some blunders exist in this example, the NSE value is negative (-8.9). The negative NSE means that the performance of the *W-Q* model is not acceptable. Moreover, blunders also distort the PBIAS. The large negative value of PBIAS (about -32%) shows that the model predicts larger than the real value in general. By looking again at Figure 4.27(h), we see that the model ignores observations in the upper part of the scatter plot. Therefore, the model predicts the discharge with a residual higher than 1 $\frac{\text{km}^3}{\text{day}}$ in the wet season.

We see that two of developed *W-Q* models along the Congo and Po river reaches suffer from mismodelling error. For developing models we assumed that there is an exponential relationship between river discharge and width. However our experiment shows that these two river reaches do not follow this assumption. Therefore in the next step, we try to develop non-parametric models for estimating the river discharge.

4.4.2 Quantile look-up table approach

The previous experiment showed that sometimes it is not feasible to model the relationship between river width and discharge with a limited number of model parame-

ters. To reduce the mismodeling error of fitting an exponential function to the scatter plot of simultaneous measurements, we develop a non parametric look-up table for estimating the river discharge based on the quantile functions of river width and discharge measurements in the training period. The look-up table presents a one-to-one relationship between river width and discharge. The potential of using quantile functions instead of the measurements in river discharge estimation is demonstrated by Tourian et al. (2013). They stated that to eliminate the need for availability of simultaneous observations, the discharge estimation model can be established by using the quantile functions of observations. In this section we estimate river discharge using this technique for two problematic river reaches (Congo and Po Rivers). Figure 4.29 presents the procedure of defining the quantile look-up table.

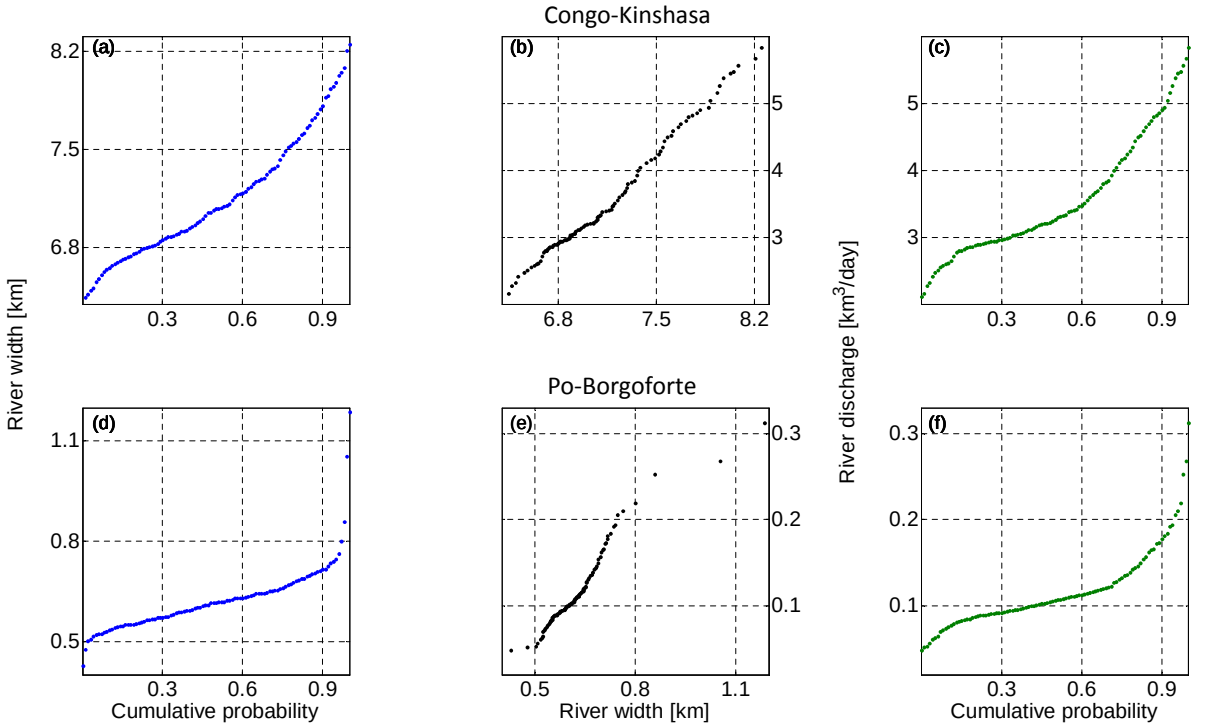

Figure 4.29: (a) and (b) are the quantile functions of river width measurements for Congo and Po River reaches. (c) and (f) are the quantile functions of in situ discharge measurements. (b) and (e) are the developed quantile look-up tables for Congo and Po River reaches.

Quantile function of a time series expresses the probability that a certain value is exceeded over the period. For example, Figure 4.29(a,c) are quantile functions of river width and discharge time series presented in Figure 4.26(b) for the Congo River reach. Since these two functions have a same x-axis (cumulative probability), it is possible to connect their y-axes directly. Figure 4.29(b) presents the scatter plot of river discharge versus river width. This scatter plot is generated from the corresponding probabilities of both quantile functions. Since only one corresponding value is available for each probability in the quantile functions, the scatter plot can be used as a look-up table. It

means that by measuring river width, the river discharge can be estimated by finding the corresponding value in the y-axis of the look-up table.

Figure 4.29(e) is the quantile look-up table for the Po River reach. We can see that the majority of points concentrate in the middle of the plot where river width is between 0.5 and 0.8 km. In this figure we see how the relationship of river discharge and width is changed when the river is wider than 0.8 km. Therefore defining an exponential function to estimate the discharge causes a large residual in the wet season. We expect that the developed quantile look-up table can estimate the discharge more accurately, since there is no need for defining a parametric model.

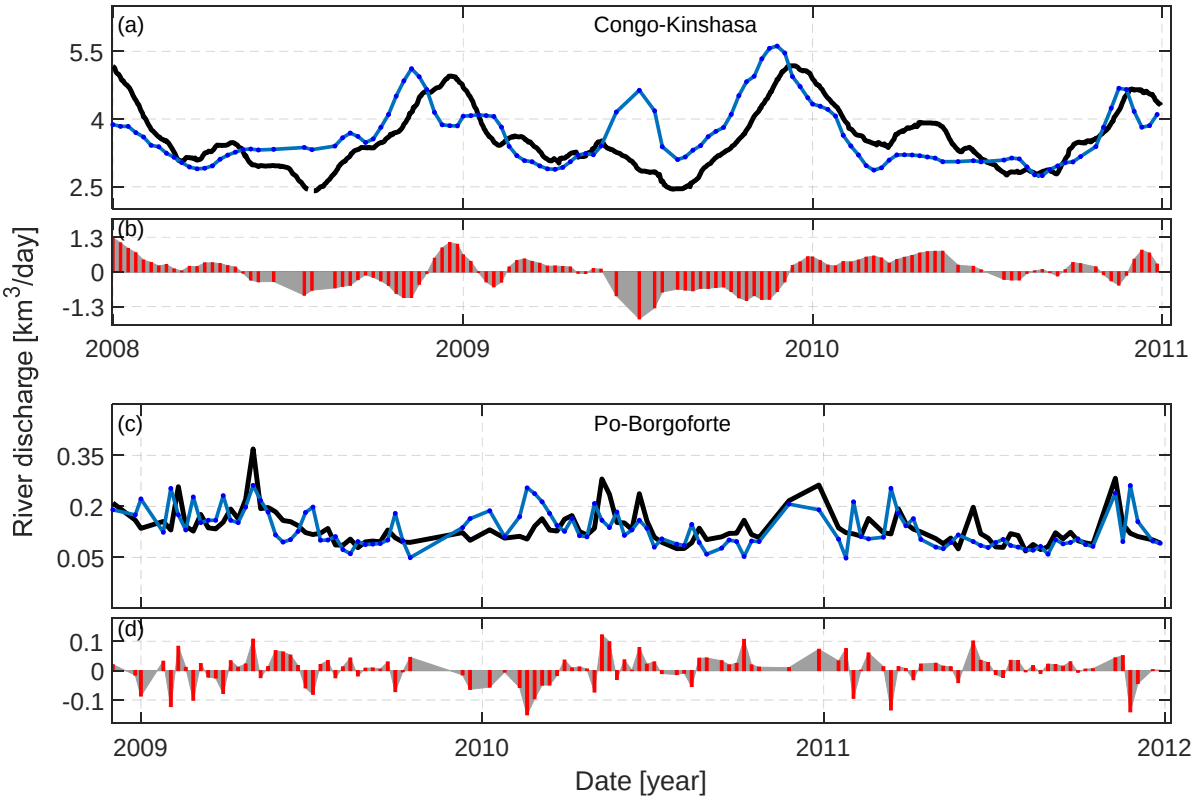

Figure 4.30: Comparison between estimated river discharge via quantile look-up table and measured discharge for Congo River (a) and Po River (c) reaches. The difference between measured and estimated values are plotted as red bars.

Figure 4.30(a) is the comparison between measured and estimated discharge using the quantile look-up table for the Congo River reach. Comparison this figure with Figure 4.28(c), we see that the look-up table can predict river discharge more efficiently. The second technique estimates discharge more accurately and the residuals are also reduced especially in the wet season . In Table 4.3 we see that the RMSE is reduced from 22.98% to 20.96%. The problem of phase shift is still visible because the origin of this error is the complex relationship between river width and discharge in this case study. However the NSE coefficient is interestingly improved from 0.17 to 0.31. Although 0.31 is not a high value for the NSE, but it is minimally acceptable in respect to the quality

of width measurements. Finally, according to the near zero PBIAS, the model does not have any tendency toward overestimating or underestimating the discharge.

Table 4.3: Statistics for evaluating the performance of quantile look-up tables.

Case	River	Station	Period	Corr.	RMSE	NSE	PBIAS
			Training Validation	[ ]	[%]	[ ]	[%]
2	Congo	Kinshasa		0.76 0.65	16.11 20.96	0.52 0.31	−0.02 −0.07
4	Po	Borgoforte		0.49 0.51	16.51 17.19	0 0.07	0.09 1.98

The Comparison between estimated discharges via the parametric W-Q model (Figure 4.28(g)) and the quantile look-up table (Figure 4.30(c)) indicates a considerable improvement using the latter technique. The quantile look-up table can estimate discharge in extreme events, so the magnitude of residuals is reduced significantly. The RMSE is reduced from 52.14% to 17.19% and the NSE value is increased from -21.96 to 0.07. The huge tendency of the previous W-Q model to overestimate the discharge (PBIAS $= -32.44$) is also improved to a slight underestimating by the latter technique (PBIAS$= 1.98$).

The comparison between the results from the previous section and this section shows us that mismodelling is a major source of error especially if the river bed presents different patterns and the measurements do not spread uniformly over the data distribution.

4.5 Summary

In this chapter, we introduced an automatic river reach area monitoring algorithm and applied it to four different river reaches using MODIS images. In this method, an MRF model was developed to consider all types of available information, including pixel intensity, and spatial and temporal interactions between pixels. Then a MAP solution for the Bayesian framework was found to determine the most probable water mask. Since the high computational effort of finding a global solution was a serious concern, we reshaped the problem as an energy minimization one. To minimize the energy function, we developed an undirected two-terminal graph and defined the max-flow solution for the graph by augmenting all the possible paths between two terminals. The final residual graph offered the binary water mask representing the MAP solution. The second aim of this chapter was the uncertainty assessment of derived river masks. Therefore, we computed the confidence level for pixels in both land and water masks by measuring the marginal probability of all nodes in the final residual graph.

The time series of water area together with their uncertainty were generated by applying the proposed method to all images of the given river reaches. The input of

the process was a time series of images. The algorithm automatically generated binary and probabilistic water masks together with water area time series, including the uncertainty range. Since cloud-covered images were detected and removed, and we considered the temporal behaviour of the river reach, the products were robust against blunders. The algorithm coped with the effect of sunglint and cloud shadow in the satellite images by considering the temporal correlation in the images. Therefore, extra post processing steps for the final time series were not necessary.

We employed our method over four river reaches with different channel behaviours and morphologies. Two of them were part of the Niger River (near Lokoja and Koulikoro stations), and the third one was a river reach containing Malebo Pool along the Congo River near Kinshasa station. The final one was part of the Po River near Borgoforte station in Italy. Based on the presented results, the method was able to cover the seasonal change in the river extent and also capture extreme events. The algorithm successfully extracted complex braided river systems and islands in the middle of a river. The algorithm proved its ability to extract the long (400 km) and narrow (average width about 600 m) Po River reach. Without considering spatial and temporal correlations, it was not possible to extract the river reach accurately.

In our examples, it only failed to extract the river branches narrower than a MODIS pixel size (250 m). As a result, the coarse pixel size of MODIS images was the main source of uncertainty in the derived water masks. We saw that, due to the orbit configuration of both ENVISAT and SARAL/AltiKa, they were not able to measure water level as frequently as water area measured by MODIS. On average, for water area time series, we had 48 values in a year, while at best only 11 water level observations were available. This highlighted the advantages of imagery for the characterization of river behaviour in comparison to satellite altimetry.

For the uncertainty estimation, we considered pixels with less than 10% confidence level as the uncertain region in both water and land masks. Although the method assigned a label for these pixels, we did not reach a firm decision about them. Most of the pixels with small marginal probabilities were located on shorelines In the probabilistic water and land masks. Considering the coarse MODIS pixel size, most of the pixels located in the river extent were partially covered by water. Therefore, the algorithm could not assign a label for pixels in this region confidently. In our examples, the magnitude of the uncertain area varied between 8%–23% of the river area for the first three case studies, and for the Po River, it varied between 40%–70%.

Since ground-truth was not available, we validated our results indirectly by comparing the obtained water area time series with the in situ river discharge and altimetric water level measurements. In the Niger examples, the high correlation between water area time series and in situ discharge (> 0.9) and altimetric water area (> 0.8) indicated that we captured the natural behaviour of river reaches, and the obtained water area estimations were accurate. In the Congo example, the correlation was lower because the in situ station was located in the urban area, and also the river included a complex braided river system. Finally in the Po River reach, correlation coefficients were lower than the previous examples (0.61 with in situ discharge and 0.62 with altimetric water

level). Complex dynamic behaviour of the river during the monitoring period and its narrow width were the main reasons for the low correlation coefficients. In addition, the natural behaviour of the river had been decreased since the river flows through a number of cities and urban areas.

Finally, we developed river discharge estimation models using the generated river masks. By dividing the river reach area by the length of the reach, effective river width was derived. Since a monotonic behaviour is available between different hydraulic parameters of a river reach, river discharge can be predicted as a product of river width. So we estimated river discharge by measuring river width if the relationship between them was already modelled. For generating a *W*-*Q* model, a training dataset including simultaneous river width and discharge measurements was developed. In this study we applied the Gauss-Helmert adjustment model since we considered inconsistencies on both sides of the observation equations. The outputs of the adjustment procedure were the model parameters and the variance-covariance matrix of the unknowns.

We validated the predicted discharges by comparing the predicted and measured discharges for the validation period. We also evaluated the performance of the developed models by computing different statistics. Two developed river discharge estimation models along the Niger River performed well. All the statistics for them were in the acceptable range. Because of a phase shift between observations in the Congo River reach, the performance of developed model was not acceptable. Near zero NSE values for Congo River reach and also Po River reach indicated that the performance of developed discharge prediction models were not acceptable. In the Po River example apart from the negative NSE value, the normalized RMSE was about 50%, because the exponential model could not express the actual relationship between river width and discharge.

In the end we developed non-parametric models for the Congo and Po River examples to reduce the mismodelling error. To do this, we matched the quantile function of river discharge to those of width measurements. Since both quantile functions shared a x-axis (cumulative probability), we developed a quantile look-up table by matching their y-axis. In both river reaches, the quantile look-up tables had relatively acceptable performance. In the Congo River example, the quantile look-up table partially overcame the problem of wide points cloud. So the NSE value increased to 0.3 which is at least in the acceptable range. The quantile look-up table for the Po River performed significantly better than the parametric *W*-*Q* model. Therefore the normalized RMSE was reduced from 52% to 17%. In this case, the quantile look-up table was able to model various behaviour of the river reach and estimated discharge even during extreme events.

Chapter 5

Concluding Remarks and Outlook

Advanced methods for detecting and monitoring inland water bodies must be further developed because of emerging new satellite imagery missions with great capabilities to capture the earth surface in different spectral bands, fine spatial resolution, global coverage and high revisit frequency. In this thesis we have introduced a number of different algorithms for detecting change in multitemporal images and generating long time series of inland water body area.

In the second chapter we investigated the potential of multispectral transformations like PCA and CCA with the following objectives:

1. Enhancing signal to noise ratio in the multispectral images by ignoring some of the principal components.

2. Highlighting the change between two multitemporal images.

To achieve these objectives we did extensive analysis in this chapter. In the following, we mention the concluding remarks:

(i) Multispectral images provide a vast amount of information about the water body, since each spectral band observes a certain part of the light spectrum and can reveal a unique characteristic of the water body. However selecting the suitable spectral bands for mapping and extracting the surface water extent remains a challenging task.

(ii) The main challenge of the first objective is to select the proper principal components to reconstruct the multispectral bands or present in the color channels.

(iii) PCs are arranged according to their contribution in the covariance matrix. Therefore selecting the primary PCs is not the best strategy for dealing with the earth surface features as they have a unique signature in different spectral bands.

(iv) An alternative strategy to arrange the PCs is based on analysing the contribution of each spectral band in the corresponding eigenvector. Applying this approach needs a careful investigation of the coefficient of each spectral band in the eigenvectors.

(v) Reducing the noise by ignoring a number of PCs also leads to an unwanted loss of information. As a result the spectral signatures of the earth features in the spectral bands are manipulated in the transformed product. Although the transformed bands contain less noise, for any further interpretation, a visual comparison with the original image bands or the RGB image is needed.

(vi) Generating the image difference of two multitemporal images is a common way to detect the change between them. However mapping the change by using the ordinary image difference bands is impractical because: 1) We can select only three bands to place in the color channels. 2) Significant changes would be influenced by trivial variations between two images, e.g. change in vegetation, solar illumination and atmospheric condition.

(vii) Applying the PCA transformation on the image difference bands is a solution since the dominant change is highlighted in the primary PCs. Therefore, the RGB map of the first three PCs may explore the major differences between two epochs.

(viii) Applying the MAD transformation for change detection between two multitemporal images is preferred because it is invariant to gain and offset between two image bands. Thus there is no need for radiometric normalization before applying MAD transformation.

(ix) The idea of isolating the noise and trivial changes in the image difference bands can be sought also by highlighting the area with a high spatial correlation. To this end, applying the MAF transformation to the PCs and MAD components is recommended.

(x) A changing pattern of cloud cover between two multitemporal images is a serious threat even for an advanced transformation like MAD+MAF.

(xi) Figure 2.23 presents a serious drawback of analysing the change using multispectral transformations. Each MAD and MAD+MAF component is a linear combination of all spectral bands, so their color composite is not a representative of the earth surface natural color. Therefore for any interpretation we need to compare them visually with the true color composite images of both epochs.

(xii) For creating the change/no-change map at least a threshold for pixel values of transformed bands must be defined. Since the pixel values in the transformed bands don't represent any physical characteristic, the threshold can be defined either by visual comparison or by a χ^2 test.

addressing the following challenges and questions leads to further development of using the multispectral transformation approach in change detection applications:

- Since PCA is separately applied to the images, it creates a different basis for each image. As a result each image has its own pixel value range. Then how can we quantitatively compare the transformed image bands?

- If PCA transformation is applied to a time series of images, the primary PCs highlight the dominant pattern in time as well. Can we extract any annual or semi-annual behaviour of the water body by analysing the first or first few PCs?
- In this thesis we have applied MAD and MAF transformations on two multitemporal images. However these algorithms have the potential to be applied to images with different number of spectral bands and more than two multitemporal images.

In the third chapter we have introduced an algorithm for monitoring lake area from MODIS imagery. Considering the presented results, the algorithm can successfully monitor the change of the lake extent and generate long time series of lake area. In the following we continue with the concluding remarks of that chapter:

(xiii) Restricting the search area is the main advantage of the algorithm. Applying the DEM-based mask and the constant-water mask not only reduces the computational effort significantly but also improves the accuracy of final water masks.

(xiv) After applying the masks and modifying the search area, the input of the classification algorithm only includes the pixels around the lake shoreline. As a result, the possibility of misclassification is significantly decreased.

(xv) As extensively discussed in the validation part of chapter 3, the coarse spatial resolution of MODIS images and the cloud cover are the main sources of the error in the derived water masks.

(xvi) Terra and Aqua MODIS are regularly and constantly providing images from the year 2000 until now. MODIS images are preferred to other satellite images like Landsat images because we can generate long and dense time series which can also represent the short-term variations of water area. Although spatial resolution is the main source of error in surface water area monitoring, the MODIS MOD09Q1 product with 250 m pixel size and 8 day revisit time holds an optimal balance between computational efficiency and image acquisition time.

(xvii) The algorithm detects and ignores images in which a major part is covered by cloud. But in the Rukwa Lake example we see that even a minor cloud coverage can spoil the final results. For improving the performance of the algorithm one can think of using auxiliary datasets, like MODIS Cloud Mask product. Ignoring the cloud-covered pixels from the image does not solve the problem because the number of pixels in the search area must be constant in all epochs.

Further development of the proposed algorithm may be pursued by replacing the ISODATA algorithm with a region-based classification. In the beginning of chapter 4 we have already discussed the performance of pixel and region-based classification algorithms. Therefore there is no doubt that the region-based algorithms generate more accurate water masks. The region-based algorithm, introduced in chapter 4, is specifically developed for determining river reach area. We sacrifice the computational efficiency of the algorithm due to the complexity of the river reach monitoring. Therefore

the current setup of the algorithm may not be applicable for a much larger search area. The following questions must be addressed in order to develop a graph cuts-based algorithm for monitoring lake area:

- How can the energy functions be modified in order to establish a balance between the run-time of the algorithm and the accuracy of the outputs?
- How can we take advantage of additional sources of information like a DEM or a bathymetric map?

In chapter 4, a graph cuts-based classification algorithm is introduced for monitoring river reach area. In the following the concluding remarks of chapter 4 are provided:

(xix) The MRF provides a convenient frame for modeling different constraints. Therefore we take advantage of all types of available information in images, including pixel intensity, spatial and temporal interactions between pixels.

(xx) The structure of the algorithm has also the potential of handling external sources of information like elevation maps or water level information.

(xxi) The algorithm is robust against cloud coverage. It can assign a correct label for a pixel partially covered by cloud based on spatial and temporal correlations. However two filters for detecting and removing cloud-covered images are available.

(xxii) The balancing parameter (λ) is determined by visual comparison of derived water masks and original images in some epochs. In future studies, a careful analysis is needed to investigate about the contribution of λ in the accuracy of derived water masks.

(xxiii) Since the graph cut algorithm cannot provide an uncertainty measure for the defined labels, the Kohli and Torr method is applied to define the probabilistic water mask. For every pixel in the probabilistic water mask, the confidence level to the label is provided. This value tells us how much we can trust on the defined label by the algorithm.

Based on the results in the validation part of chapter 4 we can say that the algorithm makes significant inroads into the issue of extracting the river mask from satellite images. Nevertheless there is room for improvement to make the algorithm computational efficient:

Using DEM map as an external source of data: Water tends to flow downstream. Therefore the elevation profile of the river reach and surrounding area can be used as a useful source of information. To summarize, the lower the altitude regionally, the higher the possibility to be covered by water.

Using global dynamic water masks as initial solution for the algorithm: The algorithm can be applied as a post-classification step to available dynamic water masks in order to improve their accuracy.

Using time-variable water coverage frequency map: The current version of the algorithm uses the same water coverage frequency map for all epochs. Due to the strong annual behaviour, one can think of developing different frequency maps for each season. Considering time-variable frequency maps provides a reasonable understanding about the temporal behaviour of the river reach.

Using a more efficient max-flow algorithm: Ordinary augmenting path algorithms, like the Dinic algorithm, always look for the shortest path between terminals. Searching for the shortest paths in each iteration increases the run-time complexity of the algorithm. For reducing the computational effort, applying a more advance max-flow algorithm is suggested. For example the algorithm introduced by Boykov & Kolmogorov (2004) can be an alternative. This algorithm works 2–5 times faster than the other algorithms because (Boykov & Kolmogorov, 2004):

- It builds two searching trees from each terminal towards the other one.
- It does not build searching trees from scratch in every iteration and reuses the same searching trees.

As a final remark, this contribution tried to provide insight into the challenges of monitoring the change in the water body area. Although a variety of advanced change detection algorithms are being introduced and new satellite imagery missions are providing high quality images, the main difficulty is to select an appropriate change detection procedure according to the specific research question. As well as selecting the change detection technique, the following factors crucially contribute to the quality of derived water area time series:

- Selecting suitable satellite images in terms of image acquisition dates, pixel size and spectral coverage.
- Maintaining precise geometrical registration and radiometric calibration between multitemporal images.
- Identifying the physical characteristic and spectral signature of the object in different spectral bands.
- Investigating the use of additional data sources like elevation models or historical maps.
- Assessing the accuracy and validating the result by comparing with in situ measurements.

Bibliography

Adams, J. B., Sabol, D. E., Kapos, V., Filho, R. A., Roberts, D. A., Smith, M. O., & Gillespie, A. R. (1995). Classification of Multispectral Images Based on Fractions of Endmembers : Application to Land-Cover Change in the Brazilian Amazon. *Remote sensing of Environment*, *52*(2). DOI: 10.1016/0034-4257(94)00098-8.

Ahtonen, P., Euro, M., Hallikainen, M., Solbø, S., Johansen, B., & Solheim, I. (2004). SAR and optical based algorithms for estimation of water bodies. Tech. rep., Technical report, FloodMan Project. Available online at projects.itek.norut.no/floodman.

Alsdorf, D. E., & Lettenmaier, D. P. (2003). Tracking fresh water from space. *Science (New York, N.Y.)*, *301*(5639), 1491–1494. DOI: 10.1126/science.1089802.

Alsdorf, D. E., Melack, J. M., Dunne, T., Mertes, L. A. K., Hess, L. L., & Smith, L. C. (2000). Interferometric radar measurements of water level changes on the Amazon flood plain. *Nature*, *404*(6774), 174–177. DOI: 10.1038/35004560.

Alsdorf, D. E., Rodríguez, E., & Lettenmaier, D. P. (2007). Measuring surface water from space. *Reviews of Geophysics*, *45*(2). DOI: 10.1029/2006RG000197.

Andreadis, K. M., Clark, E. A., Lettenmaier, D. P., & Alsdorf, D. E. (2007). Prospects for river discharge and depth estimation through assimilation of swath-altimetry into a raster-based hydrodynamics model. *Geophysical Research Letters*, *34*(10). DOI: 10.1029/2007GL029721.

Annunziato, A., Andredakis, I., & Probst, P. (2016). Impact of Flood by a Possible Failure of the Mosul Dam. Tech. rep., JRC Technical Reports, EU Commission. DOI: 10.2788/689469.

Arctic Climate Impact Assessment (ACIA) (2004). Impacts of a Warming Arctic. *Cambridge, UK: Cambridge University Press*, *1*. Available online at amap.no/documents/doc/impacts-of-a-warming-arctic-2004/786.

Baker, K. (2005). Singular value decomposition tutorial. *The Ohio State University*. Available online at site.iugaza.edu.ps/ahdrouss/files/2010/03/Singular_Value_Decomposition_Tutorial.pdf.

Ball, G. H., & Hall, D. J. (1965). ISODATA, a novel method of data analysis and pattern classification. Tech. rep., DTIC Document. Available online at dtic.mil/get-tr-doc/pdf?AD=AD0699616.

Banic, J., & Cunningham, A. (1998). Airborne laser bathymetry: A tool for the next millennium. *EEZ Technology*, *3*, 75–80. Available online at shoals.sam.usace.army.mil/downloads/Publications/32Banic_Cunningham_98.pdf.

Baumann, P. R. (2014). History of remote sensing, aerial photography. Available online at oneonta.edu/faculty/baumanpr/geosat2/RS%20History%20I/RS-History-Part-1.htm.

Berger, M. (2015). The future of remote sensing. *BELSPO - 30 years of remote sensing research*. Available online at eo.belspo.be/Docs/Resources/Presentations/HappyBEarthday2015/5.Berger.pdf.

Besag, J. (1974). Spatial interaction and the statistical analysis of lattice systems. *Journal of the Royal Statistical Society. Series B (Methodological)*, (pp. 192–236). Available online at jstor.org/stable/2984812.

Besag, J. (1986). On the statistical analysis of dirty pictures. *Journal of the Royal Statistical Society. Series B (Methodological)*, (pp. 259–302). Available online at jstor.org/stable/2345426.

Biancamaria, S., Durand, M., Andreadis, K., Bates, P., Boone, A., Mognard, N., Rodriguez, E., Alsdorf, D., Lettenmaier, D., & Clark, E. (2011). Assimilation of virtual wide swath altimetry to improve arctic river modeling. *Remote Sensing of Environment*, *115*(2), 373–381. DOI: 10.1016/j.rse.2010.09.008.

Birkinshaw, S. J., O'Donnell, G. M., Moore, P., Kilsby, C. G., Fowler, H. J., & Berry, P. A. M. (2010). Using satellite altimetry data to augment flow estimation techniques on the Mekong River. *Hydrological Processes*, *24*(26), 3811–3825. DOI: 10.1002/hyp.7811.

Bjerklie, D. M. (2007). Estimating the bankfull velocity and discharge for rivers using remotely sensed river morphology information. *Journal of hydrology*, *341*(3), 144–155. DOI: 10.1016/j.jhydrol.2004.11.022.

Bjerklie, D. M., Lawrence Dingman, S., Vorosmarty, C. J., Bolster, C. H., & Congalton, R. G. (2003). Evaluating the potential for measuring river discharge from space. *Journal of Hydrology*, *278*(1), 17–38. DOI: 10.1016/S0022-1694(03)00129-X.

Blewitt, G., & Lavallée, D. (2002). Effect of annual signals on geodetic velocity. *Journal of Geophysical Research: Solid Earth*, *107*(B7). DOI: 10.1029/2001JB000570.

Bonn, F., & Dixon, R. (2005). Monitoring flood extent and forecasting excess runoff risk with RADARSAT-1 data. *Natural Hazards*, *35*(3), 377–393. DOI: 10.1007/s11069-004-1798-1.

Borga, M. (1998). *Learning Multidimensional Signal Processing*. Ph.D. thesis, Linköping University. DOI: 10.1.1.126.9491.

Boykov, Y., & Kolmogorov, V. (2004). An experimental comparison of min-cut/max-flow algorithms for energy minimization in vision. *IEEE Transactions on Pattern Analysis and Machine Intelligence*, *26*(9), 1124–1137. DOI: 10.1109/TPAMI.2004.60.

Boykov, Y., & Veksler, O. (2006). Graph cuts in vision and graphics: Theories and applications. In *Handbook of mathematical models in computer vision*, (pp. 79–96). Springer. DOI: 10.1007/0-387-28831-7.

Boykov, Y., Veksler, O., & Zabih, R. (1998). Markov random fields with efficient approximations. In *IEEE Conference on Computer vision and pattern recognition*, (pp. 648–655). IEEE. DOI: 10.1109/CVPR.1998.698673.

Boykov, Y., Veksler, O., & Zabih, R. (2001). Fast approximate energy minimization via graph cuts. *IEEE Transactions on Pattern Analysis and Machine Intelligence*, *23*(11), 1222–1239. DOI: 10.1109/34.969114.

Boykov, Y. Y., & Jolly, M.-P. (2001). Interactive graph cuts for optimal boundary & region segmentation of objects in ND images. In *Eighth IEEE International Conference on Computer Vision, 2001. ICCV 2001. Proceedings.*, vol. 1, (pp. 105–112). IEEE. Available online at csd.uwo.ca/~yuri/Papers/iccv01.pdf.

Brakenridge, G. R., Nghiem, S. V., Anderson, E., & Chien, S. (2005). Space-based measurement of river runoff. *Eos, Transactions, American Geophysical Union*, *86*(19), 185–188. DOI: 10.1029/2005EO190001.

Brakenridge, R., & Anderson, E. (2006). MODIS-based flood detection, mapping and measurement: the potential for operational hydrological applications. In *Transboundary Floods: Reducing Risks Through Flood Management*, (pp. 1–12). Springer. DOI: 10.1007/1-4020-4902-1.

Brivio, P. A., Colombo, R., Maggi, M., & Tomasoni, R. (2002). Integration of remote sensing data and GIS for accurate mapping of flooded areas. *International Journal of Remote Sensing*, *23*(3), 429–441. DOI: 10.1080/01431160010014729.

Broomhead, D. S., & King, G. P. (1986). Extracting qualitative dynamics from experimental data. *Physica D: Nonlinear Phenomena*, *20*(2-3), 217–236. DOI: 10.1016/0167-2789(86)90031-X.

Bruzzone, L., & Prieto, D. F. (2002). An adaptive semiparametric and context-based approach to unsupervised change detection in multitemporal remote-sensing images. *IEEE Transactions on Image Processing*, *11*(4), 452–466. DOI: 10.1109/TIP.2002.999678.

Bustos, C., Campanella, O., Kpalma, K., Magnago, F., & Ronsin, J. (2011). A method for change detection with multi-temporal satellite images based on principal component analysis. In *6th International Workshop on the Analysis of Multi-temporal Remote Sensing Images*, (pp. 197–200). IEEE. DOI: 10.1109/Multi-Temp.2011.6005082.

Calkoen, C., Hesselmans, G., Wensink, G., & Vogelzang, J. (2001). The bathymetry assessment system: efficient depth mapping in shallow seas using radar images. *International Journal of Remote Sensing*, *22*(15), 2973–2998. DOI: 10.1080/01431160116928.

Canty, M. J., & Nielsen, A. A. (2008). Automatic radiometric normalization of multitemporal satellite imagery with the iteratively re-weighted MAD transformation. *Remote Sensing of Environment*, *112*(3), 1025–1036. DOI: 10.1016/j.rse.2007.07.013.

Canty, M. J., Nielsen, A. A., & Schmidt, M. (2004). Automatic radiometric normalization of multitemporal satellite imagery. *Remote Sensing of Environment*, *91*(3), 441–451. DOI: 10.1016/j.rse.2003.10.024.

Cao, W. (2013). *Change detection using SAR data*. Master's thesis, University of Stuttgart. Available online at elib.uni-stuttgart.de/opus/volltexte/2013/8682.

Carlowicz, M. (2010). World of change: global temperatures: feature articles. Available online at earthobservatory.nasa.gov/Features/WorldOfChange/decadaltemp.php.

Carroll, M., Wooten, M., DiMiceli, C., Sohlberg, R., & Kelly, M. (2016). Quantifying Surface Water Dynamics at 30 Meter Spatial Resolution in the North American High Northern Latitudes 1991–2011. *Remote Sensing*, *8*(8), 622. DOI: 10.3390/rs8080622.

Chapron, B., Collard, F., & Ardhuin, F. (2005). Direct measurements of ocean surface velocity from space: Interpretation and validation. *Journal of Geophysical Research: Oceans*, *110*(C7). DOI: 10.1029/2004JC002809.

Chen, Q., van Dam, T., Sneeuw, N., Collilieux, X., Weigelt, M., & Rebischung, P. (2013). Singular spectrum analysis for modeling seasonal signals from GPS time series. *Journal of Geodynamics*, *72*, 25–35. DOI: 10.1016/j.jog.2013.05.005.

Chow, V. (1964). Handbook of applied hydrology; a compendium of water-resources technology. Tech. rep. Available online at agris.fao.org/agris-search/search.do?recordID=XF2015027880.

Couprie, C., Grady, L., Najman, L., & Talbot, H. (2011). Power watershed: A unifying graph-based optimization framework. *IEEE Transactions on Pattern Analysis and Machine Intelligence*, *33*(7), 1384–1399. DOI: 10.1109/TPAMI.2010.200.

Crétaux, J.-F., Abarca-del Río, R., Berge-Nguyen, M., Arsen, A., Drolon, V., Clos, G., & Maisongrande, P. (2016). Lake volume monitoring from space. *Surveys in Geophysics*, *37*(2), 269–305. DOI: 10.1007/s10712-016-9362-6.

Crétaux, J.-F., & Birkett, C. (2006). Lake studies from satellite radar altimetry. *Comptes Rendus Geoscience*, *338*(14-15), 1098–1112. DOI: 10.1016/j.crte.2006.08.002.

Crist, E. P., & Cicone, R. C. (1984). A Physically-Based Transformation of Thematic Mapper Data—The TM Tasseled Cap. *IEEE Transactions on Geoscience and Remote Sensing*, *GE-22*(3), 256–263. DOI: 10.1109/TGRS.1984.350619.

Davis, P. A. (2004). Review of results and recommendations from the gcmrc 2000-2003 remote-sensing initiative for monitoring environmental resources within the colorado river ecosystem. Tech. rep. Available online at pubs.usgs.gov/of/2004/1206/.

Deer, P. (1995). Digital change detection techniques in remote sensing. Available online at dspace.dsto.defence.gov.au/dspace/bitstream/1947/4389/1/DSTO-TR-0169.pdf.

Del Genfo, A. D., Lacis, A. A., & Ruedy, R. A. (1991). Simulations of the effect of a warmer climate on atmospheric humidity. *Nature*, *351*(6325), 382–385. DOI: 10.1038/351382a0.

Dingman, S. L., & Sharma, K. P. (1997). Statistical development and validation of discharge equations for natural channels. *Journal of Hydrology*, *199*(1-2), 13–35. DOI: 10.1016/S0022-1694(96)03313-6.

Dinits, E. (1970). Algorithms for solution of a problem of maximum flow in a network with power estimation. *Soviet Math. Cokl.*, *11*, 1277–1280.

Doña, C., Chang, N.-B., Caselles, V., Sánchez, J. M., Pérez-Planells, L., Bisquert, M. d. M., García-Santos, V., Imen, S., & Camacho, A. (2016). Monitoring Hydrological Patterns of Temporary Lakes Using Remote Sensing and Machine Learning Models: Case Study of La Mancha Humeda Biosphere Reserve in Central Spain. *Remote Sensing*, *8*(8), 618. DOI: 10.3390/rs8080618.

Du, Y., Teillet, P. M., & Cihlar, J. (2002). Radiometric normalization of multitemporal high-resolution satellite images with quality control for land cover change detection. *Remote Sensing of Environment*, *82*(1), 123–134. DOI: 10.1016/S0034-4257(02)00029-9.

Durand, M., Andreadis, K. M., Alsdorf, D. E., Lettenmaier, D. P., Moller, D., & Wilson, M. (2008). Estimation of bathymetric depth and slope from data assimilation of swath altimetry into a hydrodynamic model. *Geophysical Research Letters*, *35*(20). DOI: 10.1029/2008GL034150.

Durand, M., Fu, L.-L., Lettenmaier, D. P., Alsdorf, D. E., Rodriguez, E., & Esteban-Fernandez, D. (2010). The surface water and ocean topography mission: Observing terrestrial surface water and oceanic submesoscale eddies. *Proceedings of the IEEE*, *98*(5), 766–779. DOI: 10.1109/JPROC.2010.2043031.

Eklundh, L., & Singh, A. (1993). A comparative analysis of standardised and unstandardised principal components analysis in remote sensing. *International Journal of Remote Sensing*, *14*(7), 1359–1370. DOI: 10.1080/01431169308953962.

Elmi, O. (2015). *The role of multispectral image transformations in change detection*. Master's thesis, University of Stuttgart. Available online at: elib.uni-stuttgart.de/opus/volltexte/2015/10055/.

Elmi, O., Tourian, M. J., & Sneeuw, N. (2015). River discharge estimation using channel width from satellite imagery. In *2015 IEEE International Geoscience and Remote Sensing Symposium (IGARSS)*, (pp. 727–730). IEEE. DOI: 978-1-4799-7929-5/15.

Elmi, O., Tourian, M. J., & Sneeuw, N. (2016). Dynamic River Masks from Multi-Temporal Satellite Imagery: An Automatic Algorithm Using Graph Cuts Opti-

mization. *Remote Sensing*, *8*(12). DOI: 10.3390/rs8121005.

ESA (2003). Observing the Earth: ERS 1 and 2. Available online at esa.int/Our_Activities/Observing_the_Earth/ERS_1_and_2.

Farr, T. G., Rosen, P. A., Caro, E., Crippen, R., Duren, R., Hensley, S., Kobrick, M., Paller, M., Rodriguez, E., Roth, L., et al. (2007). The shuttle radar topography mission. *Reviews of geophysics*, *45*(2). DOI: 10.1029/2005RG000183.

Fekete, B. M., & Vörösmarty, C. J. (2007). The current status of global river discharge monitoring and potential new technologies complementing traditional discharge measurements. (November 2002), 20–22. Available online at hydrologie.org/redbooks/a309/309015.pdf.

Feyisa, G. L., Meilby, H., Fensholt, R., & Proud, S. R. (2014). Automated water extraction index: A new technique for surface water mapping using landsat imagery. *Remote Sensing of Environment*, *140*, 23–35. DOI: 10.1016/j.rse.2013.08.029.

Fisher, A., & Danaher, T. (2013). A Water Index for SPOT 5 HRG Satellite Imagery, New South Wales, Australia, Determined by Linear Discriminant Analysis. *Remote Sensing*, *5*(11), 5907. DOI: 10.3390/rs5115907.

Ford, L., & Fulkerson, D. R. (1962). *Flows in networks*. Princeton Princeton University Press.

Frappart, F., Calmant, S., Cauhopé, M., Seyler, F., & Cazenave, A. (2006). Preliminary results of ENVISAT RA-2-derived water levels validation over the Amazon basin. *Remote Sensing of Environment*, *100*(2), 252–264. DOI: 10.1016/j.rse.2005.10.027.

Fu, L.-L., & Holt, B. (1982). Seasat views oceans and sea ice with synthetic aperture radar.

Fung, T., & Ledrew, E. (1987). Application of principal components analysis to change detection. *Photogrammetric engineering and remote sensing*, *53*(12), 1649–1658. Available online at asprs.org/wp-content/uploads/pers/1987journal/dec/1987_dec_1649-1658.pdf.

Gail, W. B. (2007). Remote sensing in the coming decade: the vision and the reality. *Journal of Applied Remote Sensing*, *1*(1). DOI: 10.1117/1.2539774.

Gao, B. (1996). NDWI-A normalized difference water index for remote sensing of vegetation liquid water from space. *Remote sensing of environment*, *58*(3), 257–266. DOI: 10.1016/S0034-4257(96)00067-3.

Gao, H., Birkett, C., & Lettenmaier, D. P. (2012). Global monitoring of large reservoir storage from satellite remote sensing. *Water Resources Research*, *48*(9). DOI: 10.1029/2012WR012063.

Garay, M. J., & Diner, D. J. (2007). Multi-angle Imaging SpectroRadiometer (MISR) time-lapse imagery of tsunami waves from the 26 December 2004 Sumatra–Andaman earthquake. *Remote sensing of environment*, *107*(1), 256–263. DOI:

10.1016/j.rse.2006.10.022.

Geman, S., & Geman, D. (1984). Stochastic relaxation, Gibbs distributions, and the Bayesian restoration of images. *IEEE Transactions on Pattern Analysis and Machine Intelligence*, (6), 721–741. DOI: 10.1109/TPAMI.1984.4767596.

Ghil, M., Allen, M. R., Dettinger, M. D., Ide, K., Kondrashov, D., Mann, M. E., Robertson, A. W., Saunders, A., Tian, Y., Varadi, F., & Yiou, P. (2002). Advanced spectral methods for climatic time series. *Reviews of Geophysics*, *40*(1), 1–41. DOI: 10.1029/2000RG000092.

Gilchrist, W. G. (2000). *Statistical Modelling with Quantile Functions Statistical Modelling with Quantile Functions*. CRC Press. ISBN: 1584881747.

Glasbey, C. A. (1993). An analysis of histogram-based thresholding algorithms. *CVGIP: Graphical models and image processing*, *55*(6), 532–537. DOI: 10.1006/cgip.1993.1040.

Goldberg, A. V., Hed, S., Kaplan, H., Tarjan, R. E., & Werneck, R. F. (2011). Maximum flows by incremental breadth-first search. In *Algorithms–ESA 2011*, (pp. 457–468). Springer. DOI: 10.1007/978-3-642-23719-5-39.

Goldberg, A. V., & Tarjan, R. E. (1988). A new approach to the maximum-flow problem. *Journal of the ACM (JACM)*, *35*(4), 921–940. DOI: 10.1145/48014.61051.

Goldstein, R. M., & Zebker, H. (1987). Interferometric radar measurement of ocean surface currents. *Nature*, *328*, 707–709. DOI: 10.1038/328707a0.

Gong, P. (1993). Change Detection Using Principal Component Analysis and Fuzzy Set Theory. *Canadian Journal of Remote Sensing*, *19*(1), 22–29. DOI: 10.1080/07038992.1993.10855147.

Greig, D., Porteous, B., & Seheult, A. H. (1989). Exact maximum a posteriori estimation for binary images. *Journal of the Royal Statistical Society. Series B (Methodological)*, (pp. 271–279). Available online at jstor.org/stable/2345609.

Grünler, S., Romeiser, R., & Stammer, D. (2013). Estimation of tidally influenced estuarine river discharge from space using along-track insar technology: A model-based feasibility study. *Journal of Geophysical Research: Oceans*, *118*(7), 3679–3693. DOI: 10.1002/jgrc.20269.

Gupta, H. V., Sorooshian, S., & Yapo, P. O. (1999). Status of automatic calibration for hydrologic models: Comparison with multilevel expert calibration. *Journal of Hydrologic Engineering*, *4*(2), 135–143. DOI: 10.1061/(ASCE)1084-0699(1999)4:2(135).

Habib, E., Krajewski, W. F., & Kruger, A. (2001). Sampling errors of tipping-bucket rain gauge measurements. *Journal of Hydrologic Engineering*, *6*(2), 159–166. DOI: 10.1061/(ASCE)1084-0699(2001)6:2(159).

Han, S.-C., Jekeli, C., & Shum, C. (2004). Time-variable aliasing effects of ocean tides, atmosphere, and continental water mass on monthly mean GRACE gravity field. *Journal of Geophysical Research: Solid Earth*, *109*(B4). DOI: 10.1016/j.jog.2004.08.002.

Hansen, J., Ruedy, R., Sato, M., & Lo, K. (2010). Global surface temperature change. *Reviews of Geophysics*, *48*(4). DOI: 10.1029/2010RG000345.

Hassanzadeh, E., Zarghami, M., & Hassanzadeh, Y. (2012). Determining the main factors in declining the Urmia Lake level by using system dynamics modeling. *Water Resources Management*, *26*(1), 129–145. DOI: 10.1007/s11269-011-9909-8.

Held, I. M., & Soden, B. J. (2000). Water vapor feedback and global warming. *Annual review of energy and the environment*, *25*(1), 441–475. DOI: 10.1146/annurev.energy.25.1.441.

Hotelling, H. (1936). Relations between two sets of variates. *Biometrika*, *28*(3/4), 321–377. DOI: 10.2307/2333955.

Huang, C., Chen, Y., Zhang, S., Li, L., Shi, K., & Liu, R. (2016). Surface water mapping from suomi npp-viirs imagery at 30 m resolution via blending with landsat data. *Remote Sensing*, *8*(8), 631. DOI: 10.3390/rs8080631.

Huntington, T. G. (2006). Evidence for intensification of the global water cycle: review and synthesis. *Journal of Hydrology*, *319*(1), 83–95. DOI: 10.1016/j.jhydrol.2005.07.003.

IPCC (2001). Climate Change 2001: The Scientific Basis. Contribution of Working Group I to the Third Assessment Report of the Intergovernmental Panel on Climate Change. [Houghton, J.T., Y. Ding, D.J. Griggs, M. Noguer, P.J. van der Linden, X. Dai, K. Maskell, and C.A. Johnson (eds.)]. *Cambridge University Press*, Cambridge, United Kingdom and New York, NY, USA, 881pp., ISBN: 0521 80767 0.

Ishikawa, H., & Geiger, D. (1998). Segmentation by grouping junctions. In *IEEE Conference on Computer Vision and Pattern Recognition*, (pp. 125–131). IEEE. DOI: 10.1109/CVPR.1998.698598.

Jarihani, A. A., McVicar, T. R., Van Niel, T. G., Emelyanova, I. V., Callow, J. N., & Johansen, K. (2014). Blending Landsat and MODIS data to generate multispectral indices: A comparison of "Index-then-Blend" and "Blend-then-Index" approaches. *Remote Sensing*, *6*(10), 9213–9238. DOI: 10.3390/rs6109213.

Kallio, K., Attila, J., Härmä, P., Koponen, S., Pulliainen, J., Hyytiäinen, U.-M., & Pyhälahti, T. (2008). Landsat ETM+ images in the estimation of seasonal lake water quality in boreal river basins. *Environmental management*, *42*(3), 511–522. DOI: 10.1007/s00267-008-9146-y.

Kauth, R. J., & Thomas, G. S. (1976). The tasselled cap a graphic description of the spectral temporal development of agricultural crops as seen by Landsat. In *LARS Symposia*, (p. 159). Avaible online at docs.lib.purdue.edu/lars_symp/159.

Kim, S.-W., Hong, S.-H., & Won, J.-S. (2005). An application of l-band synthetic aperture radar to tide height measurement. *IEEE transactions on geoscience and remote sensing*, *43*(7), 1472–1478. DOI: 10.1109/TGRS.2005.846857.

Klein, I., Dietz, A., Gessner, U., Dech, S., & Kuenzer, C. (2015). Results of the Global WaterPack: A novel product to assess inland water body dynamics on a daily basis. *Remote Sensing Letters*, *6*(1), 78–87. DOI: 10.1080/2150704X.2014.1002945.

Klein, I., Dietz, A. J., Gessner, U., Galayeva, A., Myrzakhmetov, A., & Kuenzer, C. (2014). Evaluation of seasonal water body extents in Central Asia over the past 27 years derived from medium-resolution remote sensing data. *International Journal of Applied Earth Observation and Geoinformation*, *26*, 335–349. DOI: 10.1016/j.jag.2013.08.004.

Klein, I., Gessner, U., Dietz, A. J., & Kuenzer, C. (2017). Global WaterPack-A 250 m resolution dataset revealing the daily dynamics of global inland water bodies. *Remote Sensing of Environment*, *198*, 345–362. DOI: 10.1016/j.rse.2017.06.045.

Koblinsky, C., Clarke, R., Brenner, A., & Frey, H. (1993). Measurement of river level variations with satellite altimetry. *Water Resources Research*, *29*(6), 1839–1848. DOI: 10.1029/93WR00542.

Kohli, P., & Torr, P. (2006). Measuring Uncertainty in Graph Cut Solutions efficiently Computing Min-marginal Energies Using Dynamic Graph Cuts. *Computer Vision ECCV 2006*, *01*, 30–43. DOI: 10.1007/11744047-3.

Kohli, P., & Torr, P. H. (2008). Measuring uncertainty in graph cut solutions. *Computer Vision and Image Understanding*, *112*(1), 30–38. DOI: 10.1016/j.cviu.2008.07.002.

Kolmogorov, V., & Zabin, R. (2004). What energy functions can be minimized via graph cuts? *IEEE Transactions on Pattern Analysis and Machine Intelligence*, *26*(2), 147–159. DOI: 10.1109/TPAMI.2004.1262177.

Künzer, C., Guo, H., Huth, J., Leinenkugel, P., Li, X., & Dech, S. (2013). Flood mapping and flood dynamics of the mekong delta: ENVISAT-ASAR-WSM based time series analyses. *Remote Sensing*, *5*(2), 687. DOI: 10.3390/rs5020687.

Künzer, C., Klein, I., Ullmann, T., Georgiou, E. F., Baumhauer, R., & Dech, S. (2015). Remote sensing of river delta inundation: exploiting the potential of coarse spatial resolution, temporally-dense modis time series. *Remote Sensing*, *7*(7), 8516–8542. DOI: 10.3390/rs70708516.

Lake Rukwa Basin Water Board (2014). Bathymetric survey report. Tech. rep. Available online at lakerukwabasin.co.tz/Lake%20Rukwa_Bathymetry_Survey_Final_Report.pdf.

Lambin, E. F., & Strahler, A. H. (1994). Indicators of land-cover change for change-vector analysis in multitemporal space at coarse spatial scales. *International Journal of Remote Sensing*, *15*(10), 2099–2119. DOI: 10.1080/01431169408954230.

Legleiter, C. J., & Roberts, D. A. (2009). A forward image model for passive optical remote sensing of river bathymetry. *Remote Sensing of Environment*, *113*(5), 1025–1045. DOI: 10.1016/j.rse.2009.01.018.

Legleiter, C. J., Roberts, D. A., & Lawrence, R. L. (2009). Spectrally based remote sensing of river bathymetry. *Earth Surface Processes and Landforms*, *34*(8), 1039–1059. DOI: 10.1002/esp.1787.

Legleiter, C. J., Roberts, D. A., Marcus, W. A., & Fonstad, M. A. (2004). Passive optical remote sensing of river channel morphology and in-stream habitat: Physical basis and feasibility. *Remote Sensing of Environment*, *93*(4), 493–510. DOI: 10.1016/j.rse.2004.07.019.

Lehner, B., & Döll, P. (2004). Development and validation of a global database of lakes, reservoirs and wetlands. *Journal of Hydrology*, *296*(1), 1–22. DOI: 10.1016/j.jhydrol.2004.03.028.

Leopold, L. B., & Maddock Jr, T. (1953). The hydraulic geometry of stream channels and some physiographic implications. Available online at pubs.usgs.gov/pp/0252/report.pdf.

Li, C. H., & Lee, C. K. (1993). Minimum cross entropy thresholding. *Pattern Recognition*, *26*(4), 617–625. DOI: 10.1016/0031-3203(93)90115-D.

Loaiciga, H. A., Valdes, J. B., Vogel, R., Garvey, J., & Schwarz, H. (1996). Global warming and the hydrologic cycle. *Journal of Hydrology*, *174*(1), 83–127. DOI: 10.1016/0022-1694(95)02753-X.

Lorenz, C., & Kunstmann, H. (2012). The hydrological cycle in three state-of-the-art reanalyses: Intercomparison and performance analysis. *Journal of Hydrometeorology*, *13*(5), 1397–1420. DOI: 10.1175/JHM-D-11-088.1.

Lu, D., Mausel, P., Brondizio, E., & Moran, E. (2004). Change detection techniques. *International journal of remote sensing*, *25*(12), 2365–2401. DOI: 10.1080/0143116031000139863.

Lu, Z., Crane, M., Kwoun, O.-I., Wells, C., Swarzenski, C., & Rykhus, R. (2005). C-band radar observes water level change in swamp forests. *EOS, Transactions American Geophysical Union*, *86*(14), 141–144. DOI: 10.1029/2005EO140002.

Maidment, D. R. (1992). *Handbook of hydrology*. McGraw-Hill Inc. ISBN: 978-0070397323.

Manabe, S., Wetherald, R. T., Milly, P., Delworth, T. L., & Stouffer, R. J. (2004). Century-scale change in water availability: Co2-quadrupling experiment. *Climatic Change*, *64*(1-2), 59–76. DOI: 10.1023/B:CLIM.0000024674.37725.ca.

Marcus, W. A., & Fonstad, M. A. (2008). Optical remote mapping of rivers at sub-meter resolutions and watershed extents. *Earth Surface Processes and Landforms*, *33*(1), 4–24. DOI: 10.1002/esp.1637.

Martinis, S. (2010). *Automatic near real-time flood detection in high resolution X-band synthetic aperture radar satellite data using context-based classification on irregular graphs*. Ph.D. thesis, Ludwig-Maximilians-University Munich, Munich, Germany. Availbe online at nbn-resolving.de/urn:nbn:de:bvb:19-123731.

Martinis, S., & Twele, A. (2010). A hierarchical spatio-temporal markov model for improved flood mapping using multi-temporal x-band sar data. *Remote Sensing*, *2*(9), 2240–2258. DOI: 10.3390/rs2092240.

Martinis, S., Twele, A., Strobl, C., Kersten, J., & Stein, E. (2013). A Multi-Scale Flood Monitoring System Based on Fully Automatic MODIS and TerraSAR-X Processing Chains. *Remote Sensing*, *5*(11), 5598–5619. DOI: 10.3390/rs5115598.

Martinis, S., Twele, A., & Voigt, S. (2009). Towards operational near real-time flood detection using a split-based automatic thresholding procedure on high resolution TerraSAR-X data. *Natural Hazards & Earth System Sciences*, *9*(2). DOI: 10.5194/nhess-9-303-2009.

Mc Candless, S. W., & Jackson, C. (2004). Principles of synthetic aperture radar. *SAR Marine User Manual*, (pp. 1–23). Avaible online at sarusersmanual.com/ManualPDF/NOAASARManual_CH01_pg001-024.pdf.

McFeeters, S. K. (1996). The use of the Normalized Difference Water Index (NDWI) in the delineation of open water features. *International journal of remote sensing*, *17*(7), 1425–1432. DOI: 10.1080/01431169608948714.

McFeeters, S. K. (2013). Using the Normalized Difference Water Index (NDWI) within a Geographic Information System to Detect Swimming Pools for Mosquito Abatement: A Practical Approach. *Remote Sensing*, *5*(7), 3544. DOI: 10.3390/rs5073544.

McGinley, M. (2013). Niger River. Available online at eoearth.org/view/article/226069.

Memarsadeghi, N., Mount, D. M., Netanyahu, N. S., & Le Moigne, J. (2007). A fast implementation of the ISODATA clustering algorithm. *International Journal of Computational Geometry & Applications*, *17*(01), 71–103. DOI: 10.1142/S0218195907002252.

Miralles, D., De Jeu, R., Gash, J., Holmes, T., & Dolman, A. (2011). Magnitude and variability of land evaporation and its componentsat the global scale. *Hydrology and Earth System Sciences*, *15*(3), 967–981. DOI: 10.5194/hess-15-967-2011.

Moser, G., & Serpico, S. B. (2006). Generalized minimum-error thresholding for unsupervised change detection from SAR amplitude imagery. *Geoscience and Remote Sensing, IEEE Transactions on*, *44*(10), 2972–2982. DOI: 10.1109/TGRS.2006.876288.

Mostafa, M., & Soussa, H. (2006). Monitoring of Lake Nasser using remote sensing and GIS techniques. In *ISPRS commission VII mid-term symposium remote sensing: from pixels to processes. Enschede, The Netherlands*. Avaible online at aun.edu.eg/megwrm/sub/workshope6/1.pdf.

Mota, G. L., Feitosa, R. Q., Coutinho, H. L., Liedtke, C.-E., Müller, S., Pakzad, K., & Meirelles, M. S. (2007). Multitemporal fuzzy classification model based on class transition possibilities. *ISPRS journal of photogrammetry and remote sensing*, *62*(3), 186–200. DOI: 10.1016/j.isprsjprs.2007.04.001.

Munyati, C. (2004). Use of principal component analysis (PCA) of remote sensing images in wetland change detection on the Kafue Flats, Zambia. *Geocarto International*, *19*(3), 11–22. DOI: 10.1080/10106040408542313.

NASA (2007). Sputnik and The Dawn of the Space Age. Available online at nasa.gov/office/pao/History/sputnik/.

Nash, J. E., & Sutcliffe, J. V. (1970). River flow forecasting through conceptual models part I-A discussion of principles. *Journal of hydrology*, *10*(3), 282–290. DOI: 10.1016/0022-1694(70)90255-6.

NAST (2001). National Assessment Synthesis Team, 2001: Climate Change Impacts on the United States: The Potential Consequences of Climate Variability and Change: Overview, US Global Change Research Program. *Cambridge University Press*, (p. 612). ISBN: 0-521-00075-0.

National Research Council (2001). *Climate change science: an analysis of some key questions*. National Research Council, National Academy Press. Available online at nap.edu/catalog/10139/climate-change-science-an-analysis-of-some-key-questions.

Nielsen, A. A. (1995). *Analysis of Regularly and Irregularly Sampled Spatial , Multivariate , and Multi-temporal Data*. Ph.D. thesis, Technical University of Denmark. Available online at compute.dtu.dk/~alan/phd/phd-no-figs.pdf.

Nielsen, A. A. (2007). The regularized iteratively reweighted MAD method for change detection in multi- and hyperspectral data. *IEEE transactions on image processing : a publication of the IEEE Signal Processing Society*, *16*(2), 463–78. DOI: 10.1109/TIP.2006.888195.

Nielsen, A. A. (2011). Kernel maximum autocorrelation factor and minimum noise fraction transformations. *IEEE Transactions on Image Processing*, *20*(3), 612–624. DOI: 10.1109/TIP.2010.2076296.

Nielsen, A. A., Conradsen, K., & Andersen, O. B. (2002). A change oriented extension of EOF analysis applied to the 1996–1997 AVHRR sea surface temperature data. *Physics and Chemistry of the Earth, Parts A/B/C*, *27*(32), 1379–1386. DOI: 10.1016/S1474-7065(02)00075-X.

Nielsen, A. A., Conradsen, K., & Simpson, J. J. (1998). Multivariate alteration detection (MAD) and MAF postprocessing in multispectral, bitemporal image data: New approaches to change detection studies. *Remote Sensing of Environment*, *64*(1), 1–19. DOI: 10.1016/S0034-4257(97)00162-4.

Niemeier, W. (2008). *Ausgleichungsrechnung: Statistische Auswertemethoden*. Walter de Gruyter. ISBN: 978-3110190557.

O'Loughlin, F., Trigg, M., Schumann, G.-P., & Bates, P. (2013). Hydraulic characterization of the middle reach of the Congo River. *Water Resources Research*, *49*(8), 5059–5070. DOI: 10.1002/wrcr.20398.

Otsu, N. (1979). A threshold selection method from gray-level histograms. *IEEE Transactions on Systems, Man, and Cybernetics*, *9*(1), 62–66. DOI: 10.1109/TSMC.1979.4310076.

Papa, F., Durand, F., Rossow, W. B., Rahman, A., & Bala, S. K. (2010). Satellite altimeter-derived monthly discharge of the Ganga-Brahmaputra River and its seasonal to interannual variations from 1993 to 2008. *Journal of Geophysical Research: Oceans*, *115*(C12). DOI: 10.1029/2009JC006075.

Pavelsky, T. M. (2012). Recent progress in development of SWOT river discharge algorithms, Department of Geological Sciences, University of North Carolina and participants in the 2012 SWOT Discharge Algorithms Workshop, June 18-20, Chapel Hill, NC. (pp. 1–9). Available online ate unc.edu/~pavelsky/Pavelsky/Home_files/Pavelsky_etal_Discharge_WhitePaper_2012_final.pdf.

Pavelsky, T. M. (2014). Using width-based rating curves from spatially discontinuous satellite imagery to monitor river discharge. *Hydrological Processes*, *28*(6), 3035–3040. DOI: 10.1002/hyp.10157.

Pelton, J. N., Madry, S., & Camacho-Lara, S. (2012). *Handbook of satellite applications*. Springer Publishing Company, ISBN:1441976701, 9781441976703.

Pengra, B. (2012). The drying of Iran's Lake Urmia and its environmental consequences. Tech. rep., UNEP-GRID, Sioux Falls, UNEP Global Environmental Alert Service (GEAS). Available online at na.unep.net/geas/getUNEPPageWithArticleIDScript.php?article_id=79.

Prigent, C., Papa, F., Aires, F., Rossow, W., & Matthews, E. (2007). Global inundation dynamics inferred from multiple satellite observations, 1993–2000. *Journal of Geophysical Research: Atmospheres (1984–2012)*, *112*(D12). DOI: 10.1029/2006JD007847.

Radke, R. J., Andra, S., Al-Kofahi, O., & Roysam, B. (2005). Image change detection algorithms: a systematic survey. *Image Processing, IEEE Transactions on*, *14*(3), 294–307. DOI: 10.1109/TIP.2004.838698.

Rice, J. (2006). *Mathematical statistics and data analysis*. Cengage Learning. Available online at staff.ustc.edu.cn/~glliu/astrostat/Mathematical_Statistics_and_Data_Analysis-3ed-Rice.pdf.

Richards, J., Woodgate, P., & Skidmore, A. (1987). An explanation of enhanced radar backscattering from flooded forests. *International Journal of Remote Sensing*, *8*(7), 1093–1100. DOI: 10.1080/01431168708954756.

Richards, J. A., & Jia, X. (1999). *Remote sensing digital image analysis*, vol. 3. Springer. ISBN: 978-3-642-30062-2.

Rodell, M., & Famiglietti, J. (1999). Detectability of variations in continental water storage from satellite observations of the time dependent gravity field. *Water Resources Research*, *35*(9). DOI: 10.1029/1999WR900141.

Romeiser, R. (2015). Surface current measurements by spaceborne along-track inSAR-terraSAR-X, tanDEM-X, and future systems. In *Current, Waves and Turbulence Measurement (CWTM), 2015 IEEE/OES Eleventh*, (pp. 1–4). IEEE. DOI: 10.1109/CWTM.2015.7098097.

Romeiser, R., Breit, H., Eineder, M., Runge, H., Flament, P., de Jong, K., & Vogelzang, J. (2005). Current measurements by sar along-track interferometry from a space shuttle. *IEEE Transactions on Geoscience and Remote Sensing*, *43*(10), 2315–2324. DOI: 10.1109/TGRS.2005.856116.

Romeiser, R., Johannessen, J., Chapron, B., Collard, F., Kudryavtsev, V., Runge, H., & Suchandt, S. (2010a). Direct surface current field imaging from space by along-track InSAR and conventional SAR. In *Oceanography from Space*, (pp. 73–91). Springer. DOI: 10.1007/978-90-481-8681-5-5.

Romeiser, R., Runge, H., Suchandt, S., Sprenger, J., Weilbeer, H., Sohrmann, A., & Stammer, D. (2007). Current Measurements in Rivers by Spaceborne Along-Track InSAR. *IEEE Transactions on Geoscience and Remote Sensing*, *45*(12), 4019–4031. DOI: 10.1109/TGRS.2007.904837.

Romeiser, R., Seibt-Winckler, A., Heineke, M., & Eppel, D. (2002). Validation of current and bathymetry measurements in the German Bight by airborne along-track interferometric SAR. In *Geoscience and Remote Sensing Symposium,IGARSS, IEEE International*, vol. 3, (pp. 1822–1824). IEEE. DOI: 10.1109/IGARSS.2002.1026266.

Romeiser, R., Suchandt, S., Runge, H., Steinbrecher, U., & Grunler, S. (2010b). First analysis of TerraSAR-X along-track InSAR-derived current fields. *IEEE Transactions on Geoscience and Remote Sensing*, *2*(48), 820–829. DOI: 10.1109/TGRS.2009.2030885.

Rosenfeld, A., & De La Torre, P. (1983). Histogram concavity analysis as an aid in threshold selection. *IEEE Transactions on Systems, Man, and Cybernetics*, (2), 231–235. DOI: 10.1109/TSMC.1983.6313118.

Rouse Jr, J., Haas, R., Schell, J., & Deering, D. (1974). Monitoring vegetation systems in the Great Plains with ERTS. *Third 80 ERTS Symposium, NASASP-351*. Available online at ntrs.nasa.gov/archive/nasa/casi.ntrs.nasa.gov/19740022614.pdf.

Ryu, J.-H., Won, J.-S., & Min, K. D. (2002). Waterline extraction from landsat tm data in a tidal flat: a case study in gomso bay, korea. *Remote Sensing of Environment*, *83*(3), 442–456. http://dx.doi.org/10.1016/S0034-4257(02)00059-7.

Sandholt, I., Nyborg, L., Fog, B., Lô, M., Bocoum, O., & Rasmussen, K. (2003). Remote sensing techniques for flood monitoring in the Senegal River Valley. *Geografisk Tidsskrift-Danish Journal of Geography*, *103*(1), 71–81. DOI: 10.1080/00167223.2003.10649481.

Schimmer, R. (2009). An Introduction to Remote Sensing & GIS Introduction. Available online at gsp.yale.edu/sites/default/files/files/An-Introduction-to-Remote-Sensing-GIS-2009.pdf.

Schwatke, C., Dettmering, D., Bosch, W., & Seitz, F. (2015). DAHITI–an innovative approach for estimating water level time series over inland waters using multi-mission satellite altimetry. *Hydrology and Earth System Sciences*, *19*(10), 4345–4364. DOI: 10.5194/hess-19-4345-2015.

Sezgin, M., & Sankur, B. (2004). Survey over image thresholding techniques and quantitative performance evaluation. *Journal of Electronic imaging*, *13*(1), 146–168. DOI: 10.1117/1.1631315.

Shippert, P. (2003). Introduction to hyperspectral image analysis. *Online Journal of Space Communication*, *3*. Available online at spacejournal.ohio.edu/pdf/shippert.pdf.

Shuchman, R. (1979). The feasibility of Measurement of Ocean Current Detection Using SAR data. In R. Beal (Ed.) *Proc. of the 13th Int. Symp on Remote Sensing of the Environment, Ann Arbor*, (pp. 93–103). Applied Physics Laboratory, Johns Hopkins University.

Singh, A. (1989). Digital change detection techniques using remotely-sensed data. *International Journal of Remote Sensing*, (pp. 37–41). DOI: 10.1080/01431168908903939.

Sissakian, V. K. (2011). Genesis and Age estimation of the Tharthar Depression, Central west Iraq. *Iraqi Bulletin of Geology and Mining*, *7*(3), 47–62.

Smith, L. C., Isacks, B. L., Bloom, A. L., & Murray, a. B. (1996). Estimation of Discharge From Three Braided Rivers Using Synthetic Aperture Radar Satellite Imagery: Potential Application to Ungaged Basins. *Water Resources Research*, *32*(7), 2021–2034. DOI: 10.1029/96WR00752.

Smith, L. C., & Pavelsky, T. M. (2008). Estimation of river discharge, propagation speed, and hydraulic geometry from space: Lena River, Siberia. *Water Resources Research*, *44*(3). DOI: 10.1029/2007WR006133.

Solberg, A. H. S., Taxt, T., & Jain, A. K. (1996). A Markov random field model for classification of multisource satellite imagery. *IEEE Transactions on Geoscience and Remote Sensing*, *34*(1), 100–113. DOI: 10.1109/36.481897.

Solbø, S., & Solheim, I. (2005). Towards operational flood mapping with satellite SAR. In *Envisat & ERS Symposium*, vol. 572. DOI: 10.1.1.380.4393.

Swenson, S., Wahr, J., & Milly, P. (2003). Estimated accuracies of regional water storage variations inferred from the Gravity Recovery and Climate Experiment (GRACE). *Water Resources Research*, *39*(8). DOI: 10.1029/2002WR001 808.

Switzer, P., & Green, A. A. (1984). Min/max autocorrelation factors for multivariate spatial imagery. Tech. rep., Department of Statistics - Stanford University, California. Available online at statistics.stanford.edu/sites/default/files/SWI%20NSF%2006.pdf.

Szeliski, R., Zabih, R., Scharstein, D., Veksler, O., Kolmogorov, V., Agarwala, A., Tappen, M., & Rother, C. (2006). A comparative study of energy minimization meth-

ods for markov random fields. In *European conference on computer vision*, (pp. 16–29). Springer. Available online at cs.cornell.edu/~rdz/Papers/SZSVKATR.pdf.

Tarlow, D., & Adams, R. P. (2012). Revisiting uncertainty in graph cut solutions. In *IEEE Conference on Computer Vision and Pattern Recognition (CVPR), 2012*, (pp. 2440–2447). IEEE. DOI: 10.1109/CVPR.2012.6247958.

Tempfli, K., Kerle, N., Huurneman, G. C., Janssen, L. L., Bakker, W. H., Feringa, W., Gieske, A. S. M., Grabmaier, K. A., Hecker, C. A., & Horn, J. A. (2009). *Principles of remote sensing*. The International Institute for Geo-Information Science and Earth Observation (ITC). Enschede, Netherlands. Available online at itc.nl/library/papers_2009/general/PrinciplesRemoteSensing.pdf.

Tourian, M., Tarpanelli, A., Elmi, O., Qin, T., Brocca, L., Moramarco, T., & Sneeuw, N. (2016). Spatiotemporal densification of river water level time series by multimission satellite altimetry. *Water Resources Research*. DOI: 10.1016/10.1002/2015WR017654.

Tourian, M. J. (2013). *Application of spaceborne geodetic sensors for hydrology*. Ph.D. thesis, University of Stuttgart, Stuttgart, Germany. DOI: 10.18419/opus-3929.

Tourian, M. J., Elmi, O., Chen, Q., Devaraju, B., Roohi, S., & Sneeuw, N. (2015a). A spaceborne multisensor approach to monitor the desiccation of Lake Urmia in Iran. *Remote Sensing of Environment*, *156*, 349–360. DOI: 10.1016/j.rse.2014.10.006.

Tourian, M. J., Elmi, O., Mohammadnejad, A., & Sneeuw, N. (2017). Estimating river depth from swot-type observables obtained by satellite altimetry and imagery. *Water*, *9*(10). DOI: 10.3390/w9100753.

Tourian, M. J., Sneeuw, N., & Bárdossy, A. (2013). A quantile function approach to discharge estimation from satellite altimetry (ENVISAT). *Water Resources Research*, *49*(7), 4174–4186. DOI: 10.1002/wrcr.20348.

Tourian, M. J., Thor, R., & Sneeuw, N. (2015b). Least-Squares Prediction of Runoff Over Ungauged Basins. In *IAG 150 Years*, (pp. 257–261). Springer. DOI: 10.1016/10.1007/1345-2015-170.

Townsend, P. A. (2001). Mapping seasonal flooding in forested wetlands using multitemporal Radarsat SAR. *Photogrammetric Engineering and Remote Sensing*, *67*(7), 857–864. Available online at asprs.org/wp-content/uploads/pers/2001journal/july/2001_jul_857-864.pdf.

Townsend, P. A., & Walsh, S. J. (1998). Modeling floodplain inundation using an integrated GIS with radar and optical remote sensing. *Geomorphology*, *21*(3), 295–312. DOI: 10.1016/S0169-555X(97)00069-X.

Trenberth, K. E. (1999). Conceptual framework for changes of extremes of the hydrological cycle with climate change. In *Weather and Climate Extremes*, (pp. 327–339). Springer. DOI: 10.1023/A:1005488920935.

Tsai, W.-H. (1985). Moment-preserving thresolding: A new approach. *Computer Vision, Graphics, and Image Processing*, *29*(3), 377–393. Available online at people.cs.nctu.edu.tw/~whtsai/Journal%20Paper%20PDFs/Tsai_CVGIP(journal)_1985.pdf.

Van Der Sande, C., De Jong, S., & De Roo, A. (2003). A segmentation and classification approach of IKONOS-2 imagery for land cover mapping to assist flood risk and flood damage assessment. *International Journal of Applied Earth Observation and Geoinformation*, *4*(3), 217–229. DOI: 10.1016/S0303-2434(03)00003-5.

Veksler, O. (1999). *Efficient graph-based energy minimization methods in computer vision*. Ph.D. thesis, Cornell University. Available online at classes.cs.uchicago.edu/archive/2004/fall/35900-2/graphcut.pdf.

Veksler, O. (2000). Image segmentation by nested cuts. In *IEEE Conference on Computer Vision and Pattern Recognition*, vol. 1, (pp. 339–344). IEEE. DOI: 10.1109/CVPR.2000.855838.

Velicogna, I., Wahr, J., & Van den Dool, H. (2001). Can surface pressure be used to remove atmospheric contributions from GRACE data with sufficient accuracy to recover hydrological signals? *Journal of Geophysical Research: Solid Earth*, *106*(B8), 16415–16434. DOI: 10.1029/2001JB000 228.

Vermote, E., Kotchenova, S., & Ray, J. (2011). Modis surface reflectance user's guide. Available online at modis-sr.ltdri.org/guide/MOD09_UserGuide_v1.4.pdf.

Verpoorter, C., Kutser, T., Seekell, D. A., & Tranvik, L. J. (2014). A global inventory of lakes based on high-resolution satellite imagery. *Geophysical Research Letters*, *41*(18), 6396–6402. DOI: 10.1002/2014GL060641.

Verpoorter, C., Kutser, T., & Tranvik, L. (2012). Automated mapping of water bodies using Landsat multispectral data. *Limnol. Oceanogr. Methods*, *10*, 1037–1050. DOI: 10.4319/lom.2012.10.1037.

Vörösmarty, C. J., Green, P., Salisbury, J., & Lammers, R. B. (2000). Global water resources: vulnerability from climate change and population growth. *science*, *289*(5477), 284. DOI: 10.1126/science.289.5477.284.

Wang, Y. (2004). Seasonal change in the extent of inundation on floodplains detected by JERS-1 Synthetic Aperture Radar data. *International Journal of Remote Sensing*, *25*(13), 2497–2508. https://doi.org/10.1080/01431160310001619562.

Wang, Y., Colby, J. D., & Mulcahy, K. A. (2002). An efficient method for mapping flood extent in a coastal floodplain using Landsat TM and DEM data. *International Journal of Remote Sensing*, *23*(18), 3681–3696. DOI: 10.1080/01431160110114484.

Weih Jr, R. C., & Riggan Jr, N. D. (2010). Object-based classification vs. pixel-based classification: comparative importance of multi-resolution imagery. *Proceedings of GEOBIA 2010: Geographic Object-Based Image Analysis*, *38*, 6. Available online at dfwm.ugent.be/geobia/proceedings/papers%20proceedings/Weih_81_Object_Based_Classification_vs_Pixel_Based_Classification_Comparitive_Importance_

of_Multi_Resolution_Imagery.pdf.

Wohlfart, C., Liu, G., Huang, C., & Kuenzer, C. (2016). A River Basin over the Course of Time: Multi-Temporal Analyses of Land Surface Dynamics in the Yellow River Basin (China) Based on Medium Resolution Remote Sensing Data. *Remote Sensing*, *8*(3), 186. DOI: 10.3390/rs8030186.

Wozencraft, J. M., & Lillycrop, W. J. (2002). Total shallow-water survey through airborne hydrography. Tech. rep., DTIC Document. Available online at dtic.mil/get-tr-doc/pdf?AD=ADA488962.

Xu, H. (2006). Modification of normalised difference water index (NDWI) to enhance open water features in remotely sensed imagery. *International journal of remote sensing*, *27*(14), 3025–3033. DOI: 10.1080/01431160600589179.

Zarghami, M. (2011). Effective watershed management; Case study of Urmia Lake, Iran. *Lake and Reservoir Management*, *27*(1), 87–94. DOI: 10.1080/07438141.2010.541327.

Zhang, G., Yao, T., Xie, H., Zhang, K., & Zhu, F. (2014). Lakes' state and abundance across the Tibetan Plateau. *Chinese science bulletin*, *59*(24), 3010–3021. DOI: 10.1007/s11434-014-0258-x.

Abbreviations

ALOS	Advanced Land Observation Satellite
ANN	Artificial Neural Networks
ASAR	Advanced Synthetic Aperture Radar
ARPA	Advanced Research Projects Agency
ATI	Along-Track Interferometry
AVHRR	Advanced Very High Resolution Radiometer
BFS	Breadth-First Search
CCA	Canonical Correlation Analysis
CNES	Centre National D 'Etudes Spatiales
CRU	Climatic Research Unit
DFS	Depth-First Search
DTM	Digital Terrain Model
EM	Electromagnetic
ENVISAT	ENVIronmental SATellite
EOF	Empirical Orthogonal Function
ERS	European Remote Sensing satellite
ESA	European Space Agency
ETa	Evapotranspiration
ETM+	Enhanced thematic mapper plus
GIS	Geospatial Information Systems
GLEAM	Global Land-surface Evaporation: the Amsterdam Methodology
GOCE	Gravity Field and Steady-State Ocean Circulation Explorer
GPCC	Global Precipitation Climatology Center
GPCP	Global Precipitation Climatology Project

GPS Global Positioning System

GRDC Global Runoff Data Centre

GRACE Gravity Recovery And Climate Experiment

InSAR Interferometric SAR

ISODATA Iterative Self-Organizing Data Analysis Technique Algorithm

IR InferaRed

KT Kauth Thomas transformation

LLH Lake Level Height

MAD Multivariate Alteration Detection

MAF Maximum Autocorrelation Factor

MAP Maximum A Posterior

MERRA Modern Era-Retrospective Analysis for Research and Application

MODIS Moderate Resolution Imaging Spectroradiometer

MMSNR Monthly Mean Signal to Noise Ratio

MRF Markov Random Fields

MSS Multispectral Scanner

NASA National Aeronautics and Space Administration

NCAR National Center for Atmospheric Research

NCEP National Centers for Environmental Prediction

NIR Near InferRed

NDVI Normalized Difference Vegetation Index

NDWI Normalized Difference Water Index

MNDWI Modification of Normalized Difference Water Index

NSE Nash Sutcliffe Efficiency

OLI Operational Land Imager

PCA Principal Component Analysis

RMS Root Mean Square

RMSE Root Mean Square Error

SA Simulated Annealing

SAR Synthetic aperture radar

SLAR Sidelooking Air-Borne Radar
SLC Scan Line Corrector
SLR Satellite Laser Ranging
SNR Signal to Noise Ratio
SPOT Satellite Pour l'Observation de la Terre
SRTM Shuttle Radar Topography Mission
SVD Singular Value Decomposition
SWIR Short-Wave InfeRred
SWOT Surface Water and Ocean Topography
TM Tematic Mapper
TIRS Thermal Infrared Sensor
TIROS Television Infrared Observation Satellites
TRMM Tropical Rainfall Measuring Mission
USACE United States Army Corps of Engineers
USGS United States Geological Survey
WGS World Geodetic System

List of Figures

1.1 Different optical and SAR imagining missions. 5
1.2 Schematic illustration of the hydrological cycle 6
1.3 Spatial distribution of gauges with available runoff data in the data base of GRDC around the world for 1970, 1985, 2000 and 2010 (Tourian et al., 2015b). 7
1.4 Number of available satellite images improves significantly during the last three decades. On the other hand, number of stations with available discharge measurements have decreased. In this figure, the variety of spatial resolution in the different missions is not considered. 13
1.5 The electromagnetic spectrum 15
1.6 River and lakes used as case study in this thesis. Red dots in river sections present the location of in situ station 25

2.1 A schematic sketch of the Tasselled Cap transformation (Kauth & Thomas, 1976) 40
2.2 RGB images of the Niger River derived from MODIS MOD09A1 at three different epochs 46
2.3 The procedure of PCA transformation on a single multispectral image . . 47
2.4 Different image bands and PCs derived from covariance and correlation matrices 48
2.5 Improving the signal to noise ratio by reconstructing the images considering few primary PCs. Original RGB images are in the first column. The reconstructed images by removing the later PCs are in the second columns. The original and reconstructed band 2 of the three epochs are presented in the third and fourth columns. 49
2.6 (a) ordinary RGB image. (b) combination of first three PCs as image bands. (c) is the selected area for more investigation. Date of the image: 2012.01.01 50
2.7 Ordinary RGB images are presented in the first column. The second column shows the reconstructed images and the maps of first three PCs are presented in the last column. 51
2.8 Comparison between RGB image and map of the selected PCs. Image date 2012.01.01 52
2.9 Comparison of original RGB images and maps generated by three selected PC. In the second row, each PCs map includes respectively PCs number: (2, 3, 6), (6, 2, 5), (5, 3, 2). 53
2.10 Procedure of applying PCA on multitemporal images 53

2.11 (left) an image composed of PCs 1, 4, 11. (right) comparison of a small part of the product with the original images. Image dates 2012.01.01 and 2012.09.19 54
2.12 Applying PCA on an image difference of two multitemporal images. . . 56
2.13 (a) and (b) are the original RGB images. Map in (c) is the ordinary spectral bands difference. (d) is the map of the first three PCs as color channels and (e) is the reconstructed map using the first three PCs. 57
2.14 Result of Tasseled Cap transformation on a Landsat 7 images mosaic of Po River. (a) is the image mosaic consisting of 3 Landsat images. In (b) brightness, greenness and wetness components are placed in the color channels. The next three maps are brightness (c), greenness (d) and wetness (e) components of the transformed image. The map of the river extracted from wetness component is presented in (f). 58
2.15 Part of Niger River from Landsat 8 images. 60
2.16 Procedure of applying MAD transformation on multitemporal images . 60
2.17 (a) is the histogram of sum of squared and normalized MADs. (b) is the map of sum of squared and normalized MADs. (c) and (d) are the binary *change/no-change* maps considering two critical values: 14.067 and 20.278 61
2.18 Variance of the MAD components 62
2.19 MAD components of the two multitemporal images 62
2.20 Color composite of the last three MADs (red: MAD2, blue: MAD1, green: MAD3) 63
2.21 The result of MAF transformation on of the MAD components 64
2.22 The map of the first three MAFs (red: MAF2, blue: MAF1, green: MAF3) . 65
2.23 (a) ordinary difference of bands 6, 5 and 4 (b) color composite of MADs, (c) color composite of MAFs 65

3.1 (a) NIR band of MODIS MOD09Q1 image of Lake Nasser (date: 2000.05.25), (b) ASTER DEM map of the Lake, (c) slope map derived from the DEM map, (d) DEM-based mask developed regarding the DEM and slope maps, (e) the result of applying the defined mask on the image (a). By applying this mask, the search area is reduced from about 58 000 km^2 to 6 082 km^2 (about just 10% of the initial image). 69
3.2 Time series of three different types of pixel value behaviour during the time. Pixel (a) is always covered by water. Pixel (b) is located outside the lake territory. Pixel (c) is located in the borderline between the water and land. 70
3.3 (a) and (b) are the maps of mean and variance of the pixel values during the monitoring period. (c) presents the water mask generated regarding the mean and variance maps. 72
3.4 Four examples of pixel value histogram of modified search area of Nasser Lake. 73

3.5 (a) is the image of the modified search area which is the input for the ISODATA algorithm. The blue part is the constant-water mask with an area of 2 602.5 km^2. After applying this water mask, the final search area is reduced to 3 479.7 km^2. (b) is the result of the ISODATA classification, the search area divided into 4 clusters. In (c), the first cluster (yellow) is labelled as water and joined to the water mask. The other clusters are labelled as land. 75
3.6 Two examples of lake extent shapefiles. The Lake area is 6 017.5 km^2 on Nov 16, 2000 and 3 671.7 km^2 on July 20, 2001. 76
3.7 Time series of Nasser Lake surface water area. Monitoring period 2002–2015 76
3.8 Water coverage frequency map of Nasser Lake for the period 2000–2015 77
3.9 Comparison between Nasser Lake water area time series with in situ water level measurements (a) and altimetric water level measurements at two virtual stations (b, c). Monitoring period: 2000–2015 78
3.10 Scatter plot of water area vs. level time series of Nasser Lake. 79
3.11 (a) and (b) are the time series of in situ water level and lake water area of Nasser Lake. (c) and (f) are probability density functions of water level and area measurements. (d) and (g) are cumulative distribution functions of the two dataset. (e) and (h) are quantile functions of in situ water level and lake area measurements. (i) is the quantile look-up table derived from both quantile functions. In (j) obtained quantile function is plotted together with simultaneous lake height and area measurements. 81
3.12 (a) Lake water area measurements and estimation via quantile look-up table. The time series in (b) is the difference between estimated and measured lake area. In this time series, two epochs with the largest positive and negative residuals are highlighted for more investigation. (c,d) The scatter plot of the measured lake area and its difference with estimated ones. 82
3.13 Comparison between Nasser Lake derived shapefile and MODIS image on 27 June, 2000 (a) and 17 November, 2006 (b). The shapefiles are compared in three different parts in (c–h). 83
3.14 (a) is the MODIS image of the Rukwa Lake on April 15, 2002. (b) is the MODIS images of the lake on October 21, 2007. (c,d) are the Lake shapefiles extracted by the algorithm. (e) is the comparison between extracted Rukwa lake shapefiles on two different dates 84
3.15 Rukwa Lake area time series. The monitoring period is 2002–2015 . . . 84
3.16 Water coverage frequency map of Rukwa Lake for the period 2002–2015 85
3.17 Comparison between Rukwa Lake water area (blue) time series with altimetric water level(black). 85
3.18 Rukwa basin monthly precipitation is plotted together with altimetric water level in (a) and lake surface area (b) 86
3.19 Five MODIS images of Rukwa Lake from different epochs 87

3.20 (a) is the MODIS image of the Mosul Dam Lake on June 1, 2002. (b) is the MODIS images of the lake on November 26, 2011. (c,d) are the lake shapefiles extracted by the algorithm. (e) is the comparison between Mosul Lake shapefiles on two different dates 88
3.21 Mosul Dam Lake area time series. The monitoring period is 2002–2017 . 88
3.22 Water coverage frequency map of Mosul Dam Lake for the period 2002–2017 89
3.23 Comparison between Mosul Dam Lake water area time series with altimetric water level together with its scatter plot 89
3.24 (a) and (b) are images of Tharthar Lake on May 24, 2004 and March 14, 2009 and (c) and (d) are their extracted shapefiles. (e) is the comparison between Tharthar Lake on two different dates 90
3.25 Tharthar Lake water area time series between the years 2002–2017. . . . 91
3.26 Water coverage frequency map for Tharthar Lake for the period 2002–2017 91
3.27 Comparison between Tharthar water area and altimetric water level . . 92
3.28 Examples of MODIS MOD09Q1 images of Urmia Lake from different years (February) 92
3.29 Shapes of the Urmia Lake over the years 2000–2016. 93
3.30 time series of Urmia Lake surface water area together with its nonlinear trend. 94
3.31 Water coverage frequency maps for Urmia Lake. (a) is for the period 2000–2017, (b) is for the first six years 2000–2006, (c) for the period 2006–2012 and (d) for the last 5 years 2012–2017. 95
3.32 Comparison between Urmia Lake surface water area and in situ water level time series. 95
3.33 Scatter plot of surface water area versus in situ water level of Urmia Lake. The scatter plot is divided into four different time periods regarding the state of the Lake: 2001–2006, 2006–2010, 2010–2015, 2015–2017. . 96
4.1 Comparison between different river mask time series of Niger River reach derived by mentioned thresholding algorithms. Monitoring period: 02.2000–09.2014. 101
4.2 A four-neighbourhood system structure for the pixel p 103
4.3 A graph with two pixels in one dimension. Here we have four vertices (two pixels; p and q, two terminals; s and t) and five edges (four t-links $t_{s,p}$, $t_{s,q}$, $t_{t,p}$, $t_{t,q}$ and one n-link $e_{p,q}$) 106
4.4 Four different cuts can be applied to a graph with 2 pixels. The cost of each cut is equal to the sum of the weight of the respective dashed lines. The scenario with the smallest weight will be selected and, regarding remaining edges in the graph, new labels for the pixels will be assigned. 107

4.5 A simple scheme of an augmenting path procedure. (a) is a residual graph after a number of iterations. Here for each edge the capacity and the current flow is presented (capacity/current flow) and all the saturated edges are removed. In (b) another path from source to sink is found, in (c) a flow equal to the maximum capacity is pushed through the path and the residual graph is updated by eliminating the saturated edge. (d) is the final configuration of the residual graph because there is no connection between source and sink anymore. So, now based on the residual graph, the final labels structure for the pixels is defined 108

4.6 (a) representation of the final residual graph of Figure 4.5. (b) to measure the flow potential for the pixel 1, we assume that an t-link with an infinite capacity is available between pixel 1 and the land terminal. Now the connection between two terminals is established and the process of finding and augmenting new s-t paths starts again. (c) after augmenting all the new paths, the flow potential for the pixel 1 assigned the label water ($C_{W,1}$) is equal to the sum of the capacity of new paths ($C_{W,1}$=25). On the other hand, $C_{L,1}$=0 because pixel 1 does not connect to the other terminal in the residual graph. 111

4.7 Models for defining the conditional probabilities in equation 4.22. T is the threshold value for separating water and land in the initial water mask. 112

4.8 Two functions introduced for assessing the temporal behaviour of the pixels 113

4.9 Example of pixel values near the water-land boundary. This pattern is considered as a piecewise smooth prior 113

4.10 Flowchart of the proposed method 115

4.11 (a-e) the cloud detection filters accept images (a, c, e), and remove images (b, d). Images 116

4.12 Water coverage frequency map for the Niger River reach near Lokoja station. 117

4.13 Four examples of generated water masks in different situations. (a) original images; (b) initial water masks; (c) final water masks; (1, 2) relate to the dry and wet seasons. (3, 4) images suffer from cloud contamination. 118

4.14 (a) original image (date: 21.09.2000), (b) modified water mask from proposed method; (c, d) are water and land marginal probability maps in the first iteration; (e, f) after the second iteration. 119

4.15 Pixel value histogram of the image in Figure 4.14 is presented in (a), water and land separated by different color. Histogram of the water and land probabilistic masks in the first iteration (b) and the second iteration (c). 120

4.16 Time series of water masks marginal probabilities for the first and second iterations. Monitoring period: 02.2000–09.2014 121

4.17 Water and land pixels present in blue and dark brown, respectively. The number of pixels with less than 10% marginal probability are shown in white. The black line represents the MAP solution in the graph. Monitoring period: 02.2000–09.2014 121
4.18 (a) Water area with its uncertainty. (d) Scatter plot of water area vs. percentage of uncertainty. (b, c) Water area is plotted with in situ discharge and altimetric water level. (e, f) Scatter plots of simultaneous water area measurements against discharge and water level. Period of monitoring: 02.2000–09.2014 122
4.19 Subfigures (1, 2) are two examples of the river reach (Niger River, Koulikoro Station) in dry and wet seasons. Subfigures (3, 4) are the river reach masks derived by the proposed algorithm 123
4.20 (a) Water area vs. uncertainty. (d) Scatter plot of water area vs. percentage of uncertainty. (b, c) Water area vs in situ discharge and altimetric water level. (e, f) Scatter plots of simultaneous water area measurements against discharge and water level. Period of monitoring: 02.2000–02.2016 124
4.21 (1, 2) are two examples of the river section (Congo River, Malebo Pool) in dry and wet seasons. (3, 4) are the water masks determined by the proposed method. 125
4.22 (a) Water area monitoring together with the uncertainty. (d) Scatter plot of water area vs. percentage of uncertainty. (b, c) Water area is plotted with in situ discharge and altimetric water level. (e, f) Scatter plots of simultaneous water area measurements against discharge and water level. Period of monitoring: 02.2000–02.2016 126
4.23 An example of the Po River image acquired in 2000.07.28 is in the top panel and in the bottom panel is the extracted river mask by applying the proposed method. 127
4.24 (a) Time series of river reach area measurements together with their uncertainties. (d) Scatter plot of river reach area vs. percentage of uncertainty. (b, c) River area is plotted with in situ discharge and altimetric water level. (e, f) Scatter plots of simultaneous water area against river discharge and water level measurements. Period of monitoring: 02.2000–07.2016 128
4.25 River reaches selected for developing river width-discharge models. (a) Niger River near Lokoja station. (b) Congo River near Brazzaville station. (c) Niger River near Koulikoro station. (d) Po River near Borgoforte station. The red dots are the in situ stations. Additional information about the in situ stations is provided in Table 1.10 130
4.26 River discharge and width measurements used to develop *W*-*Q* models for all four case studies. Time series in (a-d) are time series of river width and discharge measurements and the scatter plots of simultaneous measurements are in (e-h). 131
4.27 Scatter plots in (a-d) are the simultaneous observations used for developing models. Red and green bars are the measurement uncertainties. The *W*-*Q* rating curve models are presented in (e-h). 132

4.28 Comparison between measured and predicted river discharge via developed *W*-*Q* models. The red bars are the difference between measured and predicted values. (a) Niger (Lokoja station), (b) Congo River (Kinshasa station), (c) Niger River (Koulikoro station), (d) Po River (Borgoforte station). 134
4.29 (a) and (b) are the quantile functions of river width measurements for Congo and Po River reaches. (c) and (f) are the quantile functions of in situ discharge measurements. (b) and (e) are the developed quantile look-up tables for Congo and Po River reaches. 137
4.30 Comparison between estimated river discharge via quantile look-up table and measured discharge for Congo River (a) and Po River (c) reaches. The difference between measured and estimated values are plotted as red bars. 138

List of Tables

1.1 Description of different spectrum bands 15
1.2 Description of different spectrum bands 17
1.3 Overview of studies using satellite images to extract the water bodies. . 22
1.4 Information about case studies of this thesis 28
1.5 List of available bands in Landsat 7 29
1.6 List of available bands in Landsat 8 29
1.7 List of available bands in MODIS MOD09A1 30
1.8 Satellite images used in this thesis 31
1.9 Datasets used for validation of Lake water masks 31
1.10 Information about datasets used for validation of river water masks . . . 32

2.1 The eigenvalues and their percentage derived from both covariance and correlation matrices. 47
2.2 The eigenvalues and their percentage from the total correlation for all three measurement epochs. 48
2.3 Eigenvectors of all image bands (date: 2012.01.01) 51
2.4 Eigenvectors of combination of two multispectral image bands PC1 to PC6 55
2.5 Coefficients of Kauth-Thomas Tasseled Cap Transformation for LandSat 7 image 57

4.1 Information about training and validation datasets used for developing river width-discharge models 130
4.2 Statistics for evaluating the performance of the derived *W*-*Q* models. . . 135
4.3 Statistics for evaluating the performance of quantile look-up tables. . . . 139

Appendix A

Performance metrics

In this appendix, we introduce four statistical performance metrics used in this thesis for assessing the performance of developed results:

Correlation coefficient measures how the change in one variable can be predicted by the change in the other one:

$$r_{p,q} = \frac{\sum_{i=1}^{n} (p_i - \overline{p})(q_i - \overline{q})}{\sqrt{\sum_{i=1}^{n} (p_i - \overline{p})^2 \sum_{i=1}^{n} (q_i - \overline{q})^2}}, \tag{A.1}$$

where p and q could be either different types of observation (like river reach area and height) or measured and estimated values of a parameter (for example, the measured and estimated river discharge). n is the number of available sample. $\overline{p}$ and $\overline{q}$ are the mean of the corresponding vector. This coefficient varies between -1 and 1. There is no discernible relationship between two dataset fluctuations if the correlation coefficient equals to zero. A prefect positive correlation ($r = 1$) means that both variables always change in a same direction with a same magnitude. Therefore, a close to 1 value for correlation is representative of a strong linear relationship between them. On the other hand, a negative correlation shows that both variables move in opposite directions.

Root Mean Square Error (RMSE) measures the average difference between observed and estimated values.

$$\text{RMSE} = \sqrt{\frac{\sum_{i=1}^{n} (p_{\text{est}_i} - p_{\text{obs}_i})^2}{n}} \tag{A.2}$$

In this equation p_{est} is the vector of estimated values by the model, p_{obs} is the vector of observed values. This indicator is always positive and in ideal situation, it is near

zero. So the smaller the RMSE value, the better the model. The RMSE derived from equation (A.2) has a unit and it does not have any upper limit. So for simplifying the interpretation, it is usually normalized by the mean of the observed data and then the result is reported in percentage.

Nash-Sutcliffe Efficiency (NSE) is introduced by Nash & Sutcliffe (1970):

$$\mathrm{NSE} = 1 - \frac{\sum_{i=1}^{n} (p_{\mathrm{est}_i} - p_{\mathrm{obs}_i})^2}{\sum_{i=1}^{n} (p_{\mathrm{est}_i} - \overline{p}_{\mathrm{obs}})^2} \tag{A.3}$$

It measures the performance of the model by relating the magnitude of residuals to the variance of observed values (Gupta et al., 1999). This metric is unitless and its range is between $(-\infty, 1]$. When the NSE equals to 1 for a model, there is a perfect match between the observed and estimated values in terms of their phase and amplitude. The model predictions are as accurate as the average of measured data, if the NSE is zero. When the NSE value is negative, it is better to replace the predicted values with the mean of observed values.

Percent bias (PBIAS) calculates the average tendency of the model to predict larger or smaller than the real value (Gupta et al., 1999).

$$\mathrm{PBIAS} = \frac{\sum_{i=1}^{n} (p_{\mathrm{obs}_i} - p_{\mathrm{est}_i})}{\sum_{t=1}^{n} p_{\mathrm{obs}_i}} \tag{A.4}$$

This value is usually reported in percentage. The optimal value for the PBIAS is zero. It means than there is no systematic tendency in the predicted values to be larger or smaller than the actual values. The positive value shows that the model has an inclination to underestimate and respectively a negative PBIAS indicates that the model estimations are in average larger than the real values.

Appendix B

Gauss-Helmert adjustment model

It is assumed that a power law relationship is established between river discharge and width in a natural river section:

$$Q = aW^b \ , \tag{B.1}$$

where Q is in situ discharge measurement, W is the average width of the river reach and a and b are the unknown model parameters. Once the model parameters are defined, we are able to predict river discharge by using the river width measurements and estimated model parameters.

The observations (river discharge and width) in both sides of equation (B.1) are corrupted by noise. Therefore to estimate the model parameters (a and b), the squared sum of inconsistencies must be minimized. One approach is to reformulate the above equation as a non-linear conditional equation with unknowns. This model is called the general model of adjustment or Gauss-Helmert model.

$$f(a, b, e_{\mathrm{Q}}, e_{\mathrm{W}}) = Q - e_{\mathrm{Q}} - a(W - e_{\mathrm{W}})^b = 0 \ . \tag{B.2}$$

Solving equation (B.2) by least squares adjustment leads to the determination of the model parameters and observation inconsistencies simultaneously.

The algorithm starts with linearizing the functional equation using a Taylor series. For the Taylor point we assume that the observation inconsistency vectors (e_Q and e_W) are equal to zero. Therefore, equation (B.1) is reshaped by applying the logarithm operator to both sides.

$$\log(Q) = \log(a) + b \log(W). \tag{B.3}$$

The matrix notation of the aforementioned equation is

$$\underbrace{\begin{bmatrix} \log(Q_1) \\ \vdots \\ \log(Q_n) \end{bmatrix}}_{\boldsymbol{y}} = \underbrace{\begin{bmatrix} 1 & \log(W_1) \\ \vdots & \vdots \\ 1 & \log(W_n) \end{bmatrix}}_{\boldsymbol{A}} \underbrace{\begin{bmatrix} \log(a) \\ b \end{bmatrix}}_{\boldsymbol{x}_0}, \tag{B.4}$$

in this equation n is the number of simultaneous river discharge and width measurements. The initial values for unknown model parameters will be estimated by using the least squares adjustment.

$$\widehat{\boldsymbol{x}}_0 = (\boldsymbol{A}^T\boldsymbol{A})^{-1}\boldsymbol{A}^T\boldsymbol{y} \tag{B.5}$$

so, a_0 and b_0 are the first and second elements of $\widehat{\boldsymbol{x}}_0$. Now, we can write the Taylor series expansion:

$$\begin{aligned} f_i(a,b,Q_i,W_i) &= f_i(a_0,b_0,Q_i^0,W_i^0) + \left.\frac{\partial f_i}{\partial Q_i}\right|_0 (Q_i - Q_i^0 + e_{Q_i}) + \left.\frac{\partial f_i}{\partial W_i}\right|_0 (W_i - W_i^0 + e_{W_i}) \\ &\quad + \left.\frac{\partial f_i}{\partial a}\right|_0 (a - a_0) + \left.\frac{\partial f_i}{\partial b}\right|_0 (b - b_0). \end{aligned}$$

$$\begin{aligned} f_i(a,b,Q_i,W_i) &= \underbrace{f_i(a_0,b_0,Q_i^0,W_i^0) + \left[\left.\frac{\partial f_i}{\partial Q_i}\right|_0 \left.\frac{\partial f_i}{\partial W_i}\right|_0\right]\begin{bmatrix}\delta Q_i \\ \delta W_i\end{bmatrix}}_{\omega} + \underbrace{\left[\left.\frac{\partial f_i}{\partial Q_i}\right|_0 \quad \left.\frac{\partial f_i}{\partial W_i}\right|_0\right]}_{B^T}\begin{bmatrix}e_{Q_i} \\ e_{W_i}\end{bmatrix} \\ &\quad + \underbrace{\left[\left.\frac{\partial f_i}{\partial a}\right|_0 \quad \left.\frac{\partial f_i}{\partial b}\right|_0\right]}_{A}\begin{bmatrix}\delta a \\ \delta b\end{bmatrix}. \end{aligned} \tag{B.6}$$

In the end we can write the equation like

$$\underset{n\times 1}{\boldsymbol{\omega}} + \underset{n\times 2n}{\boldsymbol{B}^T}\,\underset{2n\times 1}{\boldsymbol{e}} + \underset{n\times 2}{\boldsymbol{A}}\,\underset{2\times 1}{\delta\xi} = 0, \tag{B.7}$$

where the vector of misclosures ($\boldsymbol{\omega}$) is

$$\boldsymbol{\omega}_{n\times 1} = \begin{bmatrix} f_1(a^0,b^0,Q_1^0,W_1^0) + \left[\left.\frac{\partial f_1}{\partial Q_1}\right|_0 \quad \left.\frac{\partial f_1}{\partial W_1}\right|_0\right]\begin{bmatrix}\delta Q_1 \\ \delta W_1\end{bmatrix} \\ \vdots \\ f_n(a^0,b^0,Q_n^0,W_n^0) + \left[\left.\frac{\partial f_n}{\partial Q_n}\right|_0 \quad \left.\frac{\partial f_n}{\partial W_n}\right|_0\right]\begin{bmatrix}\delta Q_n \\ \delta W_n\end{bmatrix} \end{bmatrix} \tag{B.8}$$

and the matrix $\boldsymbol{B}^T$ is

$$\boldsymbol{B}^T_{n\times 2n} = \begin{bmatrix} \left.\frac{\partial f_1}{\partial Q_1}\right|_0 & 0 & \cdots & 0 & \left.\frac{\partial f_1}{\partial W_1}\right|_0 & 0 & \cdots & 0 \\ 0 & \left.\frac{\partial f_2}{\partial Q_2}\right|_0 & \cdots & 0 & 0 & \left.\frac{\partial f_2}{\partial W_2}\right|_0 & \cdots & 0 \\ \vdots & \vdots & \ddots & \vdots & \vdots & \vdots & \ddots & \vdots \\ 0 & 0 & \cdots & \left.\frac{\partial f_n}{\partial Q_n}\right|_0 & 0 & 0 & \cdots & \left.\frac{\partial f_n}{\partial W_n}\right|_0 \end{bmatrix}, \tag{B.9}$$

The vector of observation inconsistencies is

$$\boldsymbol{e}_{2n\times 1} = \begin{bmatrix} e_{Q_1} & \cdots & e_{Q_n} & e_{W_1} & \cdots & e_{W_n} \end{bmatrix}^T, \tag{B.10}$$

in the first iteration we consider all elements of $\boldsymbol{e}$ vector equal to zero, but in the later iterations we will update them. Finally, the Jacobian matrix $\boldsymbol{A}$

$$\boldsymbol{A}_{n\times 2} = \begin{bmatrix} \frac{\partial f_1}{\partial a}\big|_0 & \frac{\partial f_1}{\partial b}\big|_0 \\ \vdots & \vdots \\ \frac{\partial f_n}{\partial a}\big|_0 & \frac{\partial f_n}{\partial b}\big|_0 \end{bmatrix}. \tag{B.11}$$

Now our aim is to determine the optimal values for the vectors $\boldsymbol{e}$ and $\delta\xi$ by minimizing our target function $\boldsymbol{e}^T\boldsymbol{P}\boldsymbol{e}$, where $\boldsymbol{P}$ is the weight matrix

$$\boldsymbol{P}_{2n\times 2n} = \begin{bmatrix} \frac{1}{\sigma^2_{Q_1}} & \cdots & \cdots & 0 & \cdots & \cdots & \cdots & 0 \\ 0 & \frac{1}{\sigma^2_{Q_2}} & \cdots & 0 & \cdots & \cdots & \cdots & \vdots \\ \vdots & \vdots & \ddots & \vdots & \cdots & \cdots & \cdots & \vdots \\ 0 & 0 & \cdots & \frac{1}{\sigma^2_{Q_n}} & \cdots & \cdots & \cdots & \vdots \\ \vdots & \cdots & \cdots & \cdots & \frac{1}{\sigma^2_{W_1}} & 0 & \cdots & 0 \\ \vdots & \cdots & \cdots & \cdots & 0 & \frac{1}{\sigma^2_{W_2}} & \cdots & 0 \\ \vdots & \cdots & \cdots & \cdots & \vdots & \vdots & \ddots & \vdots \\ 0 & \cdots & \cdots & \cdots & 0 & 0 & \cdots & \frac{1}{\sigma^2_{W_n}} \end{bmatrix} \tag{B.12}$$

So, we introduce the Lagrange multipliers to minimize the target function

$$\mathcal{L}(\boldsymbol{e}, \delta\xi, \boldsymbol{\lambda}) = \boldsymbol{e}^T\boldsymbol{P}\boldsymbol{e} + \boldsymbol{\lambda}^T(\boldsymbol{\omega} + \boldsymbol{B}^T\,\boldsymbol{e} + \boldsymbol{A}\,\delta\xi)\,, \tag{B.13}$$

setting the gradients to zero yields the first order optimality conditions

$$\frac{\partial\mathcal{L}}{\partial\boldsymbol{e}}(\widehat{\boldsymbol{e}}, \widehat{\delta\xi}, \widehat{\boldsymbol{\lambda}}) = 0 \qquad \Rightarrow \qquad \widehat{\boldsymbol{e}} + \boldsymbol{P}^{-1}\boldsymbol{B}\widehat{\boldsymbol{\lambda}} = 0 \tag{B.14}$$

$$\frac{\partial\mathcal{L}}{\partial\delta\xi}(\widehat{\boldsymbol{e}}, \widehat{\delta\xi}, \widehat{\boldsymbol{\lambda}}) = 0 \qquad \Rightarrow \qquad \boldsymbol{A}^T\widehat{\boldsymbol{\lambda}} = 0 \tag{B.15}$$

$$\frac{\partial\mathcal{L}}{\partial\boldsymbol{\lambda}}(\widehat{\boldsymbol{e}}, \widehat{\delta\xi}, \widehat{\boldsymbol{\lambda}}) = 0 \qquad \Rightarrow \boldsymbol{B}^T\widehat{\boldsymbol{e}} + \boldsymbol{A}\widehat{\delta\xi} + \boldsymbol{\omega} = 0 \tag{B.16}$$

By replacing the equivalent of the vector $\widehat{e}$ from the equation (B.14) into the equation (B.16), we write the matrix form of the equations

$$\begin{bmatrix} \underset{n\times n}{\boldsymbol{B}^T\boldsymbol{P}^{-1}\boldsymbol{B}} & \underset{n\times 2}{-\boldsymbol{A}} \\ \underset{2\times n}{-\boldsymbol{A}^T} & \underset{2\times 2}{\boldsymbol{0}} \end{bmatrix} \begin{bmatrix} \underset{n\times 1}{\widehat{\lambda}} \\ \underset{2\times 1}{\widehat{\delta\xi}} \end{bmatrix} = \begin{bmatrix} \underset{n\times 1}{\boldsymbol{\omega}} \\ \underset{2\times 1}{\boldsymbol{0}} \end{bmatrix} \tag{B.17}$$

The solution of this linear system will be

$$\begin{bmatrix} \widehat{\lambda} \\ \widehat{\delta\xi} \end{bmatrix} = \begin{bmatrix} \boldsymbol{B}^T\boldsymbol{P}^{-1}\boldsymbol{B} & -\boldsymbol{A} \\ -\boldsymbol{A}^T & \boldsymbol{0} \end{bmatrix}^{-1} \begin{bmatrix} \boldsymbol{\omega} \\ \boldsymbol{0} \end{bmatrix} \tag{B.18}$$

By estimating $\widehat{\lambda}$ and $\widehat{\delta\xi}$, now we can update the value for the $\widehat{e}$ vector using the equation (B.14). After each iteration the value of the initial model parameters will be updated:

$$\begin{bmatrix} a^0_{\text{new}} \\ b^0_{\text{new}} \end{bmatrix} = \begin{bmatrix} a^0_{\text{old}} + \widehat{\delta\xi}(1) \\ b^0_{\text{old}} + \widehat{\delta\xi}(2) \end{bmatrix} \tag{B.19}$$

The iteration with the updated initial model parameters and vector of inconsistencies will be continued until one of the following conditions will be satisfied

$$\|\widehat{\delta\boldsymbol{\xi}}\| < \varepsilon \ , \ \ \|\widehat{e}_{\text{new}} - \widehat{e}_{\text{old}}\| < \varepsilon \tag{B.20}$$

Apart from the model parameters, we can estimate the variance covariance matrix of the unknown parameters

$$\widehat{\Sigma}_x = (\boldsymbol{A}^T(\boldsymbol{B}^T\boldsymbol{P}\boldsymbol{B})^{-1}\boldsymbol{A})^{-1}, \tag{B.21}$$

and by estimating the posterior variance of unit weight ($\widehat{\sigma}$)

$$\widehat{\sigma} = \sqrt{\frac{\widehat{e}^T \ P \ \widehat{e}}{n-2}} \ , \tag{B.22}$$

where, n is the number of observations, $\boldsymbol{P}$ is the weight matrix and $\widehat{e}$ contains the final estimated inconsistencies of the observations. Therefore, the variance-covariance matrix of adjusted unknown parameters will be defined as

$$\widehat{\boldsymbol{\Sigma}}_{\widehat{x}} = \widehat{\sigma}\widehat{\boldsymbol{\Sigma}}_{\boldsymbol{x}} \tag{B.23}$$

Index

active system, 13
adjustment with condition equations model, 134
aerial photograph, 1, 2
aerosol, 4
affine transformation, 41, 59
Africa, 7, 24, 26, 85, 100
altimetric water level, 11, 31, 79, 80, 87, 88, 91, 94, 100
altimetric virtual station, 79, 80
annual behaviour, 24, 69, 71, 72, 78, 86, 87, 90, 91, 93, 94, 96, 97, 99
artificial lake, 78, 89, 92, 100
Asia, 24, 100, 92
Aswan Dam, 26, 78
ATI technique, 9
atmospheric absorption, 16, 17
atmospheric calibration, 14, 36
augmenting path, 110

Bani River, 24
bathymetric map, 10
binary decision classifier, 21
Borgoforte station- Po River, 32, 137, 138
breadth-first search algorithm, 110
Brazzaville city, 128

canonical variable, 41
case study
  Congo River, 26, 127, 133, 138
  Mosul Dam Lake, 27, 89–91, 100
  Nasser Lake, 26, 78–81, 83, 85, 100
  Niger River, 24, 59
  Po River, 26, 58, 129, 133
  Rukwa Lake, 26, 85–89, 100
  Tharthar Lake, 27, 92–94, 100
  Urmia Lake, 27, 94–100
CCA, 21, 41
change detection, 14, 18, 19, 24
change detection method
  advanced model, 20
  algebra, 19
  classification, 20
  GIS-based, 20
  transformation, 19
  visual analysis, 20
change/no-change map, 44, 60, 61
climate change, 4, 12, 27
cloud coverage, 3, 13, 15, 71, 72, 89, 100, 116, 118, 127, 141
cluster, 75–77, 100
coastal area, 21, 72
combinational optimization, 108
confidence measure, 113, 120
contextual information, 23
correlation coefficient, 32, 79, 80, 87, 91, 94, 97, 98, 100, 173
correlation matrix, 37, 38
covariance matrix, 37, 38
cut- graph cuts, 108

data center
  AIPO, 32
  CRU, 6
  GPCC, 6
  GPCP, 88
  GRDC, 7, 32
  USGS, 12
decision tree classification algorithm, 22
DEM, 8, 9, 21, 70, 71, 73, 94, 99
depth-first search algorithm, 110
desiccation, 27, 94–97, 99, 100
digital elevation model
  ASTER, 70
  SRTM, 8–10, 70

Dinic algorithm, 110
Doppler centroid anomalies technique, 9
drought, 4
dynamic water mask, 75, 79,127, 135, 153

Earth surface temperature, 4
edge, 108
Elbe River, 10
EM energy, 14
empirical relationship, 11
energy function, 104
energy minimization problem, 104, 141
EOF, 35
Euphrates River, 27, 92
Europa, 24
evaporation, 4, 6
evapotranspiration, 6

flood, 4, 12, 13, 26, 69, 70
flood monitoring, 13, 19, 104
floodplain, 7, 9
flow potential, 112, 113
Ford-Fulkerson augmenting paths algorithms, 109, 110

Gauss-Helmert model, 134, 143, 175
Gauss-Markov model, 134
geometrical rectification, 59
global elevation map, 8
global gridded precipitation data, 6
global warming, 4, 5, 7
Goldberg-Tarjan push-relabel algorithms, 109
graph, 105, 108
graph cuts, 104, 111
greenhouse gas, 4
groundwater, 6, 12, 95

hazard monitoring, 131
histogram, 21, 74, 75, 121
hydrological cycle, 5, 6
hydrological model, 7–9
hypersaline lake, 27, 98

image compression, 36
image difference, 56
image enhancement, 36
image registration, 59
in situ discharge measurement, 7, 11, 128, 135
in situ water level measurement, 31, 79–83, 97, 98, 100
inference algorithm, 111
initial water mask, 118
inland surface water, 8, 9
InSAR, 8, 9
inundation area, 9, 13
IR band, 2, 14
Iran, 94
ISODATA, 21, 75–77, 100, 102

k-means clustering, 21, 75, 118
Kinshasa station- Congo River, 26, 136
khor, 26, 77, 79, 85
Kohli and Torr method, 111, 120, 124
Koulikoro station- Niger River, 26, 125, 137

99
lake, 9, 12, 69–75, 77, 78, 86
lake bathymetry, 80, 98
lake boundary, 71–75, 77, 86, 89, 91, 93, 94, 100
lake extent, 69, 70, 77–80, 90, 92
lake mask, 77, 94, 99, 100
lake seabed, 96
land-cover change, 4, 18
landscape change, 19
light spectrum, 3, 16
Lokoja station- Niger River, 26, 118, 123, 135, 137

max-flow solution, 119
MAD transformation, 35, 42, 59
MAD/MAF transformation, 35, 46
MAF transformation, 35, 44, 59
Malebo Pool- Congo River, 26, 129
marginal probability, 111, 120
Markov Random Fields, 4, 107–110
max-flow algorithm, 108, 114
max-marginal probability, 112, 113, 117

Maximum A Posteriori, 103
maximum flow, 104, 109, 120
maximum likelihood classification, 21
mean map, 73, 74, 100
min-cut solution, 108
min-marginal energy, 111, 113, 120
min-marginal energy function, 111
minimum cut, 104
misclassification, 77, 84, 85
mismodeling error, 81, 84, 143
MNDWI, 18
MODIS product
    MOD09A1, 46
    MOD09Q1, 30, 31, 69, 71, 94, 95
    MOD44W, 75
multi-layer color film, 1
multispectral image, 2, 3, 16, 21, 24
MultiSpectral Scanner, 2
multispectral transformation, 24, 35
multitemporal images, 14, 44

n-link, 108, 112, 116
Nash-Sutcliffe Efficiency, 33, 141–145, 174
NDVI, 16, 22
NDWI, 17, 18, 22
neighbour interaction function, 106
Nile River, 26
NIR band, 15, 16, 69, 71, 72, 75, 100
NPP-VIIRS, 23

ocean surface elevation, 9
ocean surface velocity field, 9
online database
    DAHITI, 31, 32, 91
    HydroSat, 31, 87
optical image, 2, 3, 14, 71, 99, 100
orthogonal transformation, 37

passive system, 14
PCA transformation, 21, 35
percent bias, 34, 141–145, 174
phase shift, 87, 89
physically-based transformation, 40
piecewise smooth prior model, 115
pixel-based classification, 23, 74, 121
point cloud, 80, 82, 87, 98
power law relationship, 17, 135, 175
precipitation, 4, 6, 13, 88, 89, 100
preflow, 109
principal components, 38
probabilistic water mask, 113, 120, 141

quantile function, 81–83
quantile look-up table, 81–84, 133, 143

radar, 2–3, 6
radiometric calibration, 14, 16, 36, 44, 59
Random Forest classification algorithm, 21
rating curve, 11, 81
region-based classification, 23, 74, 103 14
repeat orbit satellite, 9
reservoir, 12, 27, 69, 70
residual graph, 109, 112, 120
river depth, 10, 11
river discharge estimation, 10, 131
river hydraulic parameter, 11, 101
river section, 7, 11, 135
river slope, 9, 101
river width, 10, 129, 135–145
root mean square error, 11, 33, 141, 173

s-t path, 109, 110, 113, 119
SAR system, 3, 4, 9, 10, 13 78
satellite altimetry, 8, 9, 23, 79
satellite image, 9, 11–13, 69, 85, 99
satellite mission
    ALOS-2, 4
    CryoSat-2, 32
    ENVISAT, 4, 9, 80, 126, 142
    ERS-1, 3
    ERS-2, 3
    Explorer I, 2
    GeoEye, 3
    GRACE, 6, 23
    IKONOS, 40
    Jason-1, 31
    Jason-2, 31, 32
    Landsat 1, 2
    Landsat 5, 2, 22, 40

Landsat 7, 22, 27, 58
Landsat 8, 2, 22, 27, 28, 59
QuickBird, 3
Saral/AltiKa, 32, 126, 142
Seasat, 3
Sentinel-1, 4
SPOT 1, 3
SPOT 5, 22
SPOT 7, 3
Sputnik I, 2
SWOT, 12
TanDEM-X, 10
Terra/Aqua MODIS, 18, 21, 27, 70, 75, 77, 84–86, 88–90, 92, 94, 126, 141
TerraSAR-X, 4, 10
TIROS, 2
TOPEX/Poseidon, 9
U-2, 2
scatter plot, 80–82, 84, 87, 91, 92, 98, 99, 128, 137–140
sea surface temperature, 35
search area, 69–75, 77, 92, 94, 99, 100
seasonal behaviour, 24, 70
Secchi depth, 10
sediment, 17
segmentation, 77
shapefile, 69, 77, 78, 84–86, 89, 90, 92, 93
shoreline, 85–87, 89, 90, 97, 99, 100
signal to noise ratio, 35, 36, 48
simulated annealing, 104
simultaneous observations, 11, 80–82, 92, 98, 99, 131
simultaneous observations approach, 133
singular spectrum analysis, 96
sink, 108
slope map, 70, 99
soil moisture, 6, 14, 17, 39
solar illumination, 3, 14, 16, 59
solar radiation, 13
source, 108
South America, 7
space agency
CNES, 12
DLR, 10
ESA, 3
NASA, 2–4, 12
spaceborne geodetic sensor, 8, 10, 11, 99
spatial correlation, 44, 74, 104
spatial pattern, 115
spatial resolution, 2–4, 7, 13, 14, 18, 69, 70, 84, 94
spectral band, 2, 3, 12, 16
spectral resolution, 14
standard deviation, 75, 76, 78, 82, 84
static water mask, 21, 27, 79
sunglint, 10, 71, 72, 141
sunlight, 16, 20, 52, 71, 72
supervised classification, 21, 23, 74
surface water roughness, 10
surface water velocity, 9, 10
SVD, 38
SWIR band, 2, 15, 17

t-link, 108, 112, 114
Tasselled Cap transformation, 39, 56
brightness component, 39, 57
greenness component, 39, 57
wetness component, 39, 57
temporal resolution, 13, 18, 69, 80, 94
terminal, 108, 110
thresholding algorithm, 21, 74, 75, 102
convex hull, 102
maximum entropy, 102
moment preserving, 102
Otsu, 102
Tigris River, 27, 89, 92
time-variable seasonal behaviour, 96
topography, 87
total energy function, 111
transpiration, 6
trend, 86, 87, 94, 96, 99, 100
tropical storm, 4

uncertain region, 122
unsupervised classification, 21, 23, 74, 75, 100

variance map, 73, 74, 100
vertex, 108

visible light region, 14, 15

W-Q model, 131, 135, 137, 142 70, 77, 92
water coverage frequency map, 78, 79, 86, 87, 91, 93, 97, 114, 118
water current measurement, 10
water cycle, 4, 5, 12, 23, 69
water depth, 10, 17
water extent, 12
water level, 9, 79–83, 87–92, 94, 97, 98
water mask, 21, 70, 72–75, 77, 94, 99, 100
water storage, 6, 7
water volume, 11, 77, 78, 90, 100
water-land boundary, 14, 16, 17, 51, 70, 86, 115
weather satellite, 6
weight function, 108, 118
wetland, 7, 18

Yellow River, 21